Computational spectroscopy of atoms and applications to the fundamental problems

Author:
Allehabi, Saleh

Publication Date:
2023

DOI:
https://doi.org/10.26190/unsworks/24968

Computational spectroscopy of atoms and applications to the fundamental problems

Saleh O. Allehabi

Supervisors :

Prof. Victor Flambaum, Dr. Vladimir Dzuba, and A. Prof. Julian Berengut

A thesis in fulfilment of the requirements for the degree of

Doctor of Philosophy

School of Physics

Faculty of Science

The University of New South Wales

July 10, 2023

THE UNIVERSITY OF NEW SOUTH WALES
Thesis/Dissertation Sheet

Surname or Family name: **Allehabi**

First name: **Saleh**

Abbreviation for degree as given in the University calendar: **PhD**

School: **School of Physics** Faculty: **Faculty of Science**

Title: Computational spectroscopy of atoms and applications to the fundamental problems

Abstract

Computations of the spectroscopic properties of several heavy atoms have been performed to establish a link between recent measurements and some problems in modern physics. Calculations for No and Fm atoms demonstrated that isotope shift measurements can be used to study nuclear structure by extracting nuclear parameters beyond the root mean square (RMS) radius, such as the quadrupole deformation. Calculations of isotope shift in Yb^+ ion indicated that observed non-linearities of the King plot can be explained by nuclear deformation. This is a major systematic effect in the search for new interactions.

Calculation of hyperfine structure (HFS) for heavy and superheavy elements provides a possibility to extract from future HFS measurements magnetic dipole and electric quadrupole moments of the nuclei. We carried out calculations of the magnetic dipole HFS constant (A) and electric quadrupole HFS constant (B) for the superheavy elements Fm and Rf and the heavy elements Cf and Es. Similar calculations have also been performed on the lighter homologs Er, Hf, Dy, and Ho, whose electronic structures are similar to Fm, Rf, Cf, and Es, respectively, to verify the calculations.

We studied many excited metastable states in many heavy atoms and ions and found promising systems which can be used as very accurate atomic clocks which are highly sensitive to new physics. A number of atomic properties, such as energy levels, transition amplitudes, lifetimes, polarizabilities of the ground and clock states, etc., have been calculated. We found that relative blackbody radiation (BBR) shifts are small, between 10^{-16} and 10^{-18}, and the effects of variation of the fine-structure constant (α) are enhanced up to 8.3 times.

Calculations of atomic systems have been done using two different approaches. The choice depends on the number of valence electrons. The first method is called CI+SD (configuration interaction with single-double coupled cluster method), which is applicable to atomic systems with a few valence electrons (up to four). The second method is called CIPT (configuration interaction with perturbation theory method). It is designed to work with atomic systems with many valence electrons (more than four).

Declaration relating to disposition of project thesis/dissertation

I hereby grant the University of New South Wales or its agents a non-exclusive licence to archive and to make available (including to members of the public) my thesis or dissertation in whole or part in the University libraries in all forms of media, now or here after known. I acknowledge that I retain all intellectual property rights which subsist in my thesis or dissertation, such as copyright and patent rights, subject to applicable law. I also retain the right to use all or part of my thesis or dissertation in future works (such as articles or books).

Signature: Witness Date: **July 10, 2023**

The University recognises that there may be exceptional circumstances requiring restrictions on copying or conditions on use. Requests for restriction for a period of up to 2 years must be made in writing. Requests for a longer period of restriction may be considered in exceptional circumstances and require the approval of the Dean of Graduate Research.

Welcome to the Research Alumni Portal, Saleh Allehabi!

You will be able to download the finalised version of all thesis submissions that were processed in GRIS here.

Please ensure to include the **completed declaration** (from the Declarations tab), your **completed Inclusion of Publications Statement** (from the Inclusion of Publications State tab) in the final version of your thesis that you submit to the Library.

Information on how to submit the final copies of your thesis to the Library is available in the completion email sent to you by the GRS.

Thesis submission for the degree of Doctor of Philosophy

Thesis Title and Abstract | **Declarations** | **Inclusion of Publications Statement** | **Corrected Thesis and Responses**

ORIGINALITY STATEMENT

☑ I hereby declare that this submission is my own work and to the best of my knowledge it contains no materials previously published or written by another person, or substantial proportions of material which have been accepted for the award of any other degree or diploma at UNSW or any other educational institution, except where due acknowledgement is made in the thesis. Any contribution made to the research by others, with whom I have worked at UNSW or elsewhere, is explicitly acknowledged in the thesis. I also declare that the intellectual content of this thesis is the product of my own work, except to the extent that assistance from others in the project's design and conception or in style, presentation and linguistic expression is acknowledged.

COPYRIGHT STATEMENT

☑ I hereby grant the University of New South Wales or its agents a non-exclusive licence to archive and to make available (including to members of the public) my thesis or dissertation in whole or part in the University libraries in all forms of media, now or here after known. I acknowledge that I retain all intellectual property rights which subsist in my thesis or dissertation, such as copyright and patent rights, subject to applicable law. I also retain the right to use all or part of my thesis or dissertation in future works (such as articles or books).

For any substantial portions of copyright material used in this thesis, written permission for use has been obtained, or the copyright material is removed from the final public version of the thesis.

AUTHENTICITY STATEMENT

☑ I certify that the Library deposit digital copy is a direct equivalent of the final officially approved version of my thesis.

Welcome to the Research Alumni Portal, Saleh Allehabi!

You will be able to download the finalised version of all thesis submissions that were processed in GRIS here.

Please ensure to include the **completed declaration** (from the Declarations tab), your **completed Inclusion of Publications Statement** (from the Inclusion of Publications State tab) in the final version of your thesis that you submit to the Library.

Information on how to submit the final copies of your thesis to the Library is available in the completion email sent to you by the GRS.

Thesis submission for the degree of Doctor of Philosophy

Thesis Title and Abstract **Declarations** **Inclusion of Publications Statement** **Corrected Thesis and Responses**

UNSW is supportive of candidates publishing their research results during their candidature as detailed in the UNSW Thesis Examination Procedure.

Publications can be used in the candidate's thesis in lieu of a Chapter provided:

- The candidate contributed **greater than 50%** of the content in the publication and are the "primary author", i.e. they were responsible primarily for the planning, execution and preparation of the work for publication.
- The candidate has obtained approval to include the publication in their thesis in lieu of a Chapter from their Supervisor and Postgraduate Coordinator.
- The publication is not subject to any obligations or contractual agreements with a third party that would constrain its inclusion in the thesis.

☑ The candidate has declared that **their thesis has publications - either published or submitted for publication - incorporated into it in lieu of a Chapter/s. Details of these publications are provided below.**.

Publication Details #1

Full Title:	Using isotope shift for testing nuclear theory: The case of nobelium isotopes
Authors:	S. O. Allehabi, V. A. Dzuba, V. V. Flambaum, A. V. Afanasjev, and S. E. Agbemava
Journal or Book Name:	Phys. Rev. C
Volume/Page Numbers:	102/024326
Date Accepted/Published:	August 2020
Status:	published
The Candidate's Contribution to the Work:	The candidate is the primary author of the paper, contributing more than 50% of the work. The candidate carried out the calculations, collected the data, and analyzed the results.
Location of the work in the thesis and/or how the work is incorporated in the thesis:	The work is presented in Chapter 2 of the thesis.

Publication Details #2

Full Title:	Nuclear deformation as a source of the nonlinearity of the King plot in the Yb^+ ion
Authors:	S. O. Allehabi, V. A. Dzuba, V. V. Flambaum, and A. V. Afanasjev
Journal or Book Name:	Phys. Rev. A
Volume/Page Numbers:	103/L030801
Date Accepted/Published:	March 2021
Status:	published
The Candidate's Contribution to the Work:	The candidate is the primary author of the paper, contributing more than 50% of the work. The candidate performed the calculations, collected the data, and analyzed the results.
Location of the work in the thesis and/or how the work is incorporated in the thesis:	The work is presented in Chapter 3 of the thesis.

Publication Details #3

Full Title:	Theoretical study of the electronic structure of hafnium (Hf, Z = 72) and rutherfordium (Rf, Z = 104) atoms and their ions: Energy levels and hyperfine-structure constants
Authors:	S. O. Allehabi, V. A. Dzuba, and V. V. Flambaum
Journal or Book Name:	Phys. Rev. A
Volume/Page Numbers:	104/052811
Date Accepted/Published:	November 2021
Status:	published
The Candidate's Contribution to the Work:	The candidate is the primary author of the paper, contributing more than 50% of the work.

	The candidate performed the calculations, collected the data, and analyzed the results. The candidate was responsible for preparing the manuscript.
Location of the work in the thesis and/or how the work is incorporated in the thesis:	The work is presented in Chapter 4 of the thesis.

Publication Details #4

Full Title:	Calculation of the hyperfine structure of Dy, Ho, Cf, and Es
Authors:	S. O. Allehabi, V. A. Dzuba, and V. V. Flambaum
Journal or Book Name:	Phys. Rev. A
Volume/Page Numbers:	107/032805
Date Accepted/Published:	March 2023
Status:	published
The Candidate's Contribution to the Work:	The candidate is the primary author of the paper, contributing more than 50% of the work. The candidate performed all calculations, collected the data, and analyzed the results. The candidate was responsible for preparing the manuscript.
Location of the work in the thesis and/or how the work is incorporated in the thesis:	The work is presented in Chapter 5 of the thesis.

Publication Details #5

Full Title:	Theoretical study of electronic structure of erbium and fermium
Authors:	S. O. Allehabi, J. Li, V. A. Dzuba, and V. V. Flambauma
Journal or Book Name:	J. Quant. Spectrosc. Radiat. Transfer
Volume/Page Numbers:	253/107137
Date Accepted/Published:	June 2020
Status:	published
The Candidate's Contribution to the Work:	The candidate is the primary author of the paper, contributing more than 50% of the work. The candidate performed the calculations, collected the data, and analyzed the results.
Location of the work in the thesis and/or how the work is incorporated in the thesis:	The work is presented in Chapter 6 of the thesis.

Publication Details #6

Full Title:	Time keeping and searching for new physics using metastable states of Cu, Ag, and Au,
Authors:	V. A. Dzuba, S. O. Allehabi, V. V. Flambaum, J. Li, and S. Schiller
Journal or Book Name:	Phys. Rev. A
Volume/Page Numbers:	103/022822
Date Accepted/Published:	February 2021
Status:	published
The Candidate's Contribution to the Work:	The candidate is the primary author of the paper, contributing more than 50% of the work. The candidate performed the calculations, collected the data, and analyzed the results.
Location of the work in the thesis and/or how the work is incorporated in the thesis:	The work is presented in Chapter 7 of the thesis.

Publication Details #7

Full Title:	Using optical clock transitions in Cu II and Yb III for timekeeping and search for new physics,
Authors:	S. O. Allehabi, V. A. Dzuba, and V. V. Flambaum
Journal or Book Name:	Phys. Rev. A
Volume/Page Numbers:	104/053109
Date Accepted/Published:	November 2021
Status:	published
The Candidate's Contribution to the Work:	The candidate is the primary author of the paper, contributing more than 50% of the study. The candidate carried out the calculations, collected the data, and analyzed the results. The candidate was responsible for preparing the paper.
Location of the work in the thesis and/or how	The work is presented in Chapter 8 of the thesis.

the work is incorporated in the thesis:

Publication Details #8

Full Title:	Atomic clocks highly sensitive to the variation of the fine structure constant based on Hf II, Hf IV, and W VI ions
Authors:	S. O. Allehabi, V. A. Dzuba, and V. V. Flambaum
Journal or Book Name:	Phys. Rev. A
Volume/Page Numbers:	106/032807
Date Accepted/Published:	September 2022
Status:	published
The Candidate's Contribution to the Work:	The candidate is the primary author of the paper, contributing more than 50% of the study. The candidate carried out all the calculations, collected the data, and analyzed the results. The candidate was responsible for preparing the paper.
Location of the work in the thesis and/or how the work is incorporated in the thesis:	The work is presented in Chapter 9 of the thesis.

Publication Details #9

Full Title:	High-accuracy optical clocks based on group-16-like highly charged ions
Authors:	Saleh O. Allehabi, S. M. Brewer, V. A. Dzuba, V. V. Flambaum, and K. Beloy
Journal or Book Name:	Phys. Rev. A
Volume/Page Numbers:	106/043101
Date Accepted/Published:	October 2022
Status:	published
The Candidate's Contribution to the Work:	The candidate is the primary author of the paper, contributing more than 50% of the study. The candidate carried out all the calculations, collected the data, and analyzed the results. The candidate was responsible for preparing the paper.
Location of the work in the thesis and/or how the work is incorporated in the thesis:	The work is presented in Chapter 10 of the thesis.

Candidate's Declaration

✓ **I confirm that where I have used a publication in lieu of a chapter, the listed publication(s) above meet(s) the requirements to be included in the thesis. I also declare that I have complied with the Thesis Examination Procedure.**

Abstract

Computations of the spectroscopic properties of several heavy atoms have been performed to establish a link between recent measurements and some problems in modern physics. Calculations for No and Fm atoms demonstrated that isotope shift measurements can be used to study nuclear structure by extracting nuclear parameters beyond the root mean square (RMS) radius, such as the quadrupole deformation. Calculations of isotope shift in Yb^+ ion indicated that observed non-linearities of the King plot can be explained by nuclear deformation. This is a major systematic effect in the search for new interactions.

Calculation of hyperfine structure (HFS) for heavy and superheavy elements provides a possibility to extract from future HFS measurements magnetic dipole and electric quadrupole moments of the nuclei. We carried out calculations of the magnetic dipole HFS constant (A) and electric quadrupole HFS constant (B) for the superheavy elements Fm and Rf and the heavy elements Cf and Es. Similar calculations have also been performed on the lighter homologs Er, Hf, Dy, and Ho, whose electronic structures are similar to Fm, Rf, Cf, and Es, respectively, to verify the calculations.

We studied many excited metastable states in many heavy atoms and ions and found promising systems which can be used as very accurate atomic clocks which are highly sensitive to new physics. A number of atomic properties, such as energy levels, transition amplitudes, lifetimes, polarizabilities of the ground and clock states, etc., have been calculated. We found that relative blackbody radiation (BBR) shifts are small, between 10^{-16} and 10^{-18}, and the effects of variation of the fine-structure constant (α) are enhanced up to 8.3 times.

Calculations of atomic systems have been done using two different approaches. The choice depends on the number of valence electrons. The first method is called CI+SD (configuration interaction with single-double coupled cluster method), which is applicable to atomic systems with a few valence electrons (up to four). The second method is called CIPT (configuration interaction with perturbation theory method). It is designed to work with atomic systems with many valence electrons (more than four).

Acknowledgement

First and foremost, I thank Allah (God) and praise Him for every blessing He bestowed upon me, which has enabled me to complete this research. Also, I cannot forget to express my gratitude to the people who have supported me throughout my four-year journey of study and research. Their support and assistance have been invaluable, and I truly appreciate their contribution to making this research possible.

I would like to express my utmost appreciation to my supervisors, Professor Victor Flambaum and Dr. Vladimir Dzuba, for their guidance, assistance, and encouragement from the first day I started until I completed my Ph.D. thesis. We kept in touch throughout the study period, which gave me the strength to persevere during difficult times. This accomplishment would not have been possible without the grace of Allah (God), then their ongoing support. You have my heartfelt thanks and appreciation for your patience and high morals.

I would also like to thank my co-supervisor, A. Prof Julian Berengut, and the other colleagues I met during my Ph.D. journey, especially Amy Geddes, Hoang Bao Tran Tan, and Bryce Lackenby, for their support and advice. As well, I would like to express my gratitude to my co-authors for their valuable collaborations and observations during my research: Dr. J. Li, Prof. A. V. Afanasjev, Dr. S. E. Agbemava, Prof. S. Schiller, Dr. S. M. Brewer, and Prof. K. Beloy.

I would like to extend my sincere thanks to the Islamic University (IU) of Madinah (Ministry of Education, Kingdom of Saudi Arabia) and the Saudi Arabian Cultural Mission (SACM) for providing me with the full financial support that made it possible for me to conduct this research at the University of NSW.

I am deeply grateful to my parents and family for their unwavering love, care, support, encouragement, and prayers throughout my life. They have given me the strength and courage to face life's challenges and strive for success. I am forever in their debt. I would also like to express my heartfelt thanks to my wife and daughters for their endless patience and encouragement at every stage of my journey. They have been my pillars of strength.

Finally, I would like to dedicate this achievement to those who have guided me,
supported me, and prayed for me throughout my study journey.

Publications and Presentations

List of Publications

Papers included in the thesis

1. S. O. Allehabi, V. A. Dzuba, V. V. Flambaum, A. V. Afanasjev, and S. E. Agbemava, Using isotope shift for testing nuclear theory: the case of nobelium isotopes, Phys. Rev. C **102**, 024326 (2020).

2. S. O. Allehabi, V. A. Dzuba, V. V. Flambaum, and A. V. Afanasjev, Nuclear deformation as a source of the nonlinearity of the King plot in the Yb^+ ion, Phys. Rev. A **103**, L030801 (2021).

3. S. O. Allehabi , V. A. Dzuba, and V. V. Flambaum, Theoretical study of the electronic structure of hafnium (Hf, Z = 72) and rutherfordium (Rf, Z = 104) atoms and their ions: Energy levels and hyperfine-structure constants, Phys. Rev. A **104**, 052811 (2021).

4. S. O. Allehabi , V. A. Dzuba, and V. V. Flambaum, Calculation of the hyperfine structure of Dy, Ho, Cf, and Es, Phys. Rev. A **107**, 032805 (2023).

5. S. O. Allehabi, J. Li, V. A. Dzuba, and V. V. Flambaum, Theoretical study of electronic structure of erbium and fermium, J. Quant. Spectrosc. Radiat. Transfer **253**, 107137 (2020).

6. V. A. Dzuba, S. O. Allehabi, V. V. Flambaum, J. Li, and S. Schiller, Time keeping and searching for new physics using metastable states of Cu, Ag, and Au, Phys. Rev. A **103**, 022822 (2021).

7. S. O. Allehabi, V. A. Dzuba, and V. V. Flambaum, Using optical clock transitions in Cu II and Yb III for timekeeping and search for new physics, Phys. Rev. A **104**, 053109 (2021).

8. S. O. Allehabi , V. A. Dzuba, and V. V. Flambaum, Atomic clocks highly sensitive to the variation of the fine structure constant based on Hf II, Hf IV, and W VI ions, Phys. Rev. A **106**, 032807 (2022).

9. S. O. Allehabi, S. M. Brewer, V. A. Dzuba, V. V. Flambaum, and K. Beloy, High-accuracy optical clocks based on group 16-like highly charged ions, Phys. Rev. A **106**, 043101 (2022).

Papers not included in the thesis

1. F. Weber, T. E. Albrecht-Schönzart, S. O. Allehabi, S. Berndt, M. Block, H. Dorrer, C. E. Düllmann, V. A. Dzuba, J. G. Ezold,V. Flambaum *et al.*, Nuclear moments and isotope shifts of the actinide isotopes $^{249-253}$Cf probed by laser spectroscopy, Phys. Rev. C **107**, 034313 (2023).
2. S. O. Allehabi, V. A. Dzuba, and V. V. Flambaum, Prospects for optical clocks combining high sensitivity to new physics with insensitivity to perturbations; the case of Sb^+, Au^+, and Hg^{2+}, arXiv preprint arXiv:2303.17456 (2023). **In progress in a journal.**

List of Presentations

Oral presentations:

1. Theoretical study of electronic structure of erbium (Er), fermium (Fm), and nobelium (No), **AIP Summer Meeting, Queensland University of Technology, Brisbane, Australia. December (2021).**
2. New optical clocks based on Cu II, Yb III, Hf II, Hf IV, and W VI ions which may be used to search for dark matter and variation of the fine structure constant, **16th workshop on the Dark Side of the Universe, the University of New South Wales, Sydney, Australia, December (2022).**
3. New optical clocks based on Cu II, Yb III, Hf II, Hf IV, and W VI ions which may be used to search for dark matter and variation of the fine structure constant, **24th Australian Institute of Physics Congress, Adelaide Convention Centre, Adelaide, Australia, December (2022).**

Contents

List of Figures

List of Tables

Chapter 1

Introduction

1.1 Testing nuclear theory based on isotope shift and hyperfine structure

1.1.1 Using isotope shift for extracting nuclear deformation and demonstrating its role in King plot nonlinearity

The study of the isotope shift (IS) of superheavy elements (SHEs) is one way to obtain vital information about their nuclear structure [1–6]. IS can contribute a great deal to the understanding of trends in the nuclear stability of SHEs. Within the nuclear theory framework, there are ongoing predictions that SHEs have long-lived isotopes [1, 2]. In the accelerator systems, however, such neutron-rich isotopes for these atoms cannot be produced due to the absence of light elements with a sufficient number of neutrons to use in the collision. Accelerator production of superheavy elements results in neutron-poor isotopes. By adding measured atomic transition frequencies in neutron-poor isotopes and calculated isotope shifts, we may predict spectra of long-lifetime neutron-rich isotopes, which may be searched in astrophysical observations [7, 8]. Combining experimental data and theoretical data on IS can be used to obtain valuable information on nuclear structure, check nuclear models, and improve predictions for stability islands [9].

Studying isotope shifts also has the advantage of extracting crucial information about nuclear physics due to their sensitivity to numerous phenomena within the nucleus. Among the notable applications of isotope shifts in nuclear physics is the analysis of changes in nuclear charge radii [12]. A recent study [13] suggests that field isotope shift (FIS), which is the change in frequency of the atomic transition caused by the change in nuclear volume, can also be used to study quadrupole deformation (β) in nuclei with zero spin which cannot have electric quadrupole moments and quadrupole hyperfine structure. This study proposes that the obtaining of FIS measurements for a minimum of two transitions, with differences in nuclear structure dependence, can assist in the extraction of both, the change of the root-mean-square (RMS) charge radius and quadrupole deformation (β) parameters. It has also been shown that IS computations can contribute to putting constraints on the strength of the electron-neutron interaction mediated by new particles. It was suggested in [14] that such interaction may also cause non-linearities of the King plot. Using such research methods can help researchers make better predictions and gain a deeper understanding of the properties of atoms.

In chapters 2 and 3, of this thesis, we explore the possibility of using IS to test nuclear theories. Different nuclear models give different predictions for the nuclear charge density, which in turn affects the IS. We demonstrate that the non-linearities of the King plot observed in Yb^+ ion can be explained by the variation of the nuclear quadrupole deformation parameter; This puts some constraints on the use of the King plot for the search for new interactions.

1.1.2 Using hyperfine structures along with energy calculations to extract nuclear parameters

Among the other methods of gaining information about nuclei is through the study of hyperfine structures (HFS), which are formed by electrons interacting with nuclear moments in atoms. This interaction provides the opportunity to study nuclear parameters such as magnetic dipole moment (μ), electric quadrupole moment (Q). Such parameters play a vital role in understanding the structure of atomic nuclei, which in turn can contribute to the advancement of nuclear theory.

Combining measurement data with atomic calculations is necessary to extract values for μ and Q parameters. Nuclear electric quadrupole moment Q is related to nuclear deformation. The larger the Q value, the greater the deformation. Nuclei in the stability island, on the other hand, are expected to be spherical with no or minimal deformation. Therefore, finding neutron-rich superheavy elements with a small Q may indicate approaching the stability island. Among superheavy elements, only the Nobelium (No^{102}) atom has been studied so far [15–17], and the Lawrencium (Lr^{103}) atom is now being considered for such study [18].

In this thesis, HFSs are studied for several atomic systems involving both heavy and superheavy elements. In chapter 4, we study the Rf atomic system, which hopefully will be the next in measurement. The study is primarily concerned with obtaining the HFS matrix elements required for the interpretation of future measurement. We perform calculations on magnetic dipoles and electric quadrupole hyperfine structures. In chapter 5, we investigate the heavy atomic systems, Cf and Es. Measurement of HFSs have recently been obtained for the Cf atom, and nuclear parameters μ and Q have been extracted using our calculations [19]. In this chapter, we include a more detailed analysis of the calculations. In respect of Es, several experimental studies have been conducted, although no theoretical research has been undertaken. Therefore, this study aims to extract and refine the accuracy of the nuclear moments by comparing the present calculations with available experimental data. In chapter 6, we present calculations for HFS of Fm. The present study is largely motivated by the observation that measurements can present two different interpretations of HFS constants, and we hope that our calculations will be able to help experimentalists to re-evaluate the experimental data and provide the experimenters with a more accurate interpretation of the experiment.

As part of studying HFS, the energy levels of these studies have also been calculated, as being necessary to present results and assess the accuracy of the calculations; this is particularly important when dealing with complex systems, such as our considered atomic systems (Fm, Rf, Cf, and Es), which are either with an open $5f$ or $6d$ subshell, which in turn makes it more challenging to perform such calculations. Therefore, by comparing the calculated energy levels to experimental results, one can gain valuable insight into the accuracy of the calculations. Our calculations also include the study of lighter atoms with similar electronic structures, Er, Hf, Dy, and Ho, respectively, for which a lot of experimental data are available. Further comparison of correlation corrections in in light and heavy atoms allows us to predict the accuracy of our approach for these elements. Additionally, in chapter 4, we calculate the energy levels of the first three ions of Rf, whereas, in chapter 6, we report twenty-eight new energy levels of the Fm atomic system.

1.2 High-accuracy optical clocks and search for new physics

The search for manifestations of new physics at low energy requires high accuracy of measurements. The highest accuracy of measurements has been achieved in optical atomic clocks, in which the relative uncertainty in many clock systems reached an unprecedented level of $\sim 10^{-18}$ [20–24]. It is, therefore, natural to try to use these measurements to search for new physics. However, the majority of operating optical clocks, unfortunately, are not very sensitive to new physics, except for Yb^+ [25–29] and Hg^+ [27, 30]. One of the most significant types of sensitivity to new physics can be described as sensitivity to the variation of the fine structure constant (α). Many manifestations of new physics can be reduced to the time variation of α. For example, an apparent variation of α may be produced by the interaction of low-mass scalar dark matter with an electromagnetic field [31,32]. Therefore, the search for dark matter may be performed using a study of variation of atomic transition frequencies. Other examples include sensitivity to the local Lorentz invariance violation, violation of the Einstein equivalence principle, etc. [20, 21, 25, 26, 33–36]. We suggest the following strategy. Search for atomic optical transitions, which satisfy all criteria of being good clock transitions as well are sensitive to the variation of α. Upon finding these transitions, it is also possible to check their sensitivity to other manifestations of new physics.

It was demonstrated in Ref. [37] that in a single-electron approximation, the highest sensitivity to the variation of the fine structure constant corresponds to the maximum possible change in the value of the total angular momentum j in the corresponding single-electron transitions. For example, the transitions between states of the $4f^n$ and $4f^{n-1}6s$ configurations are $f-s$ transitions in a single-electron approximation. Δj in such transitions is 2 or 3, which makes them sensitive to the variation of α. The $s-f$ or $p-f$ transitions, which occur in the optical region, can be found in highly-charged ions [38, 39]. Note that effects of α variation rapidly increase with nuclear charge and ion charge. On the other hand, many neutral atoms or nearly neutral ions have $s-d$ clock transitions, which are sensitive to the variation of the fine structure constant.

Throughout this thesis, we present a number of studies that propose such systems. In chapter 7, we examine clock transitions in Cu, Ag, and Au atomic systems; in chapter 8, we suggest Cu II and Yb III ions (the clock transition in Yb III is actually the f-d transition); in chapter 9, we study Hf II, Hf IV, and W VI ions (the clock transition in W VI is the $d_{3/2}$-$d_{5/2}$ transition). Many of the suggested systems have the additional advantage of having more than one clock transition. The search for a variation of α requires measuring one clock frequency against the other over a long period of time. It is very convenient when both transitions are in the same atom or ion. In addition, combining two clock frequencies into one synthetic frequency allows significantly suppressing the sensitivity to the black body radiation shift [40].

As mentioned in Sec. 1.1.1, the King plot can also be considered as an alternative method of searching for new physics by measuring isotope shifts and studying the non-linearities of the King plot. A study of this type requires at least two transitions and four stable isotopes. In Chapter 9, we study the Hf atomic system, which has six stable isotopes. Each isotope of the Hf II and Hf IV ions has two clock transitions. Therefore, these ions are good candidates for such a study.

In chapter 10, we study highly charged ions as potential high-accuracy optical clocks using laser transitions in group-16-like ions. We consider the ground (^{3}P$_2$) state to first-excited (^{3}P$_0$) state electric quadrupole transition (E2) for this class of ions. Throughout these chapters (7,8,9,10), we calculate and analyze numerous atomic properties that are important in the development of optical clocks, including determining the sensitivity of clock transitions to variations in fundamental constants and evaluating the systematic fractional uncertainty of optical clocks.

References

[1] Y. Oganessian, Eur. Phys. J. A **42**, 361(2009).

[2] J. H. Hamilton, S. Hofmann, and Y. T. Oganessian, Annu. Rev. Nucl. Part. Sci **63**, 383 (2013).

[3] Y. T. Oganessian, V. K. Utyonkov, Y. V. Lobanov, F. S. Abdullin, and A. N. Polyakov, Nucl. Phys. A **734**,109 (2004).

[4] M. Leino, EPJ Web Conf. **131**, 01002 (2016).

[5] Y. Oganessian, Acta Phys. Pol. B **43**, 167 (2012).

[6] S. A. Giuliani, Z. Matheson, W. Nazarewicz, E. Olsen, P.-G. Reinhard, J. Sadhukhan, B. Schuetrumpf, N. Schunck, and P. Schwerdtfeger, Rev. Mod. Phys. **91**, 011001 (2019).

[7] V. A. Dzuba, V. V. Flambaum, and J. K. Webb, Phys. Rev. A **95**, 062515 (2017).

[8] V. V. Flambaum, A. J. Geddes, and A. V. Viatkina, Phys. Rev. A **97**, 032510 (2018).

[9] Y. Guo, A. Borschevsky, E. Eliav, and L. F Pašteka, J. Phys. B: At. Mol. Opt. Phys. **55** 155003 (2022).

[10] V. F. Gopka, V. Yushchenko, A. V. Shavrina, D. E. Mkrtichian, A. P. Hatzes, S. M. Andrievsky, and L. V. Chernysheva, Proceed. of the Interna. Astron. Union **2004**, 734 (2004).

[11] V. F. Gopka, A. V. Yushchenko, V. A. Yushchenko, I. V. Panov, and C. Kim, Kinematics Phys. Celestial Bodies **24**, 89 (2008).

[12] P. Aufmuth, K. Heilig, and A. Steudel, At. Data Nucl. Data Tables **37**, 455 (1987).

[13] V. V. Flambaum and V. A. Dzuba, Phys. Rev. A **100**, 032511 (2019).

[14] J. C. Berengut, D. Budker, C. Delaunay, V. V. Flambaum, C. Frugiuele, E. Fuchs, C. Grojean, R. Harnik, R. Ozeri, G. Perez *et al.*, Phys. Rev. Lett. **120**, 091801 (2018).

[15] S. G. Porsev, M. S. Safronova, U. I. Safronova, V. A. Dzuba, and V. V. Flambaum, Phys. Rev. A **98**, 052512 (2018).

[16] M. Laatiaoui, W. Lauth, H. Backe *et al.*, Nature (London) **538**, 495 (2016).

[17] S. Raeder, D. Ackermann, H. Backe, R. Beerwerth, J. C. Berengut, M. Block, A. Borschevsky, B. Cheal, P. Chhetri, C. E. Dullmann *et al.*, Phys. Rev. Lett. **120**, 232503 (2018).

[18] E. V. Kahl, J. C. Berengut, M. Laatiaoui, E. Eliav, and A. Borschevsky, Phys. Rev. A **100**, 062505 (2019).

[19] F. Weber, T. E. Albrecht-Schönzart, S. O. Allehabi, S. Berndt, M. Block, H. Dorrer, C. E. Düllmann, V. A. Dzuba, J. G. Ezold,V. Flambaum *et. al.*, Phys. Rev. C **107**, 034313 (2023).

[20] S. M. Brewer, J.-S. Chen, A. M. Hankin, E. R. Clements, C. W. Chou, D. J. Wineland, D. B. Hume, and D. R. Leibrandt, Phys. Rev. Lett. **123**, 033201 (2019).

[21] N. Huntemann, C. Sanner, B. Lipphardt, C. Tamm, and E. Peik, Phys. Rev. Lett. **116**, 063001 (2016).

[22] C. W. Chou, D. B. Hume, J. C. J. Koelemeij, D. J. Wineland, and T. Rosenband, Phys. Rev. Lett. **104**, 070802 (2010).

[23] A. D. Ludlow, W. F. McGrew, X. Zhang *et al.*, *Conference on Precision Electromagnetic Measurements (CPEM), Paris, France, JUL 08-13* (IEEE, Piscataway, NJ, 2018).

[24] P. Dubé, A. A. Madej, Z. Zhou, and J. E. Bernard, Phys. Rev. A **87**, 023806 (2013).

[25] R. Lange, N. Huntemann, J. M. Rahm, C. Sanner, H. Shao, B. Lipphardt, C. Tamm, S. Weyers, and E. Peik, Phys. Rev. Lett. **126**, 011102 (2021).

[26] C. Sanner, N. Huntemann, R. Lange, C. Tamm, E. Peik, M. S. Safronova, and S. G. Porsev, Nature (London) **567**, 204 (2019).

[27] V. V. Flambaum and V. A. Dzuba, Can. J. Phys. **87**, 25 (2009).

[28] R. M. Godun, P. B. R. Nisbet-Jones, J. M. Jones, S. A. King, L. A. M. Johnson, H. S. Margolis, K. Szymaniec, S. N. Lea, K. Bongs, and P. Gill, Phys. Rev. Lett. **113**, 210801 (2014).

[29] V. A. Dzuba, V. V. Flambaum, M. S. Safronova, S. G. Porsev, T. Pruttivarasin, M. A. Hohensee, and H. Haffner, Nat. Phys. **12**, 465 (2016).

[30] V. A. Dzuba, V. V. Flambaum, and S. Schiller, Phys. Rev. A **98**, 022501 (2018).

[31] A. Arvanitaki, J. Huang, and K. Van Tilburg, Phys. Rev. D **91**, 015015 (2015).

[32] Y. V. Stadnik and V. V. Flambaum, Phys. Rev. Lett. **115**, 201301 (2015).

[33] Boulder Atomic Clock Optical Network [(BACON) Collaboration], Nature (London) **591**, 564 (2021).

[34] T. Bothwell, D. Kedar1, E. Oelker, J. M Robinson, S. L Bromley, W. L Tew, J. Ye, and C. J Kennedy, Metrologia **56**, 065004 (2019).

[35] T. L. Nicholson, S. L. Campbell, R. B. Hutson, G. E. Marti, B. J. Bloom, R. L. McNally, W. Zhang, M. D. Barrett, M. S. Safronova, G. F. Strouse, W. L. Tew, and J. Ye, Nat. Commun. **6**, 6896 (2015).

[36] B. J. Bloom, T. L. Nicholson, J. R. Williams, S. L. Campbell, M. Bishof, X. Zhang, W. Zhang, S. L. Bromley, and J. Ye, Nature (London) **506**, 71 (2014).

[37] V. A. Dzuba, V. V. Flambaum, and J. K. Webb, Phys. Rev. A **59**, 230 (1999).

[38] J. C. Berengut, V. A. Dzuba, and V. V. Flambaum, Phys. Rev. Lett. **105**, 120801 (2010).

[39] J. C. Berengut, V. A. Dzuba, V. V. Flambaum, and A. Ong, Phys. Rev. A **86**, 022517 (2012).

[40] V. I. Yudin, A. V. Taichenachev, M. V. Okhapkin, S. N. Bagayev, Chr. Tamm, E. Peik, N. Huntemann, T. E. Mehlstäubler, and F. Riehle, Phys. Rev. Lett. **107**, 030801 (2011).

Chapter 2

Using isotope shift for testing nuclear theory: The case of nobelium isotopes

2.1 Overview

In this chapter, we demonstrate that nuclear theories can be tested by comparing calculated isotope shifts with experiments. We consider five nuclear models of nuclear charge distribution in two Nobelium isotopes, ^{252,254}No. We demonstrate that parameters of nuclear charge distribution can be extracted beyond nuclear root mean square (RMS) radii (such as quadrupole deformation β). We also show that the change in nuclear shape leads to King plot nonlinearity.

This study has been published in this paper:

S. O. Allehabi, V. A Dzuba, V. V. Flambaum, A. V. Afanasjev, and S. E. Agbemava, Using isotope shift for testing nuclear theory: The case of nobelium isotopes, Phys. Rev. C **102**, 024326 (2020).

I presented this work at an international conference:

Theoretical study of electronic structure of erbium (Er), fermium (Fm), and nobelium (No), **AIP Summer Meeting, Queensland University of Technology, Brisbane, Australia. December (2021).**

2.2 Abstract

We calculate field isotope shifts for nobelium atoms using nuclear charge distributions which come from different nuclear models. We demonstrate that comparing calculated isotope shifts with experiment can serve as a testing ground for nuclear theories. It also provides a way of extracting parameters of nuclear charge distribution beyond nuclear root mean square (rms) radius, e.g., parameter of quadrupole deformation β. The measurements of at least two atomic transitions is needed to disentangle the contributions of the changes in deformation and nuclear rms radius into field isotopic shift. We argue that a previous interpretation of the isotope measurements in terms of $\delta \left\langle r^2 \right\rangle$ between ^{252,254}No isotopes should be amended when nuclear deformation is taken into account. We calculate isotope shifts for other known isotopes and for hypothetically metastable isotope ^{286}No for which the predictions of nuclear models differ substantially.

2.3 INTRODUCTION

Studying nuclear structure of superheavy elements (SHE) ($Z > 100$) is an important area of research taking nuclear physics to unexplored territory and potentially leading to the hypothetical island of stability [1–6]. The sources of experimental information are very limited since the SHE are not found in nature but produced at accelerators at a very low production rate. In addition, all produced isotopes are neutronpoor and have short lifetimes (see, e.g., reviews [1–6]). Using atomic spectroscopy to measure isotope shift and hyperfine structure (hfs) is one of the promising methods to proceed. The part of isotope shift caused by the change of nuclear volume and called "field isotope shift" (FIS) is widely used to extract the change of nuclear root-mean-square (rms) radius between two isotopes [7]. In our previous paper [8] we argue that it can also be used to study nuclear deformation. For example, using different dependence of atomic transitions on nuclear structure and having FIS measurements for at least two transitions, we could extract not only the change of rms radius but also the change in quadrupole deformation parameter β. Superheavy element E120 ($Z = 120$) was used in [8] to illustrate that if we take nuclear parameters from nuclear theory, the effect of nuclear deformation on FIS is sufficiently large to be detected by modern spectroscopic methods. The E120 element was chosen for illustration purposes because of the large value of the effect. However, real measurements for E120 are not expected any time soon. The heaviest element for which isotope shift and hfs measurements are available is nobelium ($Z = 102$) [9, 10]. The isotope shift is measured for the ^{252,253,254}No isotopes and hfs is measured for the ^{253}No isotope.

In this work we study FIS of nobelium in detail. We calculate nuclear charge densities using several nuclear models based on covariant density functional theory [11]. Then we employ these densities in atomic calculations to get the FIS and compare it to experiment. We take a closer look at the interpretation of the data and argue that nuclear deformation should be taken into account in the analysis to reduce uncertainties below 10%.

We present a formula which expresses FIS via nuclear parameters. The formula is similar to what was suggested in [8]. It is an analog of the standard formula FIS $= F\delta \langle r^2 \rangle$ but has more terms proportional to $\delta \langle r^2 \rangle^2, \Delta\beta^2, \Delta\beta^3$. The parameters of the formula are found from the fitting of the calculated FIS. The formula is more accurate than the standard one for heavy nuclei. It can be used for predicting FIS for different isotopes if nuclear parameters are taken from nuclear theory. Since the formula contains terms related to nuclear deformation, it can be used to extract the values of the change of the parameter of nuclear quadrupole deformation $\Delta\beta$ similar to how the standard formula is used to extract the change of nuclear rms radius $\delta \langle r^2 \rangle$. FIS for at least two atomic transitions is needed for this purpose. Currently the isotope shift has been measured for only one transition in nobelium. Therefore, we strongly argue in favor of new measurements and present theoretical data for three more transitions.

Finally, we make predictions for the values of the isotope shift for the hypothetically metastable isotope with neutron number $N = 184$ which has spherical shape.

2.4 CALCULATIONS

In this work we perform nuclear and atomic calculations. Nuclear calculations are used to provide nuclear charge densities which are connected then to observable effects, such as isotope shifts via atomic structure calculations.

2.4.1 Nuclear calculations

The nuclear properties have been calculated within the covariant density functional theory (CDFT) [11] using several state-of-the-art covariant energy density functionals (CEDFs) such as DD-ME2 [12], DD-MEδ [13], NL3* [14], PC-PK1 [15], and DD-PC1 [16]. In the CDFT, the nucleus is considered as a system of A nucleons which interact via the exchange of different mesons. The above-mentioned CEDFs represent three major classes of covariant density functional models, namely, the nonlinear meson-nucleon coupling model (NL) (represented by the NL3* functional), the density-dependent meson exchange (DD-ME) model (represented by the DDME2 and DD-MEδ functionals), and point coupling (PC) model (represented by the DD-PC1 and PC-PK1 functionals). The main differences between them lie in the treatment of the interaction range and density dependence. In the NL and DD-ME models, the interaction has a finite range which is determined by the mass of the mesons. For fixed density it is of Yukawa type and the range is given by the inverse of the meson masses. The third class of models (PC model) relies on the fact that for large meson masses, the meson propagator can be expanded in terms of this range, leading in zeroth order to δ forces and higher order derivative terms. Thus, in the PC model the zero-range point-coupling interaction is used instead of the meson exchange [11]. The NL, DD-ME, and PC models typically contain six to nine parameters which are fitted to experimental data on finite nuclei and nuclear matter properties, see Sec. II in Ref. [17] for details.

Pairing correlations play an important role in all open shell nuclei. In the present article, they are taken into account in the framework of relativistic Hartree-Bogoliubov (RHB) theory in which the RHB equations for the fermions are given by [11]

$$\begin{pmatrix} \hat{h}_D - \lambda & \hat{\Delta} \\ -\hat{\Delta}^* & -\hat{h}_D^* + \lambda \end{pmatrix} \begin{pmatrix} U(\boldsymbol{r}) \\ V(\boldsymbol{r}) \end{pmatrix}_k = E_k \begin{pmatrix} U(\boldsymbol{r}) \\ V(\boldsymbol{r}) \end{pmatrix}_k . \tag{2.1}$$

Here, $\hat{h}_D$ is the Dirac Hamiltonian for the nucleons with mass m; λ is the chemical potential defined by the constraints on the average particle number for protons and neutrons; $U_k(\boldsymbol{r})$ and $V_k(\boldsymbol{r})$ are quasiparticle Dirac spinors [11,17]; and E_k denotes the quasiparticle energies. The Dirac Hamiltonian

$$\hat{h}_D = \boldsymbol{\alpha p} + V_0 + \beta(m + S) \tag{2.2}$$

contains an attractive scalar potential

$$S(\boldsymbol{r}) = \mathrm{g}_\sigma \sigma(\boldsymbol{r}) \tag{2.3}$$

and a repulsive vector potential

$$V_0(\boldsymbol{r}) = \mathrm{g}_\omega \omega_0(\boldsymbol{r}) + \mathrm{g}_\rho \tau_3 \rho_0(\boldsymbol{r}) + \mathrm{e}\mathrm{A}_0(\boldsymbol{r}). \tag{2.4}$$

Since the absolute majority of nuclei are known to be axially and reflection symmetric in their ground states, we consider only axial and parity-conserving intrinsic states and solve the RHB equations in an axially deformed harmonic oscillator basis [17]. Separable pairing of the finite range of Ref. [18] is used in the particle-particle channel of the RHB calculations.

The accuracy of the description of the ground state properties (such as binding energies, charge radii, etc.) of even-even nuclei has been investigated globally in Refs. [17,19]. The best global description of experimental data on charge radii has been achieved by the DD-ME2 functional (characterized by a rms deviation of $\Delta r_{ch}^{\text{rms}} = 0.0230\text{fm}$), followed by DDPC1 (which also provides best global description of binding energies), NL3*, and finally by DD-MEδ (characterized by a rms deviation of $\Delta r_{ch}^{\text{rms}} = 0.0329\text{fm}$) (see Table VI in Ref. [17] and Fig. 7 in Ref. [19]). However, the spread of rms deviations for charge radii between the above-mentioned functionals is rather small [$\Delta\left(\Delta r_{ch}^{\text{rms}}\right) = 0.0099\text{fm}$]. On the other hand, the charge radii of some isotopic chains (especially, those with high proton number Z) are not very accurately measured. Thus, strictly speaking we have to consider the accuracy of the description of charge radii by these functionals as comparable. Note that the nobelium nuclei under study have well-pronounced prolate or spherical minima in potential energy surfaces. Thus, the equilibrium quadrupole deformations obtained in static (CDFT) and dynamic (fivedimensional collective Hamiltonian based on CDFT) calculations are expected to be very similar (see Ref. [20] for examples in higher Z superheavy nuclei).

In the context of the study of isotopic shifts in superheavy elements it is necessary to mention substantial differences in model predictions for the nuclei located beyond currently measured. This is contrary to the fact that nuclear theories in general agree on the properties of SHE which have already been measured in experiment (see, for example, Figs. 7 and 8 in Ref. [21]). For example, some CEDFs (such as NL3*, DDME2, and PC-PK1) predict a band of spherical nuclei along and near the proton number $Z = 120$ and neutron number $N = 184$ (see Figs. 6(a), (b), and (e) in Ref. [21]). However, for other functionals (DD-PC1 and DD-ME δ) oblate deformed shapes dominate at and in the vicinity of these lines (see Figs. 6(c) and (d) in Ref. [21]). Nuclear measurements of the energies of the excited 2^+ states are needed to discriminate experimentally between spherical and oblate deformed ground states. Such experiments are not possible nowadays. It would be interesting to see whether atomic measurements would be able to help with such a discrimination.

2.4.2 Atomic calculations

We start from an estimation of mass shift to demonstrate that it can be neglected. Mass shift is the sum of normal mass shift and specific mass shift which has the same order of magnitude (see, e.g., [22]). In the nonrelativistic limit the normal mass shift (NMS) between isotopes with mass numbers A_1 and A_2 is given by

$$\delta v_{\mathrm{NMS}} = \left(\frac{1}{A_1} - \frac{1}{A_2}\right) \frac{v_{\exp}}{1822.888}. \tag{2.5}$$

Substituting numbers for the $^1\ \mathrm{S}_0 - {}^1\mathrm{P}_1$ transition in ^{254}No and ^{252}No we get $\delta v_{\mathrm{NMS}} = 5 \times 10^{-4}$ cm^{-1}. Total mass shift can be several times larger than the normal mass shift, therefore a reasonable estimation for the mass shift in nobelium stands at $\approx 10^{-3}$ cm^{-1}. If the uncertainty of the isotope shift measurements is smaller than this value, then taking into account mass shift and using the King plot to separate mass shift and field shift might be important for an accurate interpretation of the measurements. We leave this for future work. In this work we focus on FIS.

Nuclear calculations produce nuclear charge density as a two-dimensional function $\rho\left(z, r_{\perp}\right)$, where z is the coordinate along the axis of symmetry and $r_{\perp}$ is the radial coordinate in the direction perpendicular to the axis of symmetry. Atomic electrons feel the nucleus as a spherically symmetric system, averaged over nuclear rotations. This is because atomic transition frequencies are three orders of magnitude smaller than nuclear rotational transition frequencies (see, e.g., [23]). Note that a correction to this picture has been calculated for hydrogen-like ions where electron frequencies are much bigger. Even in this case the correction is small [24]. Therefore, we transform $\rho\left(z, r_{\perp}\right)$ into spherical coordinates $\rho(r, \theta)$ and average it over $\theta, \rho(r) = \int \rho(r, \theta) d\theta$. The density ρ is normalized by the condition $\int \rho dV = Z$. In the end we have nuclear charge density in numerical form rather than a set of parameters as in the case of using standard Fermi distribution. However, it is often useful to have such parameters as nuclear rms radius R_p, parameter of quadrupole deformation β, etc. Having them allows to study the sensitivity of observable effects (isotope shift in our case) to the change in the values of these parameters.

In our previous work [8] we studied various types of nuclear charge distribution variations including quadrupole deformation, change of nuclear skin thickness, and density suppression in the nuclear center. The effect of the density suppression is significantly smaller than the effect of the deformation and hardly can be separated using experimental FIS data. It is known from the nuclear models that the skin thickness is approximately the same in different nuclei and it hardly produces a significant effect on FIS. Moreover, the effect of the skin thickness on FIS cannot be separated from the effect of the deformation [25], numerically they are equivalent. Therefore, we concentrate on the effect of the quadrupole deformation β. In the end, the answer to the question which type of shape variation really takes place would come from nuclear theory. We use different nuclear models to calculate FIS and compare the results with experiment. A particular nuclear model and its predictions would be endorsed by the result.

It was also demonstrated in Ref. [8] that the three types of shape variation could be distinguished from the change of nuclear rms radius because of the different behavior of the $p_{1/2}$ and $p_{3/2}$ states (see Ref. [8] for more details). Therefore in this work we restrict our discussion to just two parameters, R_p and β. Their values are found by integrating nuclear charge density.

An alternative approach is possible in which the calculations start from the standard Fermi distribution for nuclear density and the effect of nuclear deformation is modeled by increasing the nuclear skin sickness. In this approach the discrimination between nuclear models would be done on the final stage of the study when the calculated isotope shift is compared to experiment.

The results of the calculations are presented in a form in which electron and nuclear variables are factorized, so that the electron structure factors do not depend on the nuclear isotope and therefore are not affected by the nuclear calculation uncertainty. The aim of atomic calculations is to find these electron structure factors. To do this we use nuclear charge densities in a particular nuclear model for two different isotopes and integrate them to get nuclear potentials V_1 and V_2. It is assumed on this stage that nuclear density is known exactly. All nuclear uncertainties are accounted for in the actual values of the nuclear factors. FIS can be found by direct comparison of the calculations for two different isotopes. This works well for isotopes which differ by a large number of neutrons, $\Delta N \gg 1$. For neighboring isotopes, where $\Delta N \approx 1$, the FIS is small and its calculated value is affected by numerical uncertainties. To suppress numerical noise we use the so-called finite field method [27]. We construct the nuclear potential according to the formula $V_N = V_1 + \lambda\left(V_2 - V_1\right)$, where V_1 and V_2 are nuclear potentials for two isotopes and λ is a numerical factor which can be large to enhance the difference between two isotopes and thus suppress numerical noise. First, the calculations are done for $\lambda = 0$ to obtain reference transition frequencies. Then, they are performed for several values of $\lambda > 1$ and the frequencies are extrapolated to $\lambda = 1$. In practice, we use $\lambda = 2$ and $\lambda = 4$.

To perform electron structure calculations we start from the so-called CIPT method (configuration interaction with perturbation theory) [28]. It treats nobelium as a system with 16 external electrons allowing excitations from the $5f$ subshell into the CI space. The aim of this study is to check whether the mixing of the $4f^{14}7snp$ $(n = 7, 8)$ and $4f^{13}7^2s6d$ configurations has any significance for our states of interest. Such study was performed before [10,29] for the lowest odd states of No, $7s7p$ $^3\mathrm{P}^{\mathrm{o}}_1$ and $^1\mathrm{P}^{\mathrm{o}}_1$. The answer was negative. Now we want to extend our study to two more states $7s8p$ $^3\mathrm{P}^{\mathrm{o}}_1$ and $^1\mathrm{P}^{\mathrm{o}}_1$. Therefore, we performed the CIPT calculations again and found that there is no strong mixing of our states of interest with the state involving excitations from the $5f$ shell. This means that nobelium can be treated as an atom with two valence electrons above closed shells. We use the well-established CI + MBPT method [30, 31] to perform the calculations.

The effective CI hamiltonian has a form

$$H^{\mathrm{CI}}\left(r_1, r_2\right) = \hat{h}_1\left(r_1\right) + \hat{h}_1\left(r_2\right) + \frac{e^2}{r_{12}} + \Sigma_2\left(r_1, r_2\right), \tag{2.6}$$

where $\hat{h}_1$ is the single-electron part of the Hamiltonian, which is the sum of the Hartree-Fock operator $\hat{H}^{\mathrm{HF}}$ and correlation potential $\Sigma_1, \hat{h}_1 = \hat{H}^{\mathrm{HF}} + \Sigma_1$. Correlation potential

Σ_1 is an operator which includes correlations between a particular valence electron and the electrons in the core. The operator Σ_2 can be understood as a screening of the Coulomb interaction between valence electrons by core electrons. We calculate Σ_1 and Σ_2 in second order of the many-body perturbation theory. The contribution of higher orders is relatively small but not totally negligible [29, 32, 33]. To simulate them, we rescale the Σ_1 operator in the s and p waves to fit the known energy of the $^1\,\mathrm{S}_0 - {}^1\mathrm{P}^{\mathrm{o}}_1$ transition, $\Sigma_1(s) \rightarrow 0.8\Sigma_1(s)$, $\Sigma_1(p) \rightarrow 0.94\Sigma_1(p)$. The rescaling helps to make more accurate predictions for the positions of other odd levels. It also improves the wave functions used to calculate transition amplitudes.

We perform the calculations of the electric dipole transition rates between the ground and four lowest in energy odd states to see whether the rates are sufficiently large for the measurements. We use random-phase approximation (RPA) for the calculations. The RPA equations for the core states have a form

$$\left(\hat{H}^{\mathrm{HF}} + \epsilon_c\right) \delta\psi_c = -(d + \delta V)\psi_c, \tag{2.7}$$

where d is electric dipole operator, the index c numerates the states in the core, $\delta\psi_c$ is the correction to the core orbital caused by external electric field, and δV is the correction to the self-consistent Hartree-Fock potential caused by the change of all core states. The RPA equations are solved self-consistently for all states in the core. As a result, we have δV which is used to calculate transition amplitudes between valence states

$$A_{ab} = \langle a|d + \delta V|b\rangle. \tag{2.8}$$

Here, a and b are two-electron wave functions found in the CI + MBPT calculations. The rate of spontaneous decay of the state b into the state a via an electric dipole transition

Table 2.1: Excitation energies, electric dipole transition amplitudes and rates of spontaneous decay via electric dipole transitions to the ground state for four odd states of nobelium.

Upper state	Excitation energies (cm^{-1}) Present	Exp. [9]	CI+ all [29]	A_{ab} (a.u.)	Transition rate (s^{-1})
$7s7p\ ^3\mathrm{P}^o_1$	21213		21042	1.37	1.2×10^7
$7s7p\ ^1\mathrm{P}^o_1$	29963	29961	30203	4.24	3.3×10^8
$7s8p\ ^3\mathrm{P}^o_1$	41482			0.097	3.6×10^5
$7s8p\ ^1\mathrm{P}^o_1$	42926			0.86	4.0×10^7

is given by (in atomic units)

$$T_{ab} = \frac{4}{3}\left(\omega_{ab}\alpha\right)^3 \frac{A_{ab}^2}{2J_b+1}. \tag{2.9}$$

2.5 RESULTS

2.5.1 Energies and transition rates

The results of calculations for the energies and transition rates are presented in Table 2.1. Good agreement with experiment is the result of fitting. The ab initio CI+ MBPT result for the energy of the $7s7p\ ^1\mathrm{P}^o_1$ state is 31652 cm^{-1}. This value differs from the experimental one by 5.6%. Comparing it with the CI+all-order result of Ref. [29] shows that most of this difference is due to higher-order correlations.

The $7s7p\ ^1\mathrm{P}^o_1$ state has the largest electric dipole transition amplitude and largest transition rate to the ground state. There are at least two more transitions (first and last lines of Table 2.1) which are probably strong enough to be experimentally studied. Note, that at least two transitions are needed to use isotope shift to extract nuclear deformation (see below).

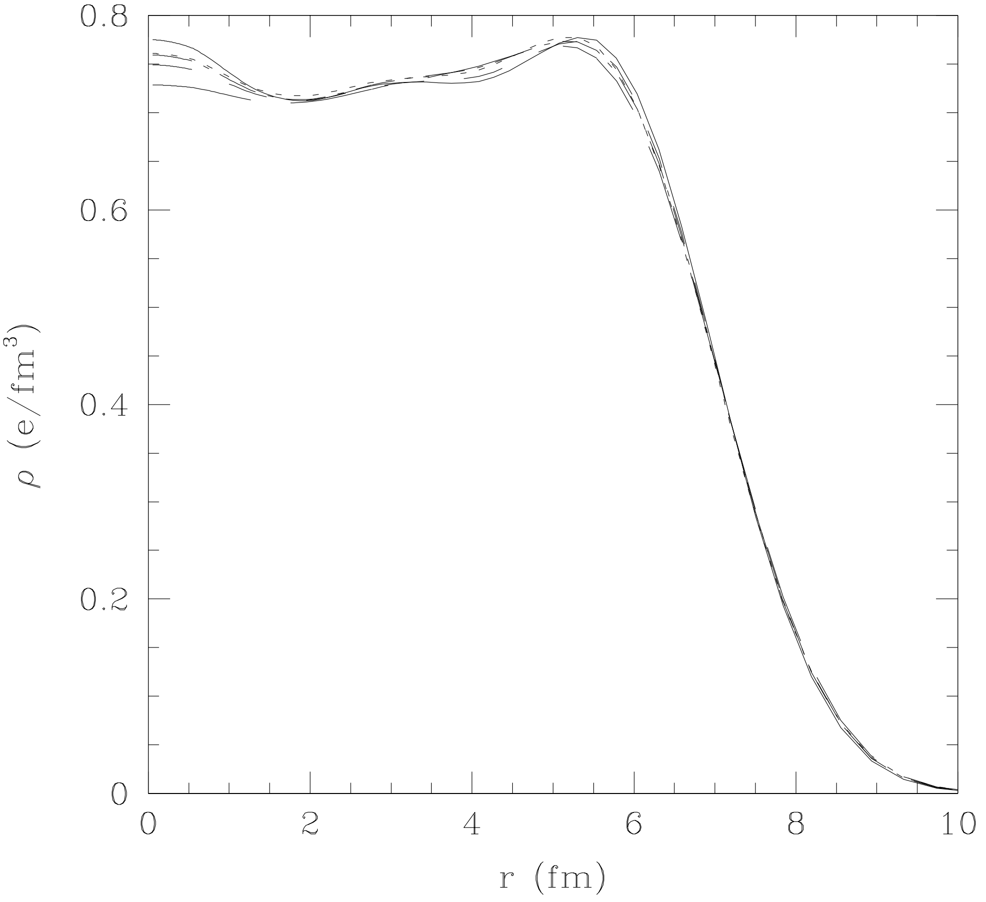

Figure 2.1: Symmetrized nuclear densities in five nuclear models considered in this work. See Fig. 2.2 for details.

2.5.2 Comparing nuclear models

Figures 2.1 and 2.2 show symmetrized nuclear densities [$\rho(r) = \int \rho(r,\theta)d\theta$] for nuclear models used in this work. Table 2.2 shows the parameters of nuclear charge distribution for these models (CEDFs) and corresponding calculated isotope shifts for the $7s^2\ ^1\mathrm{S}_0$ - $7s7p\ ^1\mathrm{P}^o_1$ line of ^{252}No and ^{254}No. Experimental value for the isotope shift is 0.336(23) cm^{-1} [10]. The DD-MEδ model leads to the best agreement of the calculated and experimental IS; the calculated value is only about 10% larger then the experimental one. Note also that this model predicts the largest value of $\Delta\beta$ between two isotopes. The

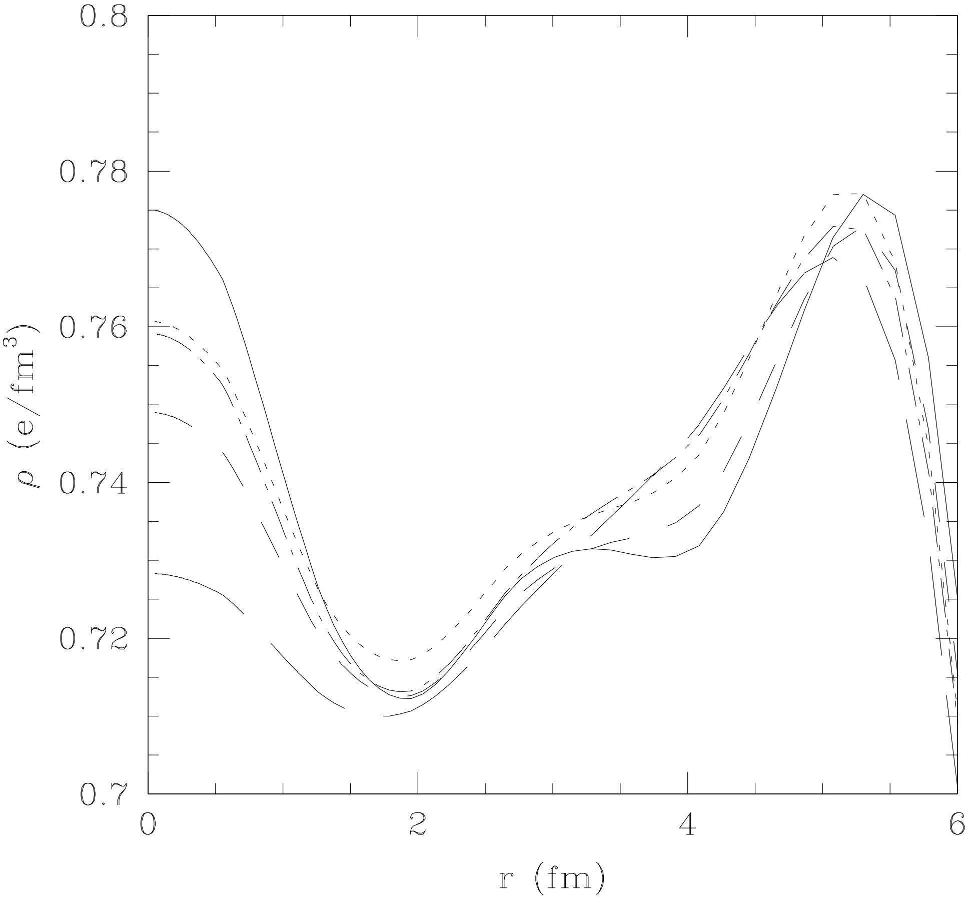

Figure 2.2: Upper left part of Fig. 2.1 showing the details of nuclear density in five nuclear models. Solid line−DD-MEδ, dotted line−DD-ME2, short dashed line−NL3*, long dashed line−PC-PK1, dot-short dashed line−DD-PC1.

last column of Table 2.2 presents the ratios of calculated isotope shift to $\delta\left\langle r^2\right\rangle$, which is the field shift constant F. In the absence of nuclear deformation FIS could be approximated by the standard formula $\delta v = F\delta\left\langle r^2\right\rangle$, where F does not depend on nuclear isotope, i.e., it should be the same for any nuclear model since FIS is dominated by one nuclear parameter $\delta\left\langle r^2\right\rangle$. However, we see that F varies significantly, i.e., there is another parameter which may affect δv. This is an indication that nuclear deformation may be important.

In Ref. [10] the nuclear field constant F was calculated without taking into account nuclear

Table 2.2: Parameters of nuclear model and corresponding calculated isotope shift for the $7s^2\ ^1\mathrm{S}_0$ - $7s7p\ ^1\mathrm{P}^o_1$ transition in ^{252,254}No. R_p is nuclear rms charge radius ($R_p = \sqrt{\langle r^2 \rangle}$), β is a parameter of nuclear quadrupole deformation, IS is calculated isotope shift, F is field shift constant ($F = \mathrm{IS}/\delta\langle r^2\rangle$). Here $\Delta\beta = \beta_1 - \beta_2$; the subscripts 1/2 correspond to the isotope with higher/lower value of neutron number.

Nuclear	^{252}No		^{254}No		$\delta\langle r^2\rangle$		IS	F
Model	R_p (fm)	β	R_p (fm)	β	fm^2	$\Delta\beta$	cm^{-1}	cm^{-1}/fm^2
DD-ME2	5.97171	0.298	5.98349	0.298	0.1408	0.000	-0.482	-3.42
DD-MEδ	5.96390	0.284	5.97259	0.278	0.1037	0.006	-0.374	-3.61
NL3s	5.97447	0.300	5.98772	0.298	0.1585	0.002	-0.503	-3.17
PC-PK1	5.98639	0.306	5.99967	0.305	0.1592	0.001	-0.538	-3.38
DD-PC1	5.97208	0.297	5.98225	0.295	0.1216	0.001	-0.431	-3.54

deformations. The CI+MBPT value of Ref. [10] is -3.47 cm^{-1}/fm^2. It is in excellent agreement with our value -3.42 cm^{-1}/fm^2 obtained with the same method and with the use of the DD-ME2 nuclear model in which $\Delta\beta = 0$ for the two isotopes (see Table 2.2). However, the calculations of FIS based on this model overestimate FIS by about 40%. If we assume that the overestimation of the FIS mostly comes from the overestimation of $\delta\langle r^2\rangle$, then the DD-MEδ results provide more consistent picture. Indeed, the transition from the DD-ME2 to DD-MEδ model leads to the reduction of $\delta\langle r^2\rangle$ from 0.1408 fm^2 down to 0.1037 fm^2 (see Table 2.2). The latter value is very close to $\delta\langle r^2\rangle = 0.105(7)(7)$ fm^2 found in Ref. [10]. In addition, the calculated FIS of the DD-MEδ model of -0.374 cm^{-1} (see Table 2.2) is very close to the experimental value of $-0.336(23)$ cm^{-1} (see Ref. [10]). Note that the best agreement with experiment is achieved with the nuclear model which gives the largest change in nuclear deformation parameter between two isotopes. This indicates that nuclear deformation may give a noticeable contribution to the FIS. However, it is not possible to include it into analysis in the current situation when isotope shift is known for only one atomic transition. At least two transitions are needed to distinguish between $\delta\langle r^2\rangle$ and $\Delta\beta$ (see next section).

Table 2.3: The parameters of formula (2.10) for isotope shifts from the ground state ($7s^2\ ^1\mathrm{S}_0$) to excited odd states of nobelium.

Odd states	F cm^{-1}/fm^2	G cm^{-2}/fm^4	a cm^{-1}	b cm^{-1}	c cm^{-1}/fm^2
$7s7p\ ^3\mathrm{P}^o_1$	−3.7828	0.0288	−1.4013	1.3708	−0.0215
$7s7p\ ^1\mathrm{P}^o_1$	−3.5042	0.0254	−1.2247	1.2234	−0.0152
$7s8p\ ^3\mathrm{P}^o_1$	−3.2063	0.0265	−1.0941	1.1304	−0.0071
$7s8p\ ^1\mathrm{P}^o_1$	−3.3112	0.0245	−1.1592	1.1919	−0.0090

2.5.3 Using isotope shift measurements to find parameters of nuclear charge distribution

It was suggested in our previous work [8] to fit the field isotope shift between two isotopes with the formula which depends on the change of two nuclear parameters, nuclear rms radius, and quadrupole deformation parameter β. Here we present the formula in a slightly different form

$$\delta\nu = F\delta\langle r^2\rangle + G(\delta\langle r^2\rangle)^2 + a\Delta(\beta^2) + b\Delta(\beta^3) + c\delta\langle r^2\rangle\Delta(\beta^2). \tag{2.10}$$

Here $\delta\langle r^2\rangle = \langle r^2\rangle_1 - \langle r^2\rangle_2$ is the change of square of nuclear rms radius, $\Delta(\beta^2) = \beta_1^2 - \beta_2^2$, $\Delta(\beta^3) = \beta_1^3 - \beta_2^3$, and the indexes 1 and 2 numerate isotopes, index 1 corresponds to an isotope with higher value of the neutron number. The coefficients F, G, a, b, c in this formula are found by a least squares fitting of calculated FIS for a wide range of nuclear parameters. The values of these parameters for four electric dipole transitions in nobelium are presented in Table 2.3. Note that the value of F for the second transition is in excellent agreement with the CI + MBPT calculations of Ref. [10].

The first term in Eq. (2.10) represents a standard formula for field IS. It ignores nuclear deformation and relativistic corrections. It was shown in Ref. [34] that relativistic effects make the field constant F isotope-dependent. It was suggested to use a modified formula $\delta v_i = F'\delta\left\langle r^{2\gamma}\right\rangle$, where $\gamma = \sqrt{1-(z\alpha)^2}$. Modified field shift constant F' does not depend on isotopes. However, this formula works well only for spherical nuclei [8]. In contrast, formula (2.10) can be used for a wide range of nuclei. Relativistic corrections in it are fitted with quadratic in the $\delta \langle r^2 \rangle$ term [second term in Eq. (2.10)]. This formula can be used to predict FIS for different isotopes and atomic transitions if nuclear parameters are taken from nuclear theory.

The formula can also be used in an opposite way: the change of nuclear parameters can be found from the isotope shift measurements. Since formula (2.10) depends on two nuclear parameters, the measurements of isotope shift for at least two atomic transitions are needed. Then standard mathematical procedures can be used to solve the system of two quadratic equations to find the change of nuclear parameters.

For neighboring isotopes the second and last terms in Eq. (2.10) can be neglected (see Table 2.3) and the remaining terms reduced to

$$\delta\nu = F\delta\langle r^2\rangle + d\Delta\beta. \tag{2.11}$$

The parameters F and d in this formula are isotope-dependent and should be calculated for one of the considered isotope. The parameter d is related to a and b in Eq. (2.10) by $d = a\left(\beta_1 + \beta_2\right) + b\left(\beta_1^2 + \beta_1\beta_2 + \beta_2^2\right)$ and $\Delta\beta = \beta_1 - \beta_2$.

So far the IS has been measured for one transition (second transition in Table 2.3) between isotopes ^{252,253,254}No. According to nuclear theory [21], all these isotopes have deformed shapes, e.g., for $^{252,254}\Delta\beta = 0.006$ for DD-MEδ CEDF (see Table 2.2). Using the formula (2.11) and the numbers from Table 2.3 we find that the contribution of the second term in Eq. (2.11) into IS is 0.003 cm^{-1}. This is 8 times smaller than the uncertainty of the measurements (measured value for IS is 0.336(23) cm^{-1} [10]). Therefore, to see the effect of nuclear deformation one has to either increase the accuracy of the measurements or use different isotopes. Note also that the measurements need to be done for at least two atomic transitions. Currently, IS is measured only for one transition in No [10].

Finally, we calculated isotope shifts between the ^{254}No and ^{286}No isotopes in different nuclear models; the results are presented in Table 2.4. Note that the ^{286}No nucleus has neutron number $N = 184$ which is a magic number in this mass region [6,21] corresponding

Table 2.4: Isotope shifts between ^{254}No and ^{286}No in different nuclear models for four electric dipole transitions from the ground state (cm^{-1}).

Nuclear model	R_p for ^{286}No (fm)	$\delta\langle r^2\rangle$ (fm^2)	Upper state $7s7p\ ^3\mathrm{P}^o_1$	$7s7p\ ^1\mathrm{P}^o_1$	$7s8p\ ^3\mathrm{P}^o_1$	$7s8p\ ^1\mathrm{P}^o_1$
DD-ME2	6.084420	1.1872	-4.52	-4.18	-3.84	-3.97
DD-MEδ	6.075497	1.2111	-4.61	-4.27	-3.90	-4.03
NL3*	6.097316	1.3029	-4.94	-4.57	-4.20	-4.34
PC-PK1	6.114652	1.3655	-5.17	-4.78	-4.39	-4.54
DD-PC1	6.085116	1.2212	-4.64	-4.29	-3.95	-4.08
Average		1.2576	-4.78(40)	-4.42(36)	-4.06(33)	-4.19(35)

to a large shell closure. Thus, according to nuclear theory this nucleus has spherical shape. It is expected to be a long-living isotope [6]. One transition frequency has been already measured in the ^{254}No isotope [9]. One can use the isotope shift from Table 2.4 to correct measured frequencies of atomic transitions from ^{254}No to ^{286}No isotopes and use the data for a search of long-living nobelium isotopes in astrophysical data [35]. Note that all nuclear models give very close predictions for the IS (see Table 2.4). We use the spread of calculated results for an estimation of the uncertainties in the predictions and an average calculated value as the central point of these predictions.

We should note that there are other corrections affecting isotopic shift including the nuclear polarization effect and QED corrections. For example, they are seen in a detailed comparison of different contributions to the isotope shift for the $2p_{1/2} - 2s$ transition in Li-like ions ^{150,142}Nd^{57+} in Ref. [37]. However, the effect of the quadrupole deformation increases with the nuclear charge significantly faster than other effects due to the singularity of the Dirac wave function at the origin-see, for example, Ref. [37]. This is why we concentrate on the effect of the quadrupole deformation when considering superheavy elements like nobelium.

2.5.4 Nuclear deformation and nonlinearity of King plot

It was suggested in Ref. [36] to use a possible nonlinearity of the King plot to search for new particles. If some presently unknown bosons mediate interaction between atomic electrons and neutrons in the nucleus, then field shift constant F would depend on the number of neutrons. This would manifest itself in the nonlinearity of the King plot. Let us consider how this consideration is affected by nuclear deformation. The only condition for the King plot to be linear is the separation of nuclear and electron variables. Let us consider standard formula for isotope shift, namely, $\delta v = F\delta\left\langle r^2\right\rangle + MN$. Here, F is field shift constant, $\delta\left\langle r^2\right\rangle$ is a nuclear factor describing change in nuclear structure between two isotopes, M is the mass factor $M = \left(M_b - M_a\right)/M_bM_a, N$ is electron structure factor related to mass shift, and the indexes a and b numerate isotopes. If F does not depend on the nucleus and $\delta\left\langle r^2\right\rangle$ does not depend on electrons then one can write for two atomic transitions

$$(\delta\nu_1/M) = \frac{F_1}{F_2}(\delta\nu_2/M) + \frac{F_1}{F_2}N_2 + N_1. \tag{2.12}$$

One can see that on the $\delta v_1/M, \delta v_2/M$ plane the points corresponding to different isotopes are all on the same line. If formula (2.11) is used for the field shift then an extra term appears in Eq. (2.12)

$$(\delta\nu_1/M) = \frac{F_1}{F_2}(\delta\nu_2/M) + \frac{F_1}{F_2}N_2 + N_1 + \frac{\Delta\beta}{M}\left(d_1 - \frac{F_1}{F_2}d_2\right). \tag{2.13}$$

This last term does depend on isotopes and thus breaks the linearity of the King plot. It is instructive to see when this term is zero. The most obvious case is $\Delta\beta = 0$, i.e., all considered isotopes have the same nuclear deformation. This is an unlikely scenario for heavy nuclei. However, the terms can be small if deformations are similar. The less obvious case is $d_1 - d_2F_1/F_2 = 0$. Note that the expression $d_1F_2 - d_2F_1$ is the determinant of the system of two linear equations for $\delta\left\langle r^2\right\rangle$ and $\Delta\beta$ if IS for two transitions is given by Eq. (2.11). The determinant is zero means that the equations are proportional to each other and cannot be resolved. This might be the case of the transitions between similar states, e.g., $7s - 7p_{3/2}$ and $7s - 8p_{3/2}$ transitions in No$^+$. Exact proportionality is unlikely but strong suppression is possible (i.e., $d_1F_2 \approx d_2F_1$). The suppression is less likely in many-electron atoms since the states are affected by configuration mixing and it is different for low and high energy states so that similar transitions can hardly be found.

2.6 CONCLUSION

We considered five nuclear models of nuclear charge distribution in two isotopes of nobelium, ^{252}No and ^{254}No, and calculated the field isotope shift for four electric dipole atomic transitions. It was demonstrated that comparing the calculated isotope shift with experiment helps to discriminate between nuclear models endorsing the predictions of the best-fit model. It was also shown that having isotope shift measurements for at least two atomic transitions can be used to extract from the measurements not only the change of nuclear rms radius but also the change in nuclear shape. Referring to the best-fit model endorses a particular type of shape change, e.g., change in nuclear quadrupole deformation, nuclear skin thickness, or nuclear density suppression in the origin. It was demonstrated that a change in nuclear shape between isotopes leads to nonlinearity of the King plot complicating its use for the search of new physics.

Acknowledgments

This work was funded in part by the Australian Research Council. The material is based upon work supported by the U.S. Department of Energy, Office of Science, Office of Nuclear Physics under Award No. DE-SC0013037.

References

[1] Y. Oganessian, Eur. Phys. J. A **42**, 361(2009).

[2] J. H. Hamilton, S. Hofmann, and Y. T. Oganessian, Annu. Rev. Nucl. Part. Sci **63**, 383 (2013).

[3] Y. T. Oganessian, V. K. Utyonkov, Y. V. Lobanov, F. S. Abdullin, and A. N. Polyakov, Nucl. Phys. A **734**,109 (2004).

[4] M. Leino, EPJ Web Conf. **131**, 01002 (2016).

[5] Y. Oganessian, Acta Phys. Pol. B **43**, 167 (2012).

[6] S. A. Giuliani, Z. Matheson, W. Nazarewicz, E. Olsen, P.-G. Reinhard, J. Sadhukhan, B. Schuetrumpf, N. Schunck, and P. Schwerdtfeger, Rev. Mod. Phys. **91**, 011001 (2019).

[7] P. Aufmuth, K. Heilig, and A. Steudel, At. Data Nucl. Data Tables **37**, 455 (1987).

[8] V. V. Flambaum and V. A. Dzuba, Phys. Rev. A **100**, 032511 (2019).

[9] M. Laatiaoui, W. Lauth, H. Backe, M. Block, D. Ackermann, B. Cheal, P. Chhetri, C. E. Dullmann, P. van Duppen, J. Even *et al.*, Nature (London) **538**, 495 (2016).

[10] S. Raeder, D. Ackermann, H. Backe, R. Beerwerth, J. C. Berengut, M. Block, A. Borschevsky, B. Cheal, P. Chhetri, C. E. Dullmann *et al.*, Phys. Rev. Lett. **120**, 232503 (2018).

[11] D. Vretenar, A. V. Afanasjev, G. A. Lalazissis, and P. Ring, Phys. Rep. **409**, 101 (2005).

[12] G. A. Lalazissis, T. Nikšić, D. Vretenar, and P. Ring, Phys. Rev. C **71**, 024312 (2005).

[13] X. Roca-Maza, X. Viñas, M. Centelles, P. Ring, and P. Schuck, Phys. Rev. C **84**, 054309 (2011).

[14] G. A. Lalazissis, S. Karatzikos, R. Fossion, D. Peña Arteaga, A. V. Afanasjev and P. Ring, Phys. Lett. B **671**, 36 (2009).

[15] P. W. Zhao, Z. P. Li, J. M. Yao, and J. Meng, Phys. Rev. C **82**, 054319 (2010).

[16] T. Nikšić, D. Vretenar, and P. Ring, Phys. Rev. C **78**, 034318 (2008).

[17] S. E. Agbemava, A. V. Afanasjev, D. Ray, and P. Ring, Phys. Rev. C **89**, 054320 (2014).

[18] Y. Tian, Z. Y. Ma, and P. Ring, Phys. Lett. B **676**, 44 (2009).

[19] A. V. Afanasjev and S. E. Agbemava, Phys. Rev. C **93**, 054310 (2016).

[20] Z. Shi, A. V. Afanasjev, Z. P. Li, and J. Meng, Phys. Rev. C **99**, 064316 (2019).

[21] S. E. Agbemava, A. V. Afanasjev, T. Nakatsukasa, and P. Ring, Phys. Rev. C **92**, 054310 (2015).

[22] M. S. Safronova and W. R. Johnson, Phys. Rev. A **64**, 052501 (2001).

[23] V. V. Flambaum and V. A. Dzuba, Phys. Rev. A **101**, 042504 (2020).

[24] G. Plunien and G. Soff, Phys. Rev. A **51**, 1119 (1995); **53**, 4614(E) (1996).

[25] At first glance, the deformation of nuclei can be integrated out by introducing effective skin thickness for spherical Fermi density distribution and using it in atomic calculations. However, in this way the connection to nuclear physics will be lost. This is because the deformation in the nuclei has a clear physical meaning and manifests itself, for example, via the rotational bands and such bands are present in the ^{252,254}No nuclei. The deformation parameter β of the nucleus can be experimentally extracted either from Coulomb measurements or from rotational spectra of ground state bands. The rotational properties and deformation parameters β of the nuclei under study are well described in the CDFT (see Ref. [26] and references quoted therein).

[26] A. V. Afanasjev and O. Abdurazakov, Phys. Rev. C **88**, 014320 (2013).

[27] W. R. Johnson, V. A. Dzuba, U. I. Safronova, and M. S. Safronova, Phys. Rev. A, **69**, 022508 (2004).

[28] V. A. Dzuba, J. C. Berengut, C. Harabati, and V. V. Flambaum, Phys. Rev. A **95**, 012503 (2017).

[29] S. G. Porsev, M. S. Safronova, U. I. Safronova, V. A. Dzuba, and V. V. Flambaum, Phys. Rev. A **98**, 052512 (2018).

[30] V. A. Dzuba, V. V. Flambaum, and M. G. Kozlov, Phys. Rev. A, **54**, 3948 (1996).

[31] V. A. Dzuba and W. R. Johnson, Phys. Rev. A, **57**, 2459 (1998).

[32] S. G. Porsev, M. G. Kozlov, M. S. Safronova, and I. I. Tupitsyn, Phys. Rev. A **93**, 012501 (2016).

[33] V. A. Dzuba, Phys. Rev. A **90**, 012517 (2014).

[34] V. V. Flambaum, A. J. Geddes, and A. V. Viatkina, Phys. Rev. A **97**, 032510 (2018).

[35] V. A. Dzuba, V. V. Flambaum, and J. K. Webb, Phys. Rev. A **95**, 062515 (2017).

[36] J. C. Berengut, D. Budker, C. Delaunay, V. V. Flambaum, C. Frugiuele, E. Fuchs, C. Grojean, R. Harnik, R. Ozeri, G. Perez, and Y. Soreq, Phys. Rev. Lett. **120**, 091801 (2018).

[37] Y. S. Kozhedub, O. V. Andreev, V. M. Shabaev, I. I. Tupitsyn, C. Brandau, C. Kozhuharov, G. Plunien, and T. Stohlker. Phys. Rev. A **77**, 032501 (2008).

Chapter 3

Nuclear deformation as a source of the nonlinearity of the King plot in the Yb^{+} ion

3.1 Overview

We have shown in chapter 2 that nuclear deformation (β) may lead to the non-linearity of the King plot. In this chapter, we continue to study the extent of the effect of the nuclear quadrupole deformation parameter (β) on King plot non-linearity. We do this by fitting the observed non-linearities of the King plot by the parameter of quadrupole deformation for all stable even-even isotopes of the Yb^{+} ion. Based on the results obtained, we find that nuclear quadrupole deformation can explain the non-linearity of the King plot observed in recent experimental results.

This study has been published in this paper:

S. O. Allehabi, V. A. Dzuba, V. V. Flambaum, and A. V. Afanasjev, Nuclear deformation as a source of the nonlinearity of the King plot in the Yb^{+} ion, Phys. Rev. A **103**, L030801 (2021).

3.2 Abstract

We perform atomic relativistic many-body calculations of the field isotope shifts and calculations of corresponding nuclear parameters for all stable even-even isotopes of the Yb$^+$ ion. We demonstrate that if we take nuclear parameters of the Yb isotopes from a range of the state of the art nuclear models, which all predict strong quadrupole nuclear deformation, and then calculate nonlinearity of the King plot caused by the difference in the deformation in different isotopes, the result is consistent with the nonlinearity observed in the experiment [I. Counts *et al.*, Phys. Rev. Lett. **125**, 123002 (2020)]. The changes of nuclear rms radius between isotopes extracted from experiment are consistent with those obtained in the nuclear calculations.

In a recent paper [1], the nonlinearity of the King plot has been observed. The authors state that the effect may indicate physics beyond the standard model (SM), or that, within the SM, they may come from the quadratic field shift (QFS). Possible nonlinearity of the King plot in Yb$^+$ was studied theoretically in Ref. [2]. In the present paper, we show that it is more likely that the observed nonlinearity of the King plot is due to a significant nonmonotonic variation of the nuclear deformation in the chain of isotopes. We perform nuclear and atomic calculations of the field isotope shift (FIS) which include nuclear deformation and demonstrate that the dependence of the deformation on isotopes leads to a nonlinearity of the King plot, which is consistent with the observations in Ref. [1]. We show that the comparison of theoretical and experimental nonlinearities can be used to discriminate between different nuclear models, favoring some and disfavoring others.

It is well known from experimental nuclear rotational spectra [3] and its theoretical interpretation [4, 5] as well as from the nuclear calculations presented below that all even-even Yb isotopes studied in Ref. [1] have deformed nuclear ground states with the parameters of the quadrupole deformation $\beta \approx 0.3$. In our previous paper [6], we demonstrated that nuclear deformation may lead to a nonlinearity of the King plot.

Therefore, in the present paper we calculate FIS in eveneven Yb isotopes with accounting for nuclear deformation. We treat Yb$^+$ as a system with one external electron above closed shells and use the correlation potential method [7]. This approach works well for Yb$^+$ as demonstrated in our earlier works [8–10]. We calculate the correlation potential $\hat{\Sigma}$ in the second order of the many-body perturbation theory. Correlation potential is the nonlocal (integration) operator responsible for the correlation corrections due to interaction between valence electron and electrons in the core. Then we use $\hat{\Sigma}$ to calculate the states of valence electron (numerated by v) in the form of the Brueckner orbitals (BO):

$$(\hat{H}^{\mathrm{HF}} + \hat{\Sigma} - \epsilon_v)\psi_v^{\mathrm{BO}} = 0. \tag{3.1}$$

Here $\hat{H}^{\mathrm{HF}}$ is the relativistic Hartree-Fock (HF) Hamiltonian for the closed-shell core of Yb$^+$,

$$\hat{H}^{\mathrm{HF}} = c\hat{\alpha}_i \cdot \hat{p}_i + (\beta - 1)mc^2 + V_{\mathrm{nuc}}(r_i) + V_{\mathrm{core}}(r_i). \tag{3.2}$$

In this expression, α and β are the Dirac matrices, V_{nuc} is nuclear potential obtained by integrating nuclear charge density, V_{core} is the self-consistent HF potential, and the index i numerates single-electron states. This method is similar to the many-body perturbation theory (MBPT) method used in Ref. [1].

FIS is calculated by varying nuclear potential V_{nuc} in (3.2). The results are presented in the form of expansion over the change in nuclear momenta (see also Ref. [1]),

$$\nu_a^{\mathrm{FIS}} = F_a \delta\langle r^2\rangle + G_a^{(2)}\delta\langle r^2\rangle^2 + G_a^{(4)}\delta\langle r^4\rangle. \tag{3.3}$$

Here v_a^{FIS} is the change of the frequency of an atomic transition (numerated by index a) which is caused by the change of nuclear size and shape between two isotopes; $\delta\left\langle r^2\right\rangle$ is the change of the nuclear rms radii squared, $\delta\left\langle r^2\right\rangle=\left\langle r^2\right\rangle_2-\left\langle r^2\right\rangle_1$ and $\delta\left\langle r^4\right\rangle=\left\langle r^4\right\rangle_2-\left\langle r^4\right\rangle_1$.

First term in Eq. (3.3) is the standard FIS; the other two terms are corrections responsible for the nonlinearity of the King plot. The term with $G_a^{(2)}$ is due to the second-order effect in the change of the nuclear Coulomb potential called the quadratic field shift (QFS) and the last term appears mainly due to the relativistic effects in the electron wave function; i.e., these terms represent different physical phenomena. On the other hand, their effects on the isotope shift are similar. It was suggested in Ref. [1] that $\left\langle r^4\right\rangle$ and $\left\langle r^2\right\rangle$ are related by $\left\langle r^4\right\rangle=b\left\langle r^2\right\rangle^2$, where b is just a numerical constant, $b=1.32$. Extra care should be taken in calculating $G^{(2)}$ and $G^{(4)}$ independently on each other. For example, they cannot be defined simultaneously in a fitting procedure. Therefore, we start the calculations by eliminating the QFS term, i.e., by considering FIS in the linear approximation. The change of the nuclear Coulomb potential between two isotopes is considered as a perturbation and is treated in the first order using the random phase approximation (RPA). The RPA equations for core electrons have the following form [7]:

$$(\hat{H}^{\mathrm{HF}}-\epsilon_c)\delta\psi_c=-(\delta V_N+\delta V_{\mathrm{core}})\psi_c, \tag{3.4}$$

where δV_N is the difference between nuclear potentials for the two isotopes, index c numerates states in the core, and δV_{core} is the change of the self-consistent HF potential induced by δV_N and the changes to all core functions $\delta\psi_c$. Equations (3.4) are solved self-consistently for all states in the core with the aim of finding δV_{core} . The FIS for a valence state v is then given by

$$\nu_v^{\mathrm{FIS}}=\langle\psi_v^{\mathrm{BO}}|\delta V_N+\delta V_{\mathrm{core}}|\psi_v^{\mathrm{BO}}\rangle. \tag{3.5}$$

Apart from eliminating the QFS, an important advantage of using the RPA method (where the small parameter, i.e., the change of the nuclear radius, is explicitly separated) is the suppression of a numerical noise. Nonlinearity of the King plot is extremely small and direct full scale calculations of the change of the atomic electron energy due to a tiny change of the nuclear radius (i.e., without the separation of the small parameter) may lead to a false effect in the King plot nonlinearity (see below). After FIS is calculated for a range of nuclear parameters, the constants F_a and $G_a^{(4)}$ are found by fitting the results of the atomic calculations by formula (3.3) (without $G^{(2)}$) by the least-square-root method.

To calculate $G^{(2)}$, we use the second-order perturbation theory

$$G_a^{(2)} = \sum_n \frac{\langle a|\delta V_N + \delta V_{\mathrm{core}}|n\rangle^2}{E_a - E_n} / \delta\langle r^2\rangle^2. \tag{3.6}$$

Here δV_N is the change of nuclear potential between two isotopes. Summation goes over complete set of the singleelectron basis states, including states in the core and negative-energy states. To include the core-valence correlations, one can use BO for single-electron states a and n. Again, the perturbation theory is used instead of the direct calculation of the change of the electron energy due to the tiny change of the nuclear radius to suppress numerical noise.

Instead of the direct summation over electron states in Eq.(3.6), one can first solve the RPA equation for the valence state a

$$(\hat{H}^{\mathrm{HF}} + \hat{\Sigma} - \epsilon_a)\delta\psi_a^{\mathrm{BO}} = -(\delta V_N + \delta V_{\mathrm{core}})\psi_a^{\mathrm{BO}}, \tag{3.7}$$

and then use

$$G_a^{(2)} = \langle \delta\psi_a^{\mathrm{BO}}|\delta V_N + \delta V_{\mathrm{core}}|\psi_a^{\mathrm{BO}}\rangle / \delta\langle r^2\rangle^2. \tag{3.8}$$

We obtain the same results using Eqs. (3.6) and (3.8) This provides a test of the numerical accuracy.

Nuclear deformation. The quadrupole nuclear deformation β provides a measure of the deviation of the nuclear density distribution from spherical shape so that nuclear ra-

Table 3.1: Calculated parameters of formula (3.3) for the FIS in two transitions of Yb$^+$; a stands for the $6s_{1/2}$-$5d_{5/2}$ transition and b stands for the $6s_{1/2}$-$5d_{3/2}$ transition. Case 1 corresponds to deformed nuclei, while case 2 corresponds to spherical nuclei.

Case	Tran- sition	F (GHz/fm^2)	$G^{(2)}$ (GHz/fm^4)	$G^{(4)}$ (GHz/fm^4)
1	a	-17.6035	0.02853	0.01308
	b	-18.0028	0.02853	0.01337
2	a	-18.3026	0.02853	0.01245
	b	-18.7201	0.02853	0.01273

dius $r_n(\theta)$ in the θ direction with respect of the axis of symmetry is written as $r_n(\theta) = r_0\,(1 + \beta Y_{20}(\theta))$. Electron feels nuclear density averaged over the nuclear rotation (see, e.g., Ref. [6]). We calculate the average density by integrating the deformed density over θ.

To determine the values of F and $G^{(4)}$ parameters in Eq.(3.3), we first vary the nuclear root-mean-square (rms) charge radius r_c and the quadrupole deformation parameter β in the range determined by the nuclear theory (see below): 5.234 fm $\leqslant r_c \leqslant$ 5.344 fm and $0.305 \leqslant \beta \leqslant 0.345$, and then fit the F and $G^{(4)}$ parameters by the formula (see also Refs. [6, 11])

$$\nu^{\text{FIS}} = F\delta\langle r^2\rangle + G^{(4)}\delta\langle r^4\rangle \tag{3.9}$$

to the results of atomic calculations of FIS for different r_c and β. The values of F and $G^{(4)}$ parameters defined in such a way are presented in Table 3.1. The table also gives the values of the $G^{(2)}$ parameters calculated using (3.6) and (3.8). Note that FIS for the d states of Yb$^+$ is about two orders of magnitude smaller than FIS for the 6s states and in QFS small matrix elements for the d states appear in the second order while in the calculations of F are in the first order. Therefore, the relative difference in the $G^{(2)}$ parameters for the s-$d_{3/2}$ and s-$d_{5/2}$ transitions is much smaller than the relative difference for the F parameters. Note that nonlinearities of the King plot are sensitive to the tiny differences in the ratios F_a/F_b, $G_a^{(2)}/G_b^{(2)}$, and $G_a^{(4)}/G_b^{(4)}$ [see Eq. (3.11) and discussion below it]. Therefore, we keep four digits for $G^{(2)}$ and $G^{(4)}$ to avoid the effect of rounding on the nonlinearity.

It was shown in Ref. [1] that $\langle r^4\rangle \approx b\langle r^2\rangle^2$, where b is just a numerical constant, $b = 1.32$ [1]. We found that the situation is different in deformed and spherical nuclei. By calculating $\langle r^4\rangle$ in both cases, we found that the results can be fitted with high accuracy by the formula

$$\langle r^4\rangle = \Big[b_0 + b_1(r_c^2 - r_0^2) + b_2(\beta - \beta_0)\Big]\, r_c^2, \tag{3.10}$$

where $r_0 = 5.179$ fm and $\beta_0 = 0.305$. For deformed nuclei $b_0 = 1.3129, b_1 = -0.0036, b_2 = 0.1$, while for spherical nuclei $b_0 = 1.2940, b_1 = -0.0038, b_2 = 0$.

To study the nonlinearity of the King plot, we need total isotope shift (including mass shift) for two transitions a and b. Then, using Eq. (3.3) one can write for the isotope shift between isotopes i and j

$$\begin{aligned}\frac{\nu_{bij}}{\mu_{ij}} =& \frac{F_b}{F_a}\frac{\nu_{aij}}{\mu_{ij}} + \left(K_b - \frac{F_b}{F_a}K_a\right) + \left(G_b^{(2)} - \frac{F_b}{F_a}G_a^{(2)}\right)\frac{\delta\langle r^2\rangle_{ij}^2}{\mu_{ij}} \\ &+ \left(G_b^{(4)} - \frac{F_b}{F_a}G_a^{(4)}\right)\frac{\delta\langle r^4\rangle_{ij}}{\mu_{ij}}.\end{aligned} \tag{3.11}$$

Here ν_{bij} is the total isotope shift for the transition b which is related to FIS [see formula (3.3)] by $\nu_{bij} = \nu_{bij}^{\text{FIS}} + K_b\mu_{ij}, K$ is the electron structure factor for the mass shift, and $\mu = 1/m_i - 1/m_j$ is the inverse mass difference. The meaning of all other parameters in (3.11) is the same as in (3.3). The first line of Eq. (3.11) corresponds to the standard King plot, and the second and third lines contain the terms which may cause the King plot nonlinearities. To calculate isotope shift and build King plot using (3.11), we use the calculated parameters $F, G^{(2)}, G^{(4)}$ from Table 3.1, the values of K and μ from Ref. [1], and the values of the change of nuclear parameters $\delta\langle r^2\rangle_{ij}$ and $\delta\langle r^4\rangle_{ij}$ which come from several nuclear models (see below).

Table 3.2: The deviations from the linearity of the King plot (in parts of 10^{-6}). The comparison between experiment [1] and calculations in different nuclear models.

		Nuclear model					
Isotope pair	Expt.	BETA	FIT	NL3*	DD-ME2	DD-MEδ	DDPC1
168,170	−0.192	0.642	−0.206	−0.037	−0.084	−0.511	−0.080
170,172	0.270	−0.607	0.281	−0.159	−0.467	0.546	−0.222
172,174	−0.489	−3.05	−0.523	−0.200	−0.028	0.392	−0.198
174,176	0.411	3.03	0.448	0.387	0.551	−0.406	0.472

To study these nonlinearities, we use the least-square fitting of Eq. (3.11) by the formula $\nu'_b = A\nu'_a + B$, where $\nu' = \nu/\mu$. The relative nonlinearities are calculated as $\Delta\nu'_b/\nu'_b$, where $\Delta\nu'_b$ is the deviation of the isotope shift ν'_b from its linear fit. To do the fitting and making King plot, we need to know the change of nuclear parameters $\delta\left\langle r^2\right\rangle$ and $\Delta\beta$ between the isotopes of interest. We use nuclear calculations for this purpose using a range of nuclear models. They include the empirical model named BETA, the parameters of which are determined from experimental data, the hypothetical model (labeled as FIT), the parameters of which are defined by the fit of nuclear parameters to experimental FIS and the deviations of King plot from nonlinearity, and the fully self-consistent covariant density functional theory (CDFT) with several functionals such as DD-ME2, DD-MEδ, NL3*, and DD-PC1 [12, 13]. Nuclear parameters of the Yb isotopes with even neutron number obtained in these models are presented in the Supplemental Material [14].

Using the parameters coming from these models, we calculate FIS, build the King plot, find its deviations from the linearity, and compare the results to the experimental data from Ref. [1]. The results are presented in Table 3.2 and Fig. 3.1. One can see that the values of the experimental and theoretical nonlinearities are of the same order of magnitude for all nuclear models. The FIT model presents almost perfect fit of the experimental data for both isotope shift and the nonlinearities. For some models (e.g., BETA, FIT, NL3*, DDPC 1[1]) there is a strong correlation between experimental and theoretical data. This means that the nuclear deformation is an important effect which has to be included into the analysis.

---

[1] We label the CDFT model by employed functional.

The origin of nonlinearity in the King plot in deformed nuclei could also be understood from nuclear theory perspective. The single-particle states are twofold degenerate in deformed nuclei and the increase of neutron Fermi level with increasing neutron number leads to the change of the occupation of the pairs of different single-particle states, emerging from different spherical subshells, located in the vicinity of neutron Fermi level. These pairs contribute differently to the charge radii and deformations of the nucleus. As a consequence, both charge radii and deformations obtained in the CDFT calculations as a function of neutron number show some staggering with respect of averaged smooth trend (see the Supplemental Material [14]). The situation is different for the Ca$^+$ ions in the chain of $^{40-48}$Ca isotopes [15] since they do not show significant nonlinearities in the King plot. This is because these nuclei are spherical and they are built by the occupation of mostly neutron $f_{7/2}$ subshell with increasing neutron number.

Quadratic field shift. Reference [1] argues that QFS is the main source of the nonlinearity of the King plot. However, their calculations only provided an upper limit on the nonlinearity since the results of CI (configuration interaction) and MBPT calculations were very different. From our point of view, the problem with the calculations in Ref. [1] is that they have not separated a small parameter, the change of the nuclear radius, and obtained FIS from the small difference in the energies of the atomic transitions calculated for different nuclear radii. This is certainly a good approach for the calculation of FIS but it is not good enough to calculate a very small nonlinearity which is extremely sensitive to numerical noise.

Our results presented earlier indicated that QFS gives a much smaller contribution to the nonlinearity of the King plot than the upper limit presented in Ref. [1]. To test this result, we performed FIS and QFS calculations by a different method assuming that all isotopes have spherical nuclear shape ($\beta = 0$). The main motivation for using RPA method in the case of nuclear deformation is the minimization of numerical noise which comes from extra integration over directions. There is no such problem for spherical nuclei and the procedure is less complicated. FIS in this case may be found from the direct variation of the nuclear radius in the nuclear Coulomb potential. We perform HF and BO calculations

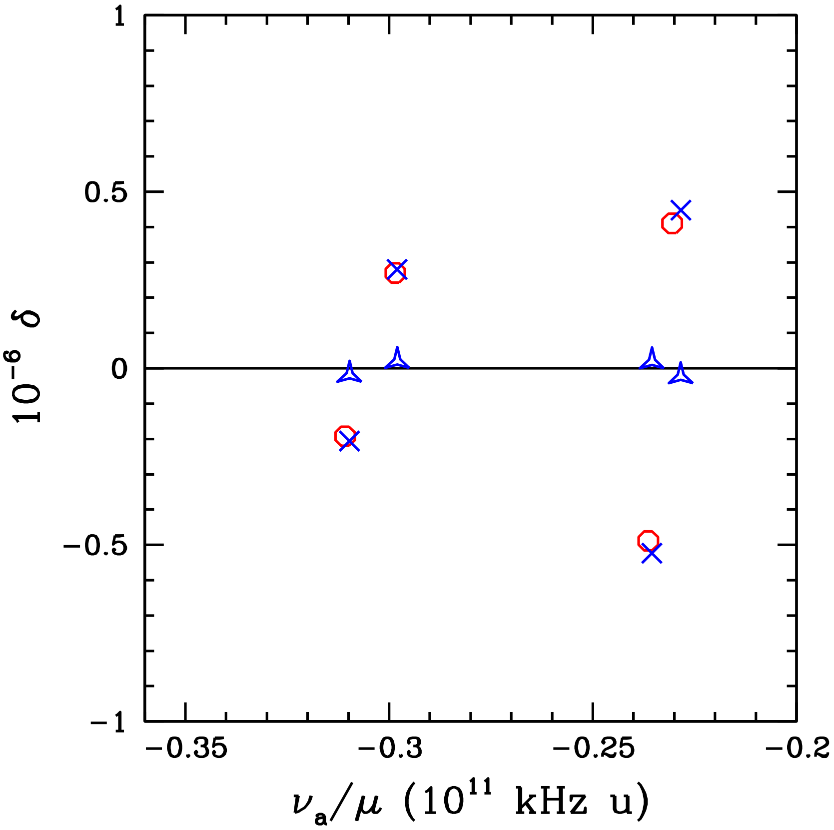

Figure 3.1: The deviations from linear King plot in experiment (solid red circles) and theory. Theoretical deviations caused by nuclear deformation are shown as blue crosses, and those by QFS are shown as blue triangles. All theoretical numbers correspond to the FIT nuclear model.

for a range of nuclear charge rms radii from $\langle r^2 \rangle = (5\text{ fm})^2$ to $\langle r^2 \rangle = (6\text{ fm})^2$ and present the results by the same formula (3.3) (see Table 3.1). As in case of deformed nuclei, the QFS parameter $G^{(2)}$ is found from the perturbation theory calculations. The values of F and $G^{(4)}$ are slightly different.

The same equation (3.11) and the same procedure were used to find the nonlinearities of the King plot. The results are presented on Fig. 3.1 and Table 3.3. As one can see, the nonlinearity caused by QFS is an order of magnitude smaller than the observations. It is also much smaller than the nonlinearity caused by the variation of the nuclear deformation.

We also performed another test calculation using constant value $\beta = 0.3$ instead of $\beta = 0$. Again, without variation of β the nonlinearity of the King plot is small.

Table 3.3: The deviations from the linearity of the King plot δ due to the quadratic field shift. The comparison between experiment [1] and calculations using the $\delta\langle r^2\rangle$ values which fit the experimental isotope shift [1]. The deviation δ is shown as a function of ν_a/μ [see Eq. (3.11)].

	Expt.		QFS	
	ν_a/μ	δ	ν_a/μ	δ
Isotope pair	10^{11} kHz u	10^{-6}	10^{11} kHz u	10^{-6}
168,170	−0.311	−0.192	−0.351	−0.017
170,172	−0.299	0.270	−0.337	0.020
172,174	−0.236	−0.489	−0.272	0.013
174,176	−0.231	0.411	−0.267	−0.016

The change of nuclear rms charge radius. Formula (3.3) with parameters $F, G^{(2)}, G^{(4)}$ from Table 3.1 can be used to find the change of the nuclear rms charge radius between isotopes by fitting experimental FIS. The values of the $\delta\left\langle r^2\right\rangle$ corresponding to the best fit (the FIT model) are presented in Table 3.4 as case A and compared with other data.

It is widely assumed in the atomic community that FIS is described by a variation of a single parameter $\langle r^2\rangle$, i.e., the change of higher nuclear momenta are ignored. On the other hand, it is claimed in Ref. [1] that inclusion of the variation of $\langle r^4\rangle$ (which is also proportional to $\delta\left\langle r^2\right\rangle$) can change $\delta\left\langle r^2\right\rangle$ extracted from the FIS experimental data by about 7%. The term with $\delta\left\langle r^4\right\rangle$ is also included in our analysis above. It is important to check what happens if this term is excluded. To do this, we perform different fitting of the RPA results. Instead of using 3.9, we use the expression in which the change of nucleus is reduced to the variation of $\langle r^2\rangle$,

$$\nu^{\mathrm{FIS}} = F\delta\left\langle r^2\right\rangle + G^{(2)}_{\mathrm{total}}\,\delta\left\langle r^2\right\rangle^2 . \tag{3.12}$$

To fit the experimental data, we add to $G^{(2)}_{\mathrm{RPA}}$ the secondorder $G^{(2)}$ from Table 3.1, $G^{(2)}_{\mathrm{total}} = G^{(2)} + G^{(2)}_{\mathrm{RPA}}$. The resulting $F, G^{(2)}_{\mathrm{RPA}}, G^{(2)}_{\mathrm{total}}$ coefficients for two transitions in Yb$^+$ are presented in Table 3.5. Then we use these numbers to fit the experimental FIS by adjusting the values of $\delta\left\langle r^2\right\rangle$. The resulting values of $\delta\left\langle r^2\right\rangle$ are presented in Table 3.4 as case B. They are practically the same as in case A. We conclude that neglecting $G^{(4)}$ actually

Table 3.4: The changes of nuclear rms charge radius ($\delta \langle r^2 \rangle$, fm^2) extracted from the isotope shift measurements. Case A of the present work corresponds to formula (3.3) while case B corresponds to formula (3.12).

Isotope pairs	Ref. [1] CI	Ref. [1] MBPT	Ref. [16, 17]	This work A	This work B
$(168, 170)$	0.156	0.149	0.1561(3)	0.138	0.137
$(170, 172)$	0.146	0.140	0.1479(1)	0.130	0.129
$(172, 174)$	0.115	0.110	0.1207(1)	0.102	0.101
$(174, 176)$	0.110	0.105	0.1159(1)	0.097	0.096

leads to the redefinition of the parameter F but practically does not affect value of $\delta \langle r^2 \rangle$ extracted from the experiment.

The comparison with other results for $\delta \langle r^2 \rangle$. It is instructive to analyze possible reasons for the difference between our results and other results for $\delta \langle r^2 \rangle$ presented in Table 3.4. There is a 12−19% difference between our results and those published in Ref. [16] (see Table 3.4). However, the latter were taken from a 50-year-old paper [17], which has no many-body calculations but only estimations based on the single-electron consideration. The uncertainty of such estimations can be well above 10% and even 20%.

There is also a 8−13% difference between our results and those of Ref. [1]. Reference [1] contains two calculations of the FIS constants performed by CI and MBPT methods with 4% difference between corresponding results. Our FIS constant F is about 13% larger than the same constant calculated in Ref. [1] using the CI method and about 8% larger than those calculated in Ref. [1] using the MBPT method. This explains the difference in the results for $\delta \langle r^2 \rangle$ (Table 3.4). When we use the numbers from Ref. [1] in Eq. (3.3), we reproduce their results for $\delta \langle r^2 \rangle$. The difference in the results seems to be due to the difference in the procedures defining the constants F and G. We use BO and the RPA method to calculate F and $G^{(4)}$ and the perturbation theory to find $G^{(2)}$, as explained above. The authors of Ref. [1] calculate F as a leading term of the Seltzer moment expansion at the origin for the total electron density (see Eq. (S11) in Ref. [1]) and then use partial derivatives of FIS to calculate constants G. Such method looks sensitive to the degeneracy of $G^{(2)}$ and $G^{(4)}$ contributions to FIS. An indication of the problem may be a

Table 3.5: Calculated parameters of formula (3.12) for the FIS in two transitions of Yb$^+$.

Transition	F (GHz/fm^2)	$G^{(2)}_{\text{RPA}}$ (GHz/fm^4)	$G^{(2)}_{\text{total}}$ (GHz/fm^4)
a	-16.7185	0.015534	0.044064
b	-17.0984	0.015883	0.044413

significant relative difference in $G^{(2)}$ parameters in Ref. [1], while we argued above that it must be very small since it appears in the second order of the small d-wave FIS matrix elements.

It is instructive to explain why the ratios $G^{(4)}/F$ are different in the s-$d_{3/2}$ and s-$d_{5/2}$ transitions (this is needed for the nonlinearity of the King plot without QFS). We suggest the following mechanism supported by the numerical calculations. According to it, only two relativistic Dirac wave functions, $s_{1/2}$ and $p_{1/2}$, penetrate into the nucleus. They have different spatial distributions inside and therefore the ratios of the $\delta \langle r^2 \rangle$ and $\delta \langle r^4 \rangle$ contributions to their energies and wave functions are noticeably different. The $d_{3/2}$ and $d_{5/2}$ wave functions interact differently with the $s_{1/2}$ and $p_{1/2}$ ones and this gives the difference in $G^{(4)}/F$.

In conclusion, we state that presented arguments indicate that nuclear deformation is the most likely source of recently observed nonlinearities of King plot in Yb$^+$. The results of the combined nuclear and atomic calculations for the effect are consistent with the observations. The contribution of the QFS is about an order of magnitude smaller. The measurements of the nonlinearity of the King may be used to study nuclear deformation in nuclei with zero spin where nuclear electric quadrupole moment cannot be extracted from atomic spectroscopy. The changes of nuclear charge RMS radii between even-even Yb isotopes extracted from atomic measurements are consistent with nuclear theory.

Acknowledgments. We are grateful for J. Berengut for useful discussion. The work was supported by the Australian Research Council Grants No. DP190100974 and No. DP200100150 and by the US Department of Energy, Office of Science, Office of Nuclear Physics under Grant No. DESC0013037.

References

[1] I. Counts, J. Hur, D. P. L. Aude Craik, H. Jeon, C. Leung, J. C. Berengut, A. Geddes, A. Kawasaki, W. Jhe, and V. Vuletic, Phys. Rev. Lett. **125**, 123002 (2020).

[2] K. Mikami, M. Tanaka, and Y. Yamamoto, Eur. Phys. J. C **77**, 896 (2017).

[3] Evaluated Nuclear Structure Data File (ENSDF) located at the website (http://www.nndc.bnl.gov/ensdf/) of Brookhaven National Laboratory. ENSDF is based on the publications presented in Nuclear Data Sheets (NDS), which is a standard for evaluated nuclear data.

[4] S. G. Nilsson and I. Ragnarsson, *Shapes and Shells in Nuclear Structure*, (Cambridge University Press, Cambridge, UK, 1995).

[5] Z.-H. Zhang, M. Huang, and A. V. Afanasjev, Phys. Rev. C **101**, 054303 (2020).

[6] S. O. Allehabi, V. A. Dzuba, V. V. Flambaum, A. V. Afanasjev, and S. E. Agbemava, Phys. Rev. C **102**, 024326 (2020).

[7] V. A. Dzuba, V. V. Flambaum, P. G. Silvestrov, and O. P. Sushkov, J. Phys. B: At. Mol. Phys. **20**, 1399 (1987).

[8] V. A. Dzuba and V. V. Flambaum, Phys. Rev. A **77**, 012515 (2008).

[9] V. A. Dzuba and V. V. Flambaum, Phys. Rev. A **83**, 052513 (2011).

[10] V. A. Dzuba, V. V. Flambaum, M. S. Safronova, S. G. Porsev, T. Pruttivarasin, M. A. Hohensee, and H. Häffner, Nat. Phys. **12**, 465 (2016).

[11] V. V. Flambaum and V. A. Dzuba, Phys. Rev. A **100**, 032511 (2019).

[12] A. V. Afanasjev and S. E. Agbemava, Phys. Rev. C **93**, 054310 (2016).

[13] S. E. Agbemava, A. V. Afanasjev, D. Ray, and P. Ring, Phys. Rev. C **89**, 054320 (2014).

[14] Please see Supplemental Material at http://link.aps.org/ supplemental/10.1103/PhysRevA.103.L030801 for more information on nuclear models used in the calculations.

[15] C. Solaro, S. Meyer, K. Fisher, J. C. Berengut, E. Fuchs, and M. Drewsen, Phys. Rev. Lett. **125**, 123003 (2020).

[16] I. Angeli and K. P. Marinova, At. Data Nucl. Data Tables **99**, 69 (2013).

[17] D. L. Clark, M. E. Cage, D. A. Lewis, and G. W. Greenlees, Phys. Rev. A **20**, 239 (1979).

Chapter 4

Theoretical study of the electronic structure of hafnium (Hf, Z=72) and rutherfordium (Rf, Z=104) atoms and their ions: Energy levels and hyperfine-structure constants

4.1 Overview

In this chapter, we study the superheavy element Rf and its first three ions by performing calculations for the energy levels and hyperfine structure constants. The results are intended to serve as a reference for future interpretations of the measurements with regard to nuclear magnetic dipoles and electric quadrupole moments. A similar calculation is performed on its lighter homolog, Hf, to verify the calculations.

This study has been published in this paper:

S. O. Allehabi, V. A. Dzuba, and V. V. Flambaum, Theoretical study of the electronic structure of hafnium (Hf, Z = 72) and rutherfordium (Rf, Z = 104) atoms and their ions: Energy levels and hyperfine-structure constants, Phys. Rev. A **104**, 052811 (2021).

4.2 Abstract

Energy levels, magnetic dipole, and electric quadrupole hyperfine structure of the superheavy element rutherfordium (Rf, $Z = 104$) and its first three ions are calculated using a combination of the configuration interaction, linearized coupled-cluster single-doubles, and many-body perturbation theory techniques. The results are to be used in future interpretations of the measurements in terms of nuclear magnetic dipole and electric quadrupole moments. To have a guide on the accuracy of the study, we perform similar calculations for hafnium (Hf, $Z = 72$) and its ions. Hf is a lighter analog of Rf with a similar electronic structure. Good agreement with the experiment for Hf and with available previous calculations of the energy levels of Rf is demonstrated.

4.3 INTRODUCTION

The study of the hyperfine structure (hfs) of the superheavy elements ($Z > 100$) is a way of obtaining important information about their nuclear structure. The measurements accompanied by atomic calculations lead to extractions of nuclear magnetic dipole and electric quadrupole moments. This serves as a test of nuclear theory leading to more reliable predictions of nuclear properties and helping in the search for the hypothetical *stability island* [1–5]. The heaviest element so far where such a study was performed is nobelium (No, $Z = 102$) [6–8]. The hfs was measured for ^{253}No isotope in the strong electric dipole transition between ground ^{1}S$_0$ and excited ^{1}P$^o_1$ state. In addition, isotope shift was measured for the ^{252,253,254}No isotopes. Similar measurements are now planned for lawrencium (Lr, $Z = 103$) [9]. Hopefully, rutherfordium (Rf, $Z = 104$) is next in line.

Most of the synthesized isotopes of Rf have odd neutron numbers [10], meaning that they have a nonzero nuclear spin and that their energy levels have hyperfine structures. The spectrum of electronic states of Rf was studied theoretically before [11–13], revealing several electric dipole transitions suitable for the measurements.

In the present work, we perform calculations of energy levels, magnetic dipole, and electric quadrupole hyperfine structure (hfs) of neutral Rf and Hf and their first three ions. The main purpose of the work is to obtain the values of the hfs matrix elements needed for the interpretation of future measurements. The energy levels are obtained as a byproduct; they are also useful for assessing the accuracy of the calculations.

We use a combination of the linearized single-double coupled-cluster method with the configuration interaction technique, the CI+SD method [14]. Calculations for Hf are performed to test the accuracy of the predictions for Rf. Hf is a lighter analog of Rf with a similar electronic structure. Good agreement with the experiment for Hf and with previous calculations of the energy levels of Rf is demonstrated. This opens a way for the interpretation of future measurements in terms of the nuclear magnetic dipole and electric quadrupole moments.

4.4 METHOD OF CALCULATION

4.4.1 Calculation of energy levels

For all considered systems, calculations start for the relativistic Hartree-Fock (RHF) procedure for the closed-shell core (Hf V and RfV). This corresponds to the use of the V^{N-M} approximation [15]. Here $N = Z$ is the total number of electrons in a neutral atom, and M is the number of valence electrons ($M = 4$ for Hf I and Rf I). The RHF Hamiltonian has the form,

$$\hat{H}^{\mathrm{RHF}} = c\alpha\hat{p} + (\beta - 1)mc^2 + V_{\mathrm{nuc}}(r) + V_{\mathrm{core}}(r), \tag{4.1}$$

where c is the speed of light, α and β are the Dirac matrices, $\hat{p}$ is the electron momentum, m is the electron mass, V_{nuc} is the nuclear potential obtained by integrating Fermi distribution of nuclear charge density, and V_{core} (r) is the self-consistent RHF potential created by the electrons of the closed-shell core.

After the self-consistent procedure for the core is completed, the full set of single-electron states is generated using the B-spline technique [16, 17]. The basis states are linear combinations of B splines, which are the eigenstates of the RHF Hamiltonian (4.1). We use 40 B splines of the order 9 in a box that has a radius $R_{\mathrm{max}} = 40a_B$ with the orbital angular momentum $0 \leqslant l \leqslant 6$. These basis states are used for solving the linearized single-double couple-cluster (SD) equations and for generating many-electron states for the configuration interaction (CI) calculations. By solving the SD equations first for the core and then for the valence states, we obtain correlation operators Σ_1 and Σ_2 [14]. Σ_1 is a one-electron operator which is responsible for correlation interaction between a particular valence electron and the core. Σ_2 is a two-electron operator that can be understood as screening of Coulomb interaction between a pair of valence electrons by core electrons. These Σ operators can be used in the subsequent CI calculations for atoms with several valence electrons to account for the corevalence and core-core correlations. Solving the SD equations for valence states also gives energies of the single-electron states for the system with one external electron above closed shells. Note that there is a small difference in the SD equations intended for obtaining these energies compared to those intended for further use in the CI calculations. In the latter case, one particular term should be removed from the SD equations since its contribution is included via the CI calculations (see Ref. [14]. for details). However, the contribution of this term is small, and the difference in the SD equations can be neglected.

The CI equations,

$$\langle a|\hat{H}^{\mathrm{CI}}|b\rangle - E\delta_{ab} = 0, \tag{4.2}$$

have the CI Hamiltonian, which includes Σ_1 and Σ_2,

$$\hat{H}^{\mathrm{CI}} = \sum_{i=1}^{M} \left(\hat{H}^{\mathrm{RHF}} + \Sigma_1\right)_i + \sum_{i<j}^{M} \left(\frac{e^2}{|r_i - r_j|} + \Sigma_{2ij}\right). \tag{4.3}$$

a and b in (4.2) are many-electron single determinant basis states which are constructed by exciting one or two electrons from one or more reference configuration(s) and then building from these configurations the states of definite values of the total momentum J. M in (4.3) is the number of valence electrons. In our cases $M = 1, 2, 3, 4$. The case of one external electron is a special one. It has no terms of the second line in the CI Hamiltonian (4.3). Taking into account that single-electron basis states are eigenstates of the RHF Hamiltonian (4.1), the CI eigenvalue problem is reduced to diagonalization of the Σ_1 matrix,

$$\langle i|\Sigma_1|j\rangle - E\delta_{ij} = 0. \tag{4.4}$$

Here i and j are single-electron basis states. Note that in spite of significant simplifications of the CI equations for $M = 1$, there is no need for the modification of the computer code. For $M = 1$ Eqs. (4.2) and (4.4) are equivalent.

There is an alternative way to perform the calculations for systems with one external electron. One can find the energies and wave functions of the valence states by solving the RHF-like equations for an external electron in which the correlation potential Σ_1 is included:

$$\left(\hat{H}^{\mathrm{RHF}} + \Sigma_1 - \epsilon_v\right)\psi_v = 0. \tag{4.5}$$

Here index v numerate states of an external electron, wave functions ψ_v are usually called the Brueckner orbitals (BO) [18], and the energies ϵ_v and wave functions ψ_v include

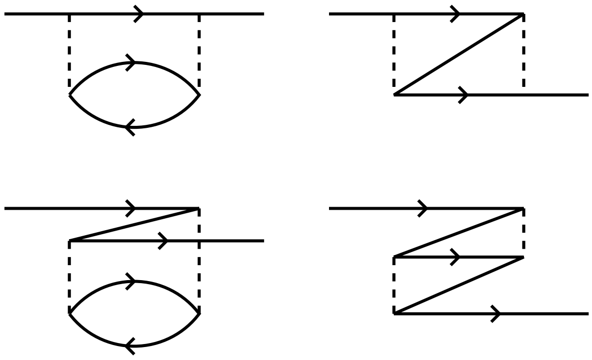

Figure 4.1: Four diagrams for the second-order correlation operator Σ_1.

correlation corrections. The BO can be used to calculate matrix elements, in particular, for the hfs (see below). Comparing two ways of the calculations is an important test of the accuracy. It is especially valuable when there is a lack of experimental data, which is the case of the present work.

The meaning of the Σ_1 operator is the same in the CI and BO equations [Eqs. (4.4) and (4.5)]. However, the Σ_1 operator, which comes from the SD calculations as a set of matrix elements between single-electron states, cannot be directly used in (4.5) since here we need the operator in the coordinate representation. Therefore, we calculate the Σ_1 for the BO in the second order of the many-body perturbation theory (see Fig. 4.1). A particular class of the higher-order correlations is included by solving Eq. (4.5) iteratively. It includes contributions $\sim \Sigma_1^2$, Σ_1^3, etc. In the end, the two ways of calculations are sufficiently different to be a good test of accuracy.

4.4.2 The CIPT method

It is very well known that the size of the CI matrix grows exponentially with the number of valence electrons. In the present work, we have up to four valence electrons (in neutral Hf and Rf), leading to the huge size of the CI matrix, the number of lines in (4.2) $\sim 10^6$. Dealing with a matrix of this size requires significant computer power. However, it can be reduced by orders of magnitude for the cost of some sacrifices in the accuracy of the result. To do this, we use the CIPT method [19] (configuration interaction with perturbation theory). The idea is to neglect off-diagonal matrix elements between highenergy states in the CI matrix (since in the perturbation theory approach, such matrix elements appear in higher orders). Then the CI matrix equation [Eq. (4.2)] can be written in a block form,

$$\begin{pmatrix} A & B \\ C & D \end{pmatrix} \begin{pmatrix} X \\ Y \end{pmatrix} = E_a \begin{pmatrix} X \\ Y \end{pmatrix}. \tag{4.6}$$

Here block A corresponds to low-energy states, block D corresponds to high-energy states, and blocks B and C correspond to cross terms. Note that since the total CI matrix is symmetric, we have $C = B'$, i.e., $c_{ij} = b_{ji}$. Vectors X and Y contain the coefficients of expansion of the valence wave function over the single-determinant many-electron basis functions,

$$\Psi(r_1, \ldots, r_M) = \sum_{i=1}^{N_1} X_i \Phi_i(r_1, \ldots, r_M) + \sum_{j=1}^{N_2} Y_j \Phi_j(r_1, \ldots, r_M). \tag{4.7}$$

Here M is the number of valence electrons, N_1 is the number of low-energy basis states, and N_2 is the number of high-energy basis states.

We neglect off-diagonal matrix elements in block D. Finding Y from the second equation of (4.6) leads to

$$Y = (E_a I - D)^{-1} C X. \tag{4.8}$$

Substituting Y to the first equation of (4.6) leads to

$$\left[A + B(E_a I - D)^{-1} C\right] X = E_v X, \tag{4.9}$$

where I is the unit matrix. Neglecting the off-diagonal matrix elements in D leads to a very simple structure of the $(E_a I - D)^{-1}$ matrix, $(E_a I - D)^{-1}_{ik} = \delta_{ik} / (E_a - E_k)$, where $E_k = \left\langle k \left| H^{\mathrm{CI}} \right| k \right\rangle$ (see [19] for more details). Equation (4.9) gives the same solution as

Table 4.1: The number of configurations and the size of the effective CI matrix for Hf and Rf. NNC is the number of nonrelativistic configurations, NRC is the number of relativistic configurations, and N_1 is the corresponding number of states with given J^p.

J^p	NNC	NRC	N_1
1^+	80	364	726
2^+	80	364	987
3^+	80	364	968
4^+	80	364	784
1^-	60	259	470
2^-	60	259	605
3^-	60	259	566

Eq. (4.6) if the energy parameter E_a in the left-hand side of (4.9) has the same value as the solution E_v. Since the value of E_v is not known in advance, we use an iterative procedure, $E_a^{(n)} = E_v^{(n-1)}$, where n is iteration number. On first iteration one can use a solution of the simplified equation $AX = E_aX$ or use some guess energy. In most cases less than 10 iterations is sufficient for full convergence.

The relative sizes of blocks A and D can be varied in the calculations in search of a reasonable compromise between the accuracy of the results and the computer power needed to obtain them. In our current calculations, the number of lines in (4.9) is $\sim 10^3$.

Note that the CI matrix is different for every combination of the value of the total angular momentum J and the parity of the states (J^p). Therefore, the choice of the N_1 parameter (i.e., the size of the effective CI matrix) should be done separately for every J^p. In doing so we follow the rule that all states of the same configuration should be treated equally, either as low-energy or high-energy states. Since for every given configuration the number of states with different values of J is different, the values of N_1 are also different for every J^p. The search for a compromise between the size of the effective CI matrix and the accuracy of the results is also done separately for every J^p. Table 4.1 shows the parameters used in the present calculations. The only external parameter chosen "by hands" is the number of nonrelativistic configurations. The values of other parameters are calculated. For example, one nonrelativistic configuration $7s^26d^2$ corresponds to three relativistic configurations: $7s^26d^2_{3/2}, 7s^26d_{3/2}6d_{5/2}$, and $7s^26d^2_{5/2}$. The total number of states included in the calculations, $N_1 + N_2$, also varies with J^p being about 10^6.

4.4.3 Calculation of hyperfine structure

To calculate hfs, we use the time-dependent Hartree-Fock (TDHF) method, which is equivalent to the well-known random-phase approximation (RPA). The RPA equations are the following:

$$\left(\hat{H}^{\mathrm{RHF}} - \epsilon_c\right)\delta\psi_c = -\left(\hat{f} + \delta V^f_{\mathrm{core}}\right)\psi_c \tag{4.10}$$

where $\hat{f}$ is an operator of an external field (an external electric field, nuclear magnetic dipole, or electric quadrupole fields). Index c in (4.10) numerates states in the core, ψ_c is a singleelectron wave function of the state c in the core, $\delta\psi_c$ is the correction to this wave function caused by an external field, and $\delta V^f_{\mathrm{core}}$ is the correction to the self-consistent RHF potential caused by changing of all core states. The nucleus is assumed to be a sphere with a uniform distribution of the nuclear electric quadrupole moment and the nuclear magnetic dipole moment. Equation (4.10) is solved self-consistently for all states in the core. As a result, an effective operator of the interaction of valence electrons with an external field is constructed as $\hat{f} + \delta V^f_{\mathrm{core.}}$. The energy shift of a many-electron state a, which is a solution of the CI equations [Eq. (4.2)], is given by

$$\delta\epsilon_a = \langle a|\sum_{i=1}^{M}\left(\hat{f} + \delta V^f_{\mathrm{core}}\right)_i|a\rangle. \tag{4.11}$$

When the wave function for the valence electrons comes as a solution of Eq. (4.9), Eq. (4.11) is reduced to

$$\delta\epsilon_a = \sum_{ij} x_i x_j \langle\Phi_i|\hat{H}^{\mathrm{hfs}}|\Phi_j\rangle, \tag{4.12}$$

where $\hat{H}^{\mathrm{hfs}} = \sum_{i=1}^{M}(\hat{f} + \delta V^f_{\mathrm{core}})_i$. For better accuracy of the results, the full expansion (4.7) might be used. Then it is convenient to introduce a new vector Z, which contains both X and $Y, Z \equiv \{X, Y\}$. Note that the solution of (4.9) is normalized by the condition

$\sum_i x_i^2 = 1$. The normalization condition for the total wave function (4.7) is different, $\sum_i x_i^2 + \sum_j y_j^2 \equiv \sum_i z_i^2 = 1$. Therefore, when X is found from (4.9), and Y is found from (4.8), both vectors should be renormalized. Then the hfs matrix element is given by the expression, which is similar to (4.12) but has many more terms,

$$\delta\epsilon_a = \sum_{ij} z_i z_j \langle \Phi_i | \hat{H}^{\text{hfs}} | \Phi_j \rangle. \tag{4.13}$$

In the case of one external electron, the calculations can also be done using the BO,

$$\delta\epsilon_v = \langle v | \hat{f} + \delta V^f_{\text{core}} | v \rangle. \tag{4.14}$$

Here v stands for a solution of the Eq. (4.5). Energy shifts (4.11), (4.14) are used to calculate hfs constants A and B using textbook formulas

$$A_a = \frac{g_I \delta\epsilon_a^{(A)}}{\sqrt{J_a(J_a+1)(2J_a+1)}}, \tag{4.15}$$

and

$$B_a = -2Q\delta\epsilon_a^{(B)} \sqrt{\frac{J_a(2J_a-1)}{(2J_a+3)(2J_a+1)(J_a+1)}}. \tag{4.16}$$

Here $\delta\epsilon_a^{(A)}$ is the energy shift (4.11) or (4.14) caused by the interaction of atomic electrons with the nuclear magnetic moment μ, $g_I = \mu/I$, I is nuclear spin; $\delta\epsilon_a^{(B)}$ is the energy shift (4.11) or (4.14) caused by the interaction of atomic electrons with the nuclear electric quadrupole moment Q [Q in (4.16) is measured in barns].

4.4.4 Further corrections to the hyperfine structure

Using Eq. (4.12) is the fastest way of calculating hfs for many-electron atoms. Sometimes it gives pretty accurate results, within ∼10% of the experimental values. This is usually the case when the hfs comes mostly from contributions of the s and p states. In our case, the contribution of the s states is suppressed because, in the leading configurations ($6s^25d^2$ and $6s^25d6p$), the $6s$ electrons are from the closed subshell and do not contribute to the

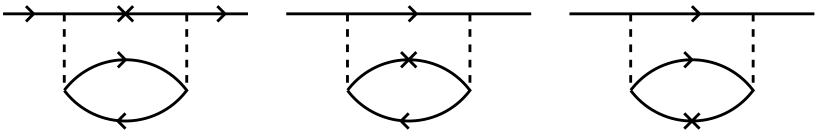

Figure 4.2: Sample SR diagrams corresponding to the first diagram in Fig. 4.1. The cross stands for the hfs operator. It goes to all internal lines of all four diagrams for the Σ_1 operator.

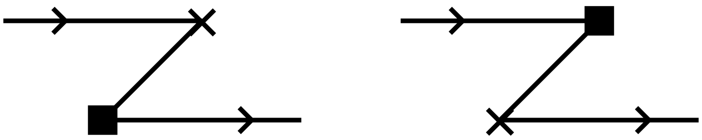

Figure 4.3: Self-energy diagrams. The cross stands for the hfs operator, and the black box stands for the correlation operator Σ_1 (see Fig. 4.1).

hfs. This means that further corrections to the hfs matrix elements should be considered. Equation (4.12) can still be used to identify states with large hfs. The accuracy of the calculations is likely to be higher for such states. This is because the small value of the hfs often comes as a result of strong cancellations between different contributions leading to poor accuracy of the results.

There are at least three classes of the higher-order corrections to the hfs matrix elements: (a) Contribution of the higher states (HS). This is the difference between (5.11) and (4.12). (b) Corrections to the single-electron matrix elements caused by the correlation operator Σ_1. This includes *the structure radiation* (SR) when the hfs operator is inside of the Σ_1 operator (see Fig. 4.2) and the self-energy correction when the hfs operator is outside of the Σ_1 operator (see Fig. 4.3) (see also [20,21]). (c) Two-particle correction [20,21], which is a correction to the Coulomb interaction between valence electrons caused by the hfs interaction (see Fig. 4.4).

To study the corrections to the single-electron matrix elements, it is convenient to have a system with one external electron above closed shells where experimental data are available for a range of valence states. The ^{135}Ba$^+$ ion is a good example of such a system. Table 4.2 presents a comparison with the measured magnetic dipole hfs constants of ^{135}Ba$^+$, calculated in different approximations. The RHF (relativistic Hartree-Fock) column cor-

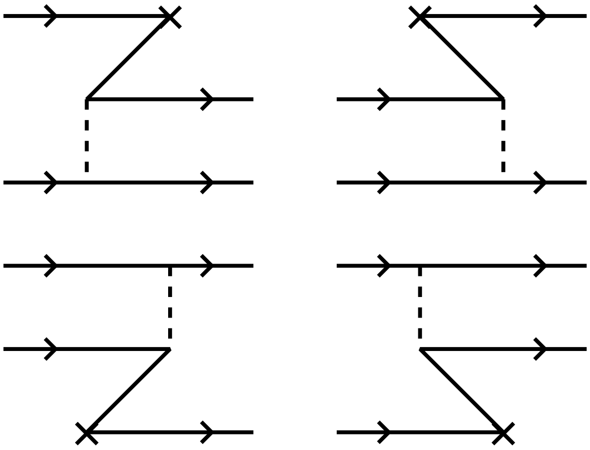

Figure 4.4: Two - particle correction to the many-electron matrix element of the hfs interaction. The cross stands for the hfs operator, and the dashed line is the Coulomb interaction.

responds to using Eq. (4.14) in which the valence state $|v\rangle$ is a Hartree-Fock orbital and the core polarization correction $\delta V^f_{\mathrm{core}}$ is absent. In the RPA column the CP correction is added, BORPA corresponds to using the BO in (4.14), and the BORPA rescaled is the same but the BO calculated with rescaled correlation operator $\lambda\Sigma_1$; the rescaling parameter λ is chosen to fit the experimental energies. The SR column is the structure radiation (Fig. 4.2), and the *total* column is the sum of the previous two columns.

The last column presents the experimental hfs constants from Ref. [22,23]. The table shows that all considered corrections are important, and including them all leads to accurate results in most cases. Therefore, all these corrections should be included in the calculations for many-electron atoms via correcting single-electron matrix elements. The inclusion of the CP and SR corrections is straightforward, but the inclusion of correlations like in the BO needs some clarification. The CI Hamiltonian (4.3) does include the correlation operator Σ_1 leading to the mixing of the states above the core and forming orbitals similar to BO. No core states are involved in this mixing. On the other hand, the BO found by solving Eq. (4.5) can be written in the first order of Σ_1 as

$$\psi_v^{\mathrm{BO}} = \sum_i |i\rangle \frac{\langle i|\Sigma_1|v\rangle}{E_v - E_i}. \tag{4.17}$$

Table 4.2: Magnetic dipole hfs constants of ^{135}Ba$^+$ (MHz) calculated in different approximations.

State	RHF	RPA	BORPA	BORPA rescaled	SR	Total	Expt. [22, 23]
$6s_{1/2}$	2603	3090	3815	3654	−63	3591	3593
$6p_{1/2}$	440	530	691	659	5	664	665
$6p_{3/2}$	64	105	134	129	−16	113	113
$5d_{3/2}$	115	133	165	161	27	188	170
$5d_{5/2}$	46	−50	−47	−48	35	−13	−10.7

Here summation goes over the complete set of the single-electron Hartree-Fock states, including states in the core. The self-energy (SE) terms (Fig. 4.3) are needed to account for this missed summation over the core states in the CI calculations. Table 4.2 shows that the considered approximation gives very accurate results for the hfs of the s and p state, while the results for the d states are less accurate. Furthermore, the relative difference between theory and experiment for $d_{3/2}$ states is about two times smaller than for the $d_{5/2}$ states. This means that while considering the hfs of many-electron atoms in which the values of the hfs constants come mostly from the contribution of the d states (like Hf and Rf), it is preferable to consider states in which the contribution of the $d_{3/2}$ states dominates over the contribution of the $d_{5/2}$ states. The accuracy of the calculations is likely to be higher for these states. To identify such states, we need to do the analysis of the partial contributions to the hfs of the many-electron atoms. We will further discuss the matter in section 4.5.2.

4.5 RESULTS

4.5.1 Energy levels of Hf, Rf, and their ions

Calculated energy levels of Hf and its first three ions are presented in Table 4.3 and are compared with the experiment. Good agreement between the sets of data indicates that applied approximation is sufficiently accurate to proceed to the calculations of the hyperfine structure. Energy levels of Hf and Hf$^+$ were calculated before (see, e.g., [13] for

Hf and [24] for Hf$^+$). We do not make a direct comparison between the results because to assess the accuracy of the method, it is sufficient to compare the result with the experiment. However, it is useful to understand the reasons for some differences in our results with the results of previous calculations of Ref. [13]. Some energy levels calculated in [13] are closer to the experiment than in the present work (e.g., low energy states); others (e.g., some high energy states) are closer to the experiment in our present work. The main reason for the differences is the use of the different versions of the CI + SD method.

Table 4.3: Excitation energies (E, cm^{-1}) for some low states of Hf I, Hf II, Hf III, and Hf IV.

No.	Conf.	Term	J	Present (CI+SD)	Expt.
		Hf I			[29]
1	$5d^26s^2$	^3F	2	0	0
2	$5d^26s^2$	^3F	3	2114	2356.68
3	$5d^26s^2$	^3F	4	4148	4567.64
4	$5d^26s^2$	^1D	2	4799	5638.62
5	$5d^26s^2$	^3P	1	5063	6572.54
6	$5d^26s^2$	^3P	2	9026	8983.75
7	$5d6s^26p$	$^1D^\mathrm{o}$	2	10634	10508.88
8	$5d^26s^2$	^1G	4	10402	10532.55
9	$5d6s^26p$	$^3D^\mathrm{o}$	1	14042	14017.81
10	$5d^36s$	^5F	1	12469	14092.26
11	$5d6s^26p$	$^3F^\mathrm{o}$	2	14092	14435.12
12	$5d6s^26p$	$^3F^\mathrm{o}$	3	14545	14541.66
13	$5d^36s$	^5F	2	12625	14740.67
14	$5d^36s$	^5F	3	13181	15673.32
15	$5d6s^26p$	$^3D^\mathrm{o}$	2	15706	16163.35
16	$5d^36s$	^5F	4	14050	16766.60

Continued on next page

Table 4.3 – continued

No.	Conf.	Term	J	Present (CI+SD)	Expt.
17	$5d^26s6p$	$^5G^o$	2	18234	18011.04
18	$5d6s^26p$	$^3P^o$	1	17969	18143.39
19	$5d6s^26p$	$^3F^o$	4	16485	18224.97
20	$5d6s^26p$	$^3D^o$	3	17824	18381.50
21	$5d^26s6p$	$^5G^o$	3	19148	19292.68
22	$5d6s^26p$	$^3P^o$	2	19490	19791.29
23	$5d^36s$	^5P	1	18363	20784.87
24	$5d^36s$	^5P	2	19085	20908.43
		Hf II			[29]
1	$5d6s^2$	^2D	3/2	0	0
2	$5d6s^2$	^2D	5/2	3054	3050.88
3	$5d^26s$	^4F	3/2	3578	3644.65
4	$5d^26s$	^4F	5/2	4312	4904.85
5	$5d^26s$	^4F	7/2	5330	6344.34
6	$5d^26s$	^4F	9/2	8039	8361.76
7	$5d^26s$	^4P	1/2	11675	11951.70
8	$5d^26s$	^2F	5/2	11783	12070.46
9	$5d^26s$	^4P	3/2	11781	12920.94
10	$5d^26s$	^4P	5/2	12581	13485.56
11	$5d^26s$	^4D	3/2	13836	14359.42
12	$5d^26s$	^2F	7/2	14410	15084.26
13	$5d6s6p$	$^4F^o$	3/2	28580	28068.79
14	$5d6s6p$	$^4D^o$	1/2	29249	29160.04
15	$5d6s6p$	$^4F^o$	5/2	29759	29405.12
16	$5d6s6p$	$^4D^o$	3/2	31903	31784.16
		Hf III			[30]

Continued on next page

Table 4.3 – continued

No.	Conf.	Term	J	Present (CI+SD)	Expt.
1	$5d^2$	^3F	2	0	0
2	$5d6s$	^3D	2	2572	3039.7
3	$5d^2$	^3F	3	1944	3288.7
4	$5d^2$	^1D	2	5212	5716
5	$5d^2$	^3F	4	5598	6095.1
6	$5d6s$	^3D	3	6443	6881.6
7	$5d^2$	^3P	2	11909	12493.2
		Hf IV			[30]
1	$4f^{14}5d$	^2D	3/2	0	0
2	$4f^{14}5d$	^2D	5/2	4721	4692
3	$4f^{14}6s$	^2S	1/2	17530	18380
4	$4f^{14}6p$	$^2P^o$	1/2	66611	67039
5	$4f^{14}6p$	$^2P^o$	3/2	76232	76614
6	$4f^{14}7s$	^2S	1/2	140329	140226

The method of Ref. [25] was used in Ref. [13], while in the present work, we use the method of Ref. [14]. Another reason for the differences comes from the fact that in the present work we do not include radiative corrections. This is because we focus mostly on the hyperfine structure. However, the method of inclusion of the radiative corrections developed in Ref. [26] and used in Ref. [13] is applicable for the energy levels and transition amplitudes but not applicable for the singular operators like the operators of hfs. Finally, in the present work, we use the CIPT technique to get a huge gain in sensitivity while making some sacrifices in accuracy (see Sec. 4.4.2 for details). This approach was not used in previous works, and this is another reason for some differences in the results.

Calculated energy levels of Rf and its first three ions are presented in Table 4.4 and compared with other calculations. Energy levels of neutral Rf were calculated in a number of earlier works [11–13, 27], and energy levels of Rf$^+$ were calculated in Refs. [11, 13]; only the ionization potential (IP) of Rf III and Rf IV were reported before [13, 27, 28]. The origin of the differences in the energies of Rf in our present work and earlier work of Ref. [13] is the same as for Hf; see discussion above.

As can be seen from the table, the results of the present calculations for Rf and Rf$^+$ are in excellent agreement with previous studies; the difference between the energies of earlier works and present results for Rf is within 300 cm^{-1} for a majority of energy levels, and it is up to ∼1000 cm^{-1} for some states. The difference for Rf$^+$ is within ∼2000 cm^{-1}, and for some states it is significantly smaller.

Table 4.4: Excitation energies (E, cm^{-1}) for some low states of Rf I, Rf II , Rf III, and Rf IV.

				Present	Other Cal.		
No.	Conf.	Term	J	(CI+SD)			
		Rf I			[11]	[12]	[13]
1	$7s^26d^2$	^{3}F	2	0	0	0	0
2	$7s^27p6d$	^{3}F^o	2	2737	2210	3923	2547
3	$7s^26d^2$	^{3}F	3	4259	4855	4869	4904
4	$7s^26d^2$	^{3}P	2	6873	7542	8704	7398
5	$7s^26d^2$	^{3}P	1	7502	8776	10051	8348
6	$7s^26d^2$	^{3}F	4	7836	7542	8597	8625
7	$7s^27p6d$	^{3}D^o	1	8028	8373	9201	8288
8	$7s^27p6d$	^{3}D^o	2	11235	10905	12889	11273
9	$7s^27p6d$	^{3}F^o	3	11328	11905	12953	11390
10	$7s^27p6d$	^{1}D^o	2	13811	–	–	14403
11	$7s^26d^2$	^{1}D	2	13841	–	–	13630
12	$7s^26d^2$	^{1}G	4	14040	–	–	14476

Continued on next page

Table 4.4 – continued

No.	Conf.	Term	J	Present (CI+SD)	Other Cal.		
13	$7s^27p6d$	^{3}P^o	1	16017	–	–	16551
14	$7s^27p6d$	^{3}D^o	3	17367	–	–	18029
15	$7s^27p6d$	^{3}F^o	4	19979	–	–	20477
16	$7s6d^27p$	^{5}G^o	2	20371	–	–	20347
17	$7s6d^3$	^{5}F	1	20626	–	–	21552
18	$7s^27p6d$	^{3}P^o	2	21031	–	–	21480
19	$7s6d^3$	^{5}F	2	21512	–	–	23079
20	$7s6d^27p$	^{5}G^o	3	22941	–	–	23325
21	$7s6d^3$	^{5}F	3	23002	–	–	25432
22	$7s^27p6d$	^{1}F^o	3	23965	–	–	24634
23	$7s6d^3$	^{5}F	4	25231	–	–	–
24	$7s6d^27p$	^{5}F^o	1	25821	–	–	–
		Rf II			[11]	[24]	
1	$7s^26d$	^{2}D	3/2	0	0	0	–
2	$7s^26d$	^{2}D	5/2	7026	7444	5680	–
3	$7s6d^2$	^{4}F	3/2	15030	–	15678	–
4	$7s6d^2$	^{4}F	5/2	16817	–	17392	–
5	$7s^27p$	^{2}P^o	1/2	19050	19390	16657	–
6	$7s6d^2$	^{4}P	1/2	23701	–	24615	–
7	$7s6d^2$	^{4}D	5/2	25392	–	26565	–
8	$7s6d^2$	^{4}P	3/2	25561	–	26648	–
9	$7s6d^2$	^{4}D	3/2	28940	–	29983	–
10	$7s7p6d$	^{4}F^o	3/2	30264	–	27846	–
11	$7s6d^2$	^{2}P	1/2	31238	–	32550	–
12	$7s7p6d$	^{4}F^o	5/2	33320	–	31031	–
13	$7s^27p$	^{2}P^o	3/2	33621	35513	31241	–

Continued on next page

Table 4.4 – continued

No.	Conf.	Term	J	Present (CI+SD)	Other Cal.		
14	$7s7p6d$	$^4\mathrm{D}^o$	1/2	37378	–	36156	–
15	$7s7p6d$	$^2\mathrm{P}^o$	3/2	40015	–	38814	–
16	$7s7p6d$	$^4\mathrm{D}^o$	5/2	40640	–	42410	–
				Rf III			
1	$7s^2$	$^1\mathrm{S}$	0	0	–	–	–
2	$7s6d$	$^3\mathrm{D}$	1	8526	–	–	–
3	$7s6d$	$^3\mathrm{D}$	2	9945	–	–	–
4	$7s6d$	$^3\mathrm{D}$	3	16878	–	–	–
5	$7s6d$	$^1\mathrm{D}$	2	19165	–	–	–
6	$6d^2$	$^3\mathrm{F}$	2	24371	–	–	–
7	$6d^2$	$^3\mathrm{F}$	3	28326	–	–	–
				Rf IV			
1	$5f^{14}7s$	$^2\mathrm{S}$	1/2	0	–	–	–
2	$5f^{14}6d$	$^2\mathrm{D}$	3/2	3892	–	–	–
3	$5f^{14}6d$	$^2\mathrm{D}$	5/2	13559	–	–	–
4	$5f^{14}7p$	$^2\mathrm{P}^\mathrm{o}$	1/2	50770	–	–	–
5	$5f^{14}7p$	$^2\mathrm{P}^\mathrm{o}$	3/2	75719	–	–	–
6	$5f^{14}8s$	$^2\mathrm{S}$	1/2	127703	–	–	–

The ionization potentials for Rf III and Rf IV have been calculated, and the results obtained are 192367 cm^{-1} and 257396 cm^{-1}, respectively. Those results are compared with experiment and other theoretical studies. In Ref. [28], the measured results achieved for the IP are 191960 cm^{-1} and 257290 cm^{-1} for Rf III and Rf IV, respectively; and in Ref. [27], the calculated results obtained are 192301 cm^{-1} and 257073 cm^{-1}, respectively. All these values are in excellent agreement with the results of the present work. For Rf

Table 4.5: Contributions to the magnetic dipole hfs constants of ^{179}Hf (MHz). The CI values correspond to formula (4.12); HS is the difference between (5.11) and (4.12); SR is structure radiation (Fig. 4.2); SE is self-energy corrections (Fig. 4.3); TP is two-particle correction (Fig. 4.4). The Sum line contains the sums of all single-particle contributions (CI,HS,SR,SE). The Total line contains also TP contributions. The Final line contains error bars calculated according to (4.18). Experimental values are taken from [31–33].

	$^3F_2$	$^3F_3$	$^3F_4$	$^1D_2$	$^3P_2$	$^3D^o_2$	$^5G^o_2$
CI	−82.18	−35.24	−16.04	−32.38	−41.36	−42.18	191.16
HS	15.34	5.70	2.90	14.29	15.24	12.22	−52.21
SR	−13.08	−16.19	−19.67	−18.35	−13.87	−16.88	−17.80
SE	−0.90	1.70	2.66	3.13	3.28	2.50	−13.30
Sum	−80.82	−44.03	−30.15	−33.31	−36.71	−44.34	107.85
TP	11.33	−8.18	−12.69	−19.34	−25.55	−4.92	37.17
Total	−69.49	−52.21	−42.84	−52.65	−62.26	−49.26	145.02
Final	−69(7)	−52(9)	−42(9)	−52(9)	−62(14)	−49(6)	145(33)
Expt.	−71.43	−50.81	−43.46	−47.68	−44.7	−46.93	128.74

III, the difference is just 407 cm^{-1} compared with [28] and 66 cm^{-1} compared with [27]; and for Rf IV, the variation is just 106 cm^{-1} compared with [28] and 323 cm^{-1} compared with [27]. This is well inside of the error bars of this work.

Comparison of the spectra of Rf and its ions (Table 4.4) with the spectra of Hf and its ions (Table 4.3) show many similarities and some differences. The most prominent difference is the difference in the ground-state configurations of the double and triple ionized ions. This difference comes from the relativistic effects, which pull s electrons closer to the nucleus, reversing the order of the $7s$ and $6d$ states of the Rf ions on the energy scale compared to the $6s$ and $5d$ states of the Hf ions.

4.5.2 Hyperfine structure of Hf I and Hf II

As it was discussed in Sec. 4.4.4, calculation of the hfs in cases when d states are involved often leads to poor accuracy of the results. This is because the density of the d states in the vicinity of the nucleus is negligible, and all values of the hfs constants come from higher-order corrections, which include mixing with s states. If leading higher-order corrections are included, then the accuracy for some states might be sufficiently good. It is

Table 4.6: Contributions of different partial waves into the magnetic dipole hfs constants of ^{179}Hf (MHz). The n.d. stands for non-diagonal contributions, which include $s_{1/2}-d_{3/2}$, $p_{1/2}-p_{3/2}$, $d_{3/2}-d_{5/2}$, etc., contributions. The TP terms are not included.

	$^3F_2$	$^3F_3$	$^3F_4$	$^1D_2$	$^3P_2$	$^3D_2^o$	$^5G_2^o$
n.d.	−37.22	0.37	23.34	27.19	8.46	−6.52	−64.55
$s_{1/2}$	18.89	−5.31	−12.34	23.69	27.71	12.46	−206.51
$p_{1/2}$	0.42	0.28	0.12	0.24	0.32	−31.63	58.40
$p_{3/2}$	0.38	0.16	0.10	−1.09	−0.31	1.94	3.61
$d_{3/2}$	−75.17	5.78	5.60	−46.41	−2.95	−41.13	177.65
$d_{5/2}$	7.92	−44.32	−44.20	−36.97	−69.08	20.59	137.18
$f_{5/2}$	2.58	0.25	−0.57	−0.27	−0.24	0.09	1.45
$f_{7/2}$	0.92	−1.01	−1.75	−0.62	−0.45	0.04	0.25
$g_{7/2}$	0.36	0.03	−0.11	0.04	0.01	−0.06	0.35
$g_{9/2}$	0.12	−0.27	0.36	−0.11	−0.18	0.03	0.01
Total	−80.82	−44.03	−30.15	−33.31	−36.71	−44.34	107.85

important to have a way of recognizing such states. Then we would be able to recommend which states of Rf or its ions should be used to extract nuclear moments from the comparison of the measured and calculated hfs. It was suggested in Sec. 4.4.4 to study partial contributions to the hfs matrix elements. It is also important to study the relative values of the higher-order corrections. In this section, we perform such a study for magnetic dipole and electric quadrupole hfs constants of Hf and Hf$^+$ for the states where experimental data are available. Table 4.5 shows leading and higher-order contributions to the magnetic dipole hfs constants A for five even and two odd states of Hf. Table 4.6 shows partial wave contributions to the same A constants of the seven states of Hf; leading and higher-order contributions to the magnetic dipole hfs constants A for five even and two odd states of Hf are taken into account. Tables 4.7 and 4.8 show similar data for the electric quadrupole hfs constant B.

Studying Tables 4.5, 4.6, 4.7, 4.8 as well as Table 4.2 reveal that accurate calculated values of the hfs constants are likely to be found for the states which satisfy three conditions:

- The value of the hfs constant is relatively large.
- There is no strong cancellation between different contributions.

Table 4.7: Contributions to the electric quadrupole hfs constants of ^{179}Hf (MHz). The meaning of the contribution titles are the same as in Table 4.5. Experimental values are taken from [31–33]. Experimental values are rounded to the last digit before decimal point. More accurate numbers together with error bars can be found in Refs. [31–33].

	$^3F_2$	$^3F_3$	$^3F_4$	$^1D_2$	$^3P_2$	$^3D_2^{\mathrm{o}}$	$^5G_2^{\mathrm{o}}$
CI	708	921	1972	−1107	−1358	153	2455
HS	−108	−193	−274	153	252	−155	−310
SR	130	49	33	−115	−52	99	162
SE	4	−12	−48	9	19	−11	7
Sum	734	765	1683	−1060	−1139	86	2314
TP	−2	17	57	−0.63	−22	28	80
Final	731	783	1740	−1061	−1162	114	2394
Error bar	(43)	(144)	(725)	(178)	(243)	(215)	(143)
Expt.	706	931	1619	−905	−1364	740	2802

Table 4.8: Contributions of different partial waves into the electric quadrupole hfs constants of ^{179}Hf (MHz). The n.d. stands for non-diagonal contributions, which include $s_{1/2} - d_{3/2}$, $p_{1/2} - p_{3/2}$, $d_{3/2} - d_{5/2}$, etc., contributions. The TP terms are not included.

	$^3F_2$	$^3F_3$	$^3F_4$	$^1D_2$	$^3P_2$	$^3D_2^{\mathrm{o}}$	$^5G_2^{\mathrm{o}}$
n.d.	865	−125	−1819	−454	144	−1117	2525
$p_{3/2}$	−5	7	26	31	−7	44	125
$d_{3/2}$	70	159	−274	294	−37	108	−19
$d_{5/2}$	−206	715	3623	−875	−1215	1041	−340
$f_{5/2}$	39	281	117	418	43	24	54
$f_{7/2}$	−56	−273	−26	−464	−80	−17	−51
$g_{7/2}$	35	48	58	77	36	0	28
$g_{9/2}$	−10	−48	−22	−87	−22	3	−8
Sum	732	765	1682	−1059	−1139	86	2314

Table 4.9: Contributions into the magnetic dipole hfs constants of the $^2D_{3/2}$ and $^4F^{\mathrm{o}}_{5/2}$ states of the ^{179}Hf$^+$ ion (MHz). Experimental values are taken from [34].

	$^2D_{3/2}$	$^4F^{\mathrm{o}}_{5/2}$		$^2D_{3/2}$	$^4F^{\mathrm{o}}_{5/2}$
			n.d.	30.66	19.71
CI+HS	2.11	−521.50	$s_{1/2}$	−23.63	105.68
SR	−28.38	−0.02	$p_{1/2}$	−0.68	38.61
SE	−1.79	23.80	$p_{3/2}$	1.09	1.57
Sum	−28.06	−497.72	$d_{3/2}$	−64.44	−667.02
TP	24.06	−58.25	$d_{5/2}$	27.67	4.72
Total	−4.00	−555.97	$f_{5/2}$	1.06	−0.89
Final	−4(9)	−556(67)	$f_{7/2}$	0.07	0.00
Expt.	−17.5(0.9)	−540(2)	Total	−28.06	−497.71

- The value of the hfs constant is dominated by partial contributions from the low angular momentum states.

As one can see, only magnetic dipole hfs of the ground state of Hf fully satisfies these conditions. The difference between theory and experiment, in this case, is about 3%. In all other cases, including the electric quadrupole hfs constant of the ground state, there is a large contribution from the $4d_{5/2}$ channel. However, the accuracy of the results is reasonably good for both types of the hfs constants for some other states as well. This means that the conditions above are rather most favorable than necessary conditions. On the other hand, all cases with poor results can be explained by strong cancellation between different contributions and a large contribution from the $d_{5/2}$ partial wave.

Studying Tables 4.2, 4.5, 4.6, 4.7, 4.8 also allows one to find a way of a rough estimation of the uncertainty of the calculations and assign specific error bars to all theoretical results. Dominating contribution to the error usually comes from the contributions of the $d_{3/2}$ and $d_{5/2}$ partial waves. The data in Table 4.2 shows that the error for the $d_{3/2}$ contribution is about 10%, while the error for the $d_{5/2}$ contribution is about 20%. The contribution of the other partial waves to the error budget can be neglected because of either a small error (s and p waves) or a small contribution. It is natural to assume that the accuracy of the nondiagonal and two-particle contributions is also ∼10% since both these contributions have matrix elements with d states. Then the total error for a state a can be calculated as

$$\sigma_a = \sqrt{\sigma^2_{an.d.} + \sigma^2_{ad_{3/2}} + \sigma^2_{ad_{5/2}} + \sigma^2_{aTP}}, \tag{4.18}$$

where $\sigma_{an.d.} = \delta_{\text{an.d.}}/10$, $\sigma_{ad_{3/2}} = \delta_{ad_{3/2}}/10$, $\sigma_{ad_{5/2}} = \delta_{ad_{5/2}}/5$, $\sigma_{TP} = \delta_{TP}/10$. Here δ stands for a particular contribution. The values of δ can be found in Tables 4.5, 4.6, 4.7, 4.8. Error bars for the hfs constants of Hf, calculated using (4.18), are presented in Tables 4.5 and 4.7. One can see that in many cases, estimated error bars are larger than the actual difference between theory and experiment. However, in some cases of externally

Table 4.10: Contributions into the electric quadrupole hfs constants of the $^2D_{3/2}$ and $^4F^{\rm o}_{5/2}$ states of the ^{179}Hf$^+$ ion (MHz). Experimental values are taken from [34].

	$^2D_{3/2}$	$^4F^{\rm o}_{5/2}$		$^2D_{3/2}$	$^4F^{\rm o}_{5/2}$
			n.d.	−342	−3228
CI+HS	1780	−897	$p_{3/2}$	6	−36
SR	63	51	$d_{3/2}$	2071	2301
SE	−32	−35	$d_{5/2}$	−9	42
Sum	1811	−881	$f_{5/2}$	34	21
TP	12	−15	$f_{7/2}$	11	−3
Total	1823	−896	$g_{7/2}$	40	23
Final	1823(208)	−896(281)	$g_{9/2}$	1	−1
Expt.	1928(21)	−728(17)	Total	1181	−881

strong cancellations between different contributions, the estimated error bars are smaller than the difference between theory and experiment. This probably means that such states should be excluded from the consideration.

We found experimental data on the hfs of Hf$^+$ for only two states, the ground state $5d6s^2$ $^2D_{3/2}$, and the excited odd state $5d6s6p$ $^4F^o_{5/2}$ [34]. Calculated contributions to the hfs of these states are presented in Table 4.9 for the magnetic dipole hfs and Table 4.10 for the electric quadrupole hfs. One can see from Table 4.9 that calculated A hfs constant of the ground state is consistent with zero due to strong cancellation between different contributions. On the other hand, the accuracy of the result for the excited state is high; the difference between theory and experiment is about 3%. This state satisfies all "most favorable" conditions discussed above.

For the electric quadrupole hfs constant B, the situation is opposite (see Table 4.10); the accuracy is high for the ground state, and it is not so high for the excited state. The latter can be explained by strong cancellation between the nondiagonal contributions and the contributions from the $d_{3/2}$ partial wave.

Table 4.11: Hyperfine structure constants A and B for Rf I and Rf II. Numeration of states corresponds to Table 4.4. Error bars are calculated with the use of Eq. (4.18).

No.	Conf.	Term	J	Energy cm^{-1}	A/g_I MHz	B/Q MHz
			Rf I			
1	$7s^26d^2$	^3F	2	0	202(108)	271(18)
7	$7s^27p6d$	$^3D^o$	1	8028	−2546(386)	716(50)
13	$7s^27p6d$	$^3P^o$	1	16017	788(259)	−738(109)
24	$7s6d^27p$	$^5F^o$	1	25821	−14460(1177)	−283(14)
2	$7s^27p6d$	$^3F^o$	2	2737	3185(485)	963(102)
8	$7s^27p6d$	$^3D^o$	2	11235	−423(418)	446(129)
10	$7s^27p6d$	$^1D^o$	2	13811	−40(150)	578(37)
9	$7s^27p6d$	$^3F^o$	3	11328	3229(423)	1015(162)
14	$7s^27p6d$	$^3D^o$	3	17367	939(273)	1139(217)
20	$7s6d^27p$	$^5G^o$	3	22941	5245(711)	776(54)
			Rf II			
1	$7s^26d$	^2D	3/2	0	−190(137)	1448(130)
5	$7s^27p$	$^2P^o$	1/2	19050	12960(280)	0
14	$7s7p6d$	$^4D^o$	1/2	37378	−21730(2636)	0
13	$7s^27p$	$^2P^o$	3/2	33621	−7798(849)	2078(113)
15	$7s7p6d$	$^2P^o$	3/2	40015	7193(937)	1414(28)
10	$7s7p6d$	$^4F^o$	3/2	30264	9650(984)	1374(43)
12	$7s7p6d$	$^4F^o$	5/2	33320	15810(1828)	417(141)
16	$7s7p6d$	$^4D^o$	5/2	40640	7582(1532)	1421(259)

4.5.3 Hyperfine structure of Rf I and Rf II

Hyperfine structure constants A and B calculated for selected states of Rf I and Rf II are presented in Table 4.11. We have calculated the hfs only for the ground state and for the low-lying states of opposite parity, which are connected to the ground state by electric dipole transitions. The frequencies of these transitions, together with the hyperfine structure, are likely to be measured first. The same method of calculations and the same analysis of the partial contributions and error bars were used for Rf I and Rf II as for Hf I and Hf II (see the previous section). We do not present tables of partial contributions for Rf I and Rf II to avoid overloading the paper with technical details. Only final results, together with the error bars, are presented in Table 4.11. As in the case of Hf I and Hf II the actual error of the calculations might be significantly smaller than the estimated uncertainties. Note that strong relativistic effects also pull the $7s$ and $7p_{1/2}$ electrons of Rf closer to the nucleus, enhancing their contribution to the hyperfine structure. This might be another reason for the higher accuracy of the calculation for Rf I and Rf II compared to what we had for Hf I and Hf II.

4.6 CONCLUSION

In this paper, the energy levels and the hyperfine structure constants A and B for low-lying states of the Rf atom and ions were calculated. Energy levels were calculated for Rf I, Rf II, Rf III, and Rf IV, while hyperfine structure constants were calculated for Rf I and Rf II. Similar calculations were performed for the lighter analog of Rf, the Hf atom, and its ions to control the accuracy of the calculations. Present results are in good agreement with other calculations and previous measurements where the data are available. The way of estimation of the uncertainty of the hfs calculations is suggested. For the majority of the states, the uncertainty is within 10%.

ACKNOWLEDGMENTS

This work was supported by the Australian Research Council Grants No. DP190100974 and No. DP200100150. This research includes computations using the computational cluster Katana supported by Research Technology Services at UNSW Sydney [35].

References

[1] Y. T. Oganessian, V. K. Utyonkov, Y. V. Lobanov, *et al.,* Heavy element research at Dubna, Nucl. Phys. A **734**, 109 (2004).

[2] Y. Oganessian, Heavy element research at FLNR (Dubna), Eur. Phys. J. A **42**, 361(2009).

[3] Y. Oganessian, Nuclei in the "Island of Stability" of Superheavy Elements, Acta Phys. Pol. B **43**, 167 (2012).

[4] J. H. Hamilton, S. Hofmann, and Y. T. Oganessian, Search for Superheavy Nuclei, Annu. Rev. Nucl. Part. Sci **63**, 383 (2013).

[5] M. Leino, Production and properties towards the island of stability, EPJ Web Conf. **131**, 01002 (2016).

[6] M. Laatiaoui, W. Lauth, H. Backe *et al.*, Atom-at-a-time laser resonance ionization spectroscopy of nobelium, Nature (London) **538**, 495 (2016).

[7] S. Raeder, D. Ackermann, H. Backe, R. Beerwerth, J. C. Berengut, M. Block, A. Borschevsky, B. Cheal, P. Chhetri, C. E. Dullmann *et al.*, Probing Sizes and Shapes of Nobelium Isotopes by Laser Spectroscopy, Phys. Rev. Lett. **120**, 232503 (2018).

[8] S. G. Porsev, M. S. Safronova, U. I. Safronova, V. A. Dzuba, and V. V. Flambaum, Nobelium energy levels and hyperfine-structure constants, Phys. Rev. A **98**, 052512 (2018).

[9] E. V. Kahl, J. C. Berengut, M. Laatiaoui, E. Eliav, and A. Borschevsky, High-precision ab initio calculations of the spectrum of Lr^+, Phys. Rev. A **100**, 062505 (2019).

[10] B. R. J. Muhyedeen, The Quantized Atomic Masses of the Elements: Part-6; Z=100-107 (Fm-Bh), Euro. J. Sci. Res. **152**, 418 (2019).

[11] E. Eliav, U. Kaldor, and Y. Ishikawa, Ground State Electron Configuration of Rutherfordium: Role of Dynamic Correlation, Phys. Rev. Lett. **74**, 1079 (1995).

[12] N. S. Mosyagin, I. I. Tupitsin, and A. V. Titov, Precision calculation of the low-lying excited states of the Rf atom, Radiochemistry **52**, 394 (2010).

[13] V. A. Dzuba, M. S. Safronova, and U. I. Safronova, Atomic properties of super-heavy elements No, Lr, and Rf, Phys. Rev. A **90**, 012504 (2014).

[14] V. A. Dzuba, Combination of the single-double coupled-cluster and the configuration-interaction methods: Application to barium, lutetium, and their ions, Phys. Rev. A **90**, 012517 (2014).

[15] V. A. Dzuba, V^{N-M} approximation for atomic calculations, Phys. Rev. A **71**, 032512 (2005).

[16] W. R. Johnson and J. Sapirstein, Computation of Second-Order Many-Body Corrections in Relativistic Atomic Systems, Phys. Rev. Lett. **57**, 1126 (1986).

[17] W. R. Johnson, S. A. Blundell, and J. Sapirstein, Finite basis sets for the Dirac equation constructed from B splines, Phys. Rev. A **37**, 307 (1988).

[18] V. A. Dzuba, V. V. Flambaum, P. G. Silvestrov, and O. P. Sushkov, Correlation potential method for the calculation of energy levels, hyperfine structure and E1 transition amplitudes in atoms with one unpaired electron, J. Phys. B **20**, 1399 (1987).

[19] V. A. Dzuba, J. C. Berengut, C. Harabati, and V. V. Flambaum, Combining configuration interaction with perturbation theory for atoms with a large number of valence electrons, Phys. Rev. A **95**, 012503 (2017).

[20] V. A. Dzuba, V. V. Flambaum, M. G. Kozlov, and S. G. Porsev, Using effective operators in calculating the hyperfine structure of atoms, J. Exp. Theor. Phys. **87**, 885 (1998).

[21] V. A. Dzuba and V. V. Flambaum, Off-diagonal hyperfine interaction and parity nonconservation in cesium, Phys. Rev. A **62**, 052101 (2000).

[22] L.-J. Ma and G. zu Putlitz, On the Electric Nuclear Quadrupole Moments of ^{135,137}Ba, Z. Phys. A **277**, 107 (1976).

[23] R. E. Silverans, G. Borghs, P. De Bisschop, and M. Van Hove, Hyperfine structure of the 5d $^{2}\mathrm{D}_{J}$ states in the alkaline-earth Ba ion by fast-ion-beam laser-rf spectroscopy, Phys. Rev. A **33**, 2117 (1986).

[24] H. Ramanantoanina, A. Borschevsky, M. Block, and M. Laatiaoui, Electronic structure of $\mathrm{Rf}^{+}(\mathrm{Z} = 104)$ from *ab initio* calculations, Phys. Rev. A **104**, 022813 (2021).

[25] M. S. Safronova, M. G. Kozlov, W. R. Johnson, and D. Jiang, Development of a configuration-interaction plus all-order method for atomic calculations. Phys. Rev. A **80**, 012516 (2009).

[26] V. V. Flambaum and J. S. M. Ginges, Radiative potential and calculations of QED radiative corrections to energy levels and electromagnetic amplitudes in many-electron atoms, Phys. Rev. A **72**, 052115 (2005).

[27] V. A. Dzuba, M. S. Safronova, U. I. Safronova, and A. Kramida, Ionization potentials of superheavy elements No, Lr, and Rf and their ions, Phys. Rev. A **94**, 042503 (2016).

[28] E. Johnson, B. Fricke, O. L. Keller, Jr., C. W. Nestor, Jr., and T. C. Tucker, Ionization potentials and radii of atoms and ions of element 104 (unnilquadium) and of hafnium (2+) derived from multiconfiguration Dirac–Fock calculations, J. Chem. Phys. **93**, 8041 (1990).

[29] A. Kramida, Yu. Ralchenko, J. Reader, and NIST ASD Team, NIST Atomic Spectra Database (Version 5.7.1), [https:// physics.nist.gov/asd] (National Institute of Standards and Technology, Gaithersburg, 2019)

[30] P. F. A. Klinkenberg, T. A. M. Van Kleef, and P. E. Noorman, Structure and Ionization Potential of Hf III and Hf IV, Physica **27**, 151 (1961).

[31] S. Büttgenbach, R. Dicke, and H. Gebauer, Hyperfine structure of the $5d^2 6s^2$ $^3\mathrm{F}_{3,4}$ metastable atomic levels of ^{179}Hf and the nuclear quadrupole moments of ^{177}Hf and ^{179}Hf, Phys. lett. A **62**, 307 (1977).

[32] N. Boos, F. Le Blanc, M. Krieg, J. Pinard, G. Huber, M. D. Lunney, D. LeDu, R. Meunier, M. Hussonnois, O. Constantinescu *et al.*, Nuclear Properties of the Exotic High-Spin Isomer $^{178}\mathrm{Hf}^{m2}$ from Collinear Laser Spectroscopy, Phys. Rev. lett. **72**, 2689 (1994).

[33] D. Zimmermann, P. Baumann, D. Kuszner, and A. Werner, Isotope shift and hyperfine structure in the atomic spectrum of hafnium by laser spectroscopy, Phys. Rev. A **50**, 1112 (1994).

[34] W. Z. Zhao, F. Buchinger, J. E. Crawford, S. Fedrigo, S. Gulick, J. K. P. Lee, O. Constantinescu, M. Hussonnois, and J. Pinard, Hyperfine structure and isotope shifts in the $5d6s^2$ $a^2D_{3/2}$–$5d6s(a^3D)6p$ $z^4F^o_{5/2}$ transition of Hf II, Hyperfine Interact. **108**, 483 (1997).

[35] Katana (shared computational cluster), [https://doi.org/10. 26190/669x-a286], University of New South Wales, Sydney, 2010.

Chapter 5

Calculation of the hyperfine structure of Dy, Ho, Cf, and Es

5.1 Overview

Our consideration in this chapter is focused on a theoretical study of the magnetic dipole hyperfine structure (HFS) constants and electric quadrupole HFS constants for two heavy actinide atoms, Cf and Es. Our calculations of magnetic dipole HFS constants and electric quadrupole HFS constants are encouraged by experiments to determine HFS of these atoms for the purpose of extracting magnetic moments μ and electric quadrupole moments Q of the nuclei of the considered isotopes.

This study has been published in this paper:

S. O. Allehabi, V. A. Dzuba, and V. V. Flambaum, Calculation of the hyperfine structure of Dy, Ho, Cf, and Es, Phys. Rev. A **107**, 032805 (2023).

5.2 Abstract

A recently developed version of the configuration interaction (CI) method for open shells with a large number of valence electrons has been used to study two heavy atoms, californium (Cf, $Z = 98$) and einsteinium (Es, $Z = 99$). Motivated by experimental work to measure the hyperfine structure (HFS) for these atoms, we perform the calculations of the magnetic dipole HFS constants A and electric quadrupole HFS constant B for the sake of interpretation of the measurements in terms of nuclear magnetic moment μ and electric quadrupole moment Q. For verification of our computations, we have also carried out similar calculations for the lighter homologs dysprosium (Dy, $Z = 66$) and holmium (Ho, $Z = 67$), whose electronic structures are similar to Cf and Es, respectively. We have conducted a revision of the nuclear moments of some isotopes of Es leading to an improved value of the magnetic moment of ^{253}Es $\left[\mu\left(^{253}\text{Es}\right) = 4.20(13)\mu_N\right]$.

5.3 INTRODUCTION

The study of atomic properties of heavy actinides has gained growing interest [1–8]. Transition frequencies and the hyperfine structure (HFS) are being measured. Measuring HFS is motivated by obtaining data on the nuclear momenta of heavy nuclei. This would advance our knowledge about the nuclear structure of superheavy nuclei benefiting the search for the hypothetical stability island. In light of this, we focus on theoretically studying the hyperfine structure for heavy actinides, californium (Cf, $Z = 98$) and einsteinium (Es, $Z = 99$). Combining the calculations with the measurements would allow for the extraction of the nuclear magnetic moment μ and electric quadrupole moments Q of the studied isotopes.

HFS constants of some states of odd isotopes of Cf $\left(^{249}\text{Cf}, ^{251}\text{Cf}, ^{253}\text{Cf}\right)$ were recently measured and nuclear moments μ and Q were extracted using our calculations [8]. This paper presents a detailed account of these calculations as well as similar calculations for Es. In the case of Es, there are no theoretical results currently available, whereas several experimental papers have been published. Using different empirical techniques, Refs. [1–3] studied the HFS of Es for three isotopes with nonzero nuclear spins, ^{253,254,255} Es.

Heavy actinides such as Cf and Es are atoms with an open $5f$ subshell. The number of electrons on open shells is 12 for Cf and 13 for Es (including the $7s$ electrons). This presents a challenge for the calculations. We use the configuration interaction with perturbation theory (CIPT) [9] method, which has been developed for such systems. To check the applicability of the method and the expected accuracy of the results we performed similar calculations for lanthanides dysprosium (Dy, $Z = 66$) and holmium (Ho, $Z = 67$), whose electronic structures are similar to Cf and Es, respectively. Both Dy and Ho were extensively studied experimentally and theoretically (see, e.g., Refs. [10–18]). Here, we compare our results to experimental data, Refs. [10, 16] for Dy and Refs. [16–18] for Ho, to check the accuracy of the method we use.

5.4 METHOD OF CALCULATION

5.4.1 Calculation of energy levels

As it was mentioned in the Introduction, the Dy and Cf atoms have 12 valence electrons, and the Ho and Es atoms have 13 valence electrons. It is well known that as the number of valence electrons increases, the size of the configuration interaction (CI) matrix increases dramatically, making the standard CI calculations practically impossible for such systems. In this work, we use the CIPT method [9] which has been especially developed for such systems and realized in a FORTRAN code.

In this approach, the size of the CI matrix is reduced by neglecting the off-diagonal matrix elements between highenergy states and reducing the contribution of these states to the perturbation-theory-like corrections to the matrix elements between low-energy states. The size of the resulting CI matrix is equal to the number of low-energy states.

The CI Hamiltonian can be written as follows,

$$\hat{H}^{\text{CI}} = \sum_{i=1}^{N_v} \hat{H}_i^{\text{HF}} + \sum_{i<j}^{N_v} \frac{e^2}{|r_i - r_j|}, \tag{5.1}$$

where i and j enumerate valence electrons and N_v is the total number of valence electrons, e is electron charge, and r is the distance. $\hat{H}_i^{\text{HF}}$ is the single-electron Hartree-Fock (HF) Hamiltonian, which has the form

$$\hat{H}_i^{\text{HF}} = c\boldsymbol{\alpha}_i \cdot \hat{\mathbf{p}}_i + (\beta - 1)mc^2 + V_{\text{nuc}}(r_i) + V^{N-1}(r_i). \tag{5.2}$$

Here, c is the speed of light, $\boldsymbol{\alpha}_i$ and β are the Dirac matrices, $\hat{\mathbf{p}}_i$ is the electron momentum, m is the electron mass, $V_{\text{nuc}}(r)$ is the nuclear potential obtained by integrating the Fermi distribution of nuclear charge density, and $V^{N-1}(r)$ is the selfconsistent HF potential obtained for the configuration with one $7s$ (or $6s$) electron removed from the ground state configuration which has N electrons. This corresponds to the V^{N-1} approximation [19,20] which is convenient for generating a single-electron basis. Single-electron basis states are calculated in the frozen V^{N-1} potential, so that they correspond to the atom with one electron excited from the ground state. External electron wave functions are expressed in terms of coefficients of expansion over single-determinant basis state functions

$$\Psi(r_1, \ldots, r_{N_v}) = \sum_{i=1}^{N_1} X_i \Phi_i(r_1, \ldots, r_{N_v}) + \sum_{j=1}^{N_2} Y_j \Phi_j(r_1, \ldots, r_{N_v}). \tag{5.3}$$

Here, N_1 is the number of low-energy basis states, and N_2 is the number of high-energy basis states.

Then the CI matrix equation can be written in a block form,

$$\begin{pmatrix} A & B \\ C & D \end{pmatrix} \begin{pmatrix} X \\ Y \end{pmatrix} = E_a \begin{pmatrix} X \\ Y \end{pmatrix}. \tag{5.4}$$

Here, block A corresponds to low-energy states, block D corresponds to high-energy states, and blocks B and C correspond to cross terms. Note that since the total CI matrix is symmetric, we have $C = B'$, i.e., $c_{ij} = b_{ji}$. Vectors X and Y contain the coefficients of expansion of the valence wave function over the single-determinant many-electron basis functions [see Eq. (5.3)].

Finding Y from the second equation of (5.4) leads to

$$Y = (E_a I - D)^{-1} C X. \tag{5.5}$$

Substituting Y to the first equation of (5.4) leads to

$$\left[A + B(E_a I - D)^{-1} C\right] X = E_a X, \tag{5.6}$$

where I is the unit matrix. Then, following Ref. [9] we neglect off-diagonal matrix elements in block D. This leads to a very simple structure of the $(E_a I - D)^{-1}$ matrix, $(E_a I - D)^{-1}_{ik} = \delta_{ik} / (E_a - E_k)$, where $E_k = \left\langle k \left| H^{\mathrm{CI}} \right| k \right\rangle$. Matrix elements of the effective CI matrix (5.6) have the form

$$\langle i|\hat{H}^{\mathrm{eff}}|j\rangle = \langle i|\hat{H}^{\mathrm{CI}}|j\rangle + \sum_k \frac{\langle i|\hat{H}^{\mathrm{CI}}|k\rangle\langle k|\hat{H}^{\mathrm{CI}}|j\rangle}{E_a - E_k}. \tag{5.7}$$

We see that the standard CI matrix elements between lowenergy states are corrected by an expression which is very similar to the second-order perturbation theory correction to the energy. This justifies the name of the method. To calculate this second-order correction we need to know the energy of the state E_a which must come as the result of the solution of the equation, i.e., it is not known in advance. Therefore, iterations are needed. We start from any reasonable guess for the energy. For example, it may come from the solution of the equation with a neglected second-order correction. Note that the energy-independent numerators of the second-order correction can be calculated only once, on the first iteration, kept on disk, and reused on every consequent iteration. This means that only the first iteration takes some time while all other iterations are very fast.

Table 5.1: Excitation energies (E, cm^{-1}), and g factors for some low states of Dy, and Ho atoms.

			This work		NIST [16]	
Conf.	Term	J	E	g	E	g
			Dy			
$4f^{10}6s^2$	^5I	8	0.000	1.242	0.000	1.2416
$4f^{10}6s^2$		7	3933	1.175	4134.2	1.1735
$4f^{10}6s^2$		6	7179	1.073	7050.6	1.0716
$4f^95d6s^2$	$^7H^o$	8	7818	1.347	7565.610	1.35246
$4f^95d6s^2$		7	9474	1.353	8519.210	1.336
$4f^{10}6s^2$	^5I	5	9589	0.909	9211.6	0.911
$4f^95d6s^2$	$^7I^o$	9	10048	1.316	9990.974	1.32
$4f^95d6s^2$	$^7H^o$	6	11052	1.417	10088.802	1.36
$4f^{10}6s^2$	^5I	4	11299	0.613	10925.3	0.618
			Ho			
$4f^{11}6s^2$	$^4I^o$	15/2	0.00	1.196	0.00	1.1951
$4f^{11}6s^2$		13/2	5205	1.107	5419.7	
$4f^{10}5d6s^2$	$(8,\frac{3}{2})$	17/2	8344	1.262	8378.91	
$4f^{10}5d6s^2$		15/2	8385	1.280	8427.11	
$4f^{11}6s^2$	$^4I^o$	11/2	8501	0.979	8605.2	1.012
$4f^{10}5d6s^2$	$(8,\frac{3}{2})$	13/2	8989	1.336	9147.08	
$4f^{10}5d6s^2$		19/2	8952	1.231	9741.50	
$4f^{11}6s^2$	$^4I^o$	9/2	10550	0.780	10695.8	0.866

As a rule, less than ten iterations are needed for full convergence. As a result, we have an energy of the state E_a and expansion coefficients X and Y.

5.4.2 Basis states

To solve the CI equations we need many-electron basis states which are constructed from single-electron states. For single-electron basis states we use the B-spline technique [21,22]. These states are defined as linear combinations of B splines that are eigenstates of the HF Hamiltonian (5.2). B-spline bases provide users with the flexibility to choose a basis that best meets their study specifications.. In our study, $40B$ splines of the order nine are calculated within a box of radius $R_{\max} = 40a_B$ (where a_B represents Bohr's radius) and an orbital angular momentum of $0 \leqslant l \leqslant 4$. Fourteen states above the core in each partial wave are used. With these parameters the basis is sufficiently saturated for the low-lying states. Increasing the values of $l_{\max}, R_{\max}$, as well as the number of B splines, do not produce any significant change in the results.

The many-electron states are found by making all possible single- and double-electron excitations from a few reference configurations. One, two, or three configurations, corresponding to the low-lying states of an atom, are considered as reference configurations. One configuration of the same parity is considered at a time. For each configuration, all possible values of the projection of the total angular momentum j of the single-electron states are considered and many-electron states with fixed values of total many-electron angular momentum J and its projection M are constructed. Usually, we take $M = J$

5.4.3 Calculation of hyperfine structure

In this section, we mostly follow our previous work on hafnium and rutherfordium [23]. To calculate HFS, we use the time-dependent Hartree-Fock (TDHF) method, which is equivalent to the well-known random-phase approximation (RPA). The RPA equations are the following,

$$\left(\hat{H}^{\mathrm{RHF}} - \epsilon_c\right) \delta\psi_c = -\left(\hat{f} + \delta V^f_{\mathrm{core}}\right) \psi_c \tag{5.8}$$

where $\hat{f}$ is an operator of an external field (nuclear magnetic dipole or electric quadrupole fields). Index c in (5.8) numerates states in the core, ψ_c is a single-electron wave function of the state c in the core, $\delta\psi_c$ is the correction to this wave function caused by an external field, and $\delta V^f_{\mathrm{core}}$ is the correction to the self-consistent relativistic Hartree-Fock (RHF) potential caused by changing of all core states. Equations (5.8) are solved self-consistently for all states in the core. As a result, an effective operator of the interaction of valence electrons with an external field is constructed as $\hat{f} + \delta V^f_{\mathrm{core}}$.

Table 5.2: Hyperfine structure constants A and B (in MHz) for low-lying states of Dy and Ho. Nuclear spin I, nuclear magnetic moment $\mu(\mu_N)$, and nuclear electric quadrupole moment $Q(b)$ values for the isotopes of the ^{161,163}Dy and ^{165}Ho are taken from Ref. [24], $g_I = \mu/I$. The last column presents references to experimental data for A and B.

Isotope				This work		Experimental results		
Nuclear Parameters	Conf.	Term	J	A	B	A	B	Ref.
^{161}**Dy**								
$\mu = -0.480$, $I = 5/2$, $Q = 2.51$	$4f^{10}6s^2$	^5I	8	−113	1127	−116.231	1091.577	[10]
	$4f^{10}6s^2$		7	−125	1057	−126.787	1009.742	[10]
	$4f^{10}6s^2$		6	−140	991	−139.635	960.889	[10]
	$4f^9 5d6s^2$	$^7H^o$	8	−88	2256	–	–	–
	$4f^9 5d6s^2$		7	−104	2397	–	–	–
	$4f^{10}6s^2$	^5I	5	−166	928	−161.971	894.027	[10]
	$4f^9 5d6s^2$	$^7I^o$	9	−80	2663	–	–	–
	$4f^9 5d6s^2$	$^7H^o$	6	−122	2901	–	–	–
	$4f^{10}6s^2$	^5I	4	−216	997	−205.340	961.156	[10]
^{163}**Dy**								
$\mu = 0.673$, $I = 5/2$, $Q = 2.65$	$4f^{10}6s^2$	^5I	8	158	1190	162.754	1152.869	[10]
	$4f^{10}6s^2$		7	176	1116	177.535	1066.430	[10]
	$4f^{10}6s^2$		6	196	1046	–	–	–

Continued on next page

Table 5.2 – continued

Isotope Nuclear Parameters	Conf.	Term	J	This work A	This work B	Experimental results A	Experimental results B	Experimental results Ref.
	$4f^95d6s^2$	$^7H^o$	8	123	2381	–	–	–
	$4f^95d6s^2$		7	146	2531	–	–	–
	$4f^{10}6s^2$	^5I	5	233	979	–	–	–
	$4f^95d6s^2$	$^7I^o$	9	112	2812	–	–	–
	$4f^95d6s^2$	$^7H^o$	6	170	3063	–	–	–
	$4f^{10}6s^2$	^5I	4	303	1053	–	–	–
^{165}Ho								
$\mu = 4.17$, $I = 7/2$, $Q = 3.58$	$4f^{11}6s^2$	$^4I^o$	15/2	787	−1943	800.583	−1668.089	[17]
	$4f^{11}6s^2$		13/2	939	−1668	937.209	−1438.065	[17]
	$4f^{10}5d6s^2$	$(8,\frac{3}{2})$	17/2	666	1085	776.4(4.5)	608(300)	[18]
	$4f^{10}5d6s^2$		15/2	763	1127	783.0(4.5)	801(300)	[18]
	$4f^{11}6s^2$	$^4I^o$	11/2	1061	−1315	1035.140	−1052.556	[17]
	$4f^{10}5d6s^2$	$(8,\frac{3}{2})$	13/2	879	1829	916.6(0.5)	2668(7)	[18]
	$4f^{10}5d6s^2$		19/2	617	1650	745.1(1.4)	1747(78)	[18]
	$4f^{11}6s^2$	$^4I^o$	9/2	1279	−1174	1137.700	−494.482	[17]

Table 5.3: Experimental and theoretical values of the first ionization potential IP_1 (in cm^{-1}).

	State		IP_1		
Atom	Initial	Final	Present	Expt.	Ref.
Dy	$4f^{10}6s^2\ {}^5I_8$	$4f^{10}6s\ \ (8,\frac{1}{2})_{17/2}$	46658	47901.76(5)	[25]
Ho	$4f^{11}6s^2\ {}^4I^o_{15/2}$	$4f^{11}6s\ \ (\frac{15}{2},\frac{1}{2})^o_8$	47819	48567(5)	[26]
Cf	$5f^{10}7s^2\ {}^5I_8$	$5f^{10}7s\ \ {}^6I_{17/2}$	50821	50663(2)	[27]
Es	$5f^{11}7s^2\ {}^4I^o_{15/2}$	$5f^{11}7s\ \ {}^5I^o_8$	51763	51358(2)	[27]
				$51364.58(14)_{\mathrm{stat}}(50)_{\mathrm{sys}}$	[28]

The energy shift of a many-electron state a is given by

$$\delta\epsilon_a = \langle a|\sum_{i=1}^{M}\left(\hat{f}+\delta V^f_{\mathrm{core}}\right)_i|a\rangle. \tag{5.9}$$

Here, M is the number of valence electrons.

When the wave function for the valence electrons comes as a solution of Eq. (5.6), Eq. (5.9)

$$\delta\epsilon_a = \sum_{ij} x_i x_j \langle\Phi_i|\hat{H}^{\mathrm{hfs}}|\Phi_j\rangle, \tag{5.10}$$

where $\hat{H}^{\mathrm{hfs}} = \sum_{i=1}^{M}\left(\hat{f}+\delta V^f_{\mathrm{core}}\right)_i$, and x_i, x_j are vector components of X (the same is true for y_i, z_i below). For better accuracy of the results, the full expansion (5.3) might be used. Then it is convenient to introduce a new vector Z, which contains both X and $Y, Z \equiv \{X, Y\}$. Note that the solution of (5.6) is normalized by the condition $\sum_i x_i^2 = 1$. The normalization condition for the total wave function (5.3) is different, $\sum_i x_i^2 + \sum_j y_j^2 \equiv \sum_i z_i^2 = 1$. Therefore, when X is found from (5.6), and Y is found from (5.5), both vectors should be renormalized. Then the HFS matrix element is given by the expression, which is similar to (5.10) but has many more terms,

$$\delta\epsilon_a = \sum_{ij} z_i z_j \langle\Phi_i|\hat{H}^{\mathrm{hfs}}|\Phi_j\rangle. \tag{5.11}$$

Energy shift (5.9) is used to calculate HFS constants A and B using textbook formulas

$$A_a = \frac{g_I \delta\epsilon_a^{(A)}}{\sqrt{J_a(J_a+1)(2J_a+1)}}, \tag{5.12}$$

and

$$B_a = -2Q\delta\epsilon_a^{(B)}\sqrt{\frac{J_a(2J_a-1)}{(2J_a+3)(2J_a+1)(J_a+1)}}. \tag{5.13}$$

Here, $\delta\epsilon_a^{(A)}$ is the energy shift (5.9) caused by the interaction of atomic electrons with the nuclear magnetic moment $\mu, g_I = \mu/I$, and I is nuclear spin; $\delta\epsilon_a^{(B)}$ is the energy shift (5.9) caused by the interaction of atomic electrons with the nuclear electric quadrupole moment Q [Q in (5.13) is measured in barns].

5.5 ENERGY LEVELS AND HFS OF DYSPROSIUM AND HOLMIUM

For the purpose of testing the accuracy of the method, we start calculating the energy levels for some low-lying states of Dy and Ho. The results are shown in Table 5.1. As can be seen, our results are consistent with the experimental results compiled in Ref. [16] of respective atomic systems. The difference between theoretical calculations and measurements is within a few hundred cm^{-1}. Calculated and experimental Landé g factors are also presented. A comparison of Landé g factors calculated with nonrelativistic expressions is helpful for identifying state labels:

$$g_{\mathrm{NR}} = 1 + \frac{J(J+1) - L(L+1) + S(S+1)}{2J(J+1)}. \tag{5.14}$$

The total orbital momentum L, and total spin S in (5.14) cannot come from relativistic calculations. Instead, we choose their values from the condition that formula (5.14) gives values very close to the calculated g factors. This allows us to link the state to the nonrelativistic notation ${}^{2S+1}L_J$. Here, J is the total angular momentum ($\mathbf{J} = \mathbf{L} + \mathbf{S}$). A good agreement is also observed between current calculations and experimental g factors of Dy and Ho whenever experimental data are available. In order to identify the states correctly, it is essential to take this into consideration. An exception stands out in state $4f^{11}6s^2\ {}^4I^o_{9/2}$ of Ho, where the theory differs significantly from the experiment. Based on the NIST database [16] of the Ho spectrum, we can observe that there are multiple states with the same parity and total angular momentum J, separated only by small energy intervals and dominated by different electron configurations. Due to this vigorous mixing, the calculations of the g factor become unstable.

The hyperfine structures of the ground states and some low-lying states of Dy and Ho have also been calculated. The Dy atom has two stable isotopes, ^{161}Dy and ^{163}Dy, and the Ho atom has one stable isotope, ^{165}Ho. The results of calculations and corresponding nuclear parameters are presented in Table 5.2. One can see that we have good agreement between theory and experiment for the magnetic dipole constant A and electric quadrupole constant B for most states of Dy and Ho. The difference between theory and experiment is within 3% for the A constant of Dy and Ho, within 4% for the B constants of Dy and ~20% for the B constant of Ho. A similar agreement between theory and experiment was found earlier for the HFS constants of Er [7]. Two states of Ho present an exception. These are the $4f^{10}5d6s^2\left(8,\frac{3}{2}\right)_{13/2}$ state, and the $4f^{11}6s^2\ {}^4I^o_{9/2}$ state. Here, the difference between theory and experiment for electric quadrupole HFS constant B is significant. In particular, it is 138% for the $4f^{11}6s^2\ {}^4I^o_{9/2}$ state. This is the same state which shows poor accuracy for the g factor, which indicates that strong configuration mixing affects the HFS as well. It should be mentioned that an earlier study performed using the multiconfiguration Dirac-Fock (MCDF) method also found that this state had a low level of accuracy with a 117% deviation from the experimental result [13].

Note that our investigations of testing the accuracy of using the CIPT method on the Er atomic system, which has a similar electronic structure, were previously performed [7]. All the above atomic properties, energies, g factors, and HFS constants A and B for the stable isotope with nonzero spin, ^{167}Er, have been calculated. There has been a good agreement between measurements and our results (see Ref. [7], Tables 1 and 6). In the end, we expect that the results for Cf and Es will be accurate as well.

Table 5.4: Calculated hyperfine structure constants A and B (in MHz) for the ground states of Dy, Ho, Cf and Es atoms.

Atom	Conf.	Term	J	A	B
Dy	$4f^{10}6s^2$	^5I	8	$587 \times g_I$	$449 \times Q$
Ho	$4f^{11}6s^2$	$^4I^o$	15/2	$661 \times g_I$	$-543 \times Q$
Cf	$5f^{10}7s^2$	^5I	8	$608 \times g_I$	$477 \times Q$
Es	$5f^{11}7s^2$	$^4I^o$	15/2	$681 \times g_I$	$-818 \times Q$

5.6 IONIZATION POTENTIALS

Calculating the ionization potential (IP) is a good way to test the theoretical approach for the ground state. The IP is obtained as a difference between the ground state energies of the neutral atom and the ion. The CIPT method, which we use in the present calculations, has a feature of having good accuracy for low-lying states, and it decreases while going up on the energy scale. The best accuracy is expected for the ground state. On the other hand, having HFS for the ground state is sufficient to extract nuclear parameters μ and Q. Therefore, we calculate the first ionization potential (IP_1) for all atoms considered in the present work. We calculate ground state energies of neutral atoms and corresponding ions in the same V^{N-1} potential and the same single-electron basis. This ensures exact cancellation of the energies associated with core electrons. The results are presented in Table 5.3 and compared with available experimental data. As can be seen from the table the accuracy of the results is 2.7% for Dy, 1.6% for Ho, 0.3% for Cf, and 0.8% for Es.

5.7 RESULTS FOR HFS

In Table 5.4, we present the results of our calculations of the HFS constants of the ground states of Dy, Ho, Cf, and Es. We have calculated both magnetic dipole HFS constant A and electric quadrupole HFS constant B, which can be used for the extraction of nuclear moments for any isotope with nonzero spin. For a better understanding of the accuracy of the calculations for heavy actinides, it is instructive to compare electron structure factors for the HFS constants with those of lighter atoms, Dy, Ho, and Er. The situation is different for the HFS constants A and B. The electron structure factor for the magnetic dipole constant A is almost the same for heavy actinides and their lighter analogs; it varies within 3%. The electron structure factors for the HFS constant B are also similar, although the variation is larger. It goes from about 20% for the Dy, Cf pair to 50% for the Ho, Es pair. This justifies using lighter analogs of heavy actinides for the estimation of the uncertainty of the calculations. We assume 3% uncertainty for the HFS constant A of all considered atoms and 16% uncertainty for the HFS constant B (as the difference between theory and experiment for the ground state of Ho). This latter assumption is rather conservative. The difference between theory and experiment for the HFS constant B of the ground state of Dy is about 3% and it is about 10% for the ground state of Er [7].

This high level of accuracy is a bit surprising for atoms with open shells. Therefore, it is instructive to see how dominating contributions are formed. First, we note that according to numerical tests, configuration mixing gives a relatively small contribution to the HFS constants. About 90% or more comes from leading configurations which is $4f^n6s^2$ for Dy and Ho and $5f^n7s^2$ for Cf and Es ($n = 10, 11$). In these configurations s electrons form a closed shell and do not contribute to the HFS. Therefore, all of the contribution comes from f electrons. It is well known that in the case of excited valence f states (e.g., $4f$ state of Cs or $5f$ state of Fr) the HF value of the energy shift due to the HFS operator $\langle 4f|\hat{f}|4f\rangle$ is small and the dominating contribution comes from the core polarization correction $\left\langle 4f \left| \delta V^f_{\text{core}} \right| 4f \right\rangle$ [see Eq. (5.9)]. The situation is different in atoms considered in the present work. The f electron states are inside the core, localized at about the same distances as other states with the same principal quantum number, i.e., it is not even the outermost shell. For example, $\langle 4f|r|4f\rangle < 1a_B$ for Dy, Ho, and Er, while $\langle 4f|r|4f\rangle \sim 20a_B$ for Cs. Being inside the core, f states penetrate to short distances near the nucleus, making a large value of the HF matrix element $\langle 4f|\hat{f}|4f\rangle$. In contrast, the core polarization correction $\left\langle 4f \left| \delta V^f_{\text{core}} \right| 4f \right\rangle$ is small (∼1%). In the end, zeroorder matrix elements are large while core polarization and configuration mixing corrections are small. This is the key to the high accuracy of the results.

Table 5.5: Hyperfine structure constants A and B (in MHz) of the ground state of Es. Nuclear spin I, nuclear magnetic moment $\mu(\mu_N)$, and nuclear electric quadrupole moment $Q(b)$ values for the isotopes of the ^{253}Es are taken from Ref. [24], while ^{254}Es and ^{255}Es parameters are taken from Ref. [3]. $g_I = \mu/I$. The last column presents references for experimental data on A and B. The values of μ and Q obtained in this work are extracted from comparison of experimental and calculated HFS constants assuming 3% uncertainty in calculation of A and 16% uncertainty in calculation of B.

Isotope			This work				Experimental results		
Nuclear Parameters	Conf.	Term	A	B	μ	Q	A	B	Ref.
^{253}**Es**									
$\mu = 4.1(7), I = 7/2, Q = 6.7(8)$	$5f^{11}7s^2$	$^4I^o_{15/2}$	798	−5481	4.12(15)	4.8(1.0)	802(18)	−3916(550)	[3]
					4.20(13)	5.3(8)	817.153(7)	−4316.254(76)	[1]
^{254}**Es**									
$\mu = 3.42(7), I = 7, Q = 9.6(1.2)$	$5f^{11}7s^2$	$^4I^o_{15/2}$	333	−7853	3.48(10)	7.6(1.3)	339(4)	−6200(300)	[3]
^{255}**Es**									
$\mu = 4.14(10), I = 7/2, Q = 5.1(1.7)$	$5f^{11}7s^2$	$^4I^o_{15/2}$	806	−4172	4.23(26)	3.7(1.8)	824(45)	−3001(1400)	[3]

Table 5.5 shows the results and analysis of the HFS for three isotopes of Es $\left(^{253-255}\text{Es}\right)$. This table serves two purposes. First, this is another confirmation of the accuracy of the calculations. However, to compare the calculations to the experiment we need to use nuclear moments, which are known to have fairly poor accuracy (see the table). For example, the uncertainty for the magnetic moment of the ^{253} Es nucleus is 17%. On the other hand, our estimated accuracy for the HFS constant A is 3%. This means that we can improve the accuracy of the nuclear moments by extracting them from a comparison of the experimental data with our calculations. The results are presented in the table. We see that real improvement is obtained for $\mu\left(^{253}\text{Es}\right)$ only. For other nuclear moments, the uncertainties are similar but the central points are shifted. New and old values are consistent when error bars are taken into account.

5.8 CONCLUSIONS

Magnetic dipole and electric quadrupole HFS constants A and B were calculated for the ground states of heavy actinides Cf and Es. Similar calculations were performed for the lighter analogs of these atoms, Dy and Ho. To establish the accuracy of the results, the comparison between theory and experiment was done for HFS constants, energy levels, g factors, and the ionization potential, everywhere where the experimental data are available. We found an uncertainty of 3% for the HFS constant A and about 16% uncertainty for the HFS constant B. Using the calculated HFS constants of those heavy elements considered, nuclear magnetic and electric quadrupole moments can be extracted from the measurement data.

ACKNOWLEDGMENTS

The authors are grateful to S. Raeder for many stimulating discussions. This work was supported by the Australian Research Council under Grants No. DP190100974 and No.

DP200100150. S.O.A. gratefully acknowledges the Islamic University of Madinah (Ministry of Education, Kingdom of Saudi Arabia) for funding his scholarship.

References

[1] L. S. Goodman, H. Diamond, and H. E. Stanton, Nuclear and atomic moments and hyperfine-structure parameters of ^{253}Es and ^{254m}Es, Phys. Rev. A **11**, 499 (1975).

[2] N. Severijns, A. A. Belyaev, A. L. Erzinkyan, P. -D. Eversheim, V. T. Filimonov, V. V. Golovko, G. M. Gurevich, P. Herzog, I. S. Kraev, A. A. Lukhanin, V. I. Noga, V. P. Parfenova, T. Phalet, A. V. Rusakov, M. Tandecki, Yu. G. Toporov, C. Tramm, E. Traykov, S. Van Gorp, V. N. Vyachin, F. Wauters, D. Zákoucký, and E. Zotov, Hyperfine field of einsteinium in iron and nuclear magnetic moment of ^{254}Es, Phys. Rev. C **79**, 064322 (2009).

[3] S. Nothhelfer, Th. E. Albrecht-Schönzart, M. Block, *et al.*, Nuclear structure investigations of $^{253-255}$Es by laser spectroscopy. Phys. Rev. C **105**, L021302 (2022).

[4] M. Laatiaoui, and S. Raeder, New Developments in the Production and Research of Actinide Elements, Atoms **10**, 61 (2022).

[5] H. Backe, A. Dretzke, S. Fritzsche, R.G. Haire, P. Kunz, W. Lauth, M. Sewtz and N. Trautmann, Laser Spectroscopic Investigation of the Element Fermium ($Z = 100$), Hyperfine Interact. **162**, 3 (2005).

[6] M. Sewtz, H. Backe, A. Dretzke, G. Kube, W. Lauth, P. Schwamb, K. Eberhardt, C. Grüning, P. Thörle, N. Trautmann, P. Kunz, J. Lassen, G. Passler, C. Z. Dong,

S. Fritzsche, and R. G. Haire, First Observation of Atomic Levels for the Element Fermium ($Z = 100$), Phys. Rev. Lett. **90**, 163002 (2003).

[7] S. O. Allehabi, J. Li, V. A. Dzuba, and V. V. Flambauma, Theoretical study of electronic structure of erbium and fermium, J. Quantitative Spectroscopy and Radiative Transfer **253**, 107137 (2020).

[8] Felix Weber, Thomas E. Albrecht-Schönzart, S. O. Allehabi, Sebastian Berndt, Michael Block, Holger Dorrer, Christoph E. Düllmann, Vladimir A. Dzuba, Julie G. Ezold, Victor Flambaum, *et al.* (to be published).

[9] V. A. Dzuba, J. C. Berengut, C. Harabati, and V. V. Flambaum, Combining configuration interaction with perturbation theory for atoms with a large number of valence electrons, Phys. Rev. A **95**, 012503 (2017).

[10] W. J. Childs, Hyperfine Structure of $^5I_{8,7}$ Atomic States of $\mathrm{Dy}^{161,163}$ and the Ground-State Nuclear Moments, Phys. Rev. A **2**, 1692 (1970).

[11] W. Ebenhöh, V. J. Ehlers, and J. Ferch, Hyperfine-Structure Measurements on Dy^{161} and Dy^{63}, Zeitschrift für Physik **200**, 84 (1967).

[12] J. Ferch, W. Dankwort, and H. Gebauer, Hyperfine structure investigations in DyI with the atomic beam magnetic resonance method, Phys. Lett. A **49**, 287 (1974).

[13] K. T. Cheng and W. J. Childs, *Ab initio* calculation of $4f^N6s^2$ hyperfine structure in neutral rare-earth atoms, Phys. Rev. A **31**, 2775 (1985).

[14] V. A. Dzuba and V. V. Flambaum, Relativistic corrections to transition frequencies of Ag I, Dy I, Ho I, Yb II, Yb III, Au I, and Hg II and search for variation of the fine-structure constant, Phys. Rev. A **77**, 012515 (2008).

[15] V. A. Dzuba, V. V. Flambaum, and M. V. Marchenko, Relativistic effects in Sr, Dy, Yb II, and Yb III and search for variation of the fine-structure constant, Phys. Rev. A **68**, 022506 (2003).

[16] A. Kramida, Yu. Ralchenko, J. Reader, and NIST ASD Team, NIST Atomic Spectra Database (ver. 5.7.1), https://physics.nist. gov/asd (2020 September 26).

[17] B. Burghardt, S. Büttgenbach, N. Glaeser, R. Harzer,G. Meisel, B. Roski, and F. Träber, Hyperfine structure measurements in metastable states of ^{165}Ho, Z. Phys. A **307**, 193 (1982).

[18] D. Stefanska, J. Ruczkowski, M. Elantkowska, and B. Furmann, Fine- and hyperfine structure investigations of the even-parity configuration system in atomic holmium, J. Quantitative Spectroscopy and Radiative Transfer **209**, 180 (2018).

[19] H. P. Kelly, Many-Body Perturbation Theory Applied to Atoms, Phys. Rev. **136**, B896 (1964).

[20] V. A. Dzuba, V^{N-M} approximation for atomic calculations, Phys. Rev. A **71**, 032512 (2005).

[21] W. R. Johnson and J. Sapirstein, Computation of Second-Order Many-Body Corrections in Relativistic Atomic Systems, Phys. Rev. Lett. **57**, 1126 (1986).

[22] W. R. Johnson, S. A. Blundell, and J. Sapirstein, Finite basis sets for the Dirac equation constructed from B splines, Phys. Rev. A **37**, 307 (1988).

[23] S. O. Allehabi , V. A. Dzuba, and V. V. Flambaum, Theoretical study of the electronic structure of hafnium (Hf, $Z = 72$) and rutherfordium (Rf, $Z = 104$) atoms and their ions: Energy levels and hyperfine-structure constants, Phys. Rev. A **104**, 052811 (2021).

[24] N. J. Stone, Table of nuclear magnetic dipole and electric quadrupole moments, At. Data Nucl. Data Tables **90**, 75 (2005).

[25] D. Studer, P. Dyrauf, P. Naubereit, R. Heinke, and K. Wendt, Resonance ionization spectroscopy in dysprosium, Hyperfine Interact. **238**, 8 (2017).

[26] E. F. Worden, R. W. Solarz, J. A. Paisner, and J. G. Conway, First ionization potentials of lanthanides by laser spectroscopy, J. Opt. Soc. Am. **68**, 52 (1978)

[27] A. Waldek, N. Erdmann, C. Grüning, G. Huber, P. Kunz, J. V. Kratz, J. Lassen, G. Passler, and N. Trautmann, RIMS measurements for the determination of the first ionization potential of the actinides actinium up to einsteinium, in *Resonance Ion ization Spectroscopy 2000: Laser Ionization and Applications Incorporating RIS; 10th International Symposium*, edited by J. E. Parks and J. P. Young, AIP Conf. Proc. Vol. 584 (AIP, Melville, NY, 2001), p. 219.

[28] F. Weber, T. E. Albrecht-Schönzart, M. Block, P. Chhetri, C. E. Düllmann, J. G. Ezold, V. Gadelshin, A. N. Gaiser, F. Giacoppo, R. Heinke *et al.*, Atomic-structure investigations of neutral einsteinium by laser resonance ionization, Phys. Rev. Research **4**, 043053 (2022).

Chapter 6

Theoretical study of electronic structure of erbium and fermium

6.1 Overview

In this chapter, we study several atomic properties of the superheavy element Fm. Among them, we calculate the HFS to help in the interpretation of experimental data. We also calculate IS, which can be used to extract information on nuclear deformation and change of nuclear RMS radius from the IS measurements. As a guide for accuracy, we also performed the same calculations on Er, which has a similar electronic structure.

This study has been published in this paper:

S. O. Allehabi, J. Li, V. A. Dzuba, and V. V. Flambauma, Theoretical study of electronic structure of erbium and fermium, J. Quant. Spectrosc. Radiat. Transfer **253**, 107137 (2020).

I presented this work at an international conference:

Theoretical study of electronic structure of erbium (Er), fermium (Fm), and nobelium

(No), **AIP Summer Meeting, Queensland University of Technology, Brisbane, Australia. December (2021).**

6.2 Abstract

We use a recently developed version of the configuration method for open shells to study electronic structure of erbium and fermium atoms. We calculate excitation energies of odd states connected to the even ground state by electric dipole transitions, the corresponding transition rates, isotope shift, hyperfine structure, ionization potentials and static scalar polarizabilities. We argue that measuring isotope shift for several transitions can be used to study nuclear deformation in even-even nuclei. This is important for testing nuclear theory and for searching for the hypothetical island of stability. Since erbium and fermium have similar electronic structures, calculations for erbium serve as a guide to the accuracy of the calculations.

6.3 Introduction

Fermium is one of the two heaviest atoms for which experimental spectroscopic data are available. It was intensively studied in the last two decades both theoretically and experimentally [1–8]. Frequencies of seven electric dipole transitions from the ground state to excited odd states have been measured [5, 6], and the first ionization potential has been determined [7, 8]. The measurements were led by theoretical predictions made with the use of the multi-configurational Dirac-Fock method (MCDF) [5]. It is clear from comparing these data to the spectrum of the erbium atom, which is a lighter analog of Fm, that a large number of Fm states still escaped experimental detection and theoretical determination. Further study of Fm is needed to understand its electronic structure and its difference from Er caused by interplay between correlation and relativistic effects.

The only other atom, heavier than Fm for which spectroscopic data are available is nobelium. Frequency of just one electric dipole transition between the ground state singlet $7s^2\ ^1\mathrm{S}_0$ and the excited odd-parity singlet $7s7p\ ^1\mathrm{P}^{\mathrm{o}}_1$ has been measured for three isotopes, ^{252,253,254}No [9, 10]. These measurements led also to determinations of the isotope shifts (IS) between these isotopes and the hyperfine structure (hfs) of the ^{253}No isotope. The study of hfs combined with atomic calculations [11] allows extraction of the values of nuclear magnetic dipole and electric quadrupole moments. The large value of the electric quadrupole moment indicates a strong nuclear deformation in the ^{253}No isotope. The information about nuclear deformation is important in search of the island of stability: metastable nuclei are expected to be spherically symmetric. The use of hfs to study nuclear deformation works only for odd isotopes. Even-even isotopes as a rule have zero nuclear spin, and thus no hfs of atomic levels. It is worth mentioning that nuclear theory is more complicated and less accurate for odd isotopes than for even-even isotopes [15].

In our previous works we suggested to use IS measurements to study nuclear deformation in even-even isotopes [12, 13]. Similar to how the change of nuclear root-mean square (RMS) radius ($\delta\langle r^2\rangle$) can be obtained from the measurements of IS in an atomic transition, the change of both, $\langle r^2\rangle$ and the parameter of nuclear quadrupole deformation β can be found from IS measurements made for at least two atomic transitions. This approach can be used for fermium as well. There are 20 known Fm isotopes from ^{241}Fm to ^{260}Fm [14]. All even-even isotopes in this range are strongly deformed [15], and the parameter β varies significantly from isotope to isotope. The maximum change is between ^{260}Fm ($\beta = 0.265$) and ^{248}Fm or ^{250}Fm ($\beta = 0.296$), i.e. $\Delta\beta_{\mathrm{max}} = 0.031$. Such a large change is relatively easy to detect. In this work we calculate parameters of the sensitivity of IS to the change in nuclear parameters, $\langle r^2\rangle$ and β.

The ground state of Fm is $5f^{12}7s^2\ ^3\mathrm{H}_6$. The seven odd states for which the measurements were done all belong to the same configuration $5f^{12}7s7p$ [5, 6]. However, it is well known that er- bium, which is a lighter analog of Fm, has a very rich spectrum, with most of the known odd states belonging to two configura- tions, $4f^{12}6s6p$ and $4f^{11}6s^25d$ [16]. It is natural to expect similar features in Fm. In this work we perform similar calculations for both atoms. Calculations for Er mostly serve as a guide to the accuracy of calculations.

Calculations for Fm demonstrate that both atoms have many properties in common. Some differences in the spectra can be explained by stronger relativistic effects in Fm. We calculate energy separations for the odd excited states connected to the ground state by electric dipole transitions, and the corresponding transition rates to identify stronger transitions easiest to detect. Our calculations are compared with the measurements and previous MCDF calculations.

6.4 Method of calculation

We use the recently developed configuration interaction with perturbation theory (CIPT) method [17, 18] to perform the calculations. The method was developed specifically for atoms with open shells that have a large number of electrons in open shells. Correlations between these electrons are treated using the configuration interaction technique. A set of single-electron basis states used for these calculations forms the valence space. The CIPT method was successfully used for atoms with open f [19, 20], d [22] and p [21] shells. The maximum number of electrons in the valence space was sixteen (Yb and No [10, 11, 19]). The main idea of the method is neglecting off-diagonal matrix elements between highenergy states in the CI matrix. The idea is used in several similar approaches [23–25]. However, in the CIPT method one more step is made, the whole CI matrix is reduced to the effective CI matrix of a much smaller size, in which matrix elements between lowlying states i and j are corrected by the expression similar to the second-order perturbative correction to the energy:

$$\langle i|H^{CI}|j\rangle \to \langle i|H^{CI}|j\rangle + \sum_k \frac{\langle i|H^{CI}|k\rangle\langle k|H^{CI}|j\rangle}{E - E_k}. \tag{6.1}$$

where E refers to the energy of the state of interest, and E_k denotes the diagonal matrix element for high-energy states, $E_k = \left\langle k \left| H^{CI} \right| k \right\rangle$. Summation in (6.1) goes over all high-energy states. The ordering of the states on the energy scale is done by the values of E_k. This ordering can be justified by moving more states from the perturbative term (second term in (6.1)) to the effective Cl matrix. The energies E and wave functions X are found by solving the matrix eigenvalue problem

$$\left(H^{CI} - EI\right) X = 0, \tag{6.2}$$

with H^{CI} matrix given by (6.1); where I is the unit matrix. Reducing the matrix size by (6.1) does not affect the resulting energies as long as the energy E is the same in (6.1) and (6.2). Since the energy is not known in advance, iterations over energy are needed. Usually five to ten iterations are enough for full convergence.

We use the B-spline technique [26] to build a single-electron basis set. These states are constructed as linear combinations of B-splines that are eigenstates of the relativistic Hartree-Fock (HF) Hamiltonian with the V^{N-1} potential. The self-consistent HF procedure is first done for an atom with one electron removed. For instance, the ground state of Er belongs to the [Xe]$4f^{12}6s^2$ configuration. The HF procedure is done for the [Xe]$4f^{12}$6s configuration, and basis states for valence electrons are calculated in the resulting V^{N-1} potential. Similarly, the [Rn]$5f^{12}7s$ configuration is used in the HF calculations for Fm. We use forty B-splines confined to a sphere of the radius $R_{\max} = 40a_B$. Fourteen out of forty lowestenergy eigenstates of the HF Hamiltonian are used in the CIPT calculations. Higher-lying states give only negligible contributions due to large energy denominators in (6.1). Many-electron basis states for the CI calculations are constructed by exciting one or two electrons from initial reference valence configurations. For example, to calculate even states of Er, we use the $4f^{12}6s^2$ configuration as a reference. All states of this configuration are used to construct the effective CI matrix. All states obtained by single and double excitations are used in the perturbative term, which is the last term in (6.1). For odd states, we use four reference configurations $4f^{12}6s6p$, $4f^{12}6s7p, 4f^{11}6s^25d$ and $4f^{12}6s5f$. All states from these three configurations go to the effective CI matrix while all states obtained by exciting electrons from these configurations go to the perturbative term. Similarly for Fm, the reference configurations are $5f^{12}7s^2$ for even states and $5f^{12}7s7p$, $5f^{12}7s8p$, $5f^{11}7s^26d$ and $5f^{12}7s6f$ for odd states.

The calculations are fully relativistic. Our single-electron operator in the HF and CI Hamiltonians comes from the Dirac equation. Moreover, the Breit and quantum electrodynamic corrections are included similar to what was done in our previous works [19–22].

To calculate amplitudes of electric dipole transitions and hyperfine structure, we need to include an external field in the equations. This is the electric field of a photon in case of electric dipole transitions or nuclear magnetic or quadrupole electric field in case of hfs. We use the time-dependent HartreeFock method [27] (equivalent to the random-phase approximation (RPA)) to do this. The RPA equations are first solved for the atom in the same V^{N-1} approximation as in the HF calculations. The RPA equations

$$\left(H^{HF} - \epsilon_i\right) \delta\psi_i = -\left(\hat{d} + \delta V^{N-1}\right) \psi_i \tag{6.3}$$

are iterated for all atomic states i in the core to find the correction to the atomic potential δV^{N-1} caused by the effect of an external field. Transition amplitudes are calculated as

$$A_{ab} = \langle a|\hat{d} + \delta V^{N-1}|b\rangle, \tag{6.4}$$

while hfs constants are found from the diagonal matrix elements. Here $|a\rangle$ and $|b\rangle$ are many-electron states obtained in the Cl calculations (6.2, $\hat{d}$ is the electric dipole operator (we use the length form, $\hat{d} = -e\sum_n r_n$) in case of electric dipole transitions or operator of nuclear magnetic dipole or electric quadrupole field in case of hfs. The rate of spontaneous emission of a photon in the transition from state b to state a is given by (in atomic units)

$$T_{ab} = \frac{4}{3} \left(\alpha\omega_{ab}\right)^3 \frac{A_{ab}^2}{2J_b + 1}, \tag{6.5}$$

where α is the fine structure constant, ω_{ab} is the frequency of the transition.

The results for energy levels and transition rates for Er are presented in Table 6.1 and compared to experiment. We see that the difference between theory and experiment for the energies is about a few hundred cm^{-1} for the states of the $4f^{12}6s6p$ configuration and up to 3000 cm^{-1} for $4f^{11}6s^25d$. Similar accuracy can be expected for Fm. Note that the difference in the spectra of Er and Fm mostly comes from relativistic effects, while the main source of numerical uncertainty is the incomplete treatment of correlations. Since Er and Fm have similar electronic structure, it is natural to assume that the correlations in both atoms are also similar. The same assumption worked well in many earlier calculations (see, e.g. [20–22]).

A comparison of transition rates with available experimental data (see Table 6.1) shows that the accuracy of calculations is significantly lower than for the energies. Most probably this is due to the fact that the high-energy states (those participating in the last term in (6.1) are not included into the resulting wave function in the current version of the computer code. In other words, perturbation theory correction is considered to correct the energies but not wave functions. Wave functions are still constructed from the reference configurations only (those included in the first part of the effective CI Hamiltonian (6.1)). In principle, it is possible to correct the wave function, too. This might be a subject for future work.

Table 6.1 also presents the values of calculated and experimental Landé g-factors. The g-factors are useful for identification of states. In some cases it is useful to compare the calculated g-factors to a non-relativistic expression

$$g_{NR} = 1 + \frac{J(J+1) - L(L+1) + S(S+1)}{2J(J+1)}. \tag{6.6}$$

Table 6.1: Excitation energies (E, cm^{-1}), transition amplitudes (A_{ab}, a.u.), electric dipole transition rates to the ground state (T_{ab}, s^{-1}), and g-factors for some low odd states of Er atom with J= 5,6,7. The discrepancy between the NIST and present energies is given by $\Delta = E_{\text{NIST}} - E_{\text{present}}$.

				E			A_{ab}	T_{ab}		g	
N	Conf.	Term	J	Present	NIST	Δ	Present	**Present**	Expt.	Present	NIST
1	$4f^{12}6s^2$	$^3H_6$	6	0	0	0	0	0	0	1.1651	1.16381
2	$4f^{11}(^4I^o_{15/2})5d_{3/2}6s^2$	$(15/2,3/2)^o$	6	4719	7177	2458	0.0012	$2.24\cdot10^{-02}$		1.3067	1.302
3	$4f^{11}(^4I^o_{15/2})5d_{3/2}6s^2$	$(15/2,3/2)^o$	7	5455	7697	2242	0.0034	$2.54\cdot10^{-01}$		1.2623	1.266
4	$4f^{11}(^4I^o_{15/2})5d_{5/2}6s^2$	$(15/2,5/2)^o$	7	8072	11,888	3816	0.2788	$5.52\cdot10^{+03}$		1.1477	1.153
5	$4f^{11}(^4I^o_{15/2})5d_{5/2}6s^2$	$(15/2,5/2)^o$	5	8129	11,401	3272	-0.1370	$1.85\cdot10^{+03}$		1.2030	1.205
6	$4f^{11}(^4I^o_{15/2})5d_{5/2}6s^2$	$(15/2,5/2)^o$	6	8572	11,800	3228	0.3254	$1.04\cdot10^{+04}$		1.1779	1.190
7	$4f^{11}(^4I^o_{13/2})5d_{3/2}6s^2$	$(13/2,3/2)^o$	5	13,476	15,185	1709	-0.3621	$5.91\cdot10^{+04}$		1.1914	1.160
8	$4f^{11}(^4I^o_{13/2})5d_{3/2}6s^2$	$(13/2,3/2)^o$	7	14,214	15,847	1633	-0.5442	$1.15\cdot10^{+05}$		1.0686	1.070
9	$4f^{11}(^4I^o_{13/2})5d_{3/2}6s^2$	$(13/2,3/2)^o$	6	14,265	16,070	1805	0.9524	$4.10\cdot10^{+05}$	$(9.2\pm0.05)\cdot10^{+05}$	1.1497	1.200
10	$4f^{11}(^4I^o_{13/2})5d_{5/2}6s^2$	$(13/2,5/2)^o$	7	15,233	17,796	2563	0.4817	$1.11\cdot10^{+05}$		1.1184	1.110
11	$4f^{11}(^4I^o_{13/2})5d_{5/2}6s^2$	$(13/2,5/2)^o$	6	15,278	17,456	2178	-0.1008	$5.64\cdot10^{+03}$		1.0650	1.070
12	$4f^{11}(^4I^o_{13/2})5d_{5/2}6s^2$	$(13/2,5/2)^o$	5	15,335	17,029	1694	0.0355	$8.34\cdot10^{+02}$		1.1042	1.150
13	$4f^{12}(^3H_6)6s6p(^3P^o_0)$	$(6,0)^o$	6	16,499	16,321	-178	-0.5998	$2.52\cdot10^{+05}$		1.2860	1.220
14	$4f^{11}(^4I^o_{11/2})5d_{3/2}6s^2$	$(11/2,3/2)^o$	7	16,697	18,774	2077	-0.2504	$3.94\cdot10^{+04}$		0.9480	0.965

Continued on next page

Table 6.1 – continued

				E			A_{ab}	T_{ab}		g	
N	Conf.	Term	J	Present	NIST	Δ	Present	Present	Expt.	Present	NIST
15	$4f^{12}(^3\mathrm{H}_6)6s6p(^3\mathrm{P}^o_1)$	$(6,1)^o$	6	17,131	17,074	-57	1.1178	$9.78{\cdot}10^{+05}$		1.0369	1.070
16	$4f^{12}(^3\mathrm{H}_6)6s6p(^3\mathrm{P}^o_1)$	$(6,1)^o$	7	17,316	17,157	-159	1.6462	$1.90{\cdot}10^{+06}$	$(1.17{\pm}0.06){\cdot}10^{+06}$	1.1879	1.195
17	$4\mathrm{f}^{11}(^4\mathrm{I}^o{}_{11/2})5\mathrm{d}_{3/2}6\mathrm{s}^2$	$(11/2,3/2)^o$	6	17,383	19,508	2125	0.0816	$5.45{\cdot}10^{+03}$		0.9874	0.960
18	$4f^{12}(^3\mathrm{H}_6)6s6p(^3\mathrm{P}^o_1)$	$(6,1)^o$	5	17,425	17,348	-77	1.3160	$1.69{\cdot}10^{+06}$	$(8.4{\pm}0.04){\cdot}10^{+05}$	1.1685	1.175
19	$4\mathrm{f}^{11}(^4\mathrm{I}^o{}_{11/2})5\mathrm{d}_{3/2}6\mathrm{s}^2$	$(11/2,3/2)^o$	5	18,021	19,563	1542	0.1200	$1.55{\cdot}10^{+04}$		0.9687	0.990
20	$4\mathrm{f}^{11}(^4\mathrm{I}^o{}_{11/2})5\mathrm{d}_{5/2}6\mathrm{s}^2$	$(11/2,5/2)^o$	7	18,962	21,168	2206	0.6728	$4.16{\cdot}10^{+05}$		1.0557	1.065
21	$4f^{12}(^3\mathrm{H}_6)6s6p(^3\mathrm{P}^o_2)$	$(6,2)^o$	7	18,987	19,125	138	0.0613	$3.47{\cdot}10^{+03}$		1.2448	1.235
22	$4f^{12}(^3\mathrm{H}_6)6s6p(^3\mathrm{P}^o_2)$	$(6,2)^o$	6	19,164	19,327	163	-1.0401	$1.19{\cdot}10^{+06}$		1.0408	1.180
23	$4f^{12}(^3\mathrm{H}_6)6s6p(^3\mathrm{P}^o_2)$	$(6,2)^o$	5	19,203	19,201	-2	-0.6045	$4.76{\cdot}10^{+05}$		1.0464	1.060
24	$4\mathrm{f}^{11}(^4\mathrm{I}^o)5\mathrm{d}6\mathrm{s}^2$	^{o}	6	19,304	20,738	1434	-0.3159	$1.12{\cdot}10^{+05}$		0.9509	0.855
25	$4\mathrm{f}^{11}(^4\mathrm{I}^o{}_{11/2})5\mathrm{d}_{5/2}6\mathrm{s}^2$	$(11/2,5/2)^o$	5	19,435	21,393	1958	-0.5741	$4.45{\cdot}10^{+05}$		0.9631	1.005
26	$4\mathrm{f}^{11}(^4\mathrm{I}^o{}_{11/2})5\mathrm{d}_{5/2}6\mathrm{s}^2$	$(11/2,5/2)^o$	6	19,628	21,702	2074	-1.2573	$1.86{\cdot}10^{+06}$	$(7.1{\pm}0.4){\cdot}10^{+06}$	1.0318	1.055
27	$4\mathrm{f}^{11}(^4\mathrm{I}^o)5\mathrm{d}6\mathrm{s}^2$	^{o}	5	19,926	20,917	991	0.4380	$2.79{\cdot}10^{+05}$		0.9062	0.980
28	$4\mathrm{f}^{11}(^4\mathrm{F}^o)5\mathrm{d}6\mathrm{s}^2$	^{o}	6	21,348	22,584	1236	1.5116	$3.46{\cdot}10^{+06}$	$(2.55{\pm}0.13){\cdot}10^{+06}$	1.0072	1.130
29	$4\mathrm{f}^{11}(^4\mathrm{I}^o)5\mathrm{d}6\mathrm{s}^2$	^{o}	5	21,843	22,673	830	1.9920	$7.61{\cdot}10^{+06}$	$(5.52{\pm}0.28){\cdot}10^{+06}$	1.0235	1.040
30	$4\mathrm{f}^{11}(^4\mathrm{I}^o)5\mathrm{d}6\mathrm{s}^2$	^{o}	7	22,566	23,081	515	0.7092	$7.80{\cdot}10^{+05}$		1.0575	1.010
31	$4f^{12}(^3\mathrm{F})6s6p(^3\mathrm{P}^o)$	^{o}	5	23,237	22,124	-1113	-0.2492	$1.43{\cdot}10^{+05}$		1.1832	1.285

Continued on next page

Table 6.1 – continued

				E			A_{ab}	T_{ab}		g	
N	Conf.	Term	J	Present	NIST	Δ	Present	Present	Expt.	Present	NIST
32	$4f^{12}(^3\mathrm{H})6s6p$	^{o}	5	23,422	23,447	25	-0.5999	$8.51\cdot10^{+05}$		1.0940	1.080
33	$4f^{12}(^3\mathrm{F})6s6p(^3\mathrm{P}^o)$	^{o}	5	23,801	23,856	55	3.0144	$2.25\cdot10^{+07}$	$(6.6\pm0.3)\cdot10^{+06}$	1.0578	1.140
34	$4f^{12}(^3\mathrm{H})6s6p$	^{o}	5	23,872	23,885	13	4.7735	$5.70\cdot10^{+07}$		1.0665	1.100
35	$4f^{12}(^3\mathrm{F})6s6p(^3\mathrm{P}^o)$	^{o}	6	24,107	23,831	-276	-1.6371	$5.85\cdot10^{+06}$		1.0939	1.250
36	$\mathrm{4f}^{11}(^4\mathrm{I}^o)\mathrm{5d6s}^2$	^{o}	6	24,393	24,457	64	-3.7556	$3.19\cdot10^{+07}$	$(3.26\pm1.6)\cdot10^{+07}$	1.0911	1.050
37	$4f^{12}(^3\mathrm{H})6s6p$	^{o}	5	24,587	24,083	-504	-5.1389	$7.22\cdot10^{+07}$	$(10.2\pm5.)\cdot10^{+07}$	1.1254	1.128
38	$4f^{12}(^3\mathrm{H})6s6p(^3\mathrm{P}^o)$	^{o}	6	24,674	24,246	-428	-0.2660	$1.66\cdot10^{+05}$		1.2273	1.085
39		^{o}	5	24,791	25,364	573	-3.6033	$3.64\cdot10^{+07}$		1.1948	1.180
40	$\mathrm{4f}^{11}(^4\mathrm{F}^o)\mathrm{5d6s}^2$	^{o}	6	24,816	25,393	577	-7.0787	$1.19\cdot10^{+08}$	$(3.19\pm1.6)\cdot10^{+07}$	1.1267	1.075
41	$4f^{12}(^3\mathrm{H})6s6p$	^{o}	7	24,845	24,943	98	10.6390	$2.34\cdot10^{+08}$	$(1.85\pm10.)\cdot10^{+08}$	1.1458	1.160
42		^{o}	7	25,379	25,159	-220	-4.7652	$5.01\cdot10^{+07}$	$(4.03\pm2.1)\cdot10^{+07}$	1.1613	1.170
43	$4f^{12}(^3\mathrm{H})6s6p$	^{o}	6	25,783	25,880	97	-2.0255	$1.09\cdot10^{+07}$	$(1.22\pm6.)\cdot10^{+08}$	1.1534	1.150
44	$4f^{12}(^3\mathrm{H})6s6p(^3\mathrm{P}^o)$	^{o}	5	25,888	26,199	311	-0.1108	$3.92\cdot10^{+04}$		1.0683	1.045
45	$\mathrm{4f}^{11}(^4\mathrm{I}^o)\mathrm{5d6s}^2$	^{o}	5	26,202	25,163	-1039	4.1159	$5.61\cdot10^{+07}$	$(3.76\pm1.9)\cdot10^{+07}$	1.0100	1.175
46		^{o}	7	26,874	27,231	357	-0.4816	$6.07\cdot10^{+05}$		1.1318	1.135

Refs. [16] Ref. [28]

This expression is convenient to use in a non-relativistic limit when total orbital momentum L and total spin S are good quantum numbers (J is total angular momentum, $\mathbf{J} = \mathbf{L} + \mathbf{S}$). This is not the case for both Er and Fm. Note however, that non-relativistic labelling of the states can be used at least in principle in a relativistic case, too. It can be done by expanding a relativistic wave function over a non-relativistic basis and taking the values of L and S that correspond to the largest term in the expansion. This was done in previous calculations for Fm [5]. Using their notations and formula (6.6) and comparing the obtained values with our calculated g-factors helps to link the results of our calculations to those of Ref. [5].

6.5 Results

The results for Fm are presented in Table 6.2. As expected, the spectrum of Fm is very similar to Er. There are some differences, mostly caused by relativistic effects, which are expected to be about two times larger in Fm than in Er. To understand the difference, we compare the outermost single-electron $7s$, $7p$ and $6d$ orbitals of Fm to the $6s, 6p$ and $5d$ orbitals of Er. The orbitals have a form

$$\psi(\mathbf{r}) = \frac{1}{r}\begin{pmatrix} f(r)\Omega_{jlm}(\mathbf{n}) \\ i\alpha g(r)\Omega_{j\tilde{l}m}(\mathbf{n}) \end{pmatrix}. \qquad (6.7)$$

Here $f(r)$ and $g(r)$ are the upper and lower radial components of the wave function, $\mathbf{n} = \mathbf{r}/r$, α is the fine structure constant, $\tilde{l} = l - 2j$, $\Omega_{jlm}(\mathbf{n})$ is a spherical spinor. Fig. 6.1 shows the upper components $f(r)$ of the Er and Fm orbitals. Stronger relativistic effects of Fm move the $7s$ and $7p_{1/2}$ orbitals closer to the nucleus than similar $6s$ and $6p_{1/2}$ orbitals in Er. This is because relativistic effects are stronger at short distances from the nucleus, where densities of the s and $p_{1/2}$ states are not negligible. On these distances relativistic effects associated with the Dirac equation act as an attraction to the nucleus. In contrast, the densities of the $p_{3/2}$, $d_{3/2}$ and $d_{5/2}$ states are small near the nucleus and relativistic effects manifest themselves via exchange interaction with the s and $p_{1/2}$ orbitals of the atomic core. Therefore, the $7p_{3/2}, 6d_{3/2}$ and $6d_{5/2}$ orbitals of Fm are farther from the nucleus than the corresponding orbitals of Er. The trend is further illustrated by the data in Table 6.3, which presents single-electron HF energies of the considered states, including also the $4f$ and $5f$ states. Note that both Fig. 6.1 and Table 6.3 show that the difference between Er and Fm is relatively small. This means that the spectra of the two atoms should be similar and that numerical uncertainty in calculated data for Fm is similar to that of Er.

Table 6.2 shows the calculated odd-parity states of Fm, which are connected to the ground state via electric dipole transitions. The corresponding transition rates are also presented to indicate which transitions might be easier to observe. There is good agreement with available experimental data and MCDF calculations [5,6]. However, it is clear that a large number of states were missed in previous studies.

Table 6.2 also presents calculated values of the Landé g-factors. They are used to generate the state labels by comparing the calculated g-factors to the non-relativistic expression (6.6) (see explanation below formula (6.6).

Comparison of the data in Tables 6.1 and 6.2 indicates that the spectra of the two atoms are very similar indeed. There are some differences, which should be attributed to relativistic effects. E.g., the gap between the ground and first excited states is larger in Fm than in Er. Also, the spread of energies within one configuration is larger in Fm than in Er. The latter is most probably due to larger fine structure of p, d and f states.

Table 6.2: Excitation energies (E, cm^{-1}), transition amplitudes (A_{ab}, a.u.), electric dipole transition rates to the ground state (T_{ab}, s^{-1}), and g-factors for some low odd states of Fm atom with $J = 5, 6, 7$. The difference between the Expt. and present energies is given by $\Delta = E_{\text{Expt.}}$ - $E_{\text{present.}}$ J^p stands for the total angular momentum and parity.

			E					A_{ab}	T_{ab}			g
N	Conf.	J^p	Present	MCDF		Expt.	Δ	Present	Present	MCDF	Expt.	Present
1	$5f^{12}7s^2$	6^+	0	^{3}H$_6$	0	0	0	0	0	0	0	1.1619
2	$5f^{11}7s^2 6d$	6^-	18,915		>13000			-0.3124	$1.0283 \cdot 10^5$			1.2880
3	$5f^{12}7s7p$	6^-	19,012					1.3588	$1.9756 \cdot 10^6$			1.2594
4	$5f^{11}7s^2 6d$	7^-	19,808					0.3820	$1.5304 \cdot 10^5$			1.2378
5	$5f^{12}7s7p$	6^-	20,077					3.0391	$1.1638 \cdot 10^7$			1.0843
6	$5f^{12}7s7p$	7^-	20,399					3.8242	$1.6751 \cdot 10^7$			1.1921
7	$5f^{12}7s7p$	5^-	20,711					-3.0248	$1.4957 \cdot 10^7$			1.1527
8	$5f^{11}7s^2 6d$	5^-	23,175					0.1828	$7.6499 \cdot 10^4$			1.1747
9	$5f^{11}7s^2 6d$	6^-	23,761					-1.1413	$2.7206 \cdot 10^6$			1.1635
10	$5f^{11}7s^2 6d$	7^-	23,858					-1.0693	$2.0954 \cdot 10^6$			1.1527
11	$5f^{12}7s7p$	5^-	24,294					-0.9523	$2.3928 \cdot 10^6$			1.2003
12	$5f^{12}7s7p$	7^-	25,202					0.0250	$1.3486 \cdot 10^3$			1.2351
13	$5f^{12}7s7p$	6^-	25,442	^{5}I$^o_6$	25,226	25,099.8±0.2	-342	-1.3421	$4.6186 \cdot 10^6$	$1.89 \cdot 10^6$	$(3.4 \pm 0.8) \cdot 10^6$	1.1861
14	$5f^{12}7s7p$	5^-	25,494	^{5}G$^o_5$	25,471	25111.8±0.2	-382	-0.9201	$2.5808 \cdot 10^6$	$1.28 \cdot 10^6$	$(3.5 \pm 0.7) \cdot 10^6$	1.1204

Continued on next page

Table 6.2 – continued

			E					A_{ab}	T_{ab}			g
N	Conf.	J^p	Present	MCDF		Expt.	Δ	Present	Present	MCDF	Expt.	Present
15	$5f^{12}7s7p$	5^-	28,520	$^3\mathrm{G}^o_5$	27,633	27,389±1.5	-1131	-5.1793	$1.1451{\cdot}10^8$	$1.98{\cdot}10^8$		1.2120
16	$5f^{12}7s7p$	6^-	28,662	$^3\mathrm{H}^o_6$	27,394	27,466±1.5	-1196	3.0233	$3.3511{\cdot}10^7$	$2.43{\cdot}10^8$	$\geq 2.9{\cdot}10^6$	1.2485
17	$5f^{12}7s7p$	5^-	28,690		28,540	28,185±1.5	-505	6.0863	$1.6097{\cdot}10^8$	$2.82{\cdot}10^5$		1.2029
18	$5f^{12}7s7p$	6^-	28,995			28,377±1.5	-618	7.8270	$2.3251{\cdot}10^8$			1.1744
19	$5f^{12}7s7p$	7^-	29,348	$^3\mathrm{I}^o_7$	27,802	28391±1.5	-957	9.7202	$3.2227{\cdot}10^8$	$3.67{\cdot}10^8$	$\geq 1.1{\cdot}10^7$	1.1455
20	$5f^{11}7s^26d$	5^-	30,236		29,359			-0.0602	$1.8429{\cdot}10^4$	$3.58{\cdot}10^7$		1.1338
21	$5f^{11}7s^26d$	6^-	30,943					-0.9144	$3.8572{\cdot}10^6$			1.0814
22	$5f^{11}7s^26d$	5^-	31,953					0.2406	$3.4736{\cdot}10^5$			1.1369
23	$5f^{12}7s7p$	5^-	32,200					0.4368	$1.1719{\cdot}10^6$			1.1124
24	$5f^{12}7s7p$	5^-	32,239					-0.1187	$8.6814{\cdot}10^4$			1.0473
25	$5f^{11}7s^26d$	6^-	32,583					0.4648	$1.1635{\cdot}10^6$			1.1403
26	$5f^{11}7s^26d$	7^-	32,693					-0.9598	$4.3436{\cdot}10^6$			1.0969
27	$5f^{12}7s7p$	5^-	33,093					0.0298	$5.9416{\cdot}10^3$			1.0494
28	$5f^{11}7s^26d$	7^-	33,328					0.7106	$2.5223{\cdot}10^6$			1.0942
29	$5f^{11}7s^26d$	5^-	33,575					0.0410	$1.1680{\cdot}10^4$			1.1448
30	$5f^{12}7s7p$	6^-	33,656					0.3889	$8.9755{\cdot}10^5$			1.0886
31	$5f^{11}7s^26d$	6^-	33,750					0.8209	$4.0337{\cdot}10^6$			1.0760

Continued on next page

Table 6.2 – continued

			E				A_{ab}	T_{ab}			g
N	Conf.	J^p	Present	MCDF	Expt.	Δ	Present	Present	MCDF	Expt.	Present
32	$5f^{11}7s^26d$	6^-	35,020				-1.5562	$1.6194{\cdot}10^7$			1.0968
33	$5f^{11}7s^26d$	7^-	35,106				1.7151	$1.7174{\cdot}10^7$			1.0834
34	$5f^{11}7s^26d$	5^-	35,442				0.8021	$5.2698{\cdot}10^6$			1.0987
35	$5f^{11}7s^26d$	6^-	36,587				2.4329	$4.5135{\cdot}10^7$			1.1463

Refs. [5,6] Ref. [8]

Table 6.3: Single-electron energies (in a.u.) of the lowest valence orbitals of Er and Fm.

Er		Fm	
Orbital	Energy	Orbital	Energy
$4f_{5/2}$	-0.7576	$5f_{5/2}$	-0.7509
$4f_{7/2}$	-0.7121	$5f_{7/2}$	-0.6711
$6s_{1/2}$	-0.4065	$7s_{1/2}$	-0.4269
$6p_{1/2}$	-0.1210	$7p_{1/2}$	-0.1240
$6p_{3/2}$	-0.1140	$7p_{3/2}$	-0.1057
$5d_{3/2}$	-0.0837	$6d_{3/2}$	-0.0819
$5d_{5/2}$	-0.0832	$6d_{5/2}$	-0.0809

6.5.1 Ionization potential

The first ionization potential (IP) of an atom is calculated as a difference in the ground state energy between the neutral atom and the singly-positive ion. The calculations are the same as those for transition energies. Our value for the IP of Er is 6.102 eV, which is in excellent agreement with the experimental value 6.1077 eV [16]. Similarly, the calculated IP of Fm, 6.559 eV, is in very good agreement with the experimental value, 6.52(13) eV [8]. In contrast to the calculation of transition energies, where very little published data can be found, calculation of the IP of Fm has been performed by many authors. A detailed review of the results can be found in Ref. [8]. Our result is the closest to the experimental value. Another very accurate result has been obtained with the CCSD(T) method in Ref. [8]. Its value is 6.469 eV. Our value is only about 1% larger. The data are summarised in Table 6.4.

6.5.2 Scalar polarizabilities of Er and Fm atoms

Scalar polarizabilities of Er and Fm were calculated in Ref. [29]. In this work we have an opportunity to calculate the polarizability in a completely different way and to compare the results. Scalar polaizabilities α_0 are given by (we use atomic units)

$$\alpha_0 = \frac{2}{3(2J_a+1)} \sum_n \frac{A_{an}^2}{E_a - E_n}, \tag{6.8}$$

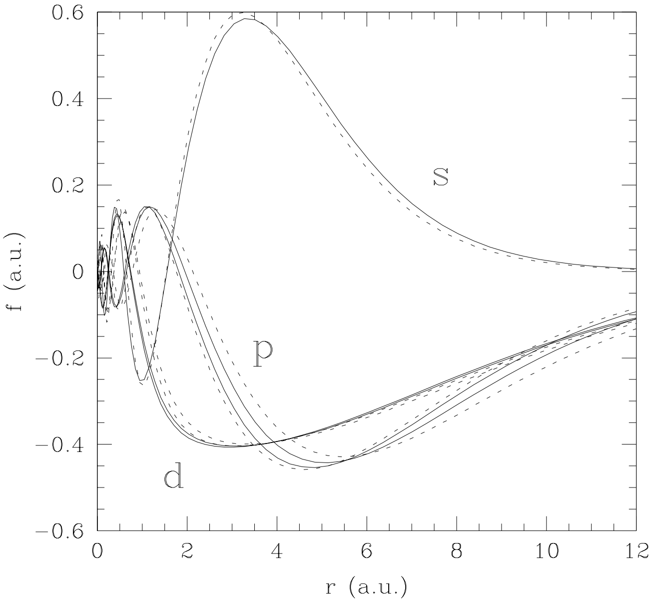

Figure 6.1: Upper components $f(r)$ (see Eq. (6.7) of the lowest valence $6s_{1/2}$, $6p_{1/2}$, $6p_{3/2}$, $5d_{3/2}$, $5d_{5/2}$ orbitals of Er (solid lines) and $7s_{1/2}$, $7p_{1/2}$, $7p_{3/2}$, $6d_{3/2}$, $6d_{5/2}$ orbitals of Fm (dot lines).

where J_a is the total angular momentum of the ground state of the atom ($J_a = 6$ for Er and Fm) , A_{an} are amplitudes (reduced matrix elements) of the electric dipole transitions from the ground state to odd excited states; $E_a - E_n$ is an excitation energy. Summation goes over the complete set of odd states. We use the amplitudes and energies from Tables 6.1 and 6.2 to perform the calculations. The results are presented in Table 6.5.

There are some significant differences in approaches used to calculate polarizabilities in the present work and in Ref. [29]. In Ref. [29] the $4f$ and $5f$ electrons were attributed to the core and the atoms were treated as two-valence electrons systems with the $6s^2$ ground state configuration for Er and $7s^2$ ground state configuration for Fm. This means that only $s-p$ electric dipole matrix elements were used in the calculations of the polarizabilities. On the other side, the summation was extended to very high energy states to ensure the saturation of the summation. In the present work we use all possible kinds of transitions, but the summation is truncated at much lower number of levels. It is limited to states presented in Tables 6.1 and 6.2.

Note that the total polarizability is the sum of the core and valence contributions. In the present work we do not calculate the core contributions but take them from Ref. [29]. There is some difference in the definitions of the core in these two works. We treat the $4f$ and $5f$ electrons as being in the valence space while in [29] they were attributed to the core. This should lead to some differences in the core polarizabilities. However, the contribution of f-electrons to the polarizabilities is small and can be neglected [29]. Another source of uncertainty is the use of calculated energies in (6.8). As can be seen from Table 6.1 the difference between theoretical and experimental energies is significant for some states. This may lead to significant errors in the polarizability. To check this we performed calculations twice, using theoretical energies in one run and experimental energies in the second run. Both results are presented in Table 6.5. The difference between them is just 0.5%. The difference between the total polarizabilities of present work and earlier calculations of Ref. [29] is 1% for Er and 10% for Fm.

Another way of estimation uncertainty is by replacing calculated transition amplitudes by experimental values when they are available. Note, however, that accuracy in a calculation of polarizability is usually much better than accuracy of calculation of transition rates, especially for weak transitions. Indeed, transition rates are very sensitive to mixing between close excited states (which is usually very strong) while polarizability is not affected by mixing of (nearly) degenerate excited states. We just need a complete set of basis states. For the same reason, replacing part of transition amplitudes by experimental values is not a way to improve accuracy (see, e.g. [30] for a more detailed discussion). In the end, we found that the uncertainty for Er is about 10%, while for Fm it might be larger.

Table 6.4: Experimental and theoretical values of the first ionization potential IP_1 (eV).

	State		IP_1					
Atoms	Initial	Final	Presesnt	CCSD(T)	MCDF	QR PP+ACPF	Semiempirical	Expt
Er	$4f^{12}6s^2\ ^6H_6$	$4f^{12}6s\ (6,1/2)_{13/2}$	6.1017		5.94	5.89		6.1077
Fm	$5f^{12}7s^2\ ^6H_6$	$5f^{12}7s\ (6,1/2)_{13/2}$	6.5587	6.469	6.22	6.26	6.50	6.52±0.13

Ref. [8]
Ref. [1,2]
Ref. [35]
Ref. [16]

Table 6.5: Scalar polarizabilities of Er and Fm atoms (in a_B^3).

		Ref. [29]			Present Work	
Atom	Conf.	Core	Valence	Total	Valence	Total
Er	$4f^{12}6s^2$	6.3	143.9	150.2	145.66	151.96
Er	$4f^{12}6s^2$	6.3			144.94	151.24
Fm	$5f^{12}7s^2$	8.4	105	113.4	115.92	124.32

This value was obtained when NIST energies were used.

6.5.3 Hyperfine structure

Studying hyperfine structure is a way to get information about the nucleus by extracting nuclear moments from the comparison between theory and measurements. There are many accurate published data on hfs of ^{167}Er [31–33]. There are also measurements of the hfs for ^{255}Fm [6]. Therefore, we perform the calculations for both atoms using erbium as a testing ground to check the accuracy of the method. We calculate magnetic dipole hfs constant A and electric quadrupole hfs constant B using the RPA and CIPT methods (see Eqs. (6.3) and (6.4)). The results for ^{167}Er are presented in Table 6.6. One can see that we have an excellent agreement between theory and experiment for magnetic dipole constant A for all states of the ground configuration. The difference does not exceed 3%, and for some states it is even smaller. For electric quadrupole constant B the difference between theory and experiment is within 10% for most states except the second one. Here the discrepancy, by a factor of two, is probably due to anomalously small value of the constant, which might be a result of cancellation between different contributions. However, the absolute difference between theory and experiment ($\sim$ 500 MHz) is about the same as for the ground state. The accuracy is almost equally good for the states of the $4f^{12}6s6p$ configuration (marked with letter P in Table 6.6), while it is somewhat worse for the states of the $4f^{11}6s^25d$ configuration (marked with letter D in Table 6.6). In the end, it is clear that the accuracy is sufficiently good to use the calculations for extracting nuclear moments.

The results of similar calculations for fermium are presented in Table 6.7. It is natural to expect that due to similar electronic structure the accuracy for fermium is similar to what we have for erbium. As one can see, the values of the hfs constants for the ground

Table 6.6: Hyperfine structure constants A and B (in MHz) of ^{167}Er. Nuclear spin $I = 7/2$, nuclear magnetic moment $\mu(^{167}\text{Er}) = -0.56385(12)\mu_N$ [36]; nuclear electric quadrupole moment $Q(^{167}\text{Er}) = 3.57(3)$ b [37]; $g_I = \mu/I$. Letters S, D, P indicate the leading configurations, $4f^{12}6s^2$, $4f^{11}6s^25d$, and $4f^{12}6s6p$, respectively. The last column gives references to experimental data.

Conf.	Energy (cm^{-1})		A_{theor}		A_{expt}	B_{theor}		B_{expt}	Ref.
	NIST [16]	CIPT							
S	0.000	0	$724g_I$	-117	-120.487	-1413Q	-5037	-4552.984	[32]
S	5035.193	5364	$752g_I$	-122	-121.9	295Q	1050	516	[31]
S	6958.329	7275	$976g_I$	-158	-159.4	-1273Q	-4539	-4120	[31]
S	10750.982	10875	$1075g_I$	-174	-173.4	-729Q	-2600	-2429	[31]
S	12377.534	13353	$827g_I$	-139	-143.4	373Q	1331	1236	[31]
S	13097.906	14624	$1063g_I$	-172	-167.2	460Q	1640	1688	[31]
D	7176.503	5419	$833g_I$	-135	-139.957	-464Q	-1655	-709.396	[33]
D	7696.956	5959	$705g_I$	-114	-125.851	-626Q	-2230	-3046.052	[33]
D	9350.106	7584	$643g_I$	-104	-119.870	-665Q	-2372	-3062.704	[33]
D	8620.565	4771	$613g_I$	-99	-113.582	-486Q	-1733	-782.987	[33]
P	17157.307	17342	$1071g_I$	-173	-172.5	-1400Q	-4992	-4440	[31]

state are also similar. For example, the magnetic dipole constant A for the ground state of Fm (655g$_I$ MHz) is only 14% smaller than for Er (724g_I MHz). The smaller value can be explained in the following way. Only f-electrons contribute to the hfs of the ground state. This is because s-electrons form a closed subshell ($6s^2$ for Er and $7s^2$ for Fm) with zero total angular momentum. The $4f$-electrons of Er are deeper in the core on the energy scale than the 5f-electrons of Fm (see Table 6.3). Therefore, the overlap of the $4f$ function with the s functions of the core is larger than for the $5f$ state. This means that the RPA correction to the hfs is also larger for Er than for Fm. Similarly, the electric quadrupole constant B for Fm (-1750Q MHz) is only 24% larger than the constant B for Er (-1413Q MHz) due to the larger gradient of electric field. There are also similarities between the hfs constants of the $4f^{12}6s6p$ and $5f^{12}7s7p$ configurations of Er and Fm. However, they are less pronounced due to the fact that the corresponding states of Fm are significantly higher on the energy scale than in Er. In the end, we see no reason to believe that the accuracy of the calculations for Fm is lower than for Er.

The extraction of nuclear moments from the comparison of theoretical and experimental hfs constants presents a problem. There is no way to get consistent results from the three

Table 6.7: Hyperfine structure constants A and B (in MHz) of ^{255}Fm. Two different interpretations of the experimental data are taken from Ref. [5]. Notations R1 and R2 are also taken from Ref. [5].

Conf.	Energy (cm^{-1})		A_{theor}	A_{expt}		B_{theor}	B_{expt}	
	Expt [6]	CIPT						
GS	0.0	0	$655g_I$	-320	-760	$-1750Q$	-22000	-8700
R1	25099.80	25442	$1810g_I$	-530	-660	$-1975Q$	-2900	-14800
R2	25111.80	25494	$195g_I$	-690	-730	$-1823Q$	-1700	-390

states (see Table 6.7). The most likely reason in our view may come from the inaccurate interpretation of measured hfs in terms of six hfs constants, the A and B constants for the three states. Ref. [5] presents two quite different interpretations, which are both included in Table 6.7 , and states that more interpretations are possible under different assumptions. We hope that our calculations would help to re-evaluate the experimental data.

6.5.4 Isotope shift

Only the field shift needs to be considered in heavy elements. The mass shift is small and can be neglected [10,12]. To calculate the IS for Fm we use nuclear parameters that come from nuclear calculations [15]. We use only two most important parameters, the nuclear RMS radius r_p and the parameter of nuclear quadrupole deformation β. The nuclear charge density is approximated by the formula

$$\rho(r,\theta) = \frac{a}{1+\exp\frac{r-r_n(\theta)}{t}}. \tag{6.9}$$

Here a is a normalization constant, t is the nuclear skin thickness (we use the standard value $t = 2.3/4\ln(3)$ fm), $r_n(\theta)$ is a variable nuclear radius, $r_n(\theta) = r_0\,(1+\beta Y_{20}(\theta))$, where Y_{20} is a spherical harmonic. Electrons feel the nuclear density averaged over nuclear rotations, $\rho(r) = \int_0^\pi \rho(r,\theta)d\theta$. The constant a in (6.9) is chosen to get $\int \rho dV = Z$. The parameter r_0 in the variable nuclear radius is treated as a fitting parameter to obtain the correct value of the nuclear RMS radius. The resulting averaged nuclear charge density $\rho(r)$ is used to calculate the nuclear potential. The IS is calculated as a difference between transition frequencies of two isotopes. It was suggested in Refs. [12,13] that the IS for a wide range of values for nuclear RMS radii and quadrupole deformation β can be approximated by a formula containing powers of $\delta \left\langle r^2 \right\rangle$ and $\Delta\beta$. It was also suggested that for neighbouring isotopes one can keep only the leading terms

$$\delta\nu = F\delta\langle r^2\rangle + d\Delta\beta. \tag{6.10}$$

Here the first term is just the standard formula for field IS. Note that relativistic consideration leads to a different formula for field isotope sift, $\delta v = F'\delta \left\langle r^{2\gamma} \right\rangle$, where $\gamma = \sqrt{1-(\alpha Z)^2}$ [38,39].. The relativistic formula can be presented as an expansion $F'\delta \left\langle r^{2\gamma} \right\rangle = F\delta \left\langle r^2 \right\rangle + G\delta \left\langle r^2 \right\rangle^2 + \ldots$. For neighbouring isotopes higher-order corrections are small and can be neglected, brining us back to (6.10). The second term in (6.10) takes into account nuclear deformation. The advantage of using a non-relativistic formula is the ability to extract the value of $\delta \left\langle r^2 \right\rangle$ from the isotope shift measurements. The disadvantage is the loss of the universality. Constants F and d in (6.10) are isotope-dependent and should be calculated from scratch for a new pair of isotopes if the number of neutrons is significantly different. The values of F and d are found from fitting the calculated IS. If the IS is measured for at least two atomic transitions, then(6.10) can be used to determine both $\delta \left\langle r^2 \right\rangle$ and $\Delta\beta$. Our calculated values of F and d for IS around the ^{255}Fm isotope are presented in Table 6.8. Note that, according to the nuclear theory [15], nuclei in this region are deformed with $\beta \sim 0.3$, and $\Delta\beta \sim 0.02$ for neighbouring isotopes. Using the data from Table 6.8 , we estimate that the contribution of nuclear deformation to the IS is ~ 0.01 cm^{-1}. This value is large enough to be detected. It means that measurements of IS can be used to study nuclear deformations. For odd isotopes like ^{255}Fm the use of IS to study nuclear deformation is complementary to the measurements of the electric quadrupole hfs. However, for even-even isotopes, such as ^{254}Fm, ^{256}Fm, which have no hfs, this is a unique way of studying nuclear deformation by means of atomic spectroscopy.

Finally, in Table 6.9 we present the calculated IS between previously studied isotope

Table 6.8: Parameters of formula (6.10) for isotope shifts for transitions from the ground state to excited odd states of ^{255}Fm.N is state number from Table 6.2, letters P and D indicate dominating configurations, $5f^{12}7s7p$ and $5f^{11}7s^{2}6d$ respectively.

N	Conf.	J	E cm^{-1}	F cm^{-1}/fm^{2}	d cm^{-1}
7	P	5	20,711	-2.92	0.423
8	D	5	23,175	0.78	0.610
11	P	5	24,294	-0.19	0.585
14	P	5	25,494	-3.14	0.397
15	P	5	28,520	-2.53	0.294
17	P	5	28,690	-1.24	0.331
2	P	6	18,915	-2.95	0.455
3	D	6	19,012	3.18	0.604
5	P	6	20,077	-2.88	0.443
9	D	6	23,761	2.95	0.741
13	P	6	25,442	-3.21	0.256
16	P	6	28,662	-3.11	0.404
18	P	6	28,995	-1.29	0.230
4	D	7	19,808	3.05	0.602
6	P	7	20,399	-2.59	0.431
10	D	7	23,858	3.31	0.745
12	P	7	25,202	-3.14	0.399
19	P	7	29,348	-2.04	0.202

Table 6.9: Isotope shift (IS, cm^{-1}) between the experimentally studied isotope ^{255}Fm and the isotope with the magic number of neutrons, ^{284}Fm. Calculations for ^{255}Fm were done with nuclear RMS radius r_p = 5.976 fm, while for ^{284}Fm r_p = 6.063 fm [15]. The last column is the difference between excitation energies for ^{284}Fm and ^{255}Fm.

			Energy (cm^{-1})		
N	Conf.	LSJ	^{255}Fm	^{284}Fm	IS
13	$5f^{12}7s7p$	$^{5}\mathrm{I}_{6}^{0}$	25,442	25435	-7
14	$5f^{12}7s7p$	$^{5}\mathrm{G}_{5}^{0}$	25,494	25487	-7
15	$5f^{12}7s7p$	$^{3}\mathrm{G}_{5}^{0}$	28,520	28515	-5
16	$5f^{12}7s7p$	$^{3}\mathrm{H}_{6}^{0}$	28,662	28656	-6
17	$5f^{12}7s7p$	$^{3}\mathrm{G}_{5}^{0}$	28,690	28685	-5
19	$5f^{12}7s7p$	$^{3}\mathrm{I}_{7}^{0}$	29,348	29343	-5
20	$5f^{11}7s^{2}6d$	$^{9}\mathrm{I}_{5}^{0}$	30,236	30243	7

^{255}Fm [5, 6] and an isotope ^{284}Fm which has a "magic" number of neutrons ($N = 184$) and thus a sphericallysymmetric nucleus [15]. We keep non-relativistic labelling of the states used in [5, 6] for easy comparison. The shift was calculated as a difference between separate calculations of transition frequencies for ^{255}Fm and ^{284}Fm. Nuclear RMS radii (r_p) were taken from nuclear calculations, $r_p = 5.976$ fm for ^{255}Fm and $r_p = 6.063$ fm for ^{284}Fm [15]. The ^{255}Fm isotope is used as a reference. These data can be useful in the search for metastable isotopes, e.g. in the astrophysical data [34].

6.6 Conclusions

All odd energy levels of Fm within the optical range ($E < 40000$ cm^{-1}) are calculated with an uncertainty of a few hundred cm^{-1}. The results are in good agreement with previous theoretical and experimental studies where the data are available. Twenty eight new levels are reported. Transition rates, hyperfine structure, static scalar polarizabilities, ionization potentials, and isotope shifts are also calculated. Transition rates might be useful for planning further experimental studies. Calculation of the hfs indicates the need to re-visit the interpretation of experimental data for Fm. Isotope shift data can be used for extracting information on the nuclear deformation and change of the nuclear RMS radius from the IS measurements. They can also be used in the search for metastable Fm isotopes with spherically-symmetric nuclei.

Acknowledgement

The authors are grateful to Hartmut Backe for stimulating discussions. This work was supported by the Australian Research Council. JGL acknowledged the financial support from the National Natural Science Foundation of China (grant no. 11874090). VAD would like to express special thanks to the Institute of Applied Physics and Computational Mathematics in Beijing for its hospitality and support. This research includes computations

using the computational cluster Katana supported by Research Technology Services at UNSW Sydney.

References

[1] Liu W, Küchle W, Dolg M. Phys Rev A 1998;1103(58).

[2] iu W, Dolg M. Phys Rev A 1998;1721(57).

[3] Cao X, Dolg M, Stoll H. J Chem Phys 2003;487(118).

[4] Moritz A, Cao X, Dolg M. Theor Chem Acc 2007;473(117).

[5] Backe H, Dretzke A, Fritzsche S, Haire RG, Kunz P, Lauth W, Sewtz M, Trautmann N. Hyperfine. Interactions 2005;3(162).

[6] Sewtz M, Backe H, Dretzke A, Kube G, Lauth W, Schwamb P, Eberhardt K, Grüning C, Thörle P, Trautmann N, Kunz P, Lassen J, Passler G, Dong CZ, Fritzsche S, Haire RG. Phys Rev Lett 2003;163002(90).

[7] Wendt K, Gottwald T, Mattolat C, Raeder S. Hyperfine. Interactions 2014;55(227).

[8] Sato TK, Asai M, Borschevsky A. J Am Chem Soc 2018;14609(140).

[9] Laatiaoui M, Lauth W, Backe H, Block M, Ackermann D, van Duppen P, Cheal B, Chhetri P, Düllmann CE, Even J. Nature (London) 2016;495(538).

[10] Raeder S, Ackermann D, Backe H, Beerwerth R, Berengut JC, Block M, Borschevsky A, Cheal B, Chhetri P, Düllmann CE. Phys Rev Lett 2018;232503(120).

[11] Porsev SG, Safronova MS, Safronova UI, Dzuba VA, Flambaum VV. Phys Rev A 2018;052512(98).

[12] Allehabi O., Saleh, Dzuba V.A., Flambaum V.V., Afanasjev A.V., Agbemava S.E.. arxiv:2001. 2020. 09422.

[13] Flambaum VV, Dzuba VA. Phys Rev A 2019;032511(100).

[14] Audi G, Kondev FG, Wang M, Huang WJ, Naimi S. Chin Phys C 2017;030001(41).

[15] Agbemava SE, Afanasjev AV, Ray D, Ring P. Phys Rev C 2014;054320(89).

[16] Kramida A., Ralchenko Y.. J. reader, and NIST ASD team (2019). NIST atomic spectra database (ver. 5.7.1). [Online]. Available: https://physics.nist.gov/asd [2019, November 11]. National Institute of Standards and Technology, Gaithersburg, MD. DOI: 10.18434/T4W30F.

[17] Dzuba VA, Berengut JC, Harabati C, Flambaum VV. Phys Rev A 2017a;012503(95).

[18] Lackenby BGC, Dzuba VA, Flambaum VV. Phys Rev A 2018a;022518(98).

[19] Dzuba VA, Flambaum VV, Schiller S. Phys Rev A 2018;022501(98).

[20] Li JG, Dzuba V. Theoretical study of the spectroscopic properties of mendelevium (z = 101). J Quant Spectrosc RadiatTransfer 2020(247). 106943

[21] Lackenby BGC, Dzuba VA, Flambaum VV. Phys Rev A 2018b;042512(98).

[22] Lackenby BGC, Dzuba VA, Flambaum VV. Phys Rev A 2019;042509(99).

[23] Parpia FA, Fischer CF, Grant IP. CPC 1996. 94, 249

[24] Geddes AJ, Czapski DA, Kahl EV, Berengut JC. Phys Rev A 2018;042508(98).

[25] Kahl EV, Berengut JC. CPC 2019. 238, 232

[26] Johnson WR, Sapirstein J. Phys RevLett 1986;1126(57).

[27] Dzuba VA, Flambaum VV, Silvestrov PG, Sushkov OP. J Phys B 1987;1399(20).

[28] Lawler JE, Wyart JF, Hartog EAD. J. PhysB 2010;235001(43).

[29] Dzuba VA, Kozlov A, Flambaum VV. Phys Rev A 2014;042507(89).

[30] Dzuba VA, Derevianko A. JPhysB 2010(43):074011.

[31] Childs WJ, Goodman LS, Pfeufer V. Phys Rev A 1983;28(3402).

[32] Cheng KT, Childs WJ. Phys Rev A 1985;31(2775).

[33] Clilds WJ, Goodman LS, Cheng KT. Phys Rev A 1986;33(1469).

[34] Dzuba VA, Flambaum VV, Webb JK. Phys Rev A 2017b;062515(95).

[35] Sugar J. JChem Phys 1974;4103(60).

[36] Stone NJ. At Data Nucl Data Tables 2005;75(90).

[37] Stone NJ. At Data Nucl Data Tables 2016;1(111–112).

[38] Zubova NA, Kozhedub YS, Shabaev VM, Tupitsyn II, Volotka V, Plunien G Brandau C, Stöhlker T. Phys Rev A 2014;062512(90).

[39] Flambaum VV, Geddes AJ, Viatkina AV. Phys Rev A 2018;032510(97).

Chapter 7

Time keeping and searching for new physics using metastable states of Cu, Ag, and Au

7.1 Overview

In this chapter, we present a detailed analysis of the study of the prospects of using the metastable states of Cu, Ag, and Au as clock states. In our calculations, we demonstrate that these metastable states satisfy the criteria for being promising candidates for atomic clocks; they have a blackbody radiation shift one or two orders of magnitude lower than in clock transition in Sr. It is also found that the metastable state of Au is highly sensitive to variations in α.

This study has been published in this paper:

V. A. Dzuba, S. O. Allehabi, V. V. Flambaum, J. Li, and S. Schiller, Time keeping and searching for new physics using metastable states of Cu, Ag, and Au, Phys. Rev. A **103**, 022822 (2021).

7.2 Abstract

We study the prospects of using the electric quadrupole transitions from the ground states of Cu, Ag, and Au to the metastable states $^2D_{5/2}$ as clock transitions in optical lattice clocks. We calculate lifetimes, transition rates, and systematic shifts and find that they are very suitable for this purpose. In particular, the elements are found to have a blackbody radiation shift that is one to two orders smaller than that of Sr. The Au clock is found to have strong sensitivities to a variation of the fine-structure constant, to effects of scalar dark matter, and to a violation of local Lorentz invariance (LLI). Cu and Ag are also suitable for tests of LLI. We identify two more metastable states ($^4F^o_{9/2}$), one in Cu and another in Au, which can serve as additional clock transitions. The α-sensitivity coefficients of the two Au clock transitions are large and have opposite sign. This doubles the overall sensitivity to variation of α and opens the possibility of a α-variation test with a single neutral atomic species. We also present more accurate or additional values of the sensitivity to local position invariance violation for several established or proposed clock transitions. These values are important for properly evaluating the effectiveness of clock-clock comparisons.

7.3 INTRODUCTION

The use of optical clock transitions for searching for new physics beyond the standard model is a promising area of research. A hypothetical manifestation of new physics at low energy is expected to be very small. Therefore, the highest possible accuracy of the measurements is needed. Fractional uncertainty of the best optical clocks currently is around 1×10^{-18} [1–7], allowing for the highest accuracy so far achieved in the history of measurements. However, apart from one exception (Yb^+), the best current optical clocks are only weakly sensitive to new physics such as time variation of the fine-structure constant, violation of local position invariance (LPI), and violation of local Lorentz invariance (LLI), etc. [8–11]. LPI, LLI, and the weak equivalence principle form the Einstein equivalence principle, which is the foundation of general relativity.

Several ideas were proposed to combine a high accuracy of optical clocks with a high sensitivity to new physics. These include the use of the highly charged ions (HCIs) [12–15], nuclear clocks [16], and metastable atomic states with a large value of the total angular momentum $J (J > 1)$ [8, 17–20]. These states are connected to the ground state via transitions, that correspond to single-electron transitions with large change of the single-electron total angular momentum j. The large Δj is what makes the transition sensitive to the variation of the fine-structure constant (see, e.g., [21]). For example, in the present work, we consider transitions between the $nd^{10}(n+1)s\ ^2S_{1/2}$ ground state and the $nd^9(n+1)s^2\ ^2D_{5/2}$ excited metastable state. This is roughly the $s_{1/2}$ to $d_{5/2}$ transition with $\Delta j = 2$.

The energy diagrams displaying seven low-lying states of Cu and Au and the five lowest states of Ag studied in this work are presented in Fig. 7.1. One metastable state of interest ($^2D_{5/2}$) is the first-excited state for Cu and Au. In Ag, the $^2P^o_{1/2}$ state lies below the $^2D_{5/2}$ clock state. However, this has no significance since the states are very weakly connected (by $E3, M2$, or hyperfine-induced $E1$ transitions with very small value of transition frequency, $\hbar\omega = 690$ cm^{-1}). Cu and Au each have another, higher-energy metastable state, $nd^9(^2D_{5/2})(n+1)s_{1/2}\ (n+1)p_{3/2}\ (^3P_2)\ ^4F^o_{9/2}$, which can be used in an additional clock transition connecting this state to the $^2D_{5/2}$ clock state via a $M2, E3$, or hyperfine-induced $E1$ transition. Having two clock transitions in one atom is a potential important advantage in using clocks for the search of α variation and LPI violation. The Au ^4F state has been observed in magnetic resonance experiments on atomic beams [22,23].

The clock transition in Ag was studied experimentally in Ref. [24] under two-photon excitation, not under E2 excitation. For an optical clock application, an E2 excitation is advantageous compared to a two-photon excitation since the involved laser intensity is much lower, leading to a lower corresponding systematic shift.

The sensitivity of the $^2D_{5/2}$ metastable states of Ag and Au to variation of the fine-structure constant was studied before [8]. In this work, we further study these two, as well as three other metastable states, in terms of their suitability for highaccuracy measurements and sensitivity to other manifestations of new physics, such as LPI violation and LLI violation.

7.4 CALCULATIONS

7.4.1 Methods

We are mostly interested in the lowest states of Cu, Ag, and Au shown in Fig. 7.1. The D, F, and some P states of all three atoms have excitations from a d shell. This means that the d shell is open and d electrons should be treated as valence ones. The total number of valence electrons, i.e., 11 , is too large for most standard computational approaches. We use a version of the configuration interaction (CI) method specifically developed for such systems (the CI with perturbation theory (CIPT) method [25]). In this method, off-diagonal matrix elements of the CI Hamiltonian between highly excited states are neglected. This allows one to reduce the CI matrix to an effective matrix of a small size in which the contribution from high states is included perturbatively.

The CI equations can be written in a matrix form via matrix blocks [25, 26]

$$\begin{aligned} AX + BY &= EX \\ CX + DY &= EY, \end{aligned} \tag{7.1}$$

where A is a matrix of small size containing matrix elements between low-energy states, which dominate in the wavefunction expansion, B and C are blocks of the CI matrix containing matrix elements between low and high states ($c_{ij} = b_{ji}$ since the CI matrix is symmetric), D is a diagonal matrix ($d_{ik} = \left\langle k \left| H^{\mathrm{CI}} \right| k \right\rangle \delta_{ik}$), E is an eigenenergy, and X and Y are parts of the eigenvector containing expansion coefficients of the wave function for valence electrons over a set of singledeterminant basis functions. From the second

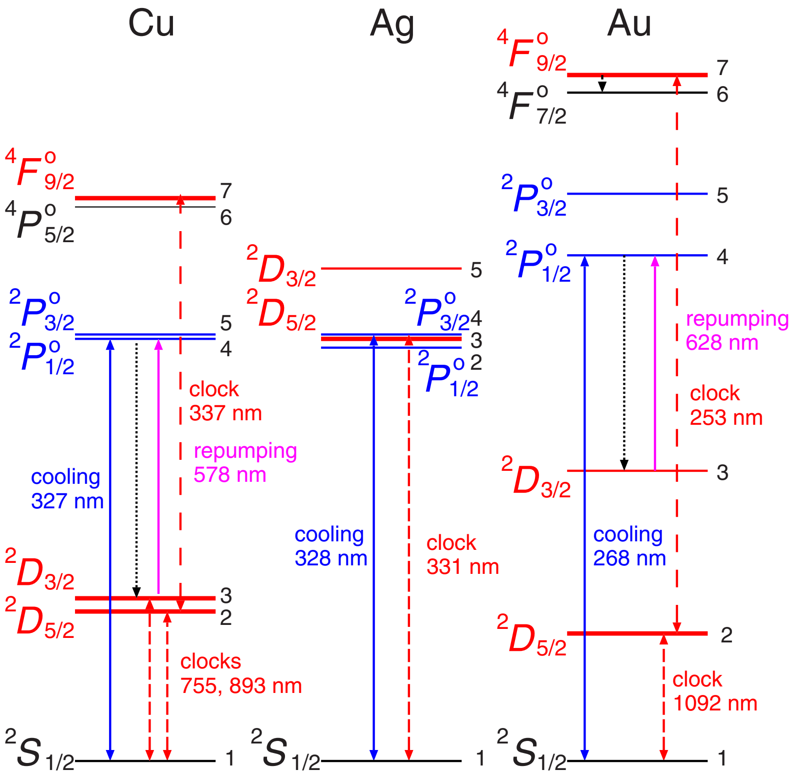

Figure 7.1: Energy diagram (approximately to scale) for the lowest states of Cu ($I = 3/2$), Ag ($I = 1/2$), and Au ($I = 3/2$). Thick red lines indicate the upper clock states. Electric quadrupole ($E2$) clock transitions are shown as short-dashed red lines. Additional clock transitions in Cu and Au are shown as long-dashed red lines. Cooling transitions are shown as solid blue lines. The presence of leakage transitions (black dotted lines) implies the need for repumping (magenta lines). Numeration of the states corresponds to one in Table 7.2.

equation (7.1), we get

$$Y = (EI - D)^{-1} CX, \tag{7.2}$$

where I is the unit matrix. Since D is a diagonal matrix, (7.2) can be rewritten as

$$y_k = \frac{1}{E - E_k} \sum_m c_{km} x_m, \tag{7.3}$$

where $E_k = \left\langle k \left| H^{\mathrm{CI}} \right| k \right\rangle$ is the diagonal CI matrix element for high-energy states.

By substituting (7.2) into (7.1), we get the CIPT equation,

$$\left[A + C(EI - D)^{-1}B\right] X = EX. \tag{7.4}$$

Once the energy E and the wave function X are found by solving (7.4) a correction to the wave function Y can be found using (7.2,7.3). Note that after Y is calculated, the total wave function should be renormalized. This is because the solution of (7.4) is normalized by $\sum_k x_k^2 = 1$, while the total wave function should be normalized by $\sum_k x_k^2 + \sum_m y_m^2 = 1$.

In our previous works [25, 27–31], only the solution of the CIPT equation (7.4) was implemented, while the correction to the wave function (7.2) was not calculated. In the present work, we calculate Y too and include it in the calculation of the matrix elements (see below).

We perform the calculations in the V^{N-1} approximation, with one electron removed from the initial relativistic HartreeFock (HF) calculations to obtain the potential for calculating single-electron basis states. The B-spline technique [32] is used to construct single-electron basis states above the core. Many-electron states for the CIPT calculations are constructed by exciting one or two electrons from a reference configuration and then using the resulting configurations to build all corresponding many-electron states of definite value of the total angular momentum J and its projection J_z. States corresponding to about 100 lowest nonrelativistic configurations go into the effective CI matrix, while higher states are treated perturbatively. Note that our calculations are completely relativistic. We only use nonrelativistic configurations to simplify the procedure of generating many-electron basis states. In the list of nonrelativistic configurations, each of them is subsequently replaced by a corresponding set of relativistic configurations. For example, the $5d^9 6s6p$ configuration is replaced by four relativistic ones, i.e., the $5d^4_{3/2}5d^5_{5/2}6s6p_{1/2}$, $5d^3_{3/2}5d^6_{5/2}6s6p_{1/2}$, $5d^4_{3/2}5d^5_{5/2}6s6p_{3/2}$, and $5d^3_{3/2}5d^6_{5/2}6s6p_{3/2}$ configurations.

To check the stability of the results, we perform calculations in a different way. We keep the minimum number of possible configurations in the effective CI matrix [block A in Eq. (7.1)], but introduce an extra term into the CI Hamiltonian, i.e., the effective

Table 7.1: Fitting parameters for the effective polarization potential (7.5).

Atom	α_s	α_p	α_d
Cu	0.72	0.88	0.22
Ag	0.71	0.81	0.24
Au	0.69	0.92	0.34

polarization potential,

$$\delta V_l = -\frac{\alpha_l}{a^4 + r^4}. \tag{7.5}$$

This term imitates the effect of core-valence correlations. Its form is chosen to coincide with the polarization potential $\left(V_p = -\alpha/r^4\right)$ on large distances. The parameter a is a cutoff parameter introduced to remove the singularity at $r = 0$. We use $a = 1a_B$ and treat α_l as a fitting parameter. Here, l is the value of the angular momentum, indicating that we use different fitting parameters in the calculation of the s, p, and d single-electron basis states. The values of α_s are chosen to fit ionization potentials (IPs), the values of α_p are chosen to fit the energies of the states of the $nd^{10}(n+1)p$ configuration, and the values of α_d are chosen to fit the energies of the states of the $nd^9(n+1)s^2$ configuration.

7.4.2 Energies

The obtained fitting parameters are presented in Table 7.1. Energy levels, calculated in the two different approaches, are presented in Table 7.2. Note the significant improvement to the energies due to the fitting. The fitting is not perfect because we use one fitting parameter for both components of the fine structure. We do this to avoid a false contribution to the fine structure (e.g., a contribution which does not vanish in the nonrelativistic limit).

Fitting also improves the wave functions, leading to more accurate values of the matrix elements. Comparing transition amplitudes and other matrix elements obtained with and without fitting is an important test of the theoretical uncertainty.

We point out that the fitting can be used for improved predictions of the spectra of systems with poor experimental data, e.g., superheavy elements or highly charged ions. To do so, we need to perform accurate fitting for a system with known spectra and electronic structure similar to the system of interest. Then the same fitting parameters can be used to calculate the unknown spectra.

7.4.3 Transition amplitudes

To calculate transition amplitudes, we use the well-known random phase approximation (RPA; see, e.g., [33]). The RPA equations for a single-electron state have the form

$$(H^{\mathrm{HF}} - \epsilon_c)\delta\psi_c = -(\hat{F} + \delta V_F^{N-1})\psi_c. \tag{7.6}$$

Here, H^{HF} is the relativistic Hartree-Fock Hamiltonian, the index c numerates single-electron states, $\hat{F}$ is the operator of an external field, $\delta\psi_c$ is a correction to the state c due to an external field, and δV_F^{N-1} is the correction to the selfconsistent Hartree-Fock potential due to the external field. The same V^{N-1} potential is used in the RPA and HF calculations. The RPA equations (7.6) are solved self-consistently for all states c in the core. Transition amplitudes are found as matrix elements between many-electron states found in the CIPT calculations for the effective operator of an external field,

$$A_{ab} = \langle b|\hat{F} + \delta V_F^{\mathrm{core}}|a\rangle. \tag{7.7}$$

Here $|a\rangle$ and $|b\rangle$ are many-electron wave functions. They have a form

$$|a\rangle = \sum_k x_k \Phi_k \tag{7.8}$$

or

$$|a\rangle = \sum_k x_k \Phi_k + \sum_m y_m \Phi_m, \tag{7.9}$$

where Φ_k is a single-determinant many-electron basis wave function, x_k comes from the solution of (7.4) and y_k comes from (7.3). In our previous works [25,27–31], we used (7.8),

Table 7.2: Excitation energies (cm^{-1}), ionisation potential (IP, cm^{-1}) and lifetimes for six states of Cu and of Au and for the four lowest excited states of Ag. Lifetime values without indicated uncertainties are theoretical values.

			Energy (cm^{-1})			Lifetime	
			NIST	Present work		Present	
N	Conf.	Term	[53]	No fitting	fitted	work	Other
				Cu			
1	$3d^{10}4s$	$^2\mathrm{S}_{1/2}$	0	0	0	∞	
2	$3d^9 4s^2$	$^2\mathrm{D}_{5/2}$	11203	10521	11277	45 s	26.76 s[a]
3	$3d^9 4s^2$	$^2\mathrm{D}_{3/2}$	13245	12270	13331	7.3 s	4.46 s[a]
4	$3d^{10}4p$	$^2\mathrm{P}^{\mathrm{o}}_{1/2}$	30535	29489	30513	7.1 ns	7.4(2) ns[b] 6.535 ns[a]
5	$3d^{10}4p$	$^2\mathrm{P}^{\mathrm{o}}_{3/2}$	30784	31115	30772	6.9 ns	7.1(2) ns[b] 6.369 ns[a]
6	$3d^9 4s4p$	$^4\mathrm{P}^{\mathrm{o}}_{5/2}$	39018	38693			
7	$3d^9 4s4p$	$^4\mathrm{F}^{\mathrm{o}}_{9/2}$	40909	40400		600 s	6897 s[a]
IP	$3d^{10}$	$^1\mathrm{S}_0$	62317	60328	62333		
				Ag			
1	$4d^{10}5s$	$^2\mathrm{S}_{1/2}$	0	0	0	∞	
2	$4d^{10}5p$	$^2\mathrm{P}^{\mathrm{o}}_{1/2}$	29552	29495	29549	6.6 ns	7.41(4) ns[c] 6.85 ns[a]
3	$4d^9 5s^2$	$^2\mathrm{D}_{5/2}$	30242	32480	30289	0.26 s	0.2 s[d]
4	$4d^{10}5p$	$^2\mathrm{P}^{\mathrm{o}}_{3/2}$	30473	30451	30437	6.1 ns	6.79(3) ns[c] 6.25 ns[a]
5	$4d^9 5s^2$	$^2\mathrm{D}_{3/2}$	34714	36430	34804	79 μs	40 μs[e] 65.8 μs[a]
IP	$4d^{10}$	$^1\mathrm{S}_0$	61106	58891	61141		
				Au			
1	$5d^{10}6s$	$^2\mathrm{S}_{1/2}$	0	0	0	∞	
2	$5d^9 6s^2$	$^2\mathrm{D}_{5/2}$	9161	10670	9161	44 s	
3	$5d^9 6s^2$	$^2\mathrm{D}_{3/2}$	21435	22096	21744	33 ms	
4	$5d^{10}6p$	$^2\mathrm{P}^{\mathrm{o}}_{1/2}$	37359	38853	36784	4.1 ns	6.0(1) ns[b]
5	$5d^{10}6p$	$^2\mathrm{P}^{\mathrm{o}}_{3/2}$	41175	43028	41217	3.3 ns	4.6(2) ns[b]
6	$5d^9 6s6p$	$^4\mathrm{F}^{\mathrm{o}}_{7/2}$	45537	46375			
7	$5d^9 6s6p$	$^4\mathrm{F}^{\mathrm{o}}_{9/2}$	48697	49166		2 s	
IP	$5d^{10}$	$^1\mathrm{S}_0$	74408	72806	74472		

[a] Reference [34].

[b] Reference [35].

[c] Reference [36].

[d] Extrapolation from Hg$^+$, see Ref. [37] and references therein.

[e] Reference [38].

while in the present work, we also include the correction to the wave function (7.3) and so use (7.9) for matrix elements. The difference in matrix elements values (7.7) when using (7.8) or (7.9) is usually a few percent. In most cases, it does not exceed 2%.

The rates of spontaneous emission are given in atomic units by

$$\Gamma_{E1,M1} = \frac{4}{3}(\alpha\omega)^3 \frac{A^2_{E1,M1}}{2J+1}, \tag{7.10}$$

for electric dipole ($E1$) and magnetic dipole ($M1$) transitions, and by

$$\Gamma_{E2,M2} = \frac{1}{15}(\alpha\omega)^5 \frac{A^2_{E2,M2}}{2J+1}, \tag{7.11}$$

for electric quadrupole ($E2$) and magnetic quadrupole ($M2$) transitions. In these formulas, α is the fine-structure constant, ω is the energy difference between the lower and upper states, A is the amplitude of the transition (7.7), and J is the total angular momentum of the upper state. The magnetic amplitudes A_{M1} and A_{M2} are proportional to the Bohr magneton, $\mu_B = |e|\hbar/2mc$. Its numerical value in Gaussian-based atomic units is $\mu_B = \alpha/2 \approx 3.65 \times 10^{-3}$. The lifetimes of the excited states are calculated by $\tau_a = 2.4189 \times 10^{-17}/\sum_b \Gamma_{ab}$, where τ_a is the lifetime of atomic state a in seconds, the summation goes over all possible transitions to lower states b, and the transition probabilities Γ_{ab} are given by (7.10) or (7.11). Lifetimes were calculated using the transition amplitudes and probabilities reported in Table 7.3. The lifetimes of the lowest states of Cu, Ag, and Au are presented in Table 7.2.

Table 7.3 presents the amplitudes calculated in the first approach (large CI matrix and no fitting). The difference between the two approaches is a few percent for large amplitudes and up to a few tens of percent for small amplitudes, e.g., amplitudes which vanish in the nonrelativistic limit. Another way to estimate the accuracy of the amplitude calculations is to compare with available experimental data or other calculations, in particular the calculations for Cu and Ag performed with the use of Cowan's code [34]. This is done in Tables 7.2 and 7.3. One can see that the accuracy for the calculated amplitudes goes down while moving from Cu to Au, coming to about 50% disagreement with the reference data for a large transition rate in Au for the $E1$ transition between states 4 and 1; see Table 7.3 (this translates into about 25% uncertainty in the transition amplitude). For weak transitions, the disagreement might be even larger. The accuracy is better for Cu and Ag. The limited accuracy for the calculated amplitudes is due to the small size of the effective CI matrix. At the present stage, the contribution of the high-energy states is included for the energies, but not for the transition amplitudes. However, the present accuracy is sufficient for the main conclusions of the paper regarding the suitability of the clock states for time keeping and the search for new physics.

It should be mentioned that states with no excitation from the upper d shell (e.g., the $5f^{10}6p_{1/2,3/2}$ states of Au) can be treated more accurately within different approaches, for example, with the use of the correlation potential method [33]. The main advantage of the current approach is that it can be used for any state of the considered atoms, including states with excitations from the upper d shell where most other methods would not work.

7.5 ANALYSIS

7.5.1 Clock transitions

Cu has three long-lived metastable states ($N = 2, 3, 7$ in Table 7.2), Ag has one ($N = 4$), and Au has two ($N = 2, 7$). The states of Cu and Au have lifetimes that are substantially larger than 1 s, comparable to those of the currently used Sr and Yb lattice clocks. The 0.2 s lifetime of the Ag upper clock state is comparatively small. Nevertheless, the natural Q factor, 1×10^{15}, is pronouncedly high and could permit a lattice clock of excellent stability. In the following, we consider the clock transitions between these six states and their respective lower clock states. Note that the two ^2D clock states of Cu are very similar and therefore, in most cases, we present the data for only the $^2D_{5/2}$ state. We also do not present a comprehensive analysis for the $^4F^o_{9/2}$ states of Cu and Au, limiting the present work to calculating the lifetimes and sensitivity to new physics.

Table 7.3: Transition amplitudes and probabilities for transitions between the seven states of Cu and Au and between the five lowest states of Ag.

Transition	Type	$\hbar\omega$ (cm^{-1})	This work $\lvert A\rvert$ (a.u)	This work Γ (s^{-1})	NIST Γ (s^{-1})
			Cu		
2-1	E2	11203	2.603	2.23[−2]	
3-1	M1	13245	$0.0002\mu_B$	6.27[−7]	
4-1	E1	30535	2.217	1.42[8]	1.376(14)[8][a]
5-1	E1	30784	3.140	1.45[8]	1.395(14)[8][a]
3-2	M1	2043	$1.549\mu_B$	0.138	
5-2	E1	19581	0.546	1.13[6]	2.0(4)[6][b]
4-3	E1	17290	0.404	8.48[6]	1.65(30)(2)[6][b]
5-3	E1	17538	0.174	8.23[4]	2.4(4)[5][b]
5-4	M1	248	$1.154\mu_B$	1.38[−4]	
7-6	E2	1891	24.1	1.6[−4]	
			Ag		
2-1	E1	29552	2.534	1.68[8]	1.3(1)[8][c]
3-1	E2	30242	2.872	3.90	
4-1	E1	30473	3.578	1.84[8]	1.4(1)[8][c]
5-1	M1	34714	$0.00015\mu_B$	6.4[−6]	
4-2	M1	921	$1.146\mu_B$	6.9[−3]	
5-2	E1	5162	0.406	1.15[4]	
4-3	E1	230	0.534	1.75	1.6(6)[d]
5-3	M1	4472	$1.536\mu_B$	1.42	
5-4	E1	4242	0.175	1.18[3]	
			Au		
2-1	E2	9161	4.359	2.29[−2]	
3-1	M1	21435	$0.0008\mu_B$	4.25[−5]	
4-1	E1	37359	2.153	2.45[8]	1.64(3)[8][e]
5-1	E1	41175	2.923	3.02[8]	1.98(14)[8][e]
3-2	M1	12274	$1.549\mu_B$	29.9	
5-2	E1	32013	0.983	1.61[6]	1.90(13)[7][e]
4-3	E1	15924	0.504	1.04[6]	3.4(1.7)[6][e]
5-3	E1	19739	0.243	2.30[5]	5.2(2.6)[5][e]
5-4	M1	3816	$1.141\mu_B$	0.488	
7-6	M1	3160	$2.4\mu_B$	5.1[−1]	

[a] Reference [39].
[b] Reference [40].
[c] Reference [41].
[d] Reference [42].
[e] Reference [35].

7.5.2 Laser cooling of Cu, Ag, and Au

7.5.2.1 Silver

Silver has been laser cooled [42]. Here, the cooling scheme is straightforward: the cooling transition is between the ground and second-excited state, $^2S_{1/2} \rightarrow {}^2P_{3/2}$, with only weak leakage to the clock state 3. A repumper laser is nevertheless needed because of the small hyperfine splitting in the excited state.

7.5.2.2 Gold

A scheme for laser cooling of Au is presented in Fig. 7.2. The main cooling transition is the electric dipole transition between the ground state and the excited odd-parity $^2P^o_{1/2}$ state. Compared to using $^2P^o_{3/2}$ as the upper level, the advantage is that only one repumper is needed and that the longer cooling wavelength is experimentally advantageous. There is leakage from the $^2P^o_{1/2}$ to the $^2D_{3/2}$ state by another electric dipole transition ($4 \rightarrow 3$). Therefore, without repumping, only ~ 250 cycles are possible. With repumping (628 nm), the cooling may go for as long as needed. Another leakage channel is too weak to affect the scheme.

7.5.2.3 Copper

A cooling scheme similar to silver can be considered for copper: $^2\mathrm{S}_{1/2} \rightarrow {}^2\mathrm{P}_{1/2}$. It requires one additional laser for repumping.

7.5.2.4 Additional remarks

Optical lattice clocks require the cooling of atoms to the μK level for efficient loading of the optical lattice with the atoms. Therefore, after cooling on the strong $E1$ transition to a temperature of the order of 1mK, a second cooling process utilizing a weak transition

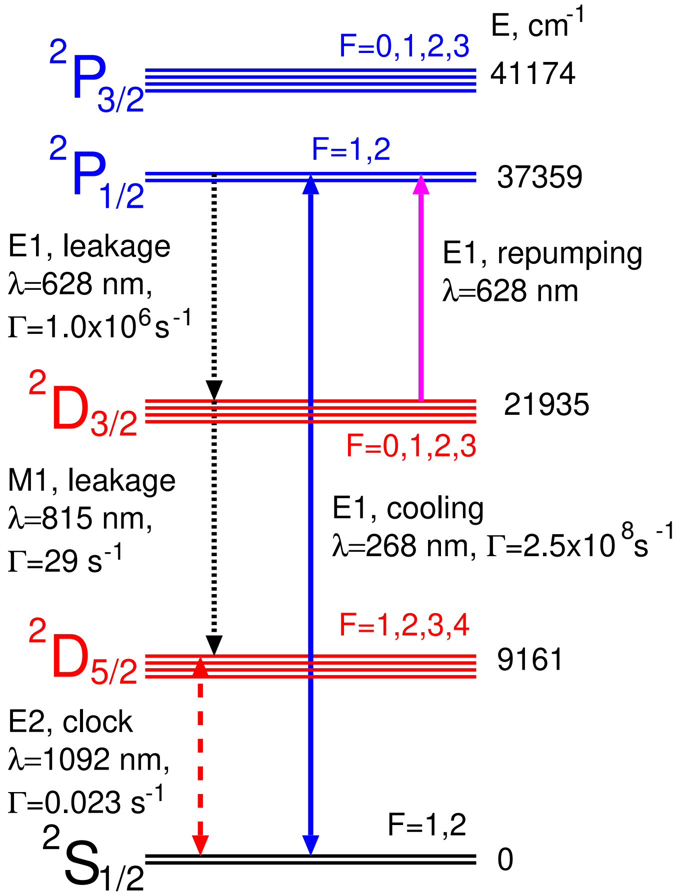

Figure 7.2: Details of the level scheme of ^{197}Au ($I = 3/2$) (not to scale) with proposed laser cooling. The hyperfine structure is shown schematically. The magenta arrow shows the repumper transition. Narrow-linewidth laser cooling is not shown. The clock transition (dashed red line) is composed of several hyperfine components.

should follow ("narrow-linewidth cooling"). One option is to cool on the $^2S_{1/2} \to {}^2D_{3/2}$ transition (1-3 for Cu, 1-5 for Ag, 1-3 for Au). These are $M1$ transitions and are very weak. However, the strengths could be increased and the lifetime of the $^2D_{3/2}$ states shortened by $E1$ coupling them to the respective ^2P states using appropriate laser waves. The 1-5 transition in Ag might be directly usable for narrow-linewidth cooling. This transition has been observed under two-photon excitation [38].

The hyperfine structure in both lower and upper laser cooling levels will typically require additional repumper fields to optimize cooling efficiency (see above). We shall not discuss such experimental details here.

Finally, we note that copper and silver atoms have been cooled using buffer-gas cooling [43].

7.5.3 Polarizabilities, blackbody radiation shifts, and magic frequencies

Knowledge of the atomic polarizabilities for both states of the clock transition is important for estimation of the frequency shift caused by blackbody radiation and for finding the magic frequency of the lattice laser field, i.e., the frequency at which the dynamic polarizabilities of both states are equal, causing no frequency shift.

The static scalar polarizability $\alpha_v(0)$ of an atom in state v is given by

$$\alpha_v(0) = \frac{2}{3(2J_v+1)} \sum_n \frac{|\langle v||D||n\rangle|^2}{E_n - E_v}, \tag{7.12}$$

where D is the electric dipole operator with the RPA correction (see the previous section), and the summation goes over the complete set of excited many-electron states.

Static scalar polarizabilities of the ground states of Cu, Ag, and Au are known from a number of calculations and measurements [44]. Table 7.4 presents the recommended values taken from Ref. [44]. In contrast, to the best of our knowledge, there is no similar data for the upper clock states of Cu, Ag, and Au. Therefore, we performed the calculations using two different approaches.

In the first approach, we stay within the CIPT method and calculate 20 odd-parity states for each value of the total angular momentum J, which satisfies the electric dipole selection rules for the transitions from the ground and clock states ($J = 1/2, 3/2, 5/2, 7/2$). Then we use formula (7.12) to perform the calculations for both states. These calculations show three important things: (a) there is good agreement with other data for the ground state, (b) there is good saturation of the summation in Eq. (7.12), (c) the summation for the clock states is strongly dominated by the transitions to the states of the $5d^96s6p$ configuration (we use the Au atom as an example).

Table 7.4: Scalar static polarizabilities (in a_B^3) and BBR frequency shifts for three clock transitions of Cu, Ag and Au. $\Delta\alpha$ is the difference between the theoretical value for the upper clock state and the experimental value of the lower clock state.

	$\alpha_{\mathrm{g}}(0)$			$\alpha_c(0)$				BBR ($T = 300\,\mathrm{K}$)	
Atom	Expt. [44]	CIPT	CI+MBPT	CIPT	CI+MBPT	Final	$\Delta\alpha$	$\Delta\nu$ (Hz)	$\Delta\nu/\nu$
Cu[a]	47(1)	54.5	43.5	46.8	42.9	45(11)	2(11)	< 0.12	$< 3.4 \times 10^{-16}$
Ag	55(8)	51.8	50.6	45.9	49.5	47(2)	-8(8)	< 0.14	$< 1.5 \times 10^{-17}$
Au	36(3)	35.7	34.0	38.9	33.2	36(3)	0(4)	< 0.03	$< 5.6 \times 10^{-17}$

[a] State c is the $^2\mathrm{D}_{5/2}$ clock state.

The last fact implies that a different approach can be used, previously suggested for atoms with open f shells [46]. In this second approach, we use the fact that the sum (7.12) is dominated by the $6s$-$6p$ transitions, while the open $5d^9$ subshell remains unchanged. Therefore, the open d shell is attributed to the core and treated as a closed shell with an occupational number of 0.9. The atom is treated as a system with two external electrons above the closed-shell core and an appropriate CI+ MBPT (many-body perturbation theory) [47] method is used (see Ref. [46] for more details). The advantage of this approach is the efficient completeness of the basis with two-electron excitations. The shortcoming is the omission of the transition amplitudes involving excitations from the d shell. In contrast, the CIPT approach includes all amplitudes; however, the summation in Eq. (7.12) is truncated much earlier.

In the end, both approaches give similar results. The results for the clock states are presented in Table 7.4 together with experimental or estimated theory uncertainties. For these estimations, we used a comparison of the two approaches for the clock states as well as a comparison of the CIPT and CI + MBPT calculations with other data for the ground states.

The results of the calculations indicate that the values of the polarizabilities of the clock states of Cu, Ag, and Au are similar to those of the ground state. This is a nonstandard situation. More often, the polarizabilities of excited states are larger. Indeed, the higher is the state on the energy scale, the smaller is the energy denominator in Eq. (7.12). The present results can be explained by the fact that the summation in Eq. (7.12). is dominated by the states of the $5d^{10}np$ configurations for the ground state (we use Au again as an example) and by the states of the $5d^9 6s6p$ configuration for the clock state. The latter states are higher on the energy scale.

The blackbody radiation (BBR) shift is given by (see, e.g., [48])

$$\delta\nu_{\mathrm{BBR}} = -\frac{2}{15}(\alpha\pi)^3 T^4 [\alpha_c(0) - \alpha_{\mathrm{g}}(0)], \tag{7.13}$$

where α is the fine-structure constant, T is the temperature, and $\alpha_c(0)$ and $\alpha_{\mathrm{g}}(0)$ are static scalar polarizabilities of the clock and ground states, respectively. For simplicity, we do not include the dynamic correction to the BBR shift. For the more complete formula, see, e.g., [48].

The similarity of the polarizabilities implies a substantial cancellation of the blackbody radiation (BBR) frequency shift, a very favorable effect. The total uncertainty of the polarizability difference $\Delta\alpha$ has been evaluated as $u_{\mathrm{tot}}^2 = u_{\mathrm{exp}}\,[\alpha_g(0)]^2 + \delta_{\mathrm{theor}}^2$, where $\delta_{\mathrm{theor}} = \alpha_c(0)_{\mathrm{CIPT}} - \alpha_c(0)_{\mathrm{CI+MBPT}}$. Since for the three species the difference between experimental values for the ground state and the mean of the two theory results for the upper clock state is smaller or similar to the estimated uncertainty u_{tot}, we can only give the upper bounds for the BBR shifts. The results are presented in Table 7.4. These bounds of the three species are significantly lower than the BBR shifts in the established strontium and ytterbium optical lattice clocks, i.e., $(-53, -25) \times 10^{-16}$, respectively [49, 50]. The bound for Ag is actually 100 times lower than the BBR shift of Sr. The bounds of Ag and Au are also smaller than the shift in the mercury lattice clock, -1.6×10^{-16}, and the theoretical shift of the recently proposed 431 nm transition in Yb (-2.9×10^{-16} [19]), listed in Table 7.8.

More accurate estimations of the BBR shift might be possible if the polarizabilities are measured or calculated to higher accuracy.

Magic frequencies can be found in the vicinity of every resonance for one of the polarizabilities, i.e., when the frequency of the lattice laser field is approximately equal to the excitation energy [energy denominator in Eq. (7.12)]. The first magic frequency is near the first resonance for the ground-state polarizability, i.e., $\hbar\omega_m \simeq 30535$ cm^{-1} (327 nm) for Cu, $\hbar\omega_m \simeq 29552$ cm^{-1}(338 nm) for Ag, and $\hbar\omega_m \simeq 37359$ cm^{-1} (267 nm) for Au. Note that since the clock states have large values of the total angular momentum ($J = 5/2$), the magic frequencies would also depend on the quadrupole contribution to the polarizabilities. The current level of computational accuracy does not allow one to find accurate values of the magic frequencies. Having more experimental data may help. In the vicinity of a resonance or a few resonances, a semiempirical formula can be used,

$$\alpha_a(\omega) \approx \alpha'_a(0) + \frac{2}{3(2J_v+1)} \sum_b \frac{A^2_{ab}}{\omega - \Delta E_{ab}}, \tag{7.14}$$

where $\alpha'_a(0)$ is chosen in such a way that $\alpha_a(\omega = 0)$ is equal to the known (e.g., experimental) static polarizability of state a. Summation in Eq. (7.14) goes over close resonances. If the static polarizability is known to sufficient accuracy and amplitudes A_{ab} of $E1$ transitions are extracted from experimental data or from accurate atomic calculations, then (7.14) can be used to find magic frequencies.

7.5.4 Stark, quadrupole, and Zeeman shifts

The interaction of atomic electrons with an external electric field and its gradient leads to Stark and electric quadrupole shifts of transition frequencies. These shifts are tiny in optical lattice clocks. We consider the shifts in more detail in Appendix 7.8.1.

The linear Zeeman shift is given by the expression

$$\Delta E_{F,F_z} = g_F \mu_B B F_z, \tag{7.15}$$

where g_F is the g factor of a particular hyperfine-structure (hfs) state. It is related to the electron g_J factor by

$$g_F = g_J \langle F, F_z = F, I, J | \hat{J}_z | F, F_z = F, I, J \rangle / F. \tag{7.16}$$

Electron g factors have approximate values $g_{1/2} \approx 2, g_{3/2} \approx 0.8$, and $g_{5/2} \approx 1.2$. More accurate values for Cu, Ag, and Au can be found in the NIST tables [53]. For a clock state with $J = 5/2$ and $F = 2$, we have $g_2 = (11/12)g_{5/2} = 1.1$. For a clock state with $J = 3/2$ and $F = 2$, we have $g_2 = (1/2)g_{3/2} = 0.4$.

Table 7.5: Magnetic dipole (A) and electric quadrupole (B) hfs constants (MHz) used in the calculation of the second-order Zeeman shift. Values are rounded to 0.1 MHz or to the last significant digit.

Atom	Ground state		Clock state			Reference
		A		A	B	
^{63}Cu	$^2S_{1/2}$	5866.9	$^2D_{5/2}$	749.1	186.0	[51, 52, 65]
^{63}Cu	$^2S_{1/2}$	5866.9	$^2D_{3/2}$	1851.0	137.4	[51, 52, 65]
^{107}Ag	$^2S_{1/2}$	−1712.5	$^2D_{5/2}$	−126		[24, 57]
^{197}Au	$^2S_{1/2}$	3049.7	$^2D_{5/2}$	80.2	−1049.8	[22, 57]

The linear Zeeman shift can be avoided if only transitions between states with $F_z = 0$ are considered, as suggested in the past for clock operation. Alternatively, one can average over the transition frequencies with positive and negative F_z in order to cancel the linear shift. However, the large individual shifts will make it difficult to achieve an accurate cancellation.

A second-order Zeeman shift is unavoidable. Therefore, it is important to know its value. If we consider transitions between definite hfs components, then the shift is strongly dominated by transitions within the same hfs multiplet. The total shift is the difference between the second-order shifts in the clock and in the ground state. Both shifts are given by

$$\delta E_{F,F_z} = \sum_{F'=F\pm1,F'_z} \frac{|\langle F'F'_zIJ|\hat{J}_z|FF_zIJ\rangle g_J\mu_B B_0|^2}{\Delta E_{\text{hfs}}(F,F')}. \tag{7.17}$$

Here, $\Delta E_{\text{hfs}}(F,F') = E(FIJ) - E(F'IJ)$ is the hfs interval. It has a different sign depending on whether this is an up or down transition.

It follows from (7.27) that

$$\Delta E_{\text{hfs}}(F,F+1) = -A(F+1) - B[2(F+1)^2 + 1 - 2J(J+1) - 2I(I+1)]$$

and

$$\Delta E_{\text{hfs}}(F,F-1) = AF + B[2F^2 + 1 - 2J(J+1) - 2I(I+1)].$$

Table 7.6: Second-order Zeeman shift $\left[\mathrm{mHz}/(\mu\mathrm{T})^2\right]$ for ^{107}Ag and comparison with other calculations. The index g is for the ground state and index c is for the excited (clock) state. It is assumed that $F_z = 0$ in both states.

F_c	F_g	$\Delta E_c/B_0^2$	$\Delta E_g/B_0^2$	$\left(\Delta E_c - \Delta E_g\right)/B_0^2$	Ref. [24]
2	0	0.186	0.114	0.072	0.07
2	1	0.186	−0.114	0.301	0.07
3	1	−0.186	−0.114	−0.072	−0.3

Using experimental values for A and B (see Table 7.5), we calculate the second-order Zeeman shift for Cu, Ag, and Au. The results are presented in Tables 7.6 and 7.7. The shift for Ag was studied theoretically before [24]. Our result differs from theirs; this may be due to a simple calculational error in the previous work. Table 7.6 presents separate contributions from the shifts in the ground and excited states. One can see that the disagreement may come from the sign error in a particular contribution. Different signs are caused by energy denominators. For example, when we move from the first to the second line of the table, the sign of the energy denominator for the ground-state contribution changes and so does the contribution itself. Since the other contribution remains the same, the total shift must change.

Table 7.7 shows the second-order Zeeman shift for ^{63}Cu and ^{197}Au. As in the case of ^{107}Ag, the shift is small. Note that Cu has one clock transition with both a tiny quadratic shift coefficient and no linear shift. By measuring two or more $F_{gz} = 0 \rightarrow F_{ez} = 0$ Zeeman components and taking appropriate combinations of the corresponding transition frequencies, the second-order shift may be substantially reduced.

The quadratic shift vanishes in the considered approximation for transitions between states with maximum value of F and its projection F_z (see the bottom lines of Table 7.7). This is because there are no terms in Eq. (7.17) which would satisfy the selection rules. Note, also, that the (nonzero) numbers in Table 7.7 should be considered as rough estimations only. This is because of uncertainties of the experimental data for the electric quadrupole hfs constant B, in particular for Cu [52]. The numbers can change several times depending on which set of data is used.

Table 7.7: Second-order Zeeman shift coefficient $[\mathrm{mHz}/(\mu\mathrm{T})^2]$ for ^{63}Cu and ^{197}Au. Gaps in the data mean that the corresponding set of quantum numbers is not possible for the transition.

				$(\Delta E_c - \Delta E_g)/B_0^2$		
				^{63}Cu	^{63}Cu	^{197}Au
F_g	F_{gz}	F_c	F_{cz}	$^2D_{5/2}$	$^2D_{3/2}$	$^2D_{5/2}$
1	0	0	0		−0.759	
1	0	1	0	0.087	0.743	0.023
1	0	2	0	0.193	0.058	0.027
1	0	3	0	−0.247	0.025	0.050
2	0	0	0		−0.792	
2	0	1	0	0.053	0.710	−0.041
2	0	2	0	0.160	0.024	−0.037
2	0	3	0	−0.281	−0.009	−0.014
2	0	4	0	0.001		−0.037
2	±2	3	±2	−0.044	0.004	0.002
2	±2	3	±3	−0.017	0.0	0.004
2	±2	4	±4	0.0		0.0

7.6 SEARCH FOR NEW PHYSICS

An exceptionally high accuracy of atomic clocks is a great advantage for using them in a search for new physics. The search is conducted by monitoring relative values of different atomic frequencies over a significant time interval. Establishing a time variation of the frequency ratio allows multiple interpretations. For example, the interaction between low-mass scalar dark matter and ordinary matter may lead to oscillation of the fine-structure constant and a transient variation effect [58–60]. In this section, we consider the sensitivities to a hypothetical time variation of the fine-structure constant, α $(\alpha = e^2/\hbar c)$, to local position invariance (LPI) violation, and to local Lorentz invariance (LLI) violation.

7.6.1 Time variation of the fine-structure constant

It is convenient to parametrize the α dependence of atomic frequencies by the formula $\omega = \omega_0 + q\left[\left(\frac{\alpha}{\alpha_0}\right)^2 - 1\right]$ [8], where α_0 and ω_0 are present-day values of the fine-structure constant and the frequency of the transition, and q is the sensitivity coefficient, which comes from the calculations. To monitor a possible frequency change with time, one atomic frequency is measured against another. Then,

$$\frac{\partial}{\partial t}\ln\frac{\omega_1}{\omega_2} = \frac{\dot{\omega}_1}{\omega_1} - \frac{\dot{\omega}_2}{\omega_2} = \left(\frac{2q_1}{\omega_1} - \frac{2q_2}{\omega_2}\right)\frac{\dot{\alpha}}{\alpha}. \tag{7.18}$$

The value $K = 2q/\omega$ is called an enhancement factor. It shows that if α changes in time, then ω changes K times faster. Calculated values of q and K for different optical clock transitions are presented in Table 7.8. We include all clock transitions of the present work and those transitions of previously studied clocks, which are sensitive to α variation. We remark that work on the historically important Hg$^+$ ion clock [9, 17] has been stopped. We nevertheless include it in the discussion. There are seven transitions where $|K| > 1$. The largest values of $|K|$ correspond to the smallest values of transition frequency ω. It would be wrong to say that all these transitions are good for searching for α variation. This is because the accuracy of the measurements is equally important (see, also, the discussion in Ref. [19]). The true figure of merit is the ratio of the relative frequency shift due to variation of α and the fractional uncertainty of the measurements, $(q/\omega)/(\delta\omega/\omega) = q/\delta\omega$. This ratio does not (directly) depend on ω. Therefore, looking for a large value of K caused by the small value of ω brings no benefit. The value of the relativistic energy shift q is more important. Comparing the values of q for different clock transitions (see Table 7.8), we see that the E2 clock transition sensitivity for Au is essentially as large as the recently proposed new transitions in neutral ytterbium [19] and only 30% smaller than the octupole transition in the ytterbium ion (Yb II). It is possible to search for α variation by comparing two clock transitions in the same atom, i.e., gold. The corresponding differential sensitivity factor is $q_{2-7} - q_{1-2} \simeq 63 \times 10^3$ cm^{-1}. This value is similar to the differential sensitivity of the two clock transitions in the ytterbium ion.

Table 7.8: Sensitivity of clock transitions to variation of the fine structure constant (q, K), to LLI violation [reduced matrix element $\langle c||T_0^{(2)}||c\rangle$ of the tensor operator (7.22) for the upper state c], and to LPI violation (relativistic factor R). Note that $\langle g||T_0^{(2)}||g\rangle$ is zero for the ground state of all clocks due to the small value of the total angular momentum $J \leqslant 1/2$.

Atom/	Transition			$\hbar\omega$[a]	q		$\langle c\|\|T_0^{(2)}\|\|c\rangle$	R	
Ion	Lower state		Upper state	(cm^{-1})	(cm^{-1})	$K = 2q/\hbar\omega$	(a.u.)	Present	Other
Cu	$3d^{10}4s\ ^2S_{1/2}$	–	$3d^94s^2\ ^2D_{5/2}$	11202.565	-4000	-0.71	-48	0.98	
Cu	$3d^{10}4s\ ^2S_{1/2}$	–	$3d^94s^2\ ^2D_{3/2}$	13245.443	-1900	-0.29	-37	0.99	
Cu	$3d^94s^2\ ^2D_{5/2}$	–	$3d^94s4p\ ^4F^o_{9/2}$	29706.54	2100	0.14	-48		
Ag	$4d^{10}5s\ ^2S_{1/2}$	–	$4d^95s^2\ ^2D_{5/2}$	30242.061	-11300	-0.75	-41	0.93	
Au	$5d^{10}6s\ ^2S_{1/2}$	–	$5d^96s^2\ ^2D_{5/2}$	9161.177	-38550	-8.4	-45	0.67	
Au	$5d^96s\ ^2D_{5/2}$	–	$5d^96s6p\ ^4F^o_{9/2}$	39535.970	24200	1.2	-44		
Yb[c]	$4f^{14}6s^2\ ^1S_0$	–	$4f^{14}6s6p\ ^3P^o_0$	17288.439	2714	0.31	0	1.12	1.20[b]
Yb[c]	$4f^{14}6s^2\ ^1S_0$	–	$4f^{13}5d6s^2 J = 2$	23188.518	-44290	-3.82	-72[d]	0.65	1.40[e]
Yb[e]	$4f^{14}6s6p\ ^1P^o_0$	–	$4f^{13}5d6s^2 J = 2$	5900.079	-43530	-15	-72[d]		
Yb II[f]	$4f^{14}6s\ ^2S_{1/2}$	–	$4f^{13}6s^2\ ^2F^o_{7/2}$	21418.75	-56737	-5.3	-135	0.58	-1.90[b]
Yb II[f]	$4f^{14}6s\ ^2S_{1/2}$	–	$4f^{14}5d\ ^2D_{3/2}$	22960.80	10118	0.88	10[d]	1.42	1.48[b]
Yb II[e]	$4f^{13}6s^2\ ^2F^o_{7/2}$	–	$4f^{14}5d\ ^2D_{3/2}$	1542.06	-66855	-87	10[d]		
Hg II[g]	$5d^{10}6s\ ^2S_{1/2}$	–	$5d^96s^2\ ^2D_{5/2}$	35514.624	-52200	-2.94		0.68	0.2[b]

[a] NIST [53].
[b] Reference [9].
[c] Reference [19].
[d] Present work.
[e] Reference [61].
[f] Reference [11, 56].
[g] Reference [8, 19].

7.6.2 LPI violation

In the standard model extension, the term in the Hamiltonian responsible for the LPI violation can be presented in the form (see, e.g., Ref.. [9])

$$\hat{H}_{\text{LPI}} = c_{00} \frac{2}{3} \frac{U}{c^2} \hat{K}, \tag{7.19}$$

where c_{00} is the unknown parameter characterizing the magnitude of the LPI violation, U is the gravitational potential, c is the speed of light, $\hat{K} = c\gamma_0 \gamma^j p_j/2$ is the relativistic operator of kinetic energy, in which γ_0 and γ^j are Dirac matrices, and $\mathbf{p} = -i\hbar\nabla$ is the electron momentum operator.

The presence of the term (7.19) in the Hamiltonian would manifest itself via a dependence of the atomic frequencies on the time of the year, caused by the changing Sun-Earth distance leading to a change of the Sun's gravitational potential U. As in the case of the α variation, at least two clock transitions are needed to measure one clock frequency against the other. The interpretation of the measurements is based on the formula [9]

$$\frac{\Delta\omega_1}{\omega_1} - \frac{\Delta\omega_2}{\omega_2} = -(R_1 - R_2) \frac{2}{3} c_{00} \frac{\Delta U}{c^2}, \tag{7.20}$$

where $\Delta\omega$ and ΔU are the change of atomic frequencies and gravitational potential between the measurements, respectively. R in Eq. (7.20) is the relativistic factor, which describes the deviation of the kinetic energy E_K from the value given by the nonrelativistic virial theorem (which states that $E_K = -E$, where E is the total energy),

$$R_{ab} = -\frac{E_{K,a} - E_{K,b}}{E_a - E_b}. \tag{7.21}$$

The values of the factor R are calculated in computer codes by varying the value of the kinetic-energy operator in the Dirac equation (see Ref. [9] for details).

The results are very sensitive to the many-body effects, which means that the effects should be treated very accurately or avoided. Otherwise, the results are unstable. A good criterion for the reliability of the results is the achievement of the nonrelativistic limit $R = 1$. This can be done by setting to zero the value of the fine-structure constant α in the computer codes. It turns out that for complicated systems such as those considered in the present work, the best results are obtained by simple estimations based on single-electron consideration. Namely, the clock transitions in Cu, Ag, and Au can be considered as $ns \rightarrow (n-1)d_{5/2}$ single-electron transitions ($n = 4, 5, 6$ for Cu, Ag, and Au, respectively). Therefore, we just use single-electron energies of theses states in Eq. (7.21). We use the same approach for $\mathrm{Hg}^+$and Yb^+.

The results are presented in Table 7.8, together with the results obtained earlier for other systems. Note that the results for the transitions involving excitation from the $5d$ shell in Hg^+ and the $4f$ shell in Yb^+ are different from what was published before. The old calculations were based on a version of the CI method [62,63] that contained a fitting parameter responsible for the correct energy interval between states of different configurations. It was assumed that this parameter does not change under variation of the kinetic-energy operator. We believe that the present results are more reliable because they are free from any assumptions and because they reproduce the nonrelativistic limit $R = 1$. Note that the values of R for transitions in Yb and Yb^+, which do not involve excitation from the $4f$ shell, are in good agreement with previous calculations ($R = 1.12$ and $R = 1.42$; see Table 7.8). This means that the present single-electron estimations work well and that accurate many-body calculations are possible for simple systems.

To study the LPI violation, one needs to compare two clocks with different values of the relativistic factors R [see formula (7.20)] over at least half of a year. An important past experiment with optical clocks was the comparison of Hg^+ clock with an Al^+clock [9, 17]. Table 7.8 shows that there are various choices for such clock pairs. In particular, the Au clock's sensitivity is comparatively strong (with a large negative deviation from the nonrelativistic value $R = 1$). Thus, it is suitable for pairing with a clock with strong, but opposite sensitivity, such as the standard Yb lattice clock ($R > 1$). It is more sensitive than the Cu-Yb pairing by a factor 2.5. The two clock transitions in Yb^+ have the largest difference $|R_1 - R_2|$.

7.6.3 LLI violation

The LLI violation term is a tensor operator,

$$\hat{H}_{\mathrm{LLI}} = -\frac{1}{6} C_0^{(2)} T_0^{(2)}, \tag{7.22}$$

where $C_0^{(2)}$ is unknown constant and the relativistic form of the $T_0^{(2)}$ operator is given by $T_0^{(2)} = c\gamma_0 \left(\gamma^j p_j - 3\gamma^3 p_3\right)$. To study the effect of the LLI violating term (7.22), one needs long-lived atomic states with a large value of the total electron angular momentum $J, J > 1/2$. All clock states of Cu, Ag, and Au satisfy this requirement. Note that the established lattice optical clocks Yb, Sr, and Hg do not satisfy this requirement and are thus not suitable for testing LLI.

The term(7.22) should cause a dependence of the atomic frequencies on the apparatus orientation in space (e.g., due to Earth rotation). Interpretation of the measurements requires knowing the values of the reduced matrix elements of the operator $T_0^{(2)}$ for the clock states. We calculate these matrix elements using the CIPT method to obtain wave functions and the RPA method to obtain the effective operator for valence electrons. The results are presented in Table 7.8. The results of earlier calculations for Yb II [11] are also presented for comparison. In contrast to the search of the α variation and LPI violation, one clock state is sufficient for the search of the LLI violation. The comparison of frequencies is done for states with different projections of the total angular momentum J [10, 11].

The large value of the matrix element is important, but it is not the most important parameter, e.g., the lifetime of the metastable state is even more important (see, e.g., [11] for more discussion). Obviously, in addition, the uncertainty of the clock is also crucial. The calculations show that Cu, Ag, and Au are suitable for the search for LLI violation.

7.7 CONCLUSION

We further advanced the CIPT method of electronic structure calculations for atoms with open shells by calculating the correction to the wave function caused by mixing with high-energy states. We used this method to study electric quadrupole transitions between ground and excited metastable states of Cu, Ag, and Au and demonstrated that the transitions have important features of optical clock transitions.

A main result of this work is that we have identified three elements for which the blackbody shift is smaller than that of the standard lattice clocks (notably strontium) by a factor of up to approximately 100. The predicted shifts for Ag and Au are also smaller than the predicted shifts in Cd, Zn, and Yb (431 nm). At present, among the neutral species, only Tm has a smaller (measured) blackbody shift [64].

Other sensitivities to external perturbing fields, such as Zeeman and Stark sensitivities, are similar to or smaller than that in current top-performing optical clocks and lead to wellcontrollable shifts. These results lead to the identification of Ag and Au as two particularly valuable candidates for nextgeneration optical lattice clocks.

We remark that as an example, the laser system required for Au is commercially available and does not require particularly difficult deep-ultraviolet wavelengths. For example, the 268 nm cooling wavelength of Au can be easily obtained as the fourth harmonic of a powerful Yb^+-doped fiber laser at 1071 nm. The narrow-linewidth cooling requires a laser, e.g., at 456 nm, which is a wavelength available from a diode laser. The clock laser radiation can be directly provided by a fiber laser.

Analyzing the performance of the new clock transitions for the search for physics beyond the standard model, we find neutral atom clock candidates that have a nonzero and relevant sensitivity to violations of local Lorentz invariance. Our finding includes the recently proposed additional clock transition of Yb (431 nm). Such tests do not require a second atomic clock.

We furthermore found that the pairing of the Au clock with the already established Yb lattice clock (578 nm transition) would be a particularly sensitive choice for a test of local position invariance as reflected in the difference of R factors.

Finally, we had previously found that the 1092 nm transition of Au also exhibits a strong sensitivity to variation of α. The sensitivity K is approximately 27 times larger than for the standard Yb lattice clock, so that a pairing with the latter represents an option. Alternatively, the search for α variation can be done by pairing two clock transitions in the Au atom. The sensitivity coefficients q in the two Au clock transitions have opposite sign and this doubles the overall sensitivity to variation of α. Note that this is only the second neutral atomic species found (besides Yb) that exhibits this feature. Thus, there now exist concrete options for lattice-clock-based tests of α variation.

A reevaluation of the relativistic factor R of four clock transitions in Yb, Yb$^+$, and Hg$^+$ has led to significant changes in the values. Use of the correct values is crucial to derive the correct upper bounds for local position invariance violation, and also for selection of suitable clock pairs in future experimental campaigns.

We emphasize that these sensitivities are to be considered together with the eventually achievable accuracy and longterm stability of the clock frequencies. It is for these reasons that we have studied some important systematic shifts here. Because of the potential of the Cu, Ag, and Au clock, our work provides a strong motivation for experimental studies of their blackbody radiation shifts and lattice-induced shifts.

ACKNOWLEDGMENTS

We thank one referee for pointing out Ref. [34] to us. This work was supported by the National Natural Science Foundation of China (Grant No. 11874090) and the Australian Research Council (Grants No. DP190100974 and No. DP200100150). V.A.D. would like to express special thanks to the Institute of Applied Physics and Computational Mathematics in Beijing for its hospitality and support. The work of S.S. was performed in the framework of Project No. Schi 431/22-1 of the Deutsche Forschungsgemeinschaft. This research includes computations using the computational cluster Katana supported by Research Technology Services at UNSW Sydney.

7.8 Appendix:

7.8.1 STARK AND ELECTRIC QUADRUPOLE SHIFTS

The Stark shift of the frequency of the transition between atomic states a and b due to interaction with residual static electric field ε is

$$\delta\omega_{ab} = -\Delta\alpha_{ab}(0)\left(\frac{\varepsilon}{2}\right)^2, \tag{7.23}$$

where $\Delta\alpha_{ab}(0)$ is the difference between the static scalar polarizabilities of states a and b. The shift is quadratic in the electric field and usually small. It is further suppressed for the considered clock transitions due to the small difference in the polarizabilities (see Table 7.4).

The energy shift due to a gradient of a residual static electric field ε is described by a corresponding term in the Hamiltonian

$$\hat{H}_Q = -\frac{1}{2}\hat{Q}\frac{\partial\varepsilon_z}{\partial z}, \tag{7.24}$$

where $\hat{Q}$ is the atomic quadrupole moment operator ($\hat{Q} = |e|r^2Y_{2m}$, which is the same as for the $E2$ transitions). The energy shift of a state with total angular momentum J is proportional to the atomic quadrupole moment of this state. It is defined as twice the expectation value of the $\hat{Q}$ operator in the stretched state,

$$Q_J = 2\langle J, J_z = J|\hat{Q}|J, J_z = J\rangle. \tag{7.25}$$

Table 7.9: Stable isotopes with nonzero nuclear spin (I) and possible values of total angular momentum $F(\mathbf{F} = \mathbf{I} + \mathbf{J})$ for ground states (GS) and clock states (CS) of Cu, Ag, and Au.

Isotopes	Transition	I	F for GS	F for CS
^{63,65}Cu, ^{197}Au	$^2S_{1/2} - {}^2D_{5/2}$	3/2	1,2	$1, 2, 3, 4$
^{63,65}Cu	$^2S_{1/2} - {}^2D_{3/2}$	3/2	1,2	$0, 1, 2, 3$
^{107,109}Ag	$^2S_{1/2} - {}^2D_{5/2}$	1/2	0,1	2,3

Calculations using the CIPT method for wave functions and the RPA method for the operator give the values $Q_J = 0.431$ a.u. for the $^2D_{5/2}$ clock state of Cu, $Q_J = 0.296$ a.u. for the $^2D_{3/2}$ clock state of Cu, $Q_J = 0.966$ a.u. for the clock state of Ag, and $Q_J = 1.47$ a.u. for the clock state of Au. The quadrupole moments of the ground states of these atoms are zero due to the small value of the total electron angular momentum ($J = 1/2$).

Consider transitions between hyperfine-structure (hfs) components of the ground and clock states with definite values of the total angular momentum F. The quadrupole shift is given by

$$\Delta E_Q = \frac{F_z^2 - F(F+1)}{2F(2F-1)} Q \frac{\partial \varepsilon_z}{\partial z}, \tag{7.26}$$

where F_z is the projection of F. For $F = 3$ and $F_z = \pm 2$, the shift is zero. Note that clock states with $F = 3$ exist for all stable isotopes of all three considered atoms (see Table 7.9). Using these states would lead to a linear Zeeman shift. It cancels out by averaging over the transition frequencies to the states with $F_z = -2$ and $F_z = 2$. For $F_z \neq \pm 2$, the estimations can be done in the following way. On the inner surface of a metallic vacuum chamber, there can be spatial variations of the electrostatic potential of the order of 0.1 V. The typical internal size of a vacuum chamber may be 10 cm. The corresponding Stark shift is $\sim 10^{-7}$ Hz. The electric-field gradient is smaller than 0.1 V/(10 cm)^2. Considering that the factor before the electric-field gradient in Eq. (7.26) is ~ 1 a.u. leads to a negligible quadrupole shift of $\sim 10^{-5}$ Hz.

7.8.2 HYPERFINE STRUCTURE

The atoms considered here all exhibit hyperfine structure in the ground state, in the clock state, and in the excited state addressed in laser cooling. The nuclear spins are given in Table 7.9. The hfs splitting is approximately given by [45]

$$E_{\mathrm{hfs}}(F) = \frac{A}{2}F(F+1) + \frac{B}{2}\{F^2(F+1)^2 + F(F+1)[1-2J(J+1)-2I(I+1)]\}. \quad (7.27)$$

The total angular momentum is $\mathbf{F} = \mathbf{J} + \mathbf{I}$, where I is nuclear spin. A and B are magnetic dipole and electric quadrupole hfs constants, respectively. They are reported in Table 7.5. In addition, for $I = 3/2$ nuclei, there is a small octupole hfs contribution [22, 23]. For example, the hyperfine structure of Au was studied experimentally with high precision in the 1960 s, and was also calculate [54, 55]. The hyperfine splitting between $F = 1, 2$ in the ground state amounts to 6.10 GHz [57]. The splittings in ${}^2D_{5/2}$ are [22]

$F = 1 \leftrightarrow F = 2 : 1.00$ GHz,

$F = 2 \leftrightarrow F = 3 : 0.71$ GHz, and

$F = 3 \leftrightarrow F = 4 : 0.52$ GHz.

The splittings in ${}^2D_{3/2}$ are [23]

$F = 0 \leftrightarrow F = 1 : 1.11$ GHz

$F = 1 \leftrightarrow F = 2 : 1.31$ GHz, and

$F = 2 \leftrightarrow F = 3 : 0.31$ GHz.

The hfs in the ${}^4F$ state has also been studied experimentally [23]. We show these numbers to indicate to experimentalists that one will need to use appropriate repumping lasers or modulators.

References

[1] A. D. Ludlow, M. M. Boyd, J. Ye, E. Peik, and P. O. Schmidt, Rev. Mod. Phys. **87**, 637 (2015).

[2] C. W. Chou, D. B. Hume, J. C. J. Koelemeij, D. J. Wineland, and T. Rosenband, Phys. Rev. Lett. **104**, 070802 (2010).

[3] N. Hinkley, J. A. Sherman, N. B. Phillips, M. Schioppo, N. D. Lemke, K. Beloy, M. Pizzocaro, C. W. Oates, and A. D. Ludlow, Science **341**, 1215 (2013).

[4] K. Beloy, N. Hinkley, N. B. Phillips, J. A. Sherman, M. Schioppo, J. Lehman, A. Feldman, L. M. Hanssen, C. W. Oates, and A. D. Ludlow, Phys. Rev. Lett. **113**, 260801 (2014).

[5] I. Ushijima, M. Takamoto, M. Das, T. Ohkubo, and H. Katori, Nat. Photon. **9**, 185 (2015).

[6] T. L. Nicholson, S. L. Campbell, R. B. Hutson, G. E. Marti, B. J. Bloom, R. L. McNally, W. Zhang, M. D. Barrett, M. S. Safronova, G. F. Strouse, W.L. Tew, and J. Ye, Nat. Commun. **6**, 6896 (2015).

[7] N. Nemitz, T. Ohkubo, M. Takamoto, I. Ushijima, M. Das, N. Ohmae, and H. Katori, Nat. Photon. **10**, 258 (2016).

[8] V. V. Flambaum and V. A. Dzuba, Can. J. Phys. **87**, 25 (2009).

[9] V. A. Dzuba and V. V. Flambaum, Phys. Rev. D **95**, 015019 (2017).

[10] R. Shaniv, R. Ozeri, M. S. Safronova, S. G. Porsev, V. A. Dzuba, V. V. Flambaum, and H. Häffner, Phys. Rev. Lett. **120**, 103202 (2018).

[11] V. A. Dzuba, V. V. Flambaum, M. S. Safronova, S. G. Porsev, T. Pruttivarasin, M. A. Hohensee, and H. Häffner, Nat. Phys. **12**, 465 (2016).

[12] S. Schiller, Phys. Rev. Lett. **98**, 180801 (2007).

[13] J. C. Berengut, V. A. Dzuba, and V. V. Flambaum, Phys. Rev. Lett. **105**, 120801 (2010).

[14] J. C. Berengut, V. A. Dzuba, V. V. Flambaum, and A. Ong, Phys. Rev. A **86**, 022517 (2012).

[15] V. A. Dzuba and V. V. Flambaum, Hyperfine Interact. **236**, 79 (2015).

[16] C. J. Campbell, A. G. Radnaev, A. Kuzmich, V. A. Dzuba, V. V. Flambaum, and A. Derevianko, Phys. Rev. Lett. **108**, 120802 (2012).

[17] T. Rosenband, D. B. Hume, P. O. Schmidt, C. W. Chou, A. Brusch, L. Lorini, W. H. Oskay, R. E. Drullinger, T. M. Fortier, J. E. Stalnaker, S. A. Diddams, W. C. Swann, N. R. Newbury, W. M. Itano, D. J. Wineland, and J. C. Bergquist, Science **319**, 1808 (2008).

[18] Z. Xiang, L. Ben-Quan, L. Ji-Guang, and Z. Hong-Xin, Acta Phys. Sin. **68**, 043101 (2019).

[19] V. A. Dzuba, V. V. Flambaum, and S. Schiller, Phys. Rev. A **98**, 022501 (2018).

[20] C. Sanner, N. Huntemann, R. Lange, C. Tamm, E. Peik, M. S. Safronova, and S. G. Porsev, Nature (London) **567**, 204 (2019).

[21] V. A. Dzuba, V. V. Flambaum, and J. K. Webb, Phys. Rev. A, **59**, 230 (1999).

[22] W. J. Childs and L. S. Goodman, Phys. Rev. **141**, 176 (1966).

[23] A. G. Blachman, D. A. Landman, and A. Lurio, Phys. Rev. **161**, 60(1967)

[24] T. Badr, M. D. Plimmer, P. Juncar, M. E. Himbert, Y. Louyer, and D. J. E. Knight, Phys. Rev. A **74**, 062509 (2006).

[25] V. A. Dzuba, J. C. Berengut, C. Harabati, and V. V. Flambaum, Phys. Rev. A **95**, 012503 (2017).

[26] F. A. Parpia, C. F. Fischer, I. P. Grant, Comput. Phys. Comm. **94**, 249 (1996).

[27] B. G. C. Lackenby, V. A. Dzuba, and V. V. Flambaum, Phys. Rev. A **98**, 022518 (2018).

[28] B. G. C. Lackenby, V. A. Dzuba, and V. V. Flambaum, Phys. Rev. A **99**, 042509 (2019).

[29] B. G. C. Lackenby, V. A. Dzuba, and V. V. Flambaum, Phys. Rev. A **98**, 042512 (2018).

[30] J. Li and V. Dzuba, J. Quantum Spectrosc. Radiat. Transfer **247**, 106943 (2020).

[31] S. O. Allehabi, J. Li, V. A. Dzuba, and V. V. Flambaum, J. Quantum Spectrosc. Radiat. Transfer **253**, 107137 (2020).

[32] W. R. Johnson, and J. Sapirstein, Phys. Rev. Lett. **57**, 1126 (1986).

[33] V. A. Dzuba, V. V. Flambaum, P. G. Silvestrov, and O. P. Sushkov, J. Phys. B **20**, 1399 (1987).

[34] R. Kurucz, Kurucz's Atomic Database, http://kurucz.harvard.edu/atoms/2900/lifemeta2900.dat and http://kurucz.harvard.edu/atoms/4700/gf4700.gam

[35] P. Hannaford, P. L. Larkins, and R. M. Lowe, J. Phys. B **14**, 2321 (1981).

[36] J. Carlsson, P. Jönsson, and L. Sturesson, Z. Phys. D **16**,87 (1990).

[37] P. L. Larkins and P. Hannaford, Z. Phys. D **32**, 167 (1994).

[38] T. Badr, M. D. Plimmer, P. Juncar, M. E. Himbert, J. D. Silver, and G. D. Rovera, Eur. Phys. J. D **31**, 3 (2004).

[39] P. S. Doidge, Spectrochim. Acta, Part B **50**, 209 (1995); **50**, 1421 (1995); **51**, 375 (1996).

[40] M. Kock and J. Richter, Z. Astrophys. **69**, 180 (1968).

[41] W. L. Wiese and G. A. Martin, in *Wavelengths and Transition Probabilities for Atoms and Atomic Ions*, Natl. Stand. Ref. Data Ser. No. NSRDS-68 (Natl. Bureau of Standards, Washington, D.C., 1980), pp. 359–406.

[42] G. Uhlenberg, J. Dirscherl, and H. Walther, Phys. Rev. A **62**, 063404 (2000).

[43] N. Brahms, B. Newman, C. Johnson, T. Greytak, D. Kleppner, and J. Doyle, Phys. Rev. Lett. **101**, 103002 (2008).

[44] P. Schwerdtfeger and J. K. Nagle, Mol. Phys. **117**, 1200 (2019).

[45] L. D. Landau and E. M. Lifshitz, *Quantum Mechanics. Non-relativistic Theory*, 2nd ed. (Pergamon, Oxford, 1965).

[46] V. A. Dzuba, A. Kozlov, and V. V. Flambaum, Phys. Rev. A **89**, 042507 (2014).

[47] V. A. Dzuba, V. V. Flambaum, and M. G. Kozlov, Phys. Rev. A, **54**, 3948 (1996).

[48] S. G. Porsev and A. Derevianko, Phys. Rev. A **74**, 020502(R) (2006); **86**, 029904(E) (2012).

[49] T. Middelmann, S. Falke, C. Lisdat, and U. Sterr, Phys. Rev. Lett. **109**, 263004 (2012).

[50] J. A. Sherman, N. D. Lemke, N. Hinkley, M. Pizzocaro, R. W. Fox, A. D. Ludlow, and C. W. Oates, Phys. Rev. Lett. **108**, 153002 (2012)

[51] J. Tenenbaum, I. Smilanski, S. Gabay, L. A. Levin, G. Erez, and S. Lavi, Opt. Commun. **32**, 473 (1980).

[52] B. K. Ankush and M. N. Deo, J. Quantum Spectrosc. Radiat. Transfer **134**, 21 (2014).

[53] A. Kramida, Yu. Ralchenko, J. Reader, and NIST ASD Team (2018), NIST Atomic Spectra Database (ver. 5.5.2), https:// physics.nist.gov/asd (National Institute of Standards and Technology, Gaithersburg, MD, 2018).

[54] W. M. Itano, J. Res. Natl. Inst. Stand. Technol. **105**, 829 (2000).

[55] J. Bieroń, C. Froese Fischer, P. Indelicato, P. Jönsson, and P. Pyykkö, Phys. Rev. A **79**, 052502 (2009).

[56] V. A. Dzuba, V. V. Flambaum, and M. V. Marchenko, Phys. Rev. A **68**, 022506 (2003).

[57] H. Dahmen and S. Penselin, Z. Phys. **200**, 456(1967).

[58] A. Arvanitaki, J. Huang, and K. Van Tilburg, Phys. Rev. D **91**, 015015 (2015).

[59] K. Van Tilburg, N. Leefer, L. Bougas, and D. Budker, Phys. Rev. Lett. **115**, 011802 (2015).

[60] Y. V. Stadnik and V. V. Flambaum, Phys. Rev. Lett. **115**, 201301 (2015).

[61] M. S. Safronova, S. G. Porsev, C. Sanner, and J. Ye, Phys. Rev. Lett. **120**, 173001 (2018).

[62] V. A. Dzuba and V. V. Flambaum, Phys. Rev. A **77**, 012514 (2008).

[63] V. A. Dzuba and V. V. Flambaum, Phys. Rev. A **77**, 012515 (2008).

[64] A. Golovizin, E. Fedorova, D. Tregubov, D. Sukachev, K. Khabarova, V. Sorokin, N. Kolachevsky, Nat Commun. **10**, 1724 (2019).

[65] Y. Ting and H. Lew, Phys. Rev. **105**, 581 (1957).

Chapter 8

Using optical clock transitions in Cu II and Yb III for timekeeping and search for new physics

8.1 Overview

This chapter considers the prospect of using two nearly neutral ions, Cu II and Yb III, for optical ion clocks. We have performed relativistic many-body calculations for atomic properties relevant to optical clock development. The sensitivity of Yb III to changes in fundamental constants and uncertainty estimates for the Yb III ion indicate that a Yb III atomic clock is likely to compete successfully with the latest generation of clocks.

This study has been published in this paper:

S. O. Allehabi, V. A. Dzuba, and V. V. Flambaum, Using optical clock transitions in Cu II and Yb III for timekeeping and search for new physics, Phys. Rev. A **104**, 053109 (2021).

I presented this work at two international conferences:

1. New optical clocks based on Cu II, Yb III, Hf II, Hf IV, and W VI ions which may be used to search for dark matter and variation of the fine structure constant, **16th workshop on the Dark Side of the Universe, the University of New South Wales, Sydney, Australia, December (2022).**
2. New optical clocks based on Cu II, Yb III, Hf II, Hf IV, and W VI ions which may be used to search for dark matter and variation of the fine structure constant, **24th Australian Institute of Physics Congress, Adelaide Convention Centre, Adelaide, Australia, December (2022).**

8.2 Abstract

We study the $^1S_0 - {}^3D_2$ and $^1S_0 - {}^3D_3$ transitions in Cu II and the $^1S_0 - {}^3P^o_2$ transition in Yb III as possible candidates for the optical clock transitions. A recently developed version of the configuration interaction method, designed for a large number of electrons above the closed-shell core, is used to carry out the calculation. We calculate excitation energies, transition rates, lifetimes, and scalar static polarizabilities of the ground, clock states, and blackbody radiation shift. We demonstrate that the considered transitions have all features of the clock transition leading to prospects of highly accurate measurements. A search for new physics, such as time variation of the fine-structure constant, is also investigated.

8.3 INTRODUCTION

Extremely high accuracy of the frequency measurements for the optical clock transitions naturally lead to the use of the transitions not only for time keeping, but also for the search of the manifestations of new physics beyond the standard model, such as local Lorentz invariance (LLI) violation and time variation of the fine-structure constant $(\alpha = e^2/\hbar c)$ (see, e.g., Refs. [1–8]). Oscillating variation of the fine-structure constant may be produced by interaction of a low-mass scalar dark matter field with a photon field (see, e.g., Refs. [9–13]). Therefore, the measurement of such variation provides an efficient method to search for dark matter using atomic clocks, which have already provided improvement of the constraints on the scalar-photon interaction constants up to 15 orders of magnitude [9–13].

The search for new physics with atomic clocks usually involves measuring the frequencies of two clock transitions against each other over a long period of time. Both transitions must be very narrow and not sensitive to perturbation to allow extremely high accuracy of the measurements. They also must have different sensitivities to new physics so that under the studied effect, frequencies change at different rates and maybe even in different directions. Having both transitions in the same atom brings additional convenience.

The relative uncertainty of the frequency measurements for the best optical clocks is on the level of 10^{-18}. For example, it is 9.4×10^{-19} for Al^+ [4], 3.0×10^{-18} for Yb^+ [6], and 1×10^{-18} for Yb [14]. Unfortunately, most of working optical clocks are not very sensitive to new physics. Among the examples listed above, only Yb^+ clock transition is highly sensitive to a variation of the fine-structure constant [2, 15, 16] and to the LLI violation [3, 17]. Therefore, there is an ongoing search for new clock transitions which may combine high accuracy of the measurements with high sensitivity to new physics, e.g., to the time variation of the fine-structure constant. One way of achieving this is to use highly charged ions [18]. This is now a large area of research with very promising perspectives (see, e.g., Refs. [19–21]).

Neutral or nearly neutral atoms are also considered. The important advantage of using them is that they are very well studied. In some cases, new promising transitions can be found in atoms that are already used for a high accuracy atomic clock. E.g., new transitions in Yb were recently suggested [22, 23] in addition to the currently used $^1S_0 - {}^3P_0^o$ clock transition. Clock transitions between metastable states in Yb II have been suggested in Ref. [24]. A good guide for finding atomic clock transitions sensitive to variations of α is to look for metastable states which are connected to the ground state (GS) via transitions that can be approximately considered as $s-d$, $s-f$, or $p-f$ single-electron transitions [25]. The $s-d$ transitions of this kind were considered in Cu, Ag, and Au atoms in Ref. [26].

In the present paper, we consider the ${}^1S_0 - {}^3D_2$ and ${}^1S_0 - {}^3D_3$ transitions in Cu II and the ${}^1S_0 - {}^3P_2^o$ transition in Yb III (see Figs. 8.1 and 8.2). Transitions in Cu II are the $s - d$ transitions, the transition in Yb III is the $s - f$ transition. In our early work [15], we suggested to use the $4f^{14}\ {}^1S_0 - 4f^{13}5d\ {}^3P_0^o$ in Yb III for the search of the variation of the fine-structure constant. The prospect for precision measurement of the frequency of this transition was considered in a recent paper [27]. However, this transition has an important drawback. There is a decay channel via magnetic dipole transition ($M1$) into the lower-lying state $4f^{13}5d\ {}^3P_1^o$. This may make the considered transition not be sufficiently narrow to ensure high accuracy of the measurements. This problem was not discussed in Refs. [15] or [27]. In the present paper, we consider a different transition, a transition from the ground state to the first excited-state $4f^{13}5d\ {}^3P_2^o$.

This is a very narrow transition with a similar sensitivity to the variation of the fine-structure constant. We demonstrate that it has all features of the atomic clock transition.

Several studies have analyzed the energies and transition probabilities for both ions, Cu II [28–30] and Yb III [31, 32] theoretically and experimentally (see also Ref [33] and references therein). This gives us an opportunity to compare results to have confidence in the accuracy of the analysis. None of the previous studies focused on transitions in Cu II and Yb III in sufficient detail to study their suitability for time keeping and searching for new physics.

8.4 METHOD OF CALCULATION

As can be seen from the spectra of the Cu II and Yb III ions, the excited states of the Cu II ion have an open $3d$ shell, and the excited states of the Yb III ion have an open $4f$ shell. Therefore, to perform the electron structure calculations for both ions, the recent version of the configuration interaction (CI) method was used, which has been designed to deal with a large number of valence electrons [34]. The method combines CI with perturbation theory (PT) and is called the CIPT method. The method reduces the size of the effective

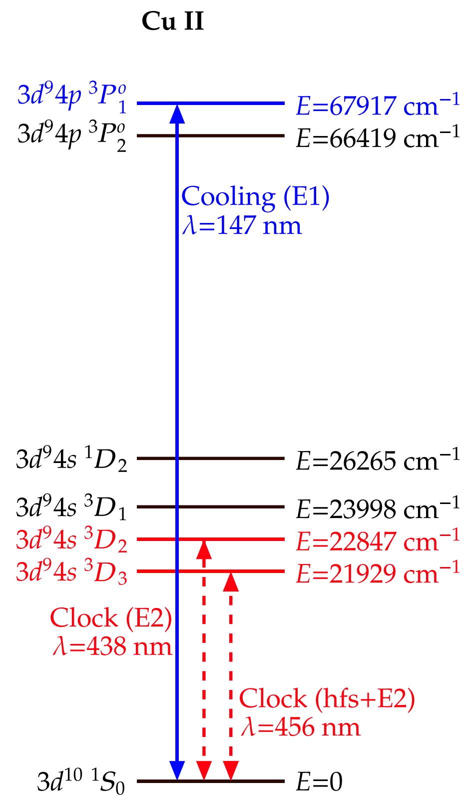

Figure 8.1: The energy diagram for the states of the Cu II ion relevant for the optical ion clock. The electric dipole cooling transition is shown as a solid blue line, and the clock transitions are shown as short-dashed red lines.

CI matrix by neglecting the off-diagonal matrix elements between high-energy basis states and reducing their contribution to PT corrections to the matrix elements between low-energy basis states.

The eigenvalues E and eigenstates ψ can be found by solving the CI equations with the effective H^{CI} matrix,

$$\left(H^{CI} - EI\right)\psi = 0, \tag{8.1}$$

where I is the unit matrix. Matrix elements of the effective CI matrix contain PT-type

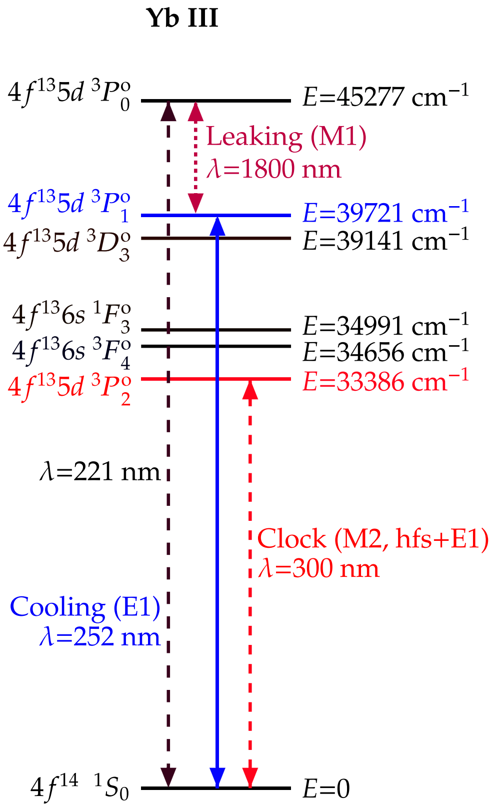

Figure 8.2: The energy diagram for the states of the Yb III ion relevant for the optical ion clock. The electric dipole cooling transition is shown as a solid blue line, the clock transition is shown as a short-dashed red line, and the purple dotted lines show the leakage transition.

corrections from the high-energy states,

$$\langle a|H^{CI}|b\rangle \to \langle a|H^{CI}|b\rangle + \sum_h \frac{\langle a|H^{CI}|h\rangle\langle h|H^{CI}|b\rangle}{E - E_h}. \tag{8.2}$$

Here a and b are low-energy states, and E_h is the diagonal matrix element between high-energy states $\left(E_h = \left\langle h \left| H^{\mathrm{CI}} \right| h \right\rangle\right)$.

To produce a set of complete single-electron basis states for both ions, we start the calculations with the Dirac-HartreeFock (DHF) method in the V^N approximation with all atomic electrons included. It seems to be natural to start from the [Ar]$3d^{10}$ configuration for Cu II and the [Xe]$4f^{14}$ configuration for Yb III. However, such a choice of initial approximation is good for calculating the ground states of the ions. Since we need to calculate excited states as well, which have excitations from the $3d$ or $4f$ subshell, the choice of initial approximation is not obvious, and it is dictated by the accuracy of the final results. It turns out that the best results are obtained if we start from the [Ar]$3d^9 4s$ configuration for Cu II and the [Xe]$4f^{14}$ configuration for Yb III.

The single-electron basis states are then constructed using B splines [35, 36] with $40B$-spline states on the order of $k = 9$ in a box of the radius $R_{\max} = 40a_B$ with orbital angular momentum $0 \leqslant l \leqslant 4$. To carry out the calculations of the transition amplitudes and hyperfine structure (hfs), we use the time-dependent HF method [37], which is equivalent to the random-phase approximation (RPA). The RPA equations can be written as

$$(\hat{H}^{RHF} - \epsilon_c)\delta\psi_c = -(\hat{d} + \delta V^N)\psi_c. \tag{8.3}$$

Here, the relativistic Hartree-Fock is (RHF), $\hat{d}$ refers to the operator of an external field, which can be any field, which is sufficiently weak to be considered in linear approximation. ϵ_c is the energy of electron state c, ψ_c is the state wave function, and δV^N denotes the correction to the self-consistent potential caused by the effect of an external field. Equation (8.3) is solved self-consistently for all states c in the core. As a result, the correction to the core potential δV^N is found. Then reduced matrix elements for valence states are calculated using the expression,

$$A_{b\to a} \equiv \langle\psi_a||\hat{d} + \delta V^N||\psi_b\rangle. \tag{8.4}$$

The electric dipole ($E1$), magnetic dipole ($M1$), electric quadrupole ($E2$), magnetic quadrupole ($M2$), and electric octupole ($E3$) transition probabilities (in atomic units) from upper state b to lower state a can be written as

$$T_{E1,M1} = \frac{4}{3}(\alpha\omega)^3 \frac{A^2_{E1,M1}}{2J_b + 1}, \tag{8.5}$$

$$T_{E2,M2} = \frac{1}{15}(\alpha\omega)^5 \frac{A^2_{E2,M2}}{2J_b+1}, \tag{8.6}$$

$$T_{E3} = 0.00169(\alpha\omega)^7 \frac{A^2_{E3}}{2J_b+1}. \tag{8.7}$$

Here α is the fine-structure constant, ω is the energy difference between the lower and the upper states, A is the transition amplitude (8.4), J_b is the total angular momentum of the upper state b. Note that magnetic amplitudes $A_{M1,M2}$ contain the Bohr magneton μ_B ($\mu_B = \alpha/2 \approx 3.65 \times 10^{-3}$ in atomic units). For some strongly forbidden transitions leading contribution comes from electromagnetic transitions mediated by the hyperfine interaction. Clock transitions in ^{63,65}Cu II and ^{171,173}Yb III are good examples of such transitions. The transition amplitude is

$$A_{\mathrm{hfs}-E1,E2}(b \to a) = \sum_n \left(\frac{\langle a|A_{\mathrm{hfs}}|n\rangle\langle n|A_{E1,E2}|b\rangle}{E_a - E_n} + \frac{\langle b|A_{\mathrm{hfs}}|n\rangle\langle n|A_{E1,E2}|a\rangle}{E_b - E_n} \right). \tag{8.8}$$

Here A_{hfs} is the operator of the magnetic dipole or electric quadrupole hfs interaction, $A_{E1,E2}$ are the operators of the $E1$ and $E2$ transitions. Summation in (8.8) goes over a complete set of intermediate states $|n\rangle$ (for more details, see, e.g., Refs. [29, 38–40]). In practice, it is usually sufficient to include few close states into the summation over n. For example, the leading contribution to the transition amplitude of the $^1S_0 - {}^3D_3$ clock transition in Cu II comes from the electric quadrupole transition mediated by the magnetic dipole hfs interaction. It is sufficient to include three intermediate states into the summation, the $3d^94s$ $^3D_2, {}^1D_2$, and $^3D_1$ states. Then Eq. (8.8) becomes

$$\begin{aligned} A_{\mathrm{hfs}-E2}(3d^94s\ {}^3D_3 \to 3d^{10}\ {}^1S_0) &= \frac{\langle {}^3D_3|A_{\mathrm{hfs}}|{}^3D_2\rangle\langle {}^3D_2|A_{E2}|{}^1S_0\rangle}{E({}^3D_3) - E({}^3D_2)} + \\ \frac{\langle {}^3D_3|A_{\mathrm{hfs}}|{}^1D_2\rangle\langle {}^1D_2|A_{E2}|{}^1S_0\rangle}{E({}^3D_3) - E({}^1D_2)} &+ \frac{\langle {}^3D_3|A_{E2}|{}^3D_1\rangle\langle {}^3D_1|A_{\mathrm{hfs}}|{}^1S_0\rangle}{E({}^1S_0) - E({}^3D_1)} \end{aligned} \tag{8.9}$$

For the ${}^1S_0 - {}^3P_2^o$ transition in the Yb III ion, the hyperfine-induced $E1$ transition amplitude is expressed as

$$A_{\text{hfs}-E1}(4f^{13}5d\ {}^3P_2^o \to 4f^{14}\ {}^1S_0) = \frac{\langle {}^3P_2^o|A_{\text{hfs}}|{}^3P_1^o\rangle\langle {}^3P_1^o|A_{E1}|{}^1S_0\rangle}{E({}^3P_2^o) - E({}^3P_1^o)} \tag{8.10}$$

Transition amplitudes (8.9), (8.10) depend on the values of the total angular momentum F of a specific hfs state ($\mathbf{F} = \mathbf{J} + \mathbf{I}$, where $\mathbf{I}$ is the nuclear spin). Detailed equations can be found in Refs. [29, 38–40]). To find corresponding transition rates, we use Eqs. (8.5) and (8.6), replacing A_{E1} by $A_{\text{hfs}-E1}$ in Eq. (8.5), and A_{E2} by $A_{\text{hfs}-E2}$ in Eq. (8.6).

Radiative lifetimes τ_b of each excited state b can be obtained as

$$\tau_b = 1 \Big/ \sum_a T_{ab}, \tag{8.11}$$

where the summation goes over all possible transitions to lower states a.

Accuracy of the calculations with the use of the CIPT method for complicated atomic systems (open p, d, and f shells) was studied in detail in our previous papers (see, e.g., Refs. [34, 41–44]). It is about a few percent for the energies of low-lying states and about a few tens of percent for the matrix elements. Accuracy tends to go down for higher states due to proximity to the high-energy states, which are treated perturbatively. It is also lower for states of complicated configurations involving more than two single-electron states. This is due to a larger number of possibilities for exciting one or two electrons to different states leading to a very large basis of many-electron states. Only a small fraction of their states are included in the effective CI matrix [Eq. (8.2)], the rest are treated perturbatively. In principle, it is possible to improve the accuracy of calculations by moving the boundary between low- and high-energy states up the energy scale leading to the increased size of the effective CI matrix. However, it is a numerically expensive procedure, requiring large computer power. In the end, the accuracy of present calculations is sufficient for the purposes of present paper, which is checking that studied atomic systems can be used as atomic clocks.

8.5 RESULTS

8.5.1 Energy levels, transition probabilities, and lifetimes.

Table 8.1 presents calculated energy levels and lifetimes of the low-energy states of Cu II and Yb III ions compared with experimental data and other calculations. The lifetimes were calculated using transition probabilities presented in Table 8.2. The results for the energies are in sufficiently good agreement with experimental data from NIST.

The average difference between the NIST and the calculated data for Cu II is $\sim$100 cm^{-1}, whereas for Yb III, the difference is $\sim$4000 cm^{-1}. Note that different sources present different state labeling for Yb III (see, e.g., Refs. [27, 33]). Therefore, for the sake of easy comparison, we present in the table state labeling based on both commonly used schemes, the J-J and L-S schemes.

Table 8.2 presents calculated transition amplitudes and transition rates and compares them to the experimental data and other theoretical values. Lifetimes of the states calculated using transition rates from Table 8.2 are presented in Table 8.1. As can be seen from the tables, the present results for the Cu II ion are in good agreement with the experimental data and other calculations. For the transition between the first excited-state $3d^94s\ ^3D_3$ and the ground state, the dominating contribution comes from the hfs-induced electric quadrupole transition [see Eq. (8.9)]. This transition was studied before in Ref. [29] using the same strategy. The results for two isotopes of Cu are compared in Table 8.3, indicating good agreement. The same table shows hfs-induced transition rates for the clock state (c.s.) of ^{171}Yb and ^{173}Yb.

For the transition rates of the Yb III ion, we compared our results with the theoretical values of Safronova and Safronova [31]. They carried out theoretical calculations using the second-order RMBPT. The results are in reasonably good agreement with our calculations. The most noticeable disagreement is about two times difference in the $M2$ transition rate between the clock and the ground states. Given that hfs-induced $E1$ transition also gives a significant contribution to the transition rate, and this contribution was not considered

Table 8.1: Excitation energies (E, cm^{-1}) and lifetimes (τ) for some low states of Cu II and Yb III ions.

			Energy (cm^{-1})			Lifetime		
				Other			Other	
No.	Conf.	Term	Present	NIST [33]	Cal.	Present	Expt.	Cal.
				Cu II				
1	$3d^{10}$	$^1S_0$	0	0	0	∞		
2	$3d^94s$	$^3D_3$	21932	21929	22469[a]	$\sim 10^8$ s		
3		$^3D_2$	22733	22847	23381[a]	7.8 s		
4		$^3D_1$	23705	23998	24495[a]			
5	$3d^94s$	$^1D_2$	25833	26265	26840[a]			
6	$3d^94p$	$^3P^o_2$	66623	66419	66984[b]			
7		$^3P^o_1$	67922	67917	68703[b]	2.2 ns	2.36 ± 0.05 ns[c]	2.39 ns, 2.21 ns[b]
				Yb III				
1	$4f^{14}$	$^1S_0$	0	0	0	∞		
2	$4f^{13}5d$	$(7/2,3/2)^o_2 \equiv {}^3P^o_2$	29208	33386	39755[d]	$\sim$2000 s[e]		6017 s[d]
3	$4f^{13}5d$	$(7/2,3/2)^o_3 \equiv {}^3D^o_3$	33839	39141	44429[d]			
4	$4f^{13}6s$	$(7/2,1/2)^o_4 \equiv {}^3F^o_4$	35000	34656	36336[d]			
5	$4f^{13}6s$	$(7/2,1/2)^o_3 \equiv {}^1F^o_3$	36418	34991	36764[d]			
6	$4f^{13}5d$	$(7/2,5/2)^o_1 \equiv {}^3P^o_1$	35288	39721	39762[d]	250 ns	230(20) ns[f]	166 ns, 270 ns[f] 181 ns[d]
7	$4f^{13}5d$	$(5/2,5/2)^o_0 \equiv {}^3P^o_0$	41059	45277	49469[d]	0.133 s		0.1490 s[d]

[a] Reference [29].

[b] Reference [30]; for the lifetime, the first value was obtained using the length gauge, and the second was obtained using the velocity gauge.

[c] Reference [28].

[d] Reference [31]; the value was obtained using the relativistic many-body perturbation theory (RMBPT) method.

[e] The $M2$ and hfs- $E1$ transitions are taken into account, see Tables 8.2 and 8.3 for details.

[f] Reference [32]; the first calculated value was obtained using the RHF method + core polarization (CP) effects, and the second calculated value was obtained using the same procedure with including $5s$, $5p$, and $4f$ to the CP effects.

Table 8.2: Transition amplitudes (A, a.u.) and transition probabilities (T, 1/s) evaluated with NIST frequencies for some low states of Cu II and Yb III ions. Semi.≡ Semiempirical.

		(ω), NIST [33]		Present		Other, T (s^{-1})		
Transition	Type	(cm^{-1})	(a.u.)	A (a.u.)	T (s^{-1})	Exp. [28]	Semi. [30]	Cal.
					Cu II			
$2 \leftrightarrow 1$	hfs-E2	21929	0.0999	$\sim 2\times10^{-4}$	$\sim 10^{-8\mathrm{a}}$			
$3 \leftrightarrow 1$	E2	22847	0.1041	0.890	0.110			$0.104, 0.157^{\mathrm{b}}$
$3 \leftrightarrow 2$	M1	918	0.0042	$2.070\mu_B$	1.790×10^{-2}			$1.70\times10^{-2\mathrm{c}}$
$5 \leftrightarrow 1$	E2	26265	0.1197	-2.727	2.080			$1.937, 2.687^{\mathrm{b}}$
$7 \leftrightarrow 1$	E1	67917	0.3095	-0.182	$6.689\times10^{+6}$	$11.3\times10^{+6}$	$8.5\times10^{+6}$	$7.6\times10^{+6}$, $7.7\times10^{+6\mathrm{d}}$
$7 \leftrightarrow 2$	E3	45988	0.2095	-0.346	5.459×10^{-8}			
$7 \leftrightarrow 3$	E1	45069	0.2054	2.489	$3.826\times10^{+8}$	$3.419\times10^{+8}$	$3.474\times10^{+8}$	$3.425\times10^{+8}$, $3.628\times10^{+8\mathrm{d}}$
$7 \leftrightarrow 4$	E1	43918	0.2001	1.097	$6.875\times10^{+7}$	$6.29\times10^{+7}$	$6.35\times10^{+7}$	$6.29\times10^{+7}$, $7.16\times10^{+7\mathrm{d}}$
$7 \leftrightarrow 5$	E1	41652	0.1898	0.379	$7.014\times10^{+6}$	$7.7\times10^{+6}$	$8.5\times10^{+6}$	$6.8\times10^{+6}$, $7.6\times10^{+6\mathrm{d}}$
$7 \leftrightarrow 6$	E2	1498	0.0068	0.656	1.211×10^{-7}			
					Yb III			
$2 \leftrightarrow 1$	M2	33386	0.1521	$5.612\mu_B$	3.895×10^{-4}			$1.662\times10^{-4\mathrm{e}}$
$2 \leftrightarrow 1$	hfs-E1	33386	0.1521	$\sim 10^{-6}$	$\sim 10^{-4\mathrm{a}}$			
$6 \leftrightarrow 1$	E1	39721	0.1810	0.308	$4.015\times10^{+6}$			$5.524\times10^{+6\mathrm{e}}$
$6 \leftrightarrow 2$	M1	6335	0.0289	$1.583\mu_B$	5.726			5.702^{e}
$6 \leftrightarrow 3$	E2	580	0.0026	0.909	2.017×10^{-9}			
$6 \leftrightarrow 5$	E2	4730	0.0216	7.202	4.579×10^{-3}			$3.516\times10^{-2\mathrm{e}}$
$7 \leftrightarrow 2$	E2	11891	0.0542	0.529	7.442×10^{-3}			$5.209\times10^{-3\mathrm{e}}$
$7 \leftrightarrow 6$	M1	5556	0.0253	$1.275\mu_B$	7.523			6.706^{e}

[a] See Table 8.3 for details.

[b] Reference [29]; the first value was obtained using the Babushkin gauge, and the second value was obtained using the Coulomb gauge.

[c] Reference [46].

[d] Reference [30]; the first value was obtained using the length gauge, and the second value was obtained using the velocity gauge.

[e] Reference [31]; the value was obtained using the RMBPT method.

Table 8.3: Rates in s^{-1} for hfs-induced transitions from the clock states of Cu II and Yb III to the ground state.

Isotope	F	This paper	Reference [29]
^{63}Cu II	7/2	8.06×10^{-9}	9.19×10^{-9}
$I = 3/2$, $\mu = 2.2233$	5/2	7.64×10^{-9}	8.72×10^{-9}
	3/2	3.76×10^{-9}	4.29×10^{-9}
^{65}Cu II	7/2	9.25×10^{-9}	1.06×10^{-8}
$I = 3/2$, $\mu = 2.3817$	5/2	8.77×10^{-9}	1.00×10^{-8}
	3/2	4.32×10^{-9}	4.93×10^{-9}
^{171}Yb III	3/2	1.23×10^{-4}	
$I = 1/2$, $\mu = 0.4919$			
^{173}Yb III	7/2	8.41×10^{-5}	
$I = 5/2$, $\mu = -0.6776$	5/2	7.97×10^{-5}	
	3/2	3.92×10^{-5}	

in Ref. [31], the total difference in the lifetime of the clock state is about three times (see Table 8.1).

The data on lifetimes for the states of both ions are presented in Table 8.1. The present results are compared with experimental and other theoretical calculations. For the Yb III ion, Zhang *et al.* [32] have obtained the lifetime result for the $4f^{13}5d^3P_1^0$ state both experimentally and theoretically. They performed the calculations using two variations of the RHF method of Cowan [45], which differ by the ways of inclusion of the CP effect.

8.5.2 Polarizabilities and blackbody radiation shifts

Static scalar polarizability $\alpha_v(0)$ of an atom in state v is given by

$$\alpha_v(0) = \frac{2}{3(2J_v + 1)} \sum_n \frac{A_{vn}^2}{\omega_{vn}}, \tag{8.12}$$

where J_v is the total angular momentum of state v, A_{vn} are the amplitudes (reduced matrix elements) of the electric dipole transitions, ω_{vn} is the frequency of the transition.

Equation (8.12) is valid when all wave-functions v and n are many-electron wave functions of the whole atom. It can also be used to calculate valence contributions to the polarizability if v and n are many-electron wave functions for the valence electrons only. Then, the contribution from core electrons should be calculated separately. For the closed-shell core (or closed-shell atom or ion, such as Cu II or Yb III in the ground state), Eq. (8.12) can be reduced to

$$\alpha_v(0) = \frac{2}{3}\sum_c \langle v|\hat{d}|\delta\psi_c\rangle, \tag{8.13}$$

where $\hat{d}$ is the operator of the electric dipole moment and $\delta\psi_c$ is the RPA correction to the core state c [see Eq. (8.3)]. The summation goes over all states in the core. We neglect the change in the RPA corrections to the core states due to the excitation of an electron from the ground to the upper clock state. This is a small effect which is beyond the accuracy of our calculations.

To calculate the polarizabilities of the clock states, we use the approach developed in Ref. [47] for atoms or ions with open shells. It is based on Eq. (8.12) and the Dalgarno-Lewis method [48], which reduces the summation over the complete set of states to solving a matrix equation (see Ref. [47] for details). This approach treats the $3d$ electrons in Cu II and $4f$ electrons in Yb III as valence electrons. To calculate the contributions of the core electrons below the $3d$ or $4f$ shells, we use Eq. (8.13) in which the summation over the core state is limited to states below $3d$ or $4f$. To minimize the error in the difference between the ground state and the clock state polarizabilities, we use the same approach for both states of both ions.

The results are presented in Table 8.4. Our results for the ground-state polarizabilities are in excellent agreement with previous calculations. The polarizabilities of the excited states of Cu II and Yb III ions are calculated here.

The shift in the frequency of the clock transition due to blackbody radiation (BBR) is given by [51]

$$\delta\nu_{\text{BBR}} = -1.6065 \times 10^{-6} \times T^4 \Delta\alpha(0), \tag{8.14}$$

where T is a temperature (e.g., room-temperature $T = 300$ K), $\Delta\alpha(0) = \alpha_0$ (c.s.) $-$ α_0 (g.s.) is the difference between the clock state and the ground-state polarizabilities. The calculated frequency shifts are presented in Table 8.4. The fractional BBR shifts for our Cu II are close in value to those of Zn: -2.54×10^{-16}, Cd: -2.8×10^{-16} [52], and Cu: -3.4×10^{-16} [26] and smaller than some other atomic clocks, such as Ca [53] and Sr [54] where the fractional BBR shift is at the level of 10^{-15}. As for the BBR shift in the Yb III clock transition, its fractional value of -5.95×10^{-17} is one of the smallest among optical clock transitions.

8.5.3 Zeeman shift and electric quadrupole shift

Clock transition frequencies might be affected by external magnetic and electric fields. Zeeman shift caused by magnetic field strongly depends on whether the atom or ion has a hyperfine structure. Both stable isotopes of copper $\left(^{63}\text{Cu}\text{ and }^{65}\text{Cu}\right)$ have nonzero nuclear spin ($I = 3/2$) and nonzero hfs. On the other hand, five stable isotopes of Yb have zero nuclear spins and in two isotopes, spin is not zero (for ^{171}Yb $I = 1/2$ for ^{173}Yb $I = 5/2$). For atoms with zero nuclear spin, the firstorder Zeeman shift can be avoided by considering transitions between states with $J_z = 0$, whereas the second-order Zeeman shift is small due to the absence of the hfs.

Below we consider isotopes with nonzero nuclear spin, ^{63}Cu and ^{171}Yb.

The linear Zeeman shift is given by

$$\Delta E_{F,F_z} = g_F \mu_B B F_z, \tag{8.15}$$

Table 8.4: Scalar static polarizabilities of the ground states α_0 (g.s.s) and clock states α_0 (c.s.s.) and BBR frequency shifts for the clock transition of ^{63}Cu II and ^{171}Yb III. $\delta \upsilon_{\mathrm{BBR}}/\omega$ is the fractional contribution of the BBR shift; where ω is the clock transition frequency.

	α_0(g.s.s) (a_B^3)		α_0(c.s.s.) (a_B^3)		BBR, (T= 300 K)		
Transition	Present	Other Cal.	Present	$\Delta\alpha(0)$	$\delta\nu_{BBR}$ (Hz)	ω (Hz)	$\delta\nu_{BBR}/\omega$
			Cu II				
$2 \leftrightarrow 1$	5.36	5.36[a]	24.12	18.76	-0.1616	$6.57\times10^{+14}$	-2.46×10^{-16}
$3 \leftrightarrow 1$	5.36	5.36[a]	24.05	18.69	-0.1610	$6.85\times10^{+14}$	-2.35×10^{-16}
			Yb III				
$2 \leftrightarrow 1$	6.39	6.55[b]	13.29	6.90	-0.0595	$1.00\times10^{+15}$	-5.95×10^{-17}

[a] Reference [49].

[b] Reference [50].

where g_F is the g factor of a particular hfs state. It is related to the electron g_J factor by

$$g_F = g_J \langle F, F_z = F, I, J | \hat{J}_z | F, F_z = F, I, J \rangle / F. \tag{8.16}$$

Electron g_J factors have values of $g_3 = 1.32$, $g_2 = 1.16$ for Cu II [33], and $g_2 = 1.46$ for Yb III (calculated value). The linear Zeeman shift can be suppressed by averaging over the transition frequencies with positive and negative F_z.

The second-order Zeeman shift for transition between definite hfs components is strongly dominated by transitions within the same hfs multiplet. Note that in this approximation, the shift is zero for the ground state (because $J = 0$). For the clock states, the shift is given by

$$\delta E_{F,F_z} = \sum_{F'=F\pm1,F'_z} \frac{|\langle F' F'_z IJ | \hat{J}_z | F F_z IJ \rangle x|^2}{\Delta E_{\mathrm{hfs}}(F, F')}, \tag{8.17}$$

where $x = g_J \mu_B B_m$ (in which g_J is electron g factors, μ_B is the electron magnetic moment, and B_m is a magnetic field), and $\Delta E_{\mathrm{hfs}}\left(F, F'\right) = E(FIJ) - E\left(F'IJ\right)$ is the hfs interval. For more details, see Ref. [26].

To calculate this shift, we need to know the hfs of the clock states. We calculated the hfs using the CIPT and RPA methods as described above. The results for magnetic dipole hfs constants A and electric quadrupole hfs constants B are presented in Table 8.5. Using these numbers and Eq. (8.17) we calculate the second-order Zeeman shift for all hfs components of the clock states of the ^{63}Cu II and ^{171}Yb III ions. The results are presented in Table 8.6. The shift is small and only slightly larger than in clock transitions of Cu, Ag, and Au [26]. As in the case considered in Ref. [26], the shift can be further suppressed by taking appropriate combinations of the transition frequencies. It might be even easier here since we need to worry only about suppressing the Zeeman shift for the clock state whereas it is already strongly suppressed for the ground state. The electric quadrupole

Table 8.5: Hyperfine structure constants A and B in (megahertz) of ^{63}Cu II and ^{171}Yb III ions. Nuclear spin I of (^{63}Cu)= 3/2 and I of (^{171}Yb) = 1/2 , nuclear magnetic moment $\mu(^{63}\mathrm{Cu}) = 2.2236(4)\mu_N$ and $\mu(^{171}\mathrm{Yb}) = 0.49367(1)\mu_N$ [55]; nuclear electric quadrupole moment $Q(^{63}\mathrm{Cu}) = -0.220(15)b$ [56] and $Q(^{171}\mathrm{Yb}) = 0$.

No.	Conf.	Term	E (cm^{-1})	hfs A	hfs B
			^{63}Cu II		
1	$3d^94s$	$^3D_3$	21932	-186.46	-1.970
2	$3d^94s$	$^3D_2$	22733	-34.62	-1.097
			^{171}Yb III		
1	$4f^{13}5d$	$^3P^o_2$	29208	-41.46	0

shift is due to the interaction of the atomic quadrupole moment Q with the trapping the electric-field gradient and a corresponding term in the Hamiltonian is

$$H_Q = -\frac{1}{2}\hat{Q}_0 \frac{\partial \mathcal{E}_z}{\partial z}. \tag{8.18}$$

Here z is the quantization axis determined by the externally applied B field. The spherical components of the quadrupole moment operator $\hat{Q}_m = |e|r^2C^{(2)}_m$ are the same as for the electric quadrupole ($E2$) transition. The energy shift of a state with total angular momentum J is proportional to the atomic quadrupole moment of this state. It is defined as twice the expectation value of the spherical component $Q_0 = Q_{zz}/2$ of the quadrupole operator in the stretched state,

$$Q_J = 2\langle J, J_z = J|\hat{Q}_0|J, J_z = J\rangle. \tag{8.19}$$

We calculate the values of Q_J using the CIPT and RPA methods. The results are $Q_3 =$ 0.537 a.u. for the $^3D_3$ clock state of Cu II, $Q_2 = 0.299$ a.u. for the $^3D_2$ clock state of Cu II, $Q_2 = -2.369$ a.u. for the clock state of Yb III. Note that $Q = 0$ for the ground states of both ions because of the zero value of the total angular momentum J.

Table 8.6: Second-order Zeeman shifts E_c [mHz/(μT)^2] for the clock states of ^{171}Yb III and ^{63}Cu II.

			$(\Delta E_c)/B_m^2$		
			^{63}Cu II		^{171}Yb III
No.	F_c	F_{cz}	$^3D_3$	$^3D_2$	$^3P_2^o$
1	1/2	±1/2		9.127	
2	3/2	±1/2	0.8687	−5.967	1.021
3	3/2	±3/2	0.5792	2.107	0.6807
4	5/2	±1/2	−0.3555	−2.265	−1.021
5	5/2	±3/2	−0.1515	−1.360	−0.6807
6	5/2	±5/2	0.2566	0.4478	0.000
7	7/2	±1/2	−0.3087	−0.8957	
8	7/2	±3/2	−0.2436	−0.7464	
9	7/2	±5/2	−0.1134	−0.4478	
10	7/2	±7/2	0.0818	0.000	
11	9/2	±1/2	−0.2045		
12	9/2	±3/2	−0.1841		
13	9/2	±5/2	−0.1432		
14	9/2	±7/2	−0.0818		
15	9/2	±9/2	0.000		

8.5.4 Sensitivity of the clock transitions to variation of the fine-structure constant

Dependence of frequencies of atomic transitions on the fine-structure constant in the vicinity of their physical values can be presented as

$$\omega = \omega_0 + q\left[\left(\frac{\alpha}{\alpha_0}\right)^2 - 1\right] \tag{8.20}$$

where α_0 and ω_0 are the present-day values of the finestructure constant and the frequency of the transition and q are sensitivity coefficients that come from the calculations [15]. When one atomic frequency is measured against another over a long period of time, their relative time change is related to the time change of α by

$$\frac{\dot{\omega}_1}{\omega_1} - \frac{\dot{\omega}_2}{\omega_2} = (K_1 - K_2)\,\frac{\dot{\alpha}}{\alpha}. \tag{8.21}$$

Table 8.7: Sensitivity of clock transitions to the variation of the fine-structure constant (q and $K = 2q/E$) for clock transitions in Cu II and Yb III.

No.	Conf.	Term	$E_{\text{exp.}}(\text{cm}^{-1})$	q (cm^{-1})	K
			Cu II		
1	$3d^9 4s$	$^3D_3$	21929	-4350	-0.40
2	$3d^9 4s$	$^3D_2$	22847	-3700	-0.32
			Yb III		
1	$4f^{13}5d$	$^3P^{\text{o}}_2$	33386	-42750	-2.56

The dimensionless value $K = 2q/\omega$ is usually called the enhancement factor. To calculate q (and K), we run computer codes at two different values of α and calculate the numerical derivative,

$$q = \frac{\omega(\delta) - \omega(-\delta)}{2\delta}, \tag{8.22}$$

where $\delta = (\alpha/\alpha_0)^2 - 1$ [see Eq. 8.20]. The value of δ must be small to ensure linear behavior but sufficiently large to suppress numerical noise. Using $\delta = 0.01$ usually gives accurate results. The calculated values of q and K for clock transitions of Cu II and Yb III are presented in Table 8.7. As one can see, the sensitivity of the clock transitions of Cu II to variation of α is not very high, so they may be used as anchor lines for a comparison with a high-K transition [see Eq. (8.21)]. The sensitivity of the Yb III clock transition is one of the highest among the systems considered so far. It is close to the sensitivities of recently suggested clock transitions in Yb [22] and Au [26] and slightly smaller than the sensitivity of the most sensitive clock transitions in Yb II and Hg II [15].

8.6 CONCLUSION

We have investigated a possibility to use Cu II and Yb III ions as optical ion clocks of high accuracy. Energy levels, lifetimes, transition rates, scalar static polarizabilities of the ground and clock states, and the BBR shifts have been calculated using the CIPT method. We have obtained a good agreement with previous data that are available to compare. Sensitivity to "new physics," such as variation of the fundamental constants has been studied. The uncertainty estimates for the Yb III ion and its high sensitivity to new physics indicate that Yb III atomic clock may successfully compete with the latest generation of clocks.

ACKNOWLEDGMENTS

This work was supported by the Australian Research Council Grants No. DP190100974 and No. DP200100150.

References

[1] Boulder Atomic Clock Optical Network [(BACON) Collaboration], Frequency ratio measurements at 18-digit accuracy using an optical clock network, Nature (London) **591**, 564 (2021).

[2] R. Lange, N. Huntemann, J. M. Rahm, C. Sanner, H. Shao, B. Lipphardt, C. Tamm, S. Weyers, and E. Peik, Improved Limits for Violations of Local Position Invariance from Atomic Clock Comparisons, Phys. Rev. Lett. **126**, 011102 (2021).

[3] C. Sanner, N. Huntemann, R. Lange, C. Tamm, E. Peik, M. S. Safronova, and S. G. Porsev, Optical clock comparison for Lorentz symmetry testing, Nature (London) **567**, 204 (2019).

[4] S. M. Brewer, J.-S. Chen, A. M. Hankin, E. R. Clements, C. W. Chou, D. J. Wineland, D. B. Hume, and D. R. Leibrandt, $^{27}\mathrm{Al}^{+}$ Quantum-Logic Clock with a Systematic Uncertainty below 10^{-18}, Phys. Rev. Lett. **123**, 033201 (2019).

[5] T. Bothwell, D. Kedar1, E. Oelker, J. M Robinson, S. L Bromley, W. L Tew, J. Ye, and C. J Kennedy, JILA SrI optical lattice clock with uncertainty of 2.0×10^{-18}, Metrologia **56**, 065004 (2019).

[6] N. Huntemann, C. Sanner, B. Lipphardt, C. Tamm, and E. Peik, Single-ion Atomic Clock with 3×10^{-18} Systematic Uncertainty, Phys. Rev. Lett. **116**, 063001 (2016).

[7] T. L. Nicholson, S. L. Campbell, R. B. Hutson, G. E. Marti, B. J. Bloom, R. L. McNally, W. Zhang, M. D. Barrett, M. S. Safronova, G. F. Strouse, W. L. Tew, and J. Ye, Systematic evaluation of an atomic clock at $2\times\ 10^{-18}$ total uncertainty, Nat. Commun. **6**, 6896 (2015).

[8] B. J. Bloom, T. L. Nicholson, J. R. Williams, S. L. Campbell, M. Bishof, X. Zhang, W. Zhang, S. L. Bromley, and J. Ye, An optical lattice clock with accuracy and stability at the 10^{-18} level, Nature (London) **506**, 71 (2014).

[9] K. Van Tilburg, N. Leefer, L. Bougas, and D. Budker, Search for Ultralight Scalar Dark Matter with Atomic Spectroscopy, Phys. Rev. Lett. **115**, 011802 (2015).

[10] Y. V. Stadnik and V. V. Flambaum, Can Dark Matter Induce Cosmological Evolution of the Fundamental Constants of Nature? Phys. Rev. Lett. **115**, 201301 (2015).

[11] Y. V. Stadnik and V. V. Flambaum, Improved limits on interactions of low-mass spin-0 dark matter from atomic clock spectroscopy, Phys. Rev. A **94**, 022111 (2016).

[12] A. Hees, J. Guena, M. Abgrall, S. Bize, and P. Wolf, Searching for an Oscillating Massive Scalar Field as a Dark Matter Candidate Using Atomic Hyperfine Frequency Comparisons, Phys. Rev. Lett. **117**, 061301 (2016)

[13] N. Leefer, A. Gerhardus, D. Budker, V. V. Flambaum, and Y. V. Stadnik, Search for the Effect of Massive Bodies on Atomic Spectra and Constraints on Yukawa-Type Interactions of Scalar Particles, Phys. Rev. Lett. **117**, 271601 (2016).

[14] A. D. Ludlow, W. F. McGrew, X. Zhang *et al.*, *Optical Frequency Measurements at 1* $\times$ *10*$^{-18}$ *Uncertainty with Ytterbium Optical Lattice Clocks, Conference on Precision Electromagnetic Measurements (CPEM), Paris, France, JUL 08-13* (IEEE, Piscataway, NJ, 2018).

.

[15] V. V. Flambaum and V. A. Dzuba, Search for variation of the fundamental constants in atomic, molecular, and nuclear spectra, Can. J. Phys. **87**, 25 (2009).

[16] R. M. Godun, P. B. R. Nisbet-Jones, J. M. Jones, S. A. King, L. A. M. Johnson, H. S. Margolis, K. Szymaniec, S. N. Lea, K. Bongs, and P. Gill, Frequency Ratio of Two Optical Clock Transitions in $^{171}\mathrm{Yb}^+$ and Constraints on the Time Variation of Fundamental Constants, Phys. Rev. Lett. **113**, 210801 (2014).

[17] V. A. Dzuba, V. V. Flambaum, M. S. Safronova, S. G. Porsev, T. Pruttivarasin, M. A. Hohensee, and H. Haffner, Strongly enhanced effects of Lorentz symmetry violation in entangled Yb^+ ions, Nat. Phys. **12**, 465 (2016).

[18] J. C. Berengut, V. A. Dzuba, and V. V. Flambaum, Enhanced Laboratory Sensitivity to Variation of the Fine-Structure Constant Using Highly-Charged Ions, Phys. Rev. Lett. **105**, 120801 (2010).

[19] M. S. Safronova, V. A. Dzuba, V. V. Flambaum, U. I. Safronova, S. G. Porsev, and M. G. Kozlov, Highly Charged Ions for Atomic Clocks, Quantum Information, and Search for α variation, Phys. Rev. Lett. **113**, 030801 (2014).

[20] V. A. Dzuba and V. V. Flambaum, Highly charged ions for atomic clocks and search for variation of the fine structure constant, Hyperfine Interact. **236**, 79 (2015).

[21] M. S. Safronova, The Search for Variation of Fundamental Constants with Clocks, Ann. Phys. (Berlin) **531**, 1800364 (2019).

[22] V. A. Dzuba, V. V. Flambaum, and S. Schiller, Testing physics beyond the standard model through additional clock transitions in neutral ytterbium, Phys. Rev. A **98**, 022501 (2018).

[23] M. S. Safronova, S. G. Porsev, C. Sanner, and J. Ye, Two Clock Transitions in Neutral Yb for the Highest Sensitivity to Variations of the Fine-Structure Constant, Phys. Rev. Lett. **120**, 173001 (2018).

[24] S. G. Porsev, V. V. Flambaum, and J. R. Torgerson. Transition frequency shifts with fine-structure constant variation for Yb II, Phys. Rev. A **80**, 042503 (2009).

[25] V. A. Dzuba, V. V. Flambaum, and J. K. Webb, Calculations of the relativistic effects in many-electron atoms and space-time variation of fundamental constants, Phys. Rev. A **59**, 230 (1999).

[26] V. A. Dzuba, S. O. Allehabi, V. V. Flambaum, J. Li, and S. Schiller, Time keeping and searching for new physics using metastable states of Cu, Ag, and Au, Phys. Rev. A **103**, 022822 (2021).

[27] N. Kimura and M. Kajita, Prospect for precision measurement of the Yb^{2+} $^1\mathrm{S}_0-^3\mathrm{P}^o_0$ transition frequency, J. Phys. Soc. Jpn. **90**, 064302 (2021).

[28] E. H. Pinnington, G. Rieger, J. A. Kernahan, and E. Biemont, Beam-laser measurements and relativistic Hartree-Fock calculations of the lifetimes of the $3\mathrm{d}^9 4\mathrm{p}$ levels in Cu II, Can. J. Phys. **75**, 1 (1997).

[29] M. Andersson, K. Yao, R. Hutton, Y. Zou, C. Y. Chen, and T. Brage, Hyperfine-state-dependent lifetimes along the Ni-like isoelectronic sequence, Phys. Rev. A **77**, 042509 (2008).

[30] C. Z. Dong and S. Fritzsche, Relativistic, relaxation, and correlation effects in spectra of Cu II, Phys. Rev. A **72**, 012507 (2005).

[31] U. I. Safronova and M. S. Safronova, Correlation and relativistic effects for the 4f-nl multipole transitions in Yb III ions, Phys. Rev. A **79**, 032511 (2009).

[32] Z. G. Zhang, Z. S. Li, S. Svanberg, P. Palmeri, P. Quinet, and E. Biémont, Experimental and theoretical lifetimes in Yb III, Eur. Phys. J. D **15**, 301 (2001).

[33] A. Kramida, Yu. Ralchenko, J. Reader, and NIST ASD Team (2019). NIST Atomic Spectra Database (ver. 5.7.1), [Online]. Available: https://physics.nist.gov/asd [2020, September 26]. National Institute of Standards and Technology, Gaithersburg, MD.

[34] V. A. Dzuba, J. C. Berengut, C. Harabati, and V. V. Flambaum, Combining configuration interaction with perturbation theory for atoms with a large number of valence electrons, Phys. Rev. A **95**, 012503 (2017).

[35] W. R. Johnson and J. Sapirstein, Computation of Second-Order Many-Body Corrections in Relativistic Atomic Systems, Phys. Rev. Lett. **57**, 1126 (1986).

[36] W. R. Johnson, S. A. Blundell, and J. Sapirstein, Finite basis sets for the Dirac equation constructed from B splines, Phys. Rev. A **37**, 307 (1988).

[37] V. A. Dzuba, V. V. Flambaum, P. G. Silvestrov, and O. P. Sushkov, Correlation potential method for the calculation of energy levels, hyperfine structure and E1 transition amplitudes in atoms with one unpaired electron, J. Phys. B: At. Mol. Phys. **20**, 1399 (1987).

[38] W. R. Johnson, Hyperfine quenching: Review of experiment and theory, Can. J. Phys. **89**, 429 (2011).

[39] S. G. Porsev and A. Derevianko, Hyperfine quenching of the metastable $^3\mathrm{P}_{0,2}$ states in divalent atoms, Phys. Rev. A **69**, 042506 (2004).

[40] V. A. Dzuba and V. V. Flambaum, Hyperfine-induced electric dipole contributions to the electric octupole and magnetic quadrupole atomic clock transitions, Phys. Rev. A **93**, 052517 (2016).

[41] B. G. C. Lackenby, V. A. Dzuba, and V. V. Flambaum, Calculation of atomic spectra and transition amplitudes for the superheavy element Db (Z = 105), Phys. Rev. A **98**, 022518 (2018).

[42] J. G. Li and V. Dzuba, Theoretical study of the spectroscopic properties of mendelevium (Z = 101), J. Quant. Spectrosc. Radiat. Trans. **247**, 106943 (2020).

[43] B. G. C. Lackenby, V. A. Dzuba, and V. V. Flambaum, Atomic structure calculations of superheavy noble element oganesson (Z=118), Phys. Rev. A **98**, 042512 (2018).

[44] B. G. C. Lackenby, V. A. Dzuba, and V. V. Flambaum, Theoretical study of the electron structure of superheavy elements with an open 6d shell: Sg, Bh, Hs, and Mt, Phys. Rev. A **99**, 042509 (2019).

[45] R. D. Cowan, *The Theory of Atomic Structure and Spectra* (University of California Press, Berkeley, CA, 1981).

[46] R. H. Garstang, Transition Probabilities of Forbidden Lines, J. Res. Nat. Bur. Stand. A. Phys. Chem. **68A**, 61 (1964).

[47] V. Dzuba, Calculation of Polarizabilities for Atoms with Open Shells, Symmetry, **12**, 1950 (2020).

[48] A. Dalgarno and J. T. Lewis, The exact calculation of longrange forces between atoms by perturbation theory, Proc. R. Soc. London A **233**, 70 (1955).

[49] W. R. Johnson, D. Kolb, and K. Huang, Electric-dipole, quadrupole, and magnetic-dipole susceptibilities and shielding factors for closed-shell ions of the He, Ne, Ar, Ni (Cu^+), Kr, Pb, and Xe isoelectronic, At. Data Nucl. Data Tables **28**, 333 (1983).

[50] S. Harder, D. Naglav, P. Schwerdtfeger, I. Nowik, and R. H. Herber, Metal atom dynamics in superbulky metallocenes: A comparison of $(\mathrm{Cp}^{\mathrm{BIG}})_2\mathrm{Sn}$ and $(\mathrm{Cp}^{\mathrm{BIG}})_2\mathrm{Eu}$, Inorg. Chem. **53**, 2188 (2014).

[51] S. G. Porsev and A. Derevianko, Multipolar theory of blackbody radiation shift of atomic energy levels and its implications for optical lattice clocks, Phy. Rev. A **74**, 020502(R) (2006); **86**, 029904(E) (2012).

[52] V. A. Dzuba and A. Derevianko, Blackbody radiation shift for the $^1\mathrm{S}_0$-$^3\mathrm{P}_0$ optical clock transition in zinc and cadmium atoms, J. Phys. B: At., Mol. Opt. Phys. **52**, 215005 (2019).

[53] G. Wilpers, C. W. Oates, S. A. Diddams *et al.*, Absolute frequency measurement of the neutral ^{40}Ca optical frequency standard at 657 nm based on microkelvin atoms, Metrologia **44**, 146 (2007).

[54] S. Blatt, A. D. Ludlow, G. K. Campbell, J. W. Thomsen, T. Zelevinsky, M. M. Boyd, J. Ye, X. Baillard, M. Fouché, R. Le Targat, A. Brusch, P. Lemonde, M. Takamoto, F.-L. Hong, H. Katori, and V. V. Flambaum, New Limits on Coupling of Fundamental Constants to Gravity Using ^{87}Sr Optical Lattice Clocks, Phys. Rev. Lett. **100**, 140801 (2008)

[55] N. J. Stone, Table of nuclear magnetic dipole and electric quadrupole moments, At. Data Nucl. Data Tables **90**, 75 (2005).

[56] N. J. Stone, Table of nuclear electric quadrupole moments, At. Data Nucl. Data Tables **111-112**, 1 (2016).

Chapter 9

Atomic clocks highly sensitive to the variation of the fine-structure constant based on Hf II, Hf IV, and W VI ions

9.1 Overview

In this chapter, we continue the search for promising atomic clock candidates by studying Hf II, Hf IV, and W VI ions. According to our results, the metastable states in these ions possess all of the properties of atomic clock transitions, which include their long-term stability and insensitivity to perturbations, which may differentiate them from other atomic states. We found that the sensitivity coefficient to the α variation of the atomic optical clock is among the highest in all operating or prospective atomic optical clocks. A significant advantage also of these systems is the existence of a sufficiently large number of stable isotopes, making possible the use of the isotopes in the search for nonlinearities of the King plot.

This study has been published in this paper:

S. O. Allehabi, V. A. Dzuba, and V. V. Flambaum, Atomic clocks highly sensitive to the variation of the fine structure constant based on Hf ii, Hf iv, and W vi ions, Phys. Rev. A **106**, 032807 (2022).

I presented this work at two international conferences:

1. New optical clocks based on Cu II, Yb III, Hf II, Hf IV, and W VI ions which may be used to search for dark matter and variation of the fine structure constant, **16th workshop on the Dark Side of the Universe, the University of New South Wales, Sydney, Australia, December (2022).**
2. New optical clocks based on Cu II, Yb III, Hf II, Hf IV, and W VI ions which may be used to search for dark matter and variation of the fine structure constant, **24th Australian Institute of Physics Congress, Adelaide Convention Centre, Adelaide, Australia, December (2022).**

9.2 Abstract

We demonstrate that several metastable excited states in Hf II, Hf IV, and W VI ions may be good clock states since they are sufficiently long-living and are not sensitive to the perturbations. The cooling electric dipole ($E1$) transition is available for Hf II, while sympathetic cooling is possible for Hf IV and W VI using Ca^+ or Sr^+ ions. Energy levels; Landé g factors; transition amplitudes for electric dipole ($E1$), electric quadrupole ($E2$), and magnetic dipole (M1) transitions; lifetimes; and electric quadrupole moments for Hf II, Hf IV, and W VI ions are investigated using a combination of several methods of relativistic many-body calculations including the configuration interaction (CI), linearized coupled-cluster single-doubles (SD), and many-body perturbation theory (CI + SD), and also the configuration interaction with perturbation theory (CIPT). Scalar polarizabilities of the ground states and the clock states have been calculated to determine the blackbody

radiation (BBR) shifts. We have found that the relative BBR shifts for these transitions range between 10^{-16} and 10^{-18}. A linear combination of two clock transition frequencies allows one to further suppress BBR. Several $5d$-$6s$ single-electron clock transitions ensure high sensitivity of the transition frequencies to the variation of the fine-structure constant α and may be used to search for dark matter producing this variation of α. The enhancement coefficient for the α variation reaches $K = 8.3$. Six stable isotopes of Hf and five stable isotopes in W allow one to make King plots and study its nonlinearities in order to put limits on the new interactions mediated by scalar particles or other mechanisms.

9.3 INTRODUCTION

Atomic clocks possess a high degree of accuracy, allowing them to be used for a wide variety of scientific and industrial applications. In recent years, the optical lattice atomic clock and the ion clock both have been significantly enhanced to achieve uncertainties or stabilities of 10^{-18} [1–8].

Due to the high accuracy of the frequency measurement of optical clock transitions, these transitions can be used not only to ensure timekeeping but also to search for new physics, such as local Lorentz invariance violation, time variation of the fundamental constants ($\alpha = e^2/\hbar c$), and other phenomena which go beyond the standard model (see, e.g., Refs. [1, 3, 6, 7, 9–14]).

Most of operating optical clocks use the $^1S_0$ to $^3P_0$ transition between states of the $ns^2_{1/2}$ and $ns_{1/2}np_{1/2}$ configurations. These transitions have low sensitivity to variation of the finestructure constant [15, 16]. It was shown in Ref. [12, 13] that maximum sensitivity to the α variation corresponds to the maximum change in the total angular momentum j of the equivalent single-electron transitions. However, the abovementioned transitions are the $ns_{1/2}$ to $np_{1/2}$ transitions with $\Delta j = 0$. It was suggested in Refs. [12, 13, 17] to use transitions between states of different configurations. The most prominent example of this kind among operating optical clocks is the clock based on the Yb$^+$ ion, in which the $4f_{7/2}$-

$6s_{1/2}$ and $6s_{1/2}$-$5d_{5/2}$ transitions are used for timekeeping and constraining of the time variation of the fine-structure constant [18–20]. A number of the promising transitions were studied in earlier works [17, 21–23]. In the present paper we continue the search for promising candidates and study the s-d and $d_{3/2}$-$d_{5/2}$ clock transitions in Hf II, Hf IV, and W VI. An important advantage of these systems is the existence of a sufficiently large number of stable isotopes of Hf and W. Hf has six stable isotopes, including four isotopes with zero nuclear spin (this includes a long-living ^{174}Hf isotope with a lifetime of $\sim 2 \times 10^{15}$ years and a natural abundance of 0.16%). W has five stable isotopes with three zero nuclear spin isotopes. This allows the use of the isotopes in the search for nonlinearities of the King plot. The minimal requirements for this include having four stable isotopes and two transitions where high accuracy of the measurements is possible. This is the case for both Hf and W. The study of the nonlinearity may help to obtain information on nuclear structure and put constraints on new interactions mediated by scalar particles [24, 25]. In addition, the Hf II ion has three metastable states, making it possible to construct two independent combinations of the frequencies of the clock transitions with suppressed blackbody radiation shift. Measuring one such combined frequency against the other over a long period of time is a highly sensitive tool for the search of the time variation of the fine-structure constant.

We provide a detailed analysis of the electronic characteristics of certain low-lying states of these systems. We use the CI + SD (configuration interaction with single-double coupled-cluster [26]) and the CIPT (configuration interaction with perturbation theory [27]) methods for our calculations. Our studies investigate the energy levels; Landé g factors; transition amplitudes; $E1$, $M1$, and $E2$ transitions for the low-lying states; lifetimes; and quadrupole moments. Using the technique described in Ref. [28], we also calculate the scalar polarizabilities of the ground and excited clock states in order to determine the blackbody radiation (BBR) shifts. The sensitivity to the variation of the fine-structure constant is estimated by calculating excitation energies with different values of α in the computer codes. We demonstrate that the considered clocks are good candidates for very accurate timekeeping and are sensitive to new physics.

9.4 METHOD OF CALCULATION

9.4.1 Calculation of energy levels

The Hf II, Hf IV, W VI ions have similar electron structure with the $[1s^2, \ldots, 5s^2 5p^6 4f^{14}]$ closed-shell core and three valence electrons in Hf II and one valence electron in Hf IV and W VI. The calculations are performed by combining the configuration interaction (CI) technique with the linearized single-double coupled-cluster (SD) method, as described in Ref. [26]. We start with the relativistic Hartree-Fock (RHF) calculations for the closed-shell core, which corresponds to the V^{N-M} approximation [29]. Here N is the total number of electrons in an atom or ion, and M is the number of valence electrons ($M = 3$ for Hf II and $M = 1$ for Hf IV and W VI). The RHF Hamiltonian has the following form:

$$\hat{H}^{\mathrm{RHF}} = c\boldsymbol{\alpha} \cdot \boldsymbol{p} + (\beta - 1)mc^2 + V_{\mathrm{nuc}}\,(r) + V_{\mathrm{core}}\,(r), \tag{9.1}$$

where c is the speed of light, $\boldsymbol{\alpha}$ and β are the Dirac matrices, $\boldsymbol{p}$ is the electron momentum, m is the electron mass, V_{nuc} is the nuclear potential obtained by integrating the Fermi distribution of nuclear charge density, and $V_{\mathrm{core}}\,(r)$ is the self-consistent RHF potential created by the electrons of the closed-shell core.

The B-spline method is used to construct the set of singleelectron basis states [30,31]. The states are defined as linear combinations of B-splines which are eigenstates of the RHF Hamiltonian(9.1). Forty B-splines of the order 9 are calculated within a box of radius $R_{\max} = 40a_B$ (where a_B represents Bohr's radius) and an orbital angular momentum of $0 \leqslant l \leqslant 6$. It was found that this choice of parameters leads to the basis which is sufficiently saturated for the low-lying states of interest. Further increase in the values of $l_{\max}$ and $R_{\max}$ and the number of B-splines leads to negligible change in the results. The basis states are used for solving the linearized SD equations and for generating the many-electron states for CI calculations.

The SD equations for the core have the following form [26, 32]

$$\begin{aligned}
&(\epsilon_a-\epsilon_m)\rho_{ma}=\sum_{bn}\tilde{g}_{mban}\rho_{nb}+\sum_{bnr}g_{mbnr}\tilde{\rho}_{nrab}-\sum_{bcn}g_{bcan}\tilde{\rho}_{mnbc},\\
&(\epsilon_a+\epsilon_b-\epsilon_m-\epsilon_n)\rho_{mnab}=g_{mnab}+\sum_{cd}g_{cdab}\rho_{mncd}+\sum_{rs}g_{mnrs}\rho_{rsab} \qquad (9.2)\\
&+\sum_{r}g_{mnrb}\rho_{ra}-\sum_{c}g_{cnab}\rho_{mc}+\sum_{rc}\tilde{g}_{cnrb}\tilde{\rho}_{mrac}+\sum_{r}g_{nmra}\rho_{rb}\\
&-\sum_{c}g_{cmba}\rho_{nc}+\sum_{rc}\tilde{g}_{cmra}\tilde{\rho}_{nrbc}
\end{aligned}$$

Here parameters g are Coulomb integrals,

$$g_{\mathrm{mnab}}=\iint\psi_m^{\dagger}(r_1)\,\psi_n^{\dagger}(r_2)\,\frac{e^2}{r_{12}}\psi_a(r_1)\,\psi_b(r_2)\,d\mathbf{r}_1d\mathbf{r}_2,$$

and parameters ϵ are the single-electron Hartree-Fock energies. The coefficients ρ_{ma} and ρ_{mnab} are the expansion coefficients for the atomic wave function which are to be found by solving the equations iteratively.

The tilde above g or ρ means the sum of direct and exchange terms, e.g.,

$$\tilde{\rho}_{nrbc}=\rho_{nrbc}-\rho_{nrcb}.$$

Indexes a, b, and c numerate states in the atomic core; indexes m, n, r, and s numerate states above the core; and indexes i and j numerate any state.

The SD equations for valence states are obtained from Eq.(9.2) by replacing the core index a by the valence index v, removing the term $\sum_r g_{mnrb}\rho_{rv}$ which has only valence excitations, and replacing ϵ_a by ϵ_0. The energy parameter ϵ_0 is fixed and relates to the valence state of interest. It is convenient to introduce the correlation operators $\hat{\Sigma}_1$ and $\hat{\Sigma}_2$, which describe the correlation interaction of external electrons with the core. Using the SD equations for valence states one can write

$$\langle v|\hat{\Sigma}_1|m\rangle=(\epsilon_0-\epsilon_m)\rho_{mv} \qquad (9.3)$$

and

$$\begin{aligned}
q_{mnvw} &= g_{mnvw} + \sum_{cd} g_{cdvw}\rho_{mncd} - \sum_{c}\left(g_{cnvw}\rho_{mc} + g_{cmwv}\rho_{nc}\right) \\
&+ \sum_{rc}\left(g_{cnrw}\tilde{\rho}_{mrvc} + g_{cmrv}\tilde{\rho}_{nrwc} + g_{cnwr}\rho_{mrvc} + g_{cmvr}\rho_{nrwc}\right. \\
&\left.-g_{cmwr}\rho_{nrcv} - g_{cnvr}\rho_{mrcw}\right) \\
&\equiv g_{mnvw} + \langle mn|\hat{\Sigma}_2|vw\rangle
\end{aligned} \tag{9.4}$$

The one-electron Σ_1 operator represents the correlation interaction between valence electrons and electrons in the core [33]. The two-electron Σ_2 operator is interpreted as the screening of Coulomb interaction between valence electrons by core electrons [34].

The CI Hamiltonian with the Σ_1 and Σ_2 operators included is

$$\hat{H}^{\text{eff}} = \sum_{i=1}^{M}\left(\hat{H}^{\text{RHF}} + \Sigma_1\right)_i + \sum_{i<j}^{M}\left(\frac{e^2}{|r_i - r_j|} + \Sigma_{2ij}\right). \tag{9.5}$$

Here summation goes over valance electrons, i and j numerate valence electrons, and e is the electron charge. The size of the CI matrix is huge if the number of valence electrons is large ($M \geqslant 3$). In calculations for Hf II we use the CIPT technique [27] for dramatic increase of the efficiency of the calculations at the cost of very little sacrifice in the accuracy of the results. This is achieved by constructing the CI matrix for the N_{eff} 's lowest (on the energy scale) many-electron basis state and treating the other states perturbatively. The CI matrix in the CIPT method has the form

$$\langle i|H^{\text{CI}}|j\rangle \to \langle i|H^{\text{CI}}|j\rangle + \sum_{k}\frac{\langle i|H^{\text{CI}}|k\rangle\langle k|H^{\text{CI}}|j\rangle}{E - E_k}. \tag{9.6}$$

Here $i, j \leqslant N_{\text{eff}},\ N_{\text{eff}} < k \leqslant N_{\text{total}},\ E_k = \left\langle k\left|H^{\text{CI}}\right|k\right\rangle$, and E is the energy of the state of interest. Since $N_{\text{eff}} \ll N_{\text{total}}$ the task of matrix diagonalization is significantly simplified (see Ref. [27] for details).

The Landé g factors for low-lying states are investigated in all systems. These factors are calculated as expectation values of the magnetic dipole ($M1$) operator and are compared with the nonrelativistic expression

$$g(J,L,S) = 1 + \frac{J(J+1) - L(L+1) + S(S+1)}{2J(J+1)}, \tag{9.7}$$

where S is the total spin and L is the total angular momentum for the valence electrons, and J is the corresponding total momentum ($J = L + S$). This comparison of g factors helps in the level identification.

9.4.2 Calculation of transition amplitudes and lifetimes

The time-dependent Hartree-Fock (TDHF) method [which corresponds to the well-known random-phase approximation (RPA)] is used to compute transition amplitudes. The RPA equation for the core can be written as

$$\left(\hat{H}^{\mathrm{RHF}} - \epsilon_c\right) \delta\psi_c = -\left(\hat{f} + \delta V^f_{\mathrm{core}}\right) \psi_c. \tag{9.8}$$

The operator $\hat{f}$ refers to an external field. The index c denotes single-electron states in the core, ψ_c is a single-electron wave function, $\delta\psi_c$ is a correction to the state c due to an external field, and $\delta V^f_{\mathrm{core}}$ is the correction to the self-consistent RHF potential caused by the change of all core states in the external field (see, e.g., Ref. [33]). The RPA equations (9.8) is solved selfconsistently for all states in the core. The transition amplitudes are found by calculating matrix elements between states a and b by the formula

$$A_{ab} = \left\langle b \left| \hat{f} + \delta V^f_{\mathrm{core}} \right| .a \right\rangle \tag{9.9}$$

Here, $|a\rangle$ and $|b\rangle$ are the many-electron wave functions calculated with the CI method described above.

In this study, electric dipole ($E1$), electric quadrupole ($E2$), and magnetic dipole ($M1$) rates are taken into account, and they are calculated according to the following equations (in atomic units):

$$(T_{ab})_{E1,M1} = \frac{4}{3}(\alpha\omega)^3 \frac{(A_{ab}^2)_{E1,M1}}{2J_b+1}, \tag{9.10}$$

$$(T_{ab})_{E2} = \frac{1}{15}(\alpha\omega)^5 \frac{(A_{ab}^2)_{E2}}{2J_b+1}. \tag{9.11}$$

Here α is the fine-structure constant $\left(\alpha \approx \frac{1}{137}\right), \omega_{ab}$ is the frequency of the transition, A_{ab} is the transition amplitude (9.9), and J_b is the total angular momentum of the upper state b. Note that magnetic amplitudes $(A_{ab})_{M1}$ contain the Bohr magneton μ_B ($\mu_B = \alpha/2 \approx 3.65 \times 10^{-3}$ in atomic units).

The lifetimes τ_b of each excited state b, expressed in seconds, can be found as follows:

$$\tau_b = 2.41 \times 10^{-17} \Big/ \sum_a T_{ab} \tag{9.12}$$

where the summation goes over all possible transitions to lower states a.

9.5 RESULTS

9.5.1 Energy levels, Landé *g* factors, transition amplitudes, and lifetimes

The results for energy levels, *g* factors, and lifetimes of low-lying states of Hf II, Hf IV, and W VI are presented in Table 9.1 and compared with available experimental data. The data in the table indicate excellent agreement between theory and experiment. In most states, the deviations of the calculated energies from the observed values are within 1000 cm^{-1}. The agreement is also good between calculated and experimental *g* factors of Hf II, where experimental data are available. This is important for correct identification of the states. One noticeable exemption refers to states 12 and 13 where the difference between theory and experiment is significant. These states have the same parity and total momentum J, and the energy interval between them is small ($\sim$1000 cm^{-1}). This means that the states are strongly mixed. Note that the sums of the theoretical and experimental g factors of these states are very close. This indicates that the two-level mixing approximation works very well for this pair of states. In principle, mixing coefficients can be corrected using experimental g factors. See the discussion of the sensitivity of the clock states to the variation of the fine-structure constant (Sec. 9.5.4).

Table 9.1 presents one odd state for each ion. These are the lowest odd states which are connected to the ground state by the electric dipole ($E1$) transition. These transitions can be used for cooling, at least in principle. However, the only transition in the Hf II ion is in the ultraviolet region (wavelength is 356 nm), where lasers are available. A more realistic option for Hf IV and W VI ions is to use sympathetic cooling [36, 37]. It is done by co-trapping the ions with other ions (which are called "logic" ions) with a close charge-to-mass ratio for which laser cooling is possible. The Ca$^+$ ion seems to be a good logic ion for W VI, while either Ca$^+$ or Sr$^+$ can be used for Hf IV.

Our results for transition amplitudes and transition probabilities, together with experimental data and earlier calculated results, where available, are shown in Table 9.2. We consider only those low-lying states which are connected to clock or cooling states through electric dipole ($E1$), magnetic dipole ($M1$), or electric quadrupole ($E2$) transitions. Comparing our results on the transition rates with those from previous studies, we find good agreement. Note that experimental values of the frequencies from the NIST database have been used to calculate transition probabilities.

Table 9.1: Excitation energies (E), Landé g-factors, and lifetimes (τ) for the first excited states of Hf II, Hf IV and W VI. Possible clock states are indicated by bold state numbers. Odd states can be used for cooling.

				E (cm^{-1})		g factor		τ	
No.	Conf.	Term	J	Present	Expt.	Present	NIST [35]	Present	Ref.
		Hf II			[35]				[39]$_{\mathrm{Expt.}}$
1	$5d6s^2$	^{2}D	3/2	0	0	0.793	0.787		
2	$5d6s^2$	^{2}D	5/2	3054	3050.88	1.175	1.173	3.23 s	
3	$5d^26s$	^{4}F	3/2	3578	3644.65	0.415	0.425	66.6 s	
4	$5d^26s$	^{4}F	5/2	4312	4904.85	1.055	1.052	9.7 s	
5	$5d^26s$	^{4}P	1/2	11675	11951.70	2.653	2.598		
6	$5d^26s$	^{2}F	5/2	11783	12070.46	0.901	0.964		
7	$5d^26s$	^{4}P	3/2	11781	12920.94	1.694	1.664		
8	$5d^26s$	^{4}P	5/2	12581	13485.56	1.467	1.410		
9	$5d^26s$	^{2}D	3/2	13836	14359.42	1.075	1.034		
10	$5d^26s$	^{2}P	1/2	13995	15254.29	0.690	0.737		
11	$5d^26s$	^{2}D	5/2	17352	17368.87	1.200	1.273		
12	$5d^26s$	^{2}P	3/2	17199	17830.34	0.670	1.122		
13	$5d^3$	^{4}F	3/2	18528	18897.64	0.839	0.446		
14	$5d^3$	^{4}F	5/2	18284	20134.94	1.118	1.030		

Continued on next page

Table 9.1 – continued

				E (cm^{-1})		g factor		τ	
No.	Conf.	Term	J	Present	Expt.	Present	NIST [35]	Present	Ref.
15	$5d^3$	^{4}P	1/2	24773	26996.51	2.610	2.58		
16	$5d^3$	^{4}P	3/2	25797	27285.13	1.697	1.643		
17	$5d6s6p$	^{4}F^o	3/2	28580	28068.79	0.516	0.512	40.3 ns	39.4± 0.2 ns
		Hf IV			[38]				
1	$5d$	^{2}D	3/2	0	0	0.800			
2	$5d$	^{2}D	5/2	4721	4692	1.200		0.90 s	
3	$6s$	^{2}S	1/2	17530	18380	2.000		0.321 s	
4	$6p$	^{2}P^o	1/2	66611	67039	0.667		0.78 ns	
		W VI			[35]				[40]$_{\text{Theo.}}$
1	$5d$	^{2}D	3/2	0	0	0.800			
2	$5d$	^{2}D	5/2	8726	8709.3	1.200		0.14 s	0.14 s
3	$6s$	^{2}S	1/2	78316	79431.3	2.000			
4	$6p$	^{2}P^o	1/2	146912	147553.1	0.667		0.18 ns	0.184 ns

Based on the transition rates displayed in Table 9.2., we derived the lifetimes of the excited states (clock and cooling states) of all the atomic systems using Eq. (9.12) and we present them in Table 9.1. The lifetimes of the states presented in the table were calculated with taking into account all possible transitions to lower states. The results show consistency with previous studies.

Table 9.2: Transition amplitudes (A, in a.u.) and transition probabilities (T, in s^{-1}) evaluated with NIST frequencies for some low states. 5.67[−3] means 5.67×10^{-3}, etc.

		ω, NIST [35]		Present		Ref.
Transition	Type	(cm^{-1})	(a.u.)	A (a.u.)	T (s^{-1})	T (s^{-1})
		Hf II				[39]$_{\text{Expt.}}$
2-1	M1	3050.88	0.0139	5.67[−3]	0.309	
2-1	E2	3050.88	0.0139	−0.309	4.697[−7]	
3-1	M1	3644.65	0.0166	−7.49[−4]	1.375[−2]	
3-1	E2	3644.65	0.0166	0.265	1.259[−6]	
3-2	M1	593.7	0.0027	3.53[−3]	1.318[−3]	
3-2	E2	593.7	0.0027	0.341	0.241[−9]	
4-1	M1	4904.85	0.0223	−7.54[−4]	2.261[−2]	
4-1	E2	4904.85	0.0223	−0.420	9.325[−6]	
4-2	M1	1853.97	0.0084	−1.63[−3]	5.743[−3]	
4-2	E2	1853.97	0.0084	−0.259	2.734[−8]	
4-3	M1	1260.2	0.0057	1.05[−2]	7.497[−2]	
4-3	E2	1260.2	0.0057	1.56	1.439[−7]	
17-1	E1	28068.79	0.1279	1.200	16.11[6]	17.6[6] ± 0.9
17-2	E1	25017.91	0.1140	−0.068	3.674[4]	
17-3	E1	24424.14	0.1113	1.024	7.728[6]	7.0[6] ± 0.4
17-4	E1	23163.94	0.1055	0.016	1.660[3]	
17-5	E1	16117.09	0.0734	0.068	9.712[3]	2.1[4] ± 0.003
17-6	E1	15998.33	0.0729	0.522	0.565[6]	0.50[6] ± 0.09

Continued on next page

Table 9.2 – continued

		ω, NIST [35]		Present		Ref.
Transition	Type	(cm^{-1})	(a.u.)	A (a.u.)	T (s^{-1})	T (s^{-1})
17-7	E1	15147.85	0.0690	0.110	0.021[6]	
17-8	E1	14583.23	0.0664	0.128	0.026[6]	0.060[6] ± 0.011
17-9	E1	13709.37	0.0625	0.030	0.012[5]	
17-10	E1	12814.5	0.0584	−0.301	0.096[6]	0.054[6] ± 0.011
17-11	E1	10699.92	0.0488	0.224	0.031[6]	
17-12	E1	10238.45	0.0466	0.517	0.145[6]	
17-13	E1	9171.15	0.0418	0.342	0.046[6]	0.081[6] ± 0.019
17-14	E1	7933.85	0.0361	−0.265	0.018[6]	
17-15	E1	1072.28	0.0049	−0.069	2.964	
17-16	E1	783.66	0.0036	0.023	0.127	
		Hf IV				
2-1	M1	4692	0.0214	−5.66[−3]	1.115	
2-1	E2	4692	0.0214	−2.43	2.501[−4]	
3-1	M1	18380	0.0837	2.22[−6]	3.091[−5]	
3-1	E2	18380	0.0837	4.40	2.267	
3-2	E2	13688	0.0624	−5.62	0.850	
4-1	E1	67039	0.3055	1.62	7.996[8]	
4-3	E1	48659	0.2217	2.04	4.860[8]	
		W VI				[40]$_{\text{Theo.}}$
2-1	M1	8709.3	0.0397	−5.65[−3]	7.126	7.12
2-1	E2	8709.3	0.0397	−1.60	2.400[−3]	2.54[−3]
4-1	E1	147553.1	0.6723	1.18	4.529[9]	
4-3	E1	68121.8	0.3104	1.70	9.218[8]	

9.5.2 Polarizabilities and blackbody radiation shifts

Scalar polarizability is one of the key properties of atoms that sets their chemical characteristics. For establishing optical clocks, the values of the static and dynamic scalar polarizabilities should be taken into account. Scalar polarizabilities provide the value of the blackbody radiation (BBR) shift of the clock state frequency, which is a primary source of uncertainty for a clock.

The scalar polarizability α_{0v} of an atomic system in state v can be expressed as a sum over a complete set of states n (these states are constructed using the B-spline technique described above; the use of the B-splines ensures the completeness of the basis):

$$\alpha_{0v} = \frac{2}{3(2J_v+1)} \sum_n \frac{A_{vn}^2}{E_n - E_v}. \tag{9.13}$$

Here J_v is the total angular momentum of state v, and A_{vn} is the electric dipole transition amplitude (reduced matrix element). Notations v and n refer to the many-electron atomic states. It is convenient to present the polarizability as a sum of two terms, the polarizability of the closed-shell core and the contribution from the valence electrons. The polarizability of the core is given in the RPA approximation by

$$\alpha_{0\text{core}} = \frac{2}{3} \sum_{cn} \frac{\langle c||\hat{d} + \delta V^d_{\text{core}}||n\rangle\langle n||\hat{d}||c\rangle}{E_n - E_c}. \tag{9.14}$$

Here summation over c goes over core states, summation over n is over a complete set of single-electron basis states, $\hat{d} = -er$ is the $E1$ operator in the length form, δV^d_{core} is the core polarization correction to the $E1$ operator [see Eq.(9.9)]. Note that the RPA correction goes only into one of the two reduced matrix elements in Eq. (9.14) [41].

For the calculation of the valence contribution to the polarizabilities of the ground and clock states of Hf II we apply the technique developed in Ref. [28] for atoms or ions with open shells. The method relies on Eq. (9.13) and the Dalgarno-Lewis approach [42], which reduces the summation in Eq. (9.13) to the solving of the matrix equation (see Refs. [28,42]

for more details). For Hf IV and W VI, which both have only one external electron above closed shells, we use direct summation in Eq. (9.13) over the complete set of single-electron basis states.

There is also a core-valence contribution to the polarizabilities which comes from the fact that calculation of the core polarizabilities is affected by valence electrons via Pauli blocking. We include this contribution by omitting in the summation over n in Eq.(9.14) states occupied by valence electrons.

The present results for the polarizabilities of the ground states and clock states for all considered atomic systems are shown in Table 9.3. According to the calculations, clock states of all atomic systems have polarizabilities similar to those of their ground states, with the notable exception of the Hf IV third excited state, where this difference is approximately 14 a_b^3. This is because of the difference in the electronic configurations. The external electron in the ground state is in the $5d_{3/2}$ state, while in the clock state it is in the $6s_{1/2}$ state.

By using the values of scalar polarizability, we can figure out the BBR shift of a clock state at 300 K. The BBR shift in Hz is determined by the following expression (see, e.g., Ref. [8]):

$$\delta\omega_{\text{BBR}} = -8.611 \times 10^{-3} \left(\frac{T}{300\ K}\right)^4 \Delta\alpha_0, \tag{9.15}$$

where T is a temperature in K (e.g., room-temperature $T = 300$ K), $\Delta\alpha_0 = \alpha_0(\text{CS}) - \alpha_0(\text{GS})$ is the difference between the clock state and the ground-state polarizabilities presented in atomic units. The BBR shifts for clock states investigated in this paper are presented in Table 9.3. The relative BBR shifts in the 2-1 transition in Hf IV and the 2-1 transition in W VI are among the smallest considered so far, they are 4.3×10^{-18} and 2.3×10^{-18} respectively, while BBR shifts in other transitions are $\sim 10^{-16}$, similar to BBR shifts in other atomic clocks (see, e.g., Refs. [23,43–46]). A linear combination of two clock transition frequencies allows one to cancel BBR shifts [47].

Table 9.3: Scalar static polarizabilities of the ground states, α_0(GS), and clock states, α_0(CS), and BBR frequency shifts for the clock transition. $\delta\omega_{BBR}/\omega$ is the fractional contribution of the BBR shift; where ω is the clock transition frequency. Total means total scalar polarizability (core + valence).

Clock	α_0(GS)(units of a_B^3)			α_0(CS)(units of a_B^3)				BBR, (T= 300 K)		
transition	Core	Valence	Total	Core	Valence	Total	$\Delta\alpha_0$	$\delta\omega_{BBR}$(Hz)	ω(Hz)	$\delta\omega_{BBR}/\omega$
					Hf II					
2-1	2.72	48.04	50.76	2.72	43.22	45.94	-4.93	0.043	1.093[14]	3.9[-16]
3-1	2.72	48.04	50.76	2.61	40.10	42.71	-8.05	0.070	1.093[14]	6.4[-16]
4-1	2.72	48.04	50.76	2.61	42.84	45.45	-5.31	0.046	1.470[14]	3.2[-16]
					Hf IV					
2-1	3.06	2.86	5.92	2.98	2.86	5.85	-0.07	0.60[-3]	1.404[14]	4.3[-18]
3-1	3.06	2.86	5.92	3.13	16.84	19.97	14.05	-0.12	5.510[14]	-2.2[-16]
					W VI					
2-1	1.96	0.76	2.73	1.92	0.75	2.66	-0.07	0.60[-3]	2.611[14]	2.3[-18]

9.5.3 Electric quadrupole moments

As is discussed above, the search for clock transitions sensitive to the variation of the fine-structure constant leads us to transitions with large changes of the total momentum of the equivalent singe-electron transitions. As a consequence, at least one of the states may have a relatively large value of the total momentum J (e.g., $J > 1$). This means that the state is sensitive to the electric quadrupole shift. Therefore, it is important to know the value of this shift. The corresponding term in the Hamiltonian is (see, e.g., Ref. [48])

$$H_Q = \sum_{q=1}^{-1} (-1)^q \nabla \mathcal{E}_q^{(2)} \hat{\Theta}_{-q} \tag{9.16}$$

The tensor $\nabla \mathcal{E}_q^{(2)}$ is the external electric field gradient at the position of the system, Θ_q describes the electric-quadrupole operator, and $\hat{\Theta}_q = |e| r^2 C_q^{(2)}$, the same as for $E2$ transitions.

The electric quadrupole moment Θ is defined as the expectation value of Θ_0 for the extended state:

$$\begin{aligned} \Theta &= \left\langle nJJ \left| \hat{\Theta}_0 \right| nJJ \right\rangle \\ &\equiv \left\langle J \| \hat{\Theta} \| J \right\rangle \sqrt{\frac{J\,(2J-1)}{(2J+3)\,(2J+1)\,(J+1)}}, \end{aligned} \tag{9.17}$$

where $\langle J \| \hat{\Theta} \| J \rangle$ is the reduced matrix element (ME) of the electric quadrupole operator. We compute the values of Θ using the CI+SD and RPA methods described in the previous section.

In Table 9.4 we display the reduced ME of the electric quadrupole operator and the quadrupole moment Θ values for all considered states. The quadrupole momentum of the ground state of Hf II is anomalously small. This is due to the mixing between states of the $6s^2 5d$ and $6s5d^2$ configurations leading to strong cancellation between terms proportional to the $\left\langle 5d_{3/2} || \hat{\Theta} || 5d_{3/2} \right\rangle$ ME and terms proportional to the $\left\langle 6s_{1/2} || \hat{\Theta} || 5d_{3/2} \right\rangle$ ME. Strong

Table 9.4: Quadrupole moment (Θ, in a.u.) of the ground state and the considered optical clock states.

No.	Conf.	Term	J	E (cm^{-1})	ME (a.u.) $\left\langle J \| \hat{\Theta} \| J \right\rangle$	Θ
			Hf II			
1	$5d6s^2$	^{2}D	3/2	0	$-2.910[-2]$	$-6.507[-3]$
2	$5d6s^2$	^{2}D	5/2	3050.88	$-5.806[-1]$	$-1.415[-1]$
3	$5d^26s$	^{4}F	3/2	3644.65	-1.797	-0.401
4	$5d^26s$	^{4}F	5/2	4904.85	-1.621	-0.395
			Hf IV			
1	$5d$	^{2}D	3/2	0	-3.608	-0.807
2	$5d$	^{2}D	5/2	4692	-4.956	-1.210
			W VI			
1	$5d$	^{2}D	3/2	0	-2.381	-0.532
2	$5d$	^{2}D	5/2	8709.3	-3.263	-0.796

cancellation is probably accidental, which means that the result is likely to be not very stable and may vary significantly under variation of the computation procedure. In states where the $6s5d^2$ configuration dominates, the value of the quadrupole moment is not suppressed and stable. This means that the uncertainty of the calculated values of the quadrupole moment is of the order of the quadrupole moment itself in cases when it is small (first two lines of Table 9.4). For larger values of Θ the absolute uncertainty might be similar while the relative uncertainty is much smaller. The values of the quadrupole moments for both excited clock states are almost the same. In the case of the Hf IV ion, the difference between the values in the ground state and in the excited state is much smaller than that in the Hf$^+$ ion. The quadrupole moment in the ground state is about 1.5 times larger than that in the first excited state. This is because both states (the ground and the excited) have the same electron configuration. Note that the quadrupole moment of the second excited state $\left(6s\ ^2S_{1/2}\right)$ is zero because the total angular momentum J is 1/2. The W VI ion has differences similar to those in the Hf IV ion.

It is worth noting that the quadrupole shift in odd isotopes of Hf II and Hf IV (^{177}Hf, $I = 7/2$, and ^{179}Hf, $I = 9/2$) can be totally avoided when working with specific hyperfine components of the states, namely, substates with $F = 3$ and $F_z = 2$, since $\Delta E \sim 3F_z^2 - F(F+1)$. Such substates exist for both ground and clock states in both isotopes. Another way of suppressing the quadrupole shift is by averaging over transitions between different hyperfine or Zeeman components [21,48]. Averaging over Zeeman components should work for even isotopes too.

9.5.4 Sensitivity of the clock transitions to the variation of the fine-structure constant

It has been shown that optical atomic clock transitions can be used to search for the time variation of the fine-structure constant α [12,13,16]. The frequencies of these transitions depend differently on α. By comparing the ratio of two clock frequencies over long periods of time, one can link any possible change in the ratio of frequencies to the time variation of α. The ratio of frequencies does not depend on the units one uses. In atomic units, dependence of the optical transition frequencies appears to be due to the relativistic corrections proportional to α^2. Therefore, we present the frequency as

$$\omega = \omega_0 + q\left[\left(\frac{\alpha}{\alpha_0}\right)^2 - 1\right], \tag{9.18}$$

where α_0 and ω_0 are the present-day values of the finestructure constant and the frequency of the transition, and q is the sensitivity coefficient which comes from the atomic calculations [12,13,16]. The rate of the variation of ω_1/ω_2 is

$$\frac{\dot{\omega}_1}{\omega_1} - \frac{\dot{\omega}_2}{\omega_2} = (K_1 - K_2)\frac{\dot{\alpha}}{\alpha}. \tag{9.19}$$

The dimensionless value $K = 2q/\omega$ is often called the enhancement factor. We use the computer codes to calculate q and K by performing calculations of the frequencies with different values of α and calculating the derivative numerically as

$$q = \frac{\omega(\delta) - \omega(-\delta)}{2\delta}, \qquad (9.20)$$

where $\delta = (\alpha/\alpha_0)^2 - 1$ [see Eq. (9.18)]. In order to achieve linear behavior, the value of δ must be small; however, it must be large enough to suppress numerical noise. Most accurate results can be obtained by using $\delta = 0.01$. The calculated values of q and K for all considered clock transitions are summarized in Table 9.5. We see that all values of the enhancement coefficient K are significantly bigger than 1. The enhancement factor for the 2-1 interval is 3.65. This is the fine-structure interval and under normal circumstances the interval $\propto (Z\alpha)^2$ and $K = 2$. Here the factor is significantly larger due to strong mixing of the upper state with the states of the $5d^26s$ configuration. Note that values of K are positive, with only one negative K factor for the $5d_{3/2}$-$6s_{1/2}$ transition in the Hf IV ion. Indeed, the simple analytical estimate performed in Refs. [12, 13] indicates that the transition from a lower j orbital in the ground state to a higher j orbital gives a positive K while the transition from a higher j orbital to a lower j orbital gives a negative K.

It was shown in Ref. [47] that having two clock transitions in one atom or ion allows one to construct a "synthetic" frequency which is not sensitive to the BBR shift. They also proposed a realization of the method with the use of an optical frequency comb generator stabilized to both clock frequencies. The synthetic frequency is generated as one of the components of the comb spectrum (see Ref. [47] for details).

Using such frequencies may benefit the search for the time variation of the fine-structure constant. The Hf II ion has three clock transitions. This means that one can contract two independent "synthetic" frequencies nonsensitive to the BBR shift. Measuring one such frequency against the other over a long period of time allows highly sensitive search for the variation of the fine-structure constant. Following Ref. [47] we write a synthetic frequency

Table 9.5: Sensitivity of clock transitions to variation of the fine-structure constant (q, K).

No.	Conf.	Term	J	ω (cm^{-1})	q (cm^{-1})	K
			Hf II			
2	$5d6s^2$	^{2}D	5/2	3050.88	5631	3.65
3	$5d^26s$	^{4}F	3/2	3644.65	15060	8.30
4	$5d^26s$	^{4}F	5/2	4904.85	15002	6.16
			Hf IV			
2	$5d$	^{2}D	5/2	4692	4342	1.85
3	$6s$	^{2}S	1/2	18380	−24268	−2.64
			W VI			
2	$5d$	^{2}D	5/2	8709.3	8609	1.98

as

$$\omega_{ij} = \omega_i - \epsilon_{ij}\omega_j, \tag{9.21}$$

where $\epsilon_{ij} = \Delta\alpha_{0i}/\Delta\alpha_{0j}$. Since BBR shift $\propto \Delta\alpha_0$ [see Eq. (9.15)], the synthetic frequency (9.21) is not sensitive to it. If the fine-structure constant α varies in time, then the synthetic frequency varies as

$$\frac{\dot{\omega}_{ij}}{\omega_{ij}} = \frac{K_i\omega_i - \epsilon_{ij}K_j\omega_j}{\omega_i - \epsilon_{ij}\omega_j}\frac{\dot{\alpha}}{\alpha} \equiv K_{ij}\frac{\dot{\alpha}}{\alpha}. \tag{9.22}$$

Table 9.6 shows three possible synthetic frequencies for Hf II. Any two of these frequencies can be used for searching of the time variation of the fine-structure constant. For example, if the ω_{32} and ω_{42} frequencies are used, then

$$\frac{\dot{\omega}_{32}}{\omega_{32}} - \frac{\dot{\omega}_{42}}{\omega_{42}} = -20\frac{\dot{\alpha}}{\alpha}. \tag{9.23}$$

The combinations of frequencies which are not sensitive to the BBR shift turn out to be very sensitive to the time variation of the fine-structure constant.

Table 9.6: Synthetic frequencies of Hf II clock transitions and their sensitivity to variation of the fine-structure constant. Indexes i and j correspond to the clock transitions from state number i or j (see Table 9.1) to the ground state.

i	j	ϵ_{ij}	ω_{ij} (cm^{-1})	K_{ij}
3	2	1.633	1336.86	-9.03
4	2	1.077	1618.83	11.26
4	3	0.660	2500.66	4.10

9.6 CONCLUSIONS

Metastable states of Hf II, Hf IV, and W VI ions are studied as candidates for high-accuracy optical clocks which are highly sensitive to the variation of the fine-structure constant α. Slow drift and oscillating variation of α may be due to the interaction between the scalar dark matter field and electromagnetic field [49–52]. The Yukawa-type scalar field affecting α may also be produced by massive bodies [53]. Transient α variation may be produced by the passing of macroscopic forms of dark matter such as Bose stars and topological defects [54].

Six stable isotopes of Hf and five stable isotopes of W, as well as several clock transitions in Hf and W ions, make it possible to make King plots and study their nonlinearities in order to put limits on the new interactions mediated by scalar particles or other mechanisms [24, 25].

Energy levels, lifetimes, transition rates, scalar polarizabilities of the clock and ground states, and BBR shifts have been calculated, and the possibility for high accuracy of the timekeeping has been demonstrated. The studied transitions correspond to the *s*-*d* or *d*-*s* transitions between singleelectron states.

The sensitivity coefficients K to α variation have been calculated and found to be among the highest compared to other operating or prospective atomic optical clocks. We found that constructing synthetic frequencies with suppressed sensitivity to the BBR shift leads to further increase in sensitivity to the variation of the fine-structure constant.

ACKNOWLEDGMENTS

This work was supported by the Australian Research Council under Grants No. DP190100974 and No. DP200100150. This research includes computations using the computational cluster Katana supported by Research Technology Services at UNSW Sydney [55]. S.O.A. gratefully acknowledges the Islamic University of Madinah (Ministry of Education, Saudi Arabia) for funding his scholarship.

References

[1] S. M. Brewer, J.-S. Chen, A. M. Hankin, E. R. Clements, C. W. Chou, D. J. Wineland, D. B. Hume, and D. R. Leibrandt, $^{27}\text{Al}^{+}$ Quantum-Logic Clock with a Systematic Uncertainty below 10^{-18}, Phys. Rev. Lett. **123**, 033201 (2019).

[2] A. D. Ludlow, W. F. McGrew, X. Zhang *et al.*, Optical frequency measurements at 1×10^{-18} uncertainty with ytterbium optical lattice clocks, in *Proceedings of the Conference on Precision Electromagnetic Measurements (CPEM), Paris, France, July 08–13* (IEEE, Piscataway, NJ, 2018).

[3] N. Huntemann, C. Sanner, B. Lipphardt, Chr. Tamm, and E. Peik, Single-Ion Atomic Clock with 3×10^{-18} Systematic Uncertainty, Phys. Rev. Lett. **116**, 063001 (2016).

[4] W. McGrew, X. Zhang, R. Fasano, S. Schäffer, K. Beloy, D. Nicolodi, R. Brown, N. Hinkley, G. Milani, M. Schioppo *et al.*, Atomic clock performance enabling geodesy below the centimetre level, Nature (London) **564**, 87 (2018).

[5] I. Ushijima, M. Takamoto, M. Das, T. Ohkubo, and H. Katori, Cryogenic optical lattice clocks, Nat. Photonics **9**, 185 (2015).

[6] T. L. Nicholson, S. L. Campbell, R. B. Hutson, G. E. Marti, B. J. Bloom, R. L. McNally, W. Zhang, M. D. Barrett, M. S. Safronova, G. F. Strouse, W. L. Tew, and J. Ye, Systematic evaluation of an atomic clock at $2\times\ 10^{-18}$ total uncertainty, Nat. Commun. **6**, 6896 (2015).

[7] R. Lange, N. Huntemann, J. M. Rahm, C. Sanner, H. Shao, B. Lipphardt, Chr. Tamm, S. Weyers, and E. Peik, Improved Limits for Violations of Local Position Invariance from Atomic Clock Comparisons, Phys. Rev. Lett. **126**, 011102 (2021).

[8] S. G. Porsev and A. Derevianko, Multipolar theory of blackbody radiation shift of atomic energy levels and its implications for optical lattice clocks, Phys. Rev. A **74**, 020502(R) (2006); **86**, 029904(E) (2012).

[9] Boulder Atomic Clock Optical Network (BACON) Collaboration. Frequency ratio measurements at 18-digit accuracy using an optical clock network, Nature (London) **591**, 564 (2021).

[10] C. Sanner, N. Huntemann, R. Lange, C. Tamm, E. Peik, M. S. Safronova, and S. G. Porsev, Optical clock comparison for Lorentz symmetry testing, Nature (London) **567**, 204 (2019).

[11] T. Bothwell, D. Kedar1, E. Oelker, J. M Robinson, S. L Bromley, W. L Tew, J. Ye and C. J Kennedy, JILA SrI optical lattice clock with uncertainty of 2.0×10^{-18}, Metrologia **56**, 065004 (2019).

[12] V. A. Dzuba, V. V. Flambaum, and J. Webb, Space-Time Variation of Physical Constants and Relativistic Corrections in Atoms, Phys. Rev. Lett. **82**, 888 (1999).

[13] V. A. Dzuba, V. V. Flambaum, and J. K. Webb, Calculations of the Relativistic Effects in Many-Electron Atoms and Space-Time Variation of Fundamental Constants, Phys. Rev. A **59**, 230 (1999).

[14] B. J. Bloom, T. L. Nicholson, J. R. Williams, S. L. Campbell, M. Bishof, X. Zhang, W. Zhang, S. L. Bromley, and J. Ye, An optical lattice clock with accuracy and stability at the 10^{-18} level, Nature **506**, 71 (2014).

[15] E. J. Angstmann, V. A. Dzuba, and V. V. Flambaum, Relativistic effects in two valence-electron atoms and ions and search for variation of the fine structure constant, Phys. Rev. A **70**, 014102 (2004).

[16] V. V. Flambaum and V. A. Dzuba, Search for variation of the fundamental constants in atomic, molecular and nuclear spectra, Can. J. Phys. **87**, 25 (2009).

[17] E. J. Angstmann, V. A. Dzuba, V. V. Flambaum, A. Yu. Nevsky, and S. G. Karshenboim, Narrow atomic transitions with enhanced sensitivity to variation of the fine structure constant, J. Phys. B: At. Mol. Phys. **39**, 1937 (2006).

[18] V. A. Dzuba, V. V. Flambaum, and M. V. Marchenko, Relativistic effects in Sr, Dy, Yb II and Yb III, and search for variation of the fine structure constant, Phys. Rev. A **68**, 022506 (2003).

[19] V. A. Dzuba and V. V. Flambaum, Relativistic corrections to transition frequencies of Ag I, Dy I, Ho I, Yb II, Yb III, Au I and Hg II and search for variation of the fine structure constant, Phys. Rev. A **77**, 012515 (2008).

[20] R. M. Godun, P. B. R. Nisbet-Jones, J. M. Jones, S. A. King, L. A. M. Johnson, H. S. Margolis, K. Szymaniec, S. N. Lea, K. Bongs, and P. Gill, Frequency Ratio of Two Optical Clock Transitions in ^{171}Yb^{+} and Constraints on the Time Variation of Fundamental Constants, Phys. Rev. Lett. **113**, 210801 (2014).

[21] V. A. Dzuba, V. V. Flambaum, and S. Schiller, Testing physics beyond the standard model through additional clock transitions in neutral ytterbium Phys. Rev. A **98**, 022501 (2018).

[22] V. A. Dzuba, S. O. Allehabi, V. V. Flambaum, Jiguang Li, and S. Schiller, Time keeping and searching for new physics using metastable states of Cu, Ag, and Au Phys. Rev. A **103**, 022822 (2021).

[23] S. O. Allehabi, V. A. Dzuba, and V. V. Flambaum, Using optical clock transitions in Cu II and Yb III for timekeeping and search for new physics, Phys. Rev. A **104**, 053109 (2021).

[24] J. C. Berengut, D. Budker, C. Delaunay, V. V. Flambaum, C. Frugiuele, E. Fuchs, C. Grojean, R. Harnik, R. Ozeri, G. Perez, and Y. Soreq, Probing New

Long-Range Interactions by Isotope Shift Spectroscopy, Phys. Rev. Lett. **120**, 091801 (2018)

[25] V. V. Flambaum, A. Geddes, and A. V. Viatkina, Isotope shift, nonlinearity of King plot and search for new particles, Phys. Rev. A **97**, 032510 (2018).

[26] V. A. Dzuba, Combination of the single-double coupled-cluster and the configuration-interaction methods: Application to barium, lutetium, and their ions, Phys. Rev. A **90**, 012517 (2014).

[27] V. A. Dzuba, J. C. Berengut, C. Harabati, and V. V. Flambaum, Combining configuration interaction with perturbation theory for atoms with a large number of valence electrons, Phys. Rev. A **95**, 012503 (2017).

[28] V. Dzuba, Calculation of polarizabilities for atoms with open shells, Symmetry **12**, 1950 (2020).

[29] V. A. Dzuba, V^{N-M} approximation for atomic calculations, Phys. Rev. A **71**, 032512 (2005).

[30] W. R. Johnson and J. Sapirstein, Computation of Second-Order Many-Body Corrections in Relativistic Atomic Systems, Phys. Rev. Lett. **57**, 1126 (1986).

[31] W. R. Johnson, S. A. Blundell, and J. Sapirstein, Finite basis sets for the Dirac equation constructed from B splines, Phys. Rev. A **37**, 307 (1988).

[32] S. A. Blundell, W. R. Johnson, Z. W. Liu, and J. Sapirstein, Relativistic all-order calculations of energies and matrix elements for Li and Be^+, Phys. Rev. A **40**, 2233 (1989).

[33] V. A. Dzuba, V. V. Flambaum, P. G. Silvestrov, and O. P. Sushkov, Correlation potential method for the calculation of energy levels, hyperfine structure and E1 transition amplitudes in atoms with one unpaired electron, J. Phys. B **20**, 1399 (1987).

[34] V. A. Dzuba, V. V. Flambaum, and M. G. Kozlov. Combination of the many-body perturbation theory with the configuration interaction method. Phys. Rev. A **54**, 3948 (1996).

[35] A. Kramida, Yu. Ralchenko, J. Reader, and NIST ASD Team (2019), NIST Atomic Spectra Database (ver. 5.7.1), available at https://physics.nist.gov/asd (2020, September 26), National Institute of Standards and Technology, Gaithersburg, MD.

[36] P. O. Schmidt *et al.*, Spectroscopy using quantum logic, Science **309**, 749 (2005).

[37] J. B. Wübbena, S. Amairi, O. Mandel, and P. O. Schmidt, Sympathetic cooling of mixed-species two-ion crystals for precision spectroscopy, Phys. Rev. A **85**, 043412 (2012).

[38] P. F. A. Klinkenberg, Th. A. M. Van Kleef, and P. E. Noorman, Structure and Ionization Potential of Hf III and Hf IV, Physica **27**, 151 (1961).

[39] J. E. Lawler, E. A. Den Hartog, Z. E. Labby, C. Sneden, J. J. Cowan, and I. I. Ivans, Improved laboratory transition probabilities for Hf II and hafnium abundances in the sun and 10-metal-poor stars, Astrophys. J., Suppl. Ser. **169**, 120 (2007).

[40] S. E. Yoca, P. Palmeri, P. Quinet, G. Jumet, and É. Biémont, Radiative properties and core-polarization effects in the W^{5+} ion, J. Phys. B **45**, 035002 (2012).

[41] A.-M. Mårtensson-Pendrill, Calculation of a P- and T-Nonconserving Weak Interaction in Xe and Hg with Many-Body Perturbation Theory, Phys. Rev. Lett. **54**, 1153 (1985).

[42] A. Dalgarno and J. T. Lewis, The exact calculation of long-range forces between atoms by perturbation theory, Proc. R. Soc. London A **233**, 70 (1955).

[43] C. A. Holliman, M. Fan, A. Contractor, S. M. Brewer, and A. M. Jayich, Radium Ion Optical Clock, Phys. Rev. Lett. **128**, 033202 (2022).

[44] N. Nemitz, T. Gotoh, F. Nakagawa, H. Ito, Y. Hanado, T. Ido, and H. Hachisu, Absolute frequency of ^{87}Sr at 1.8×10^{-16} uncertainty by reference to remote primary frequency standards, Metrologia, **58**, 025006 (2021).

[45] V. A. Dzuba and A. Derevianko, Blackbody radiation shift for the optical $^1S_0 -^3 P_0$ clock transition in zinc and cadmium atoms, J. Phys. B: At., Mol. Opt. Phys. **52**, 215005 (2019).

[46] A. Kozlov, V. A. Dzuba, and V. V. Flambaum, Optical atomic clocks with suppressed blackbody-radiation shift, Phys. Rev. A **90**, 042505 (2014).

[47] V. I. Yudin, A. V. Taichenachev, M. V. Okhapkin, S. N. Bagayev, Chr. Tamm, E. Peik, N. Huntemann, T. E. Mehlstaubler, and F. Riehle. Atomic clocks with suppressed blackbody radiation shift, Phys. Rev. Lett. **107**, 030801 (2011).

[48] W. Itano, External-field shifts of the ^{199}Hg$^+$ optical frequency standard, J. Res. Natl. Inst. Stand. Technol. **105**, 829 (2000).

[49] K. Van Tilburg, N. Leefer, L. Bougas, and D. Budker, Search for Ultralight Scalar Dark Matter with Atomic Spectroscopy, Phys. Rev. Lett. **115**, 011802 (2015).

[50] Y. V. Stadnik and V. V. Flambaum, Can Dark Matter Induce Cosmological Evolution of the Fundamental Constants of Nature?, Phys. Rev. Lett. **115**, 201301 (2015).

[51] Y. V. Stadnik and V. V. Flambaum, Improved limits on interactions of low-mass spin-0 dark matter from atomic clock spectroscopy, Phys. Rev. A **94**, 022111 (2016).

[52] A. Hees, J. Guena, M. Abgrall, S. Bize, and P. Wolf, Searching for an Oscillating Massive Scalar Field as a Dark Matter Candidate Using Atomic Hyperfine Frequency Comparisons, Phys. Rev. Lett. **117**, 061301 (2016).

[53] N. Leefer, A. Gerhardus, D. Budker, V. V. Flambaum, and Y. V. Stadnik, Search for the Effect of Massive Bodies on Atomic Spectra and Constraints on Yukawa-Type Interactions of Scalar Particles, Phys. Rev. Lett. **117**, 271601 (2016).

[54] A. Derevianko and M. Pospelov, Hunting for topological dark matter with atomic clocks, Nat. Phys. **10**, 933 (2014).

[55] Katana (shared computational cluster), University of New South Wales, Sydney, 2010, https://doi.org/10.26190/669x-a286.

Chapter 10

High-accuracy optical clocks based on group-16-like highly charged ions

10.1 Overview

In chapters 7,8,9, we investigated new promising atomic clocks by considering neutral or nearly neutral ions. In this chapter, we examine the potential to construct high-accuracy optical clocks using highly charged ions, group-16-like systems. Highly charged ions, due to their small size compared to neutral atoms, have the important advantage of being less sensitive to perturbations. For example, they have very small black body radiation shifts. In addition, considered systems have anomalous fine structures. The first excited state is $^3\mathrm{P}_0$ instead of $^3\mathrm{P}_1$, which means that there is a narrow E2 transition between the ground and the first excited state, which can be used as a clock transition. The wavelengths of these transitions are also favorable.

This study has been published in this paper:

Saleh O. Allehabi, S. M. Brewer, V. A. Dzuba, V. V. Flambaum, and K. Beloy, High-accuracy optical clocks based on group-16-like highly charged ions, Phys. Rev. A **106**, 043101 (2022).

10.2 Abstract

We identify laser-accessible transitions in group-16-like highly charged ions as candidates for high-accuracy optical clocks, including S-, Se-, and Te-like systems. For this class of ions, the ground ^3P_J fine-structure manifold exhibits irregular (nonmonotonic in J) energy ordering for large enough ionization degree. We consider the $|^3P_2\rangle \longleftrightarrow |^3P_0\rangle$ (ground to first-excited state) electric quadrupole transition, performing relativistic many-body calculations of several atomic properties important for optical clock development. All ions discussed are suitable for production in small-scale ion sources and lend themselves to sympathetic cooling and quantum-logic readout with singly charged ions.

10.3 INTRODUCTION

The performance of optical clocks has improved rapidly over the last few decades [1]. This has led to improvements in frequency metrology as well as tests of fundamental physics using atomic clocks [2]. The highest performance optical clocks are currently based on ensembles of neutral atoms trapped in optical lattices or singly charged ions stored in electromagnetic traps [3–6]. However, in recent years, several clocks based on highly charged ions (HCIs) have been proposed as both improved optical frequency standards and as systems with enhanced sensitivity to possible new physics [7–9] (see also Ref. [10] and references therein). Optical clocks based on HCIs provide several systematic advantages over current optical clocks including reduced blackbody radiation (BBR), Zeeman, and electric quadrupole shifts [10, 11]. Here, we identify group 16-like HCIs as optical clock candidates. For this class of ions, the ground ^3P_J fine structure manifold exhibits irregular (nonmonotonic in J) energy ordering for large enough ionization degree, with the $^3P_1$

state lying above the $^3P_2$ (ground) and $^3P_0$ (first-excited) states. Given this irregular ordering, the $^3P_0$ excited state lacks a magnetic dipole ($M1$) decay channel, resulting in a relatively long lifetime and making the $|^3P_2\rangle \longleftrightarrow |^3P_0\rangle$ electric quadrupole ($E2$) transition a viable clock transition. This irregular energy ordering is illustrated in Fig. 10.1. Due to the high nuclear charge, the ordering is irregular for Te-like systems beginning with neutral tellurium. In the case of O-, S-, and Se-like systems, the ionization degree must be increased before the irregular ordering is observed. Specifically, for O-like ions, the irregular ordering is not observed until Mn^{17+}. For this system, the clock transition wavelength (≈ 150 nm [12, 13]) is outside the range of current clock lasers. The S-, Se-, and Te-like systems offer more favorable clock transition wavelengths. In the present work, we perform relativistic many-body calculations of relevant properties for optical clock development. While we present results only for select S-, Se-, and Te-like systems, other group 16-like systems not explicitly considered may also be of interest.

The present work is a broader study of the group-16-like systems started in our previous work with just Ba^{4+} [17]. We include Ba^{4+} in the list of ions considered here. Broadly speaking, similar computational techniques are used here as in Ref. [17]. The results of Ref. [17] are reproduced with only small deviations, with two exceptions. First, a small clerical error is corrected, giving a second-order Zeeman shift that is a factor of 2 larger. The essential conclusion that this shift is negligible remains valid. Second, an improved method is used to calculate the scalar differential polarizability $\Delta\alpha$, which predicts a much larger degree of cancellation between the clock state polarizabilities. While the revised value of $\Delta\alpha$ does not support cancellation between the trap-induced Stark and micromotion time-dilation shifts (by operating at a "magic" rf trap drive [18]), it does offer highly suppressed Stark shifts, including the BBR shift. We find similar cancellation between the clock state polarizabilities for the other group-16-like systems, resulting in similarly small $\Delta\alpha$.

In the present work, we focus on the isotopes with zero nuclear spin to avoid complications caused by the hyperfine structure (hfs). In particular, the second-order Zeeman shift is enhanced in isotopes with hfs, by small hfs energy intervals. In contrast, the second-order

Zeeman shift is small and can be neglected in spin-zero isotopes.

10.4 METHOD

10.4.1 Calculation of energy levels

The calculations are carried out using a combination of the configuration interaction (CI) technique with the linearized single-double-coupled-cluster (SD) method, as described in Ref. [19]. The combined method (CI +SD) has been demonstrated to be efficient and very precise for systems with several valence electrons. With the SD technique, it is possible to accurately determine the core-valence and core-core electron correlations, while the CI method takes the valencevalence correlations into account. Our calculations are done using the V^{N-M} approximation [19], where N is the total number of electrons and M is the number of valence electrons. For all atomic systems considered (see, e.g., Table 10.1), the calculations begin with the relativistic Hartree-Fock (RHF) method for a closed-shell core, which removes all valence electrons. We treat all systems as $M = 6$ valence systems, except for Te and Sr^{22+}, which are treated as $M = 4$ valence systems; this is because NIST data [12] indicate that Te and Sr^{22+} have no low-lying states with the excitations from the $5s$ and $3s$ subshells, respectively. Therefore, it is reasonable to treat $5s$ electrons in Te and $3s$ electrons in Sr^{22+} as core electrons. The RHF Hamiltonian has the following form:

$$\hat{H}^{\mathrm{RHF}} = c\boldsymbol{\alpha} \cdot \mathbf{p} + (\beta - 1)mc^2 + V_{\mathrm{nuc}}(r) + V_{\mathrm{core}}(r), \tag{10.1}$$

where c is the speed of light, $\boldsymbol{\alpha}$ and β are the Dirac matrices, $\boldsymbol{p}$ is the electron momentum, m is the electron mass, V_{nuc} is the nuclear potential obtained by integrating the Fermi distribution of the nuclear charge density, and $V_{\mathrm{core}}\,(r)$ is the self-consistent RHF potential created by the electrons of the closed-shell core.

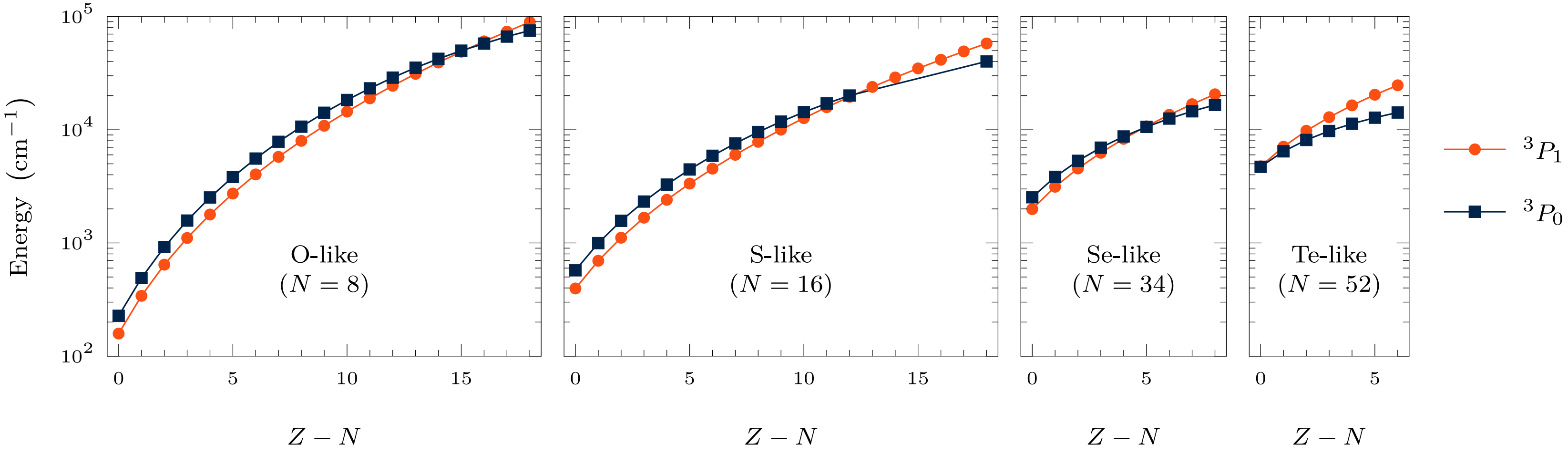

Figure 10.1: Experimental energies for group 16-like atomic systems. For each system, the lowest-lying electronic states are part of a ^3P_J fine structure manifold, with the $^3P_2$ ground state taken to have zero energy. Energies of the $^3P_1$ and $^3P_0$ states are plotted versus ionization degree $Z-N$ for the isoelectronic sequences, where Z and N denote the number of protons and electrons, respectively. For the O, S, and Se isoelectronic sequences, the ^3P_J energy ordering transitions from regular ordering (monotonic in J) at low ionization degree to irregular ordering at high ionization degree. For the Te isoelectronic sequence, the ordering is irregular already for the neutral Te system. For the systems with irregular energy ordering, the $^3P_0$ state lacks an $M1$ decay channel. Energies are from the NIST Atomic Spectra Database [12] and Refs. [14–16]. The curves are interpolating functions intended to guide the eye.

Following the completion of the self-consistent procedure for the core, the B-spline technique [20,21] is used to develop a complete set of single-electron wave functions. Based on B splines, one can make linear combinations of basis states, which are eigenstates of the RHF Hamiltonian. The basis set is built up of $40B$ splines of order 9 in a box that has a radius $R_{\max} = 40a_B$, where a_B is the Bohr radius, with the orbital angular momentum $0 \leqslant l \leqslant 6$. There are two types of basis states: core states and valence states. Core states are used to calculate the effective potential of the core. Valence states are used as a basis for the SD equations and for obtaining the many-electron states required for the CI calculations.

In the process of solving the SD equations for the core and valence states, we generate correlation operators Σ_1 and Σ_2 [19, 22, 23]. Σ_1 is the correlation interaction between a particular valence electron and the core, and accordingly, one-body part $\hat{h}_1$ can be described as follows:

$$\hat{h}_1 = \hat{H}^{\mathrm{RHF}} + \Sigma_1. \tag{10.2}$$

Σ_2 represents the screening of the Coulomb interaction between a pair of valence electrons; hence, the two-body Coulomb interaction operator, $\hat{h}_2$, is modified so as to include the two-body part of the core-valence interaction as follows (we use Gaussian electromagnetic expressions; e is electron charge):

$$\hat{h}_2 = \frac{e^2}{|r_i - r_j|} + \Sigma_2. \tag{10.3}$$

Whenever there is more than one valence electron above the closed-shell core, these Σ operators can be used in the subsequent CI calculations to account for the core-valence and core-core correlations. By solving the SD equations for external states, the single-electron energies of an atom or ion with one valence electron can also be obtained. However, we note that there are slight differences between the SD equations used for this purpose and those to be used for CI calculations. In this case, one term in the SD equations needs to be eliminated because its contribution is accounted for by the CI calculations (refer to Ref. [19]). This contribution is relatively small; therefore, differences in the SD equations can be ignored.

In the CI approach, we build the effective CI + SD Hamiltonian for many valence electrons as a sum of one- and two-electron parts with the addition of Σ_1 and Σ_2 operators in order to account for the correlation between core and valence electrons,

$$\hat{H}^{\mathrm{eff}} = \sum_{i=1}^{M} \left(\hat{H}^{\mathrm{RHF}} + \Sigma_1\right)_i + \sum_{i<j}^{M} \left(\frac{e^2}{|r_i - r_j|} + \Sigma_{2ij}\right), \tag{10.4}$$

where i and j enumerate valence electrons.

It is well recognized that increasing the number of valence electrons exponentially increases the size of the CI matrix. Our present work has up to six valence electrons, which leads to an extremely large CI matrix. In order to deal with a matrix of this magnitude, it would require considerable computational power. However, the size of the CI matrix can be decreased by orders of magnitude at the expense of some accuracy. In order to accomplish this, we use the recently developed version of the CI method called the CIPT method [24]. The method combines CI with perturbation theory and is used to ignore the off-diagonal matrix elements between highenergy states in the CI matrix. This step is justified because the high-energy states provide only a minimal correction to the wave function.

The wave function for valence electrons is presented as an expansion over single-determinant basis states, which is divided into two parts:

$$\Psi\left(r_1, \ldots, r_M\right) = \sum_{i=1}^{N_{\mathrm{eff}}} c_i \Phi_i\left(r_1, \ldots, r_M\right) + \sum_{i=N_{\mathrm{eff}}+1}^{N_{\mathrm{total}}} c_i \Phi_i\left(r_1, \ldots, r_M\right). \tag{10.5}$$

Here c_i are the expansion coefficients and Φ_i are singledeterminant many-electron basis functions. The first part of the wave function represents a small number of low-energy terms that contribute a great deal to the CI valence wave function ($1 \leqslant i \leqslant N_{\mathrm{eff}}$, where

N_{eff} is the number of low-energy basis states), while the second part represents a large number of high-energy states that introduce minor corrections to the valence wave function ($N_{\text{eff}} < i \leqslant N_{\text{total}}$, where N_{total} is the total number of the basis states). Consequently, this allows us to truncate the CI Hamiltonian by ignoring the off-diagonal matrix elements between terms in the second summation in Eq. (10.5) $\left(\left\langle i \left| H^{\text{eff}} \right| h \right\rangle = 0\right.$ for $N_{\text{eff}} < i, h \leqslant N_{\text{total}}$), which in turn reduces computation time with a negligible loss in precision.

The matrix elements between low-energy states i and g are corrected by the following formula similar to the second-order perturbative correction to the energy:

$$\langle i|H^{\text{eff}}|g\rangle \rightarrow \langle i|H^{\text{eff}}|g\rangle + \sum_k \frac{\langle i|H^{\text{eff}}|k\rangle\langle k|H^{\text{eff}}|g\rangle}{E - E_k}. \tag{10.6}$$

Here, $i, g \leqslant N_{\text{eff}}$, $N_{\text{eff}} < k \leqslant N_{\text{total}}$, E is the energy of the state of interest, and E_k denotes the diagonal matrix element for high-energy states, $E_k = \left\langle k \left| H^{\text{eff}} \right| k \right\rangle$. The summation in (10.6) runs over all high-energy states. Note that neglecting off-diagonal matrix elements between highly excited states corresponds to neglecting the third-order contribution

$$\delta E^{(3)}_{ig} = \sum_{k,l} \frac{\langle i|H^{\text{eff}}|k\rangle\langle k|H^{\text{eff}}|l\rangle\langle l|H^{\text{eff}}|g\rangle}{(E - E_k)(E - E_l)}. \tag{10.7}$$

This contribution is suppressed by large energy denominators. Neglecting the third-order corrections over the second-order corrections cannot cause any false contributions to the spinorbit splitting or break the symmetry of the CI Hamiltonian.

The problem of finding the wave function and corresponding energy can be reduced to a modified CI matrix eigenvalue equation $\hat{H}^{\text{eff}}$ [Eq. (10.4)] with size N_{eff}

$$\left(\hat{H}^{\text{eff}} - EI\right) X = 0, \tag{10.8}$$

where I is the identity matrix and X is the vector $\{c_1, \ldots, c_{N_{\text{eff}}}\}$. Note that for accurate solution the energy parameter E must be the same in Eqs. (10.6) and (10.8). Since this energy is not known in advance, the equations (10.6) and (10.8) are solved by iterations. The starting point for the iterations can be, e.g., the solution of (10.8) with the matrix (10.6) without the second-order corrections. A more comprehensive description of this technique is given in Ref. [24].

10.4.2 Calculation of transition amplitudes and lifetimes

The method we use for computing transition amplitudes is based on the time-dependent Hartree-Fock method [22], which is the same as the well-known random-phase approximation (RPA). The RPA equations are defined as

$$\left(\hat{H}^{\mathrm{RHF}} - \epsilon_c\right) \delta\psi_c = -\left(\hat{f} + \delta V^f_{\mathrm{core}}\right) \psi_c, \tag{10.9}$$

where the operator $\hat{f}$ refers to an external field. The index c denotes single-electron states, ψ_c is a single-electron wave function with corresponding energy ϵ_c, $\delta\psi_c$ is a correction to the wave function due to the external field, and $\delta V^f_{\mathrm{core}}$ is the correction to the self-consistent RHF potential caused by the amendment of all core states in the external field. For all states in the core, the RPA equations (10.9) are solved self-consistently. The transition amplitudes are found by calculating matrix elements between states a and b using the formula

$$A_{ab} = \left\langle b \left| \hat{f} + \delta V^f_{\mathrm{core}} \right| a \right\rangle. \tag{10.10}$$

Here, $|a\rangle$ and $|b\rangle$ are the many-electron wave functions calculated with the method described above. These wave functions are given by Eq. (10.5). In the present work, only the rates of $E2$ transitions are taken into account. The rates are computed as follows (in atomic units):

$$T_{ab} = \frac{1}{15}\left(\alpha\omega_{ab}\right)^5 \frac{A_{ab}^2}{2J_b+1}, \tag{10.11}$$

where α is the fine-structure constant $\left(\alpha \approx \frac{1}{137}\right), \omega_{ab}$ is the frequency of the transition, J_b is the total angular momentum of the upper state b, and A_{ab} represents the transition amplitude (reduced matrix element) of the $E2$ operator. The lifetimes of each excited state b, τ_b, expressed in seconds, are given as

$$\tau_b = 2.4189 \times 10^{-17} \Big/ \sum_a T_{ab} \tag{10.12}$$

where the summation runs over all possible transitions to lower states a.

10.5 RESULTS

10.5.1 Energy levels, transition amplitudes, and lifetimes of the systems

Table 10.1 presents the calculated energy levels of the systems and compares them to the results of previous work; note that all earlier data presented in the table are either experimental or semiempirical, except for the value for Cd^{14+}, which has been calculated. The calculated energies are in good agreement with experiment, within a few percent. In Table 10.1, we also present the $E2$ amplitudes and corresponding decay rates for excited clock states decaying to the ground state. The rates are in good agreement with previous studies. The rates and lifetimes of the excited clock states were calculated using calculated amplitudes and experimental energies.

Table 10.1: Excitation energies (E), wavelength transitions (λ), $E2$ amplitudes (A), decay rates (T), and lifetimes (τ) for the excited clock states. Note that for calculating λ, the experimental energies (where available) have been used.

		E (cm^{-1})			A(a.u)	T (s^{-1})		τ (s)
System	State	Present	Other	λ (nm)	Present	Present	Other cal.	Present
				Te-like systems				
Te	$5p^4\ {}^3P_0$	4630	4706[a]	2124.9	−5.483	0.0078	0.0073[e]; 0.0097[f]	128.21
Xe^{2+}	$5s^25p^4\ {}^3P_0$	8515	8130[a]	1230.0	−3.163	0.0398	0.04451[f]	25.13
Ba^{4+}	$5s^25p^4\ {}^3P_0$	11548	11302[a]	884.8	−2.351	0.1141	0.1253[f]	8.76
Ce^{6+}	$5s^25p^4\ {}^3P_0$	14697	14210[b]	703.7	−1.825	0.2159	0.2437[f]	4.63
				Se-like systems				
Zr^{6+}	$4s^24p^4\ {}^3P_0$	12722	12557[c]	796.4	−1.131	0.0447	0.0468[g]	22.37
Cd^{14+}	$4s^24p^4\ {}^3P_0$	28909	28828[d]	345.9	0.585	0.7612	–	1.31
				S-like systems				
Ge^{16+}	$3s^23p^4\ {}^3P_0$	33635	33290[a]	300.4	0.228	0.2377	0.2502[g]	4.21
Kr^{20+}	$3s^23p^4\ {}^3P_0$	47618	46900[a]	213.2	0.176	0.7859	0.8322[g]	1.27
Sr^{22+}	$3p^4\ {}^3P_0$	50911	53400[a]	187.3	−0.160	1.2434	1.257[g]	0.805

[a] Ref. [12]; The values are compiled from the NIST database; Te-like systems [Expt.], S-like systems [Expt. or Semi.].

[b] Ref. [15]; Expt.

[c] Ref. [16]; Expt.

[d] Ref. [25]; Expt.

[e] Ref. [26]; Theor.

[f] Ref. [27]; Theor.

[g] Ref. [28]; Theor.

10.5.2 Ionization potential, Landé g factors, and electric quadrupole moments

Table 10.2 presents the results of the calculated ionization potential (IP) of all atomic systems. The IP of a system can be calculated as a difference in the ground state energy between the system of interest (E^M) and the following ion (E^{M-1}), $\mathrm{IP} = E^{M-1} - E^M$. The results of our calculations are compared with data compiled by NIST. With the exception of the first two systems, the NIST data have large uncertainties ranging from 6800 cm^{-1} to 22000 cm^{-1}. Within these uncertainties, our calculations agree with the NIST data. In Table 10.2, we also present the calculated values of the Landé g factors for the ground states of all systems. The g factors are calculated as expectation values of the $M1$ operator.

Electric quadrupole shifts are known to be caused by an interaction between the quadrupole moment of an atomic state and an external electric-field gradient, and in the Hamiltonian, the corresponding term is given as [30]

$$H_Q = \sum_{q=1}^{-1} (-1)^q \nabla \mathcal{E}_q^{(2)} \hat{\Theta}_{-q}. \tag{10.13}$$

Here, the tensor $\nabla \mathcal{E}_q^{(2)}$ represents the external electric field gradient at the atom's position, and $\hat{\Theta}_q$ describes the electricquadrupole operator for the atom. It is the same as for the $E2$ transitions, $\hat{\Theta}_q = r^2 C_q^{(2)}$, where $C_q^{(2)}$ is the normalized spherical function and q indicates the operator component. The electric quadrupole moment, Θ, is defined as the expectation value of $\hat{\Theta}_0$ for the extended state

$$\begin{aligned} \Theta &= \left\langle nJJ \left| \hat{\Theta}_0 \right| nJJ \right\rangle \\ &= \left\langle nJ \| \hat{\Theta} \| nJ \right\rangle \sqrt{\frac{J\,(2J-1)}{(2J+3)\,(2J+1)\,(J+1)}}, \end{aligned} \tag{10.14}$$

where $\langle nJ \| \hat{\Theta} \| nJ \rangle$ indicates the reduced matrix element of the electric quadrupole operator. We compute the values of Θ using the CI + SD and RPA methods described in the

Table 10.2: Ionization potential (IP; cm^{-1}), quadrupole moment (Θ; a.u.), and Landé g factor of the ground state.

System	State	IP		Θ	g factor
		Present	NIST		
		Te-like systems			
Te	$5p^4\ ^3P_2$	70939	72669.006(0.047)	1.22	1.467[a]
Xe^{2+}	$5s^25p^4\ ^3P_2$	247505	250400(300)	0.53	1.441
Ba^{4+}	$5s^25p^4\ ^3P_2$	475734	468000(15000)	0.32	1.424[b]
Ce^{6+}	$5s^25p^4\ ^3P_2$	748287	734000(16000)	0.19	1.407
		Se-like systems			
Zr^{6+}	$4s^24p^4\ ^3P_2$	913400	903000(16000)	0.23	1.457
Cd^{14+}	$4s^24p^4\ ^3P_2$	2894809	2887000(22000)	0.062	1.407
		S-like systems			
Ge^{16+}	$3s^23p^4\ ^3P_2$	4916400	4912400(6800)	0.042	1.445
Kr^{20+}	$3s^23p^4\ ^3P_2$	7126586	7120300(10100)	0.024	1.420
Sr^{22+}	$3p^4\ ^3P_2$	8378219	8372100(12000)	0.019	1.413

[a] Experimental value is 1.460(4) [12].
[b] The same as in our previous calculations, 1.42 [17].

previous section. The results are presented in Table 10.2. Note that the excited clock states of all atomic systems have $\Theta = 0$ since the total angular momentum J is zero. Some of these atomic systems have been investigated before. In our early work [31] a different approach was used leading to quadrupole moments $Q(\mathrm{Te}) = -2.58$ a.u. and $Q(\mathrm{Xe}^{2+}) = -1.17$ a.u. It should be noted that in this earlier work [31], the electric quadrupole moment Q is defined in a way which differs from our definition by a factor of 2 , so that $\Theta = Q/2$. Taking this into account, the results for the two calculations are in good agreement.

10.5.3 Polarizabilities, blackbody radiation shifts, and second-order Zeeman shifts

The scalar polarizability $\alpha_v(0)$ of an atomic system in state v is given by a sum over a complete set of excited states n connected to state v by the electric-dipole ($E1$) reduced matrix elements (we use atomic units)

$$\alpha_v(0) = \frac{2}{3(2J_v+1)} \sum_n \frac{A_{vn}^2}{\omega_{vn}}, \tag{10.15}$$

where J_v is the total angular momentum of state v and ω_{vn} is the frequency of the transition. Notations v and n refer to many-electron atomic states. For the calculations of the polarizabilities of clock states, we apply the technique developed in Ref. [32] for atoms or ions with open shells. The method relies on Eq. (10.15) and the Dalgarno-Lewis approach [33], which reduces the summation in Eq. (10.15) to solving a matrix equation (see Ref. [32] for more details).

Results for the polarizabilities of the ground and excited clock states are shown in Table 10.3. It appears that the polarizabilities of the ground and excited clock states of all atomic systems are similar in values. This is because both clock states belong to the same fine-structure manifold, and the energy intervals between them are significantly smaller than the excitation energies to the opposite-parity states [see Eq. (10.15)]. Some of these atomic systems have previously been studied for their polarizabilities. Review [29], and references therein have investigated the ground state polarizability of Te both theoretically and experimentally, and the recommended value has been determined to be 38 ± 4 a.u. Compared with the recommended value, our calculation (37.3 a.u.) is in excellent agreement. In our earlier work [31] a simplified approach was used leading to larger values of polarizabilities of Te and Xe^{2+}; 45.96 and 47.80 a.u. for lower and upper clock states of Te, and 14.69 and 14.79 a.u. for lower and upper clock states of Xe^{2+}. These results are in reasonable agreement with our present calculations.

In our previous work [17], we calculated the polarizability of the ground and excited clock states for Ba^{4+} and found the values to be 4.4 and 1.4 a.u., respectively. Those results are in disagreement with the present results. The reason for the disagreement comes from the fact that direct summation was used in Ref [17]. This method works well if the summation is strongly dominated by the contribution of the low-lying states of opposite parity. This is not the case for Ba^{4+} or the other systems considered here.

Table 10.3: Scalar static polarizabilities of the ground and excited clock states [α_0(GS) and α_0(ES), respectively], and BBR frequency shifts for the clock transition. $\delta\nu_{\mathrm{BBR}}/\nu$ is the fractional contribution of the BBR shift, where ν is the clock transition frequency. "Total" means total scalar polarizability (core + valence). Error bars were obtained on the assumption that the accuracy for the polarizability is 10%. The last column shows the second-order Zeeman shifts, $\delta\nu_{\mathrm{SZ}}$. The notation $x[y]$ abbreviates $x \times 10^y$.

	α_0 (a.u.)	α_0(GS) (a.u.)		α_0(ES) (a.u.)			BBR (T = 300 K)			$\delta\nu_{\mathrm{SZ}}$
System	Core	Valence	Total	Valence	Total	$\Delta\alpha(0)$	$\delta\nu_{\mathrm{BBR}}$ (Hz)	ν (Hz)	$\delta\nu_{\mathrm{BBR}}/\nu$	[Hz/(mT)^2]
				Te-like systems						
Te	8.84	28.5	37.3[a]	29.6	38.4	< 7	$< 6[-2]$	1.411[14]	$< 4[-16]$	−87
Xe^{2+}	0.835	10.1	10.9	10.4	11.2	< 2	$< 2[-2]$	2.437[14]	$< 7[-17]$	−2.02
Ba^{4+}	0.578	5.46	6.04	5.56	6.14	< 1	$< 1[-2]$	3.388[14]	$< 3[-17]$	−0.55
Ce^{6+}	0.421	3.43	3.85	3.49	3.91	< 0.6	$< 5[-3]$	4.260[14]	$< 1[-17]$	−0.22
				Se-like systems						
Zr^{6+}	0.083	1.87	1.95	1.89	1.97	< 0.1	$< 1[-3]$	3.764[14]	$< 1[-18]$	−3.72
Cd^{14+}	0.024	0.466	0.490	0.467	0.491	$< 1[-2]$	$< 1[-5]$	8.642[14]	$< 1[-20]$	−0.08
				S-like systems						
Ge^{16+}	0.002	0.142	0.144	0.142	0.144	$< 1[-3]$	$< 1[-5]$	9.980[14]	$< 1[-20]$	−0.39
Kr^{20+}	0.001	0.0812	0.0822	0.0810	0.0820	$< 1[-3]$	$< 1[-5]$	1.406[15]	$< 1[-20]$	−0.08
Sr^{22+}	0.063	0.0276	0.0906	0.0273	0.0903	$< 1[-3]$	$< 1[-5]$	1.601[15]	$< 1[-20]$	−0.04

[a] The polarizability of the Te atom has been studied before, and the recommended result is 38 ± 4 a.u. [29].

In this paper, we use the more accurate method described above. The accuracy of the current approach can be judged by recalling our earlier calculations [34–36]. Deviation of the calculated polarizabilities from the experimental values varies from fraction of percent for noble elements [34] to few percent for atoms with more complicated electron structure. Given also that we have excellent agreement for Te with the recommended value from literature, which has 10% uncertainty, we conclude that the accuracy of our present calculations is in the range from 1% to 10%.

BBR can have a significant impact on the clock transition frequency in atomic clocks. The shift in the clock transition frequency caused by BBR can be calculated as

$$\delta\nu_{\mathrm{BBR}} = -1.063 \times 10^{-12} T^4 \Delta\alpha(0), \tag{10.16}$$

where T is the temperature and $\Delta\alpha(0) = \alpha_0(\mathrm{ES}) - \alpha_0(\mathrm{GS})$ is the difference between the excited and ground clock-state polarizabilities. The proportionality factor here is for a shift in hertz, temperature in kelvin, and differential polarizability in atomic units. The results of the fractional BBR shifts at room temperature are shown in Table 10.3. It can be seen from the table that the differential polarizabilities are extremely small, which results in small values for BBR shifts. Note that even the use of the most optimistic assumption about the accuracy of the calculation of the polarizabilities (1%) leads to large uncertainties in the BBR shift. This means that the numbers for the BBR shift in Table 10.3 should be considered as upper limits.

In order to calculate the second-order Zeeman shift (δv_{SZ}), we have to take into account an influence caused by a weak homogeneous external magnetic field. For the determination of δv_{SZ}, the following formula can be used [37]

$$\delta\nu_{\mathrm{SZ}} = -\frac{1}{2h}\Delta\alpha^{\mathrm{M1}} B^2, \tag{10.17}$$

where h is Planck's constant, B is the magnetic field, and $\Delta\alpha^{\mathrm{M1}}$ is the difference between the magnetic-dipole polarizability of the ground and excited clock states, $\Delta\alpha^{\mathrm{M1}} =$

$\alpha^{\mathrm{M1}}(\mathrm{ES}) - \alpha^{\mathrm{M1}}(\mathrm{GS})$. The $M1$ polarizability can be calculated using Eq. (10.15), but the amplitude of the electric-dipole transitions (A_{vn}) should be replaced with the amplitude of the magnetic-dipole transitions. Our results are shown in Table 10.3. It should be mentioned that the magnetic-dipole polarizabilities can be calculated with just a few low-lying states since their contributions dominate. In the case of the atomic systems considered here, only the first two low-lying states belonging to the same configuration give significant contributions. Here only the scalar contribution is presented. A tensor contribution of similar magnitude also exists, though it can be canceled with certain averaging schemes. In any case, the scalar results illustrate the scale of the second-order Zeeman shift, which is negligibly small for small ($\sim \mu$T) magnetic fields.

10.5.4 Sensitivity of the clock transitions to variation of the fine-structure constant

Variations in the fine-structure constant could lead to an observable effect on the clock transition frequency. The relationship between the clock frequency and the fine-structure constant in the vicinity of their physical values can be expressed as

$$\omega = \omega_0 + q \left[\left(\frac{\alpha}{\alpha_0} \right)^2 - 1 \right], \tag{10.18}$$

where α_0 and ω_0 are the laboratory values of the fine-structure constant and the transition frequency, respectively, and q is the sensitivity coefficient that is determined from atomic calculations [38]. Note that we do not consider variation of atomic unit of energy $m_e e^4/\hbar^2$ since it cancels out in the ratio of frequencies. Variation of dimensionful parameters like $m_e e^4/\hbar^2$ depend on the units one uses. For example, in atomic units it is equal to 1 and does not vary. Therefore, dependence of frequencies on α appears due to relativistic corrections.

Table 10.4: Sensitivity of clock transitions to variation of the fine-structure constant (q, K).

System	State	ω (cm^{-1})	q (cm^{-1})	K
		Te-like systems		
Te	$5p^4\ ^3P_0$	4706	3261	1.39
Xe^{2+}	$5s^25p^4\ ^3P_0$	8130	5611	1.38
Ba^{4+}	$5s^25p^4\ ^3P_0$	11302	5976	1.06
Ce^{6+}	$5s^25p^4\ ^3P_0$	14210	5907	0.83
		Se-like systems		
Zr^{6+}	$4s^24p^4\ ^3P_0$	12557	8939	1.42
Cd^{14+}	$4s^24p^4\ ^3P_0$	28828	8837	0.61
		S-like systems		
Ge^{16+}	$3s^23p^4\ ^3P_0$	33290	18484	1.11
Kr^{20+}	$3s^23p^4\ ^3P_0$	46900	17252	0.74
Sr^{22+}	$3p^4\ ^3P_0$	53400	14130	0.53

The change in a frequency ratio ω_1/ω_2 caused by a change in α is

$$\delta\left(\frac{\omega_1}{\omega_2}\right) = \frac{\delta\omega_1}{\omega_1} - \frac{\delta\omega_2}{\omega_2} = (K_1 - K_2)\,\frac{\delta\alpha}{\alpha}. \tag{10.19}$$

The value $K = 2q/\omega$ is often called the enhancement factor. We calculate q and K by using two different values of α and calculating the numerical derivative

$$q = \frac{\omega(x) - \omega(-x)}{2x}, \tag{10.20}$$

where $x = (\alpha/\alpha_0)^2 - 1$ [see Eq. (10.18)]. In order to achieve linear behavior, the x value must be small; however, it must be large enough to suppress numerical noise. Accurate results can be obtained by using $x = 0.01$. A summary of the calculated values of q and K is given in Table 10.4.

10.6 EXPERIMENTAL OUTLOOK

Here, we discuss the experimental outlook for the development of optical atomic clocks based on these systems. The systematic shifts considered in previous sections are limited

Table 10.5: Lifetime-limited frequency instability for a single clock ion and the optimal logic ion based on charge-to-mass ratio ((q/m)); m are the average values of mass over all isotopes, taken from NIST data [12]. The notation $x[y]$ abbreviates $x \times 10^y$.

System	ν (Hz)	σ_y (1s)	Logic Ion	$\frac{(q/m)_{\text{Logic Ion}}}{(q/m)_{\text{Clock Ion}}}$
		Te-like systems		
Te	1.411[14]	2.6[−16]	–	–
Xe^{2+}	2.437[14]	3.4[−16]	Sr^+	0.749
Ba^{4+}	3.388[14]	4.1[−16]	Ca^+	0.857
Ce^{6+}	4.260[14]	4.5[−16]	Mg^+	0.961
		Se-like systems		
Zr^{6+}	3.764[14]	2.3[−16]	Be^+	1.687
Cd^{14+}	8.642[14]	4.2[−16]	Be^+	0.891
		S-like systems		
Ge^{16+}	9.980[14]	2.0[−16]	Be^+	0.504
Kr^{20+}	1.406[15]	2.6[−16]	Be^+	0.465
Sr^{22+}	1.601[15]	2.9[−16]	Be^+	0.442

by the atomic properties of the respective system. However, when estimating the expected clock performance, it is important to also consider systematic shifts due to ion motion (time dilation) and the expected frequency instability. To estimate the frequency instability, we consider a Ramsey interrogation sequence for a single ion with interrogation time equal to the natural lifetime, assuming the instability to be limited by fundamental quantum projection noise [39]. Under these conditions, the fractional instability is given by [10,40]

$$\sigma_y(t) = \frac{0.412}{\nu\sqrt{\tau t}}, \tag{10.21}$$

where ν is the clock frequency, τ is the lifetime of the excited clock state, and t is the averaging time. These results are summarized in Table 10.5. All systems exhibit frequency instabilities, for a single clock ion, of $\sigma_y(t) < 5 \times 10^{-16}/\sqrt{t/\text{s}}$. This level of performance is comparable to recent demonstrations in $Al^+$and Yb^+ [3,41,42]. Since none of the ions proposed here possess electric-dipole-allowed ($E1$) transitions for cooling and state readout, it will be necessary to utilize a scheme such as quantum-logic spectroscopy (QLS) for clock operations [43]. The application of QLS requires the clock ion to be cotrapped with an auxiliary readout "logic" ion which does possess a laser-accessible transition for cooling and state readout operations. In addition, ion-based optical clocks are susceptible to time-dilation shifts due to driven excess micromotion (EMM) and secular (thermal) motion due to the finite ion temperature. The secular motion can be reduced by applying sympathetic cooling of the clock ion via the cotrapped logic ion. The most efficient sympathetic cooling occurs when the charge-to-mass ratio of the clock ion is equal to that of the logic ion [44]. For each ion considered here, we estimate the logic ion which would be the best match for sympathetic cooling. These results are listed in Table 10.5.

The excess micromotion shift is a result of imperfections in the trap potential, typically caused by stray electric fields and/or phase shifts between rf drive electrodes that lead to residual rf fields at the location of the ion [18]. This shift can be minimized by using a trap design which has been shown to have low EMM [3, 45].

10.7 SUMMARY

In conclusion, we identify group-16-like ions as promising candidates for high-accuracy optical clocks. This class of ions exhibit irregular ordering in the ground ^3P_J fine-structure manifold for large enough ionization degree, leading to $E2$ clock transitions with narrow natural linewidths. Due to the increased charge state, several common systematic shifts are reduced compared to many of the current species used for optical clocks.

Acknowledgments

The authors thank C.-C. Chen, G. Hoth, and D. Slichter for their careful reading of the manuscript. S.O.A. gratefully acknowledges the Islamic University of Madinah (Ministry of Education, Kingdom of Saudi Arabia) for funding his scholarship. This work was supported by the National Institute of Standards and Technology/Physical Measurement Laboratory. This work was also supported by the Australian Research Council Grants No. DP190100974 and No. DP200100150 and by NSF Grant No. PHY-2110102 and ONR Grant No. N00014-22-1-2070. This research includes computations using the computa-

tional cluster Katana supported by Research Technology Services at UNSW Sydney [46].

References

[1] A. D. Ludlow, M. M. Boyd, J. Ye, E. Peik, and P. O. Schmidt, Optical atomic clocks, Rev. Mod. Phys. **87**, 637 (2015).

[2] M. S. Safronova, D. Budker, D. DeMille, Derek F. Jackson Kimball, A. Derevianko, and C. W. Clark, Search for new physics with atoms and molecules, Rev. Mod. Phys. **90**, 025008 (2018).

[3] S. M. Brewer, J. S. Chen, A. M. Hankin, E. R. Clements, C. W. Chou, D. J. Wineland, D. B. Hume, and D. R. Leibrandt, $^{27}\mathrm{Al}^{+}$ Quantum-Logic Clock with a Systematic Uncertainty below 10^{-18}, Phys. Rev. Lett. **123**, 033201 (2019).

[4] W. F. McGrew, X. Zhang, R. J. Fasano, S. A. Schäffer, K. Beloy, D. Nicolodi, R. C. Brown, N. Hinkley, G. Milani, M. Schioppo et al., Atomic clock performance enabling geodesy below the centimetre level, Nature **564**, 87 (2018).

[5] T. Bothwell, D. Kedar, E. Oelker, J. M. Robinson, S. L. Bromley, W. L. Tew, J. Ye, and C. J. Kennedy, JILA SrI optical lattice clock with uncertainty of 2.0×10^{-18}, Metrologia **56**, 065004 (2019).

[6] N. Huntemann, C. Sanner, B. Lipphardt, C. Tamm, and E. Peik, Single-Ion Atomic Clock with 3×10^{-18} Systematic Uncertainty, Phys. Rev. Lett. **116**, 063001 (2016).

[7] J. C. Berengut, V. A. Dzuba, and V. V. Flambaum, Enhanced Laboratory Sensitivity to Variation of the Fine-Structure Constant using Highly Charged Ions, Phys. Rev. Lett. **105**, 120801 (2010).

[8] J. C. Berengut, V. A. Dzuba, V. V. Flambaum, and A. Ong, Electron-Hole Transitions in Multiply Charged Ions for Precision Laser Spectroscopy and Searching for Variations in α, Phys. Rev. Lett. **106**, 210802 (2011).

[9] J. C. Berengut, V. A. Dzuba, V. V. Flambaum, and A. Ong, Optical Transitions in Highly Charged Californium Ions with High Sensitivity to Variation of the Fine-Structure Constant, Phys. Rev. Lett. **109**, 070802 (2012).

[10] M. G. Kozlov, M. S. Safronova, J. R. Crespo López-Urrutia, and P. O. Schmidt, Highly charged ions: Optical clocks and applications in fundamental physics, Rev. Mod. Phys. **90**, 045005 (2018).

[11] J. C. Berengut, V. A. Dzuba, V. V. Flambaum, and A. Ong, Highly charged ions with $E1, M1$, and $E2$ transitions within laser range, Phys. Rev. A **86**, 022517 (2012).

[12] A. Kramida, Y. Ralchenko, J. Reader, and NIST ASD Team, NIST Atomic Spectra Database (ver. 5.7.1), https://physics. nist.gov/asd (National Institute of Standards and Technology, Gaithersburg, MD, 2020).

[13] K. Cheng, Y.-K. Kim, and J. Desclaux, Electric dipole, quadrupole, and magnetic dipole transition probabilities of ions isoelectronic to the first-row atoms, LI through F, At. Data Nucl. Data Tables **24**, 111 (1979).

[14] R. Gayasov, Y. N. Joshi, and A. Tauheed, Sixth spectrum of lanthanum (La VI): analysis of the $\mathrm{5s^25p^4, 5s5p^5}$ and $\mathrm{5s^25p^3(5d + 6s\ )}$ configurations, J. Phys. B: At., Mol. Opt. Phys. **30**, 873 (1997).

[15] A. Tauheed and Y. N. Joshi, The $\mathrm{5s^25p^4}$-$\mathrm{(5s5p^5 + 5p^36s)}$ transitions in Ce VII and $\mathrm{5s^25p^3\ ^4s - 5s5p^4\ ^4}p$ transitions in Ce VIII, Can. J. Phys. **86**, 714 (2008).

[16] J. Reader and N. Acquista, $4s^24p^4 - 4s4p^5$ transitions in Zr VII, Nb VIII, and Mo IX, J. Opt. Soc. Am. **66**, 896 (1976).

[17] K. Beloy, V. A. Dzuba, and S. M. Brewer, Quadruply Ionized Barium as a Candidate for a High-Accuracy Optical Clock, Phys. Rev. Lett. **125**, 173002 (2020).

[18] D. J. Berkeland *et al.*, Minimization of ion micromotion in a Paul trap, J. Appl. Phys. **83**, 5025 (1998).

[19] V. A. Dzuba, Combination of the single-double-coupled-cluster and the configuration-interaction methods: Application to barium, lutetium, and their ions, Phys. Rev. A **90**, 012517 (2014).

[20] W. R. Johnson and J. Sapirstein, Computation of Second-Order Many-Body Corrections in Relativistic Atomic Systems, Phys. Rev. Lett. **57**, 1126 (1986).

[21] W. R. Johnson, S. A. Blundell, and J. Sapirstein, Finite basis sets for the Dirac equation constructed from B splines, Phys. Rev. A **37**, 307 (1988).

[22] V. A. Dzuba, V. V. Flambaum, P. G. Silvestrov, and O. P. Sushkov, Correlation potential method for the calculation of energy levels, hyperfine structure and E1 transition amplitudes in atoms with one unpaired electron, J. Phys. B: At. Mol. Phys. **20**, 1399 (1987).

[23] V. A. Dzuba, V. V. Flambaum, and M. G. Kozlov, Combination of the many-body perturbation theory with the configuration interaction method, Phys. Rev. A **54**, 3948 (1996).

[24] V. A. Dzuba, J. C. Berengut, C. Harabati, and V. V. Flambaum, Combining configuration interaction with perturbation theory for atoms with a large number of valence electrons, Phys. Rev. A **95**, 012503 (2017).

[25] K. Wang, X. Yang, Z. Chen, R. Si, C. Chen, J. Yan, X. H. Zhao, and W. Dang, Energy levels, lifetimes, and transition rates for the selenium isoelectronic sequence Pd XIII-Te XIX, Xe XXI-Nd XXVII, W XLI, At. Data Nucl. Data Tables **117-118**, 1 (2017).

[26] R. H. Garstang, Transition probabilities of forbidden lines, J. Res. Natl. Bur. Stand. Sect. A **68A**, 61 (1964).

[27] E. Biémont, J. E. Hansen, P. Quinet, and C. J. Zeippen, Forbidden transitions of astrophysical interest in the 5p^k($k = 1-5$) configurations, Astron. Astrophys., Suppl. Ser. **111**, 333 (1995).

[28] E. Biémont and J. E. Hansen, Forbidden transitions in $3p^4$ and $4p^4$ configurations, Phys. Scr. **34**, 116 (1986).

[29] P. Schwerdtfeger and J. K. Nagle, 2018 table of static dipole polarizabilities of the neutral elements in the periodic table, Mol. Phys. **117**, 1200 (2019).

[30] W. Itano, External-field shifts of the ^{199}Hg$^+$ optical frequency standard, J. Res. Natl. Inst. Stand. Technol. **105**, 829 (2000).

[31] A. Kozlov, V. A. Dzuba, and V. V. Flambaum, Optical atomic clocks with suppressed blackbody-radiation shift, Phys. Rev. A **90**, 042505 (2014).

[32] V. Dzuba, Calculation of polarizabilities for atoms with open shells, Symmetry **12**, 1950 (2020).

[33] A. Dalgarno and J. T. Lewis, The exact calculation of longrange forces between atoms by perturbation theory, Proc. R. Soc. London, Ser. A **233**, 70 (1955).

[34] V. A. Dzuba, V. V. Flambaum, J. S. M. Ginges, and M. G. Kozlov, Electric dipole moments of $\mathrm{Hg, Xe, Rn, Ra, Pu}$, and TIF induced by the nuclear Schiff moment and limits on timereversal violating interactions, Phys. Rev. A **66**, 012111 (2002).

[35] V. A. Dzuba and V. V. Flambaum, Calculation of the (T, P)-odd electric dipole moment of thallium and cesium, Phys. Rev. A **80**, 062509 (2009).

[36] V. A. Dzuba and A. Derevianko, Dynamic polarizabilities and related properties of clock states of the ytterbium atom, J. Phys. B **43**, 074011 (2010).

[37] S. G. Porsev and M. S. Safronova, Calculation of higher-order corrections to the light shift of the $5s^2\ ^1S_0 - 5s5p\ ^3P_0^o$ clock transition in Cd, Phys. Rev. A **102**, 012811 (2020).

[38] V. V. Flambaum and V. A. Dzuba, Search for variation of the fundamental constants in atomic, molecular, and nuclear spectra, Can. J. Phys. **87**, 25 (2009).

[39] W. M. Itano, J. C. Bergquist, J. J. Bollinger, J. M. Gilligan, D. J. Heinzen, F. L. Moore, M. G. Raizen, and D. J. Wineland, Quantum projection noise: Population flucturation in two-level systems, Phys. Rev. A **47**, 3554 (1993).

[40] E. Peik, T. Schneider, and C. Tamm, Laser frequency stabilization to a single ion, J. Phys. B **39**, 145 (2006).

[41] E. R. Clements, M. E. Kim, K. Cui, A. M. Hankin, S. M. Brewer, J. Valencia, J.-S. Chen, C.-W. Chou, D. R. Leibrandt, and D. B. Hume, Lifetime-Limited Interrogation of Two Independent $^{27}\mathrm{Al}^{+}$ Clocks using Correlation Spectroscopy, Phys. Rev. Lett. **125**, 243602 (2020).

[42] C. Sanner, N. Huntemann, R. Lange, C. Tamm, E. Peik, M. S. Safronova, and S. G. Porsev, Optical clock comparison for Lorentz symmetry testing, Nature (London) **567**, 204 (2019).

[43] P. O. Schmidt, T. Rosenband, C. Langer, W. M. Itano, J. C. Bergquist, and D. J. Wineland, Spectroscopy using quantum logic, Science **309**, 749 (2005).

[44] J. B. Wübbena, S. Amairi, O. Mandel, and P. O. Schmidt, Sympathetic cooling of mixed-species two-ion crystals for precision spectroscopy, Phys. Rev. A **85**, 043412 (2012).

[45] K. Pyka, N. Herschbach, J. Keller, and T. E. Mehlstäubler, A high-precision segmented Paul trap with minimized micromo- tioin for an optical multiple-ion clock, Appl. Phys. B **114**, 231 (2014).

[46] Katana (shared computational cluster), University of New South Wales, Sydney, https://doi.org/10.26190/669x-a286.

Chapter 11

Conclusion

In conclusion, we have undertaken a number of studies of the electronic structure of several heavy atomic systems using IS and hyperfine structures. In the first study, we calculated field isotope shift for four electric dipole atomic transitions in two nobelium isotopes (^{252,254}No). This study demonstrated that comparing calculated isotope shifts with experiments can help to distinguish between nuclear models endorsing predictions from best-fit models. We also showed that if we have isotope shift measurements for at least two atomic transitions, we can extract not only the change in nuclear RMS radius, but also the change in nuclear shape.

We also used IS to study the nonlinearity observed in the recent experiment with the Yb$^+$ ion. We have examined the theoretical aspect of this nonlinearity by taking the nuclear parameters of the Yb isotopes from a range of state-of-the-art nuclear models. According to our findings, recently observed King plot nonlinearities in Yb$^+$ are most likely the result of nuclear deformation. In addition, the study demonstrated that measurements of King plot nonlinearity can be used to study nuclear deformation in zero-spin nuclei where the nuclear electric quadrupole moment cannot be obtained through atomic spectroscopy.

As part of our hyperfine structure study, we have performed calculations of the magnetic dipole HFS constant (A) and electric quadrupole HFS constant (B) for the superheavy elements Fm and Rf and the heavy elements Cf and Es. Calculation of the hyperfine structure (HFS) for heavy and superheavy elements provides a possibility to extract from future HFS measurements magnetic dipole and electric quadrupole moments of the nuclei. Similar calculations have also been carried out on the lighter homologs Er, Hf, Dy, and Ho, whose electronic structures are analogous to Fm, Rf, Cf, and Es, respectively, to verify the calculations.

This thesis also included a number of studies investigating many excited metastable states in atoms and ions to reveal promising atomic clocks. As a result of these studies, promising systems have been identified that are capable of acting as very accurate atomic clocks, and being highly sensitive to new physics. Numerous atomic properties, such as energy levels, transition amplitudes, lifetimes, polarizabilities of the ground and clock states, etc., have been calculated. We found that relative blackbody radiation (BBR) shifts are small, between 10^{-16} and 10^{-18}, and the effects of variation of the fine-structure constant (α) are enhanced up to 8.3 times. Our results also showed that most of the proposed atomic systems have the additional benefit of having more than one clock transition in the same system. It is necessary to measure two clock frequencies against each other over a long period of time to search for a variation of the fine structure constant. It is very convenient to have both transitions in the same atomic system. A combination of two clock frequencies into one synthetic frequency also allows for significantly suppressing sensitivity to black body radiation shifts.

The calculations of spectra and transition amplitudes of atomic systems in all these studies have been performed using two different versions of the configuration interaction (CI) method. The choice depends on the number of valence electrons. The first method is called CI+SD (configuration interaction with the single-double coupled cluster method), which is applicable to atomic systems with a few valence electrons (up to four). The second method is called CIPT (configuration interaction with the perturbation theory method). It is designed to work with atomic systems with many valence electrons (more than four).

The studies presented in this thesis point to great opportunities which atomic systems with metastable states present for time-keeping, studying the nuclear structure, and searching for new physics. Different systems have different advantages in terms of making measurements and interpreting the data. We plan to continue the search for suitable candidates by taking a closer look at more complex atomic systems; this may include a more detailed study of the atomic systems with open d or f shells, as well as the study of highly charged ions with optical transitions between states of different configurations.